Organic-based hybrid materials for Thermoelectric Applications

by

VIJITHA I.

10PP14A39010

A thesis submitted to the

Academy of Scientific & Innovative Research

for the award of the degree of

DOCTOR OF PHILOSOPHY

in

SCIENCE

Under the supervision of

Dr. Biswapriya Deb

CSIR-National Institute for Interdisciplinary Science and Technology (CSIR-NIIST)

Thiruvananthapuram

Academy of Scientific and Innovative Research

AcSIR Headquarters, CSIR-HRDC campus

Sector 19, Kamla Nehru Nagar,

Ghaziabad, U.P. – 201 002, India

December 2021

Dedicated to

My beloved father

Late Mr. Ignatious Joseph

CSIR - National Institute for Interdisciplinary Science and Technology (NIIST)

Council of Scientific & Industrial Research (CSIR)
Industrial Estate P.O., Trivandrum - 695 019, INDIA

Biswapriya Deb, Ph.D.
Principal Scientist & Assoc. Prof. (AcSIR)
Photosciences and Photonics
Chemical Sciences and Technology Division

Tel: +91-471-2515-478 (Office)
+91-949-521-0200 (Mob)
E-mail: biswapriya.deb@niist.res.in
biswapriya.deb@gmail.com

CERTIFICATE

This is to certify that the work incorporated in this Ph.D. thesis entitled "*Organic-based hybrid materials for Thermoelectric Applications*," submitted by *Vijitha I.* to the Academy of Scientific and Innovative Research (AcSIR), in partial fulfillment of the requirements for the award of the Degree of *DOCTOR OF PHILOSOPHY in SCIENCE*, embodies original research work carriedout by the student. We further certify that this work has not been submitted to any other University or Institution in part or full for the award of any degree or diploma. Research material(s) obtained from other source(s) and used in this research work has/have been duly acknowledged in the thesis. Image(s), illustration(s), figure(s), table(s) etc., used in the thesis from other source(s), have also been duly cited and acknowledged.

8/12/21

Vijitha I.

8/12/2024

Dr. Biswapriya Deb

STATEMENTS OF ACADEMIC INTEGRITY

I Vijitha I., a Ph.D. student of theAcademy of Scientific and Innovative Research (AcSIR) with Registration No.10PP14A39010hereby undertake that the thesis entitled"Organic-based hybrid materials for Thermoelectric Applications" has been prepared by me and that the document reports original work carried out by me and is free of any plagiarism in compliance with the UGC Regulations on "Promotion of Academic Integrity and Prevention of Plagiarism in Higher Educational Institutions (2018)" and the CSIR Guidelinesfor "Ethics in Research and in Governance (2020)".

8/12/21

Vijitha I.

Date: 08/12/2021

Place: Thiruvananthapuram

It is hereby certified that the work done by the student under my supervision is plagiarismfreein accordance with the UGC Regulations on "Promotion of Academic Integrity andPrevention of Plagiarism in Higher Educational Institutions (2018)" and the CSIR Guidelinesfor "Ethics in Research and in Governance (2020)".

8/12/2021

Dr. Biswapriya Deb

Date: 08/12/2021

Place: Thiruvananthapuram

DECLARATION

I, Vijitha I., bearing AcSIR RegistrationNo. 10PP14A39010,declare that my thesis entitled "Organic-based hybrid materials for Thermoelectric Applications" isplagiarism free in accordance with the UGC Regulations on "Promotion of Academic Integrity and Prevention of Plagiarism in Higher Educational Institutions (2018)" andthe CSIR Guidelines for "Ethics in Research and in Governance (2020)".I would be solely held responsible if any plagiarized content in my thesis is detected, which is violative of the UGC regulations 2018.

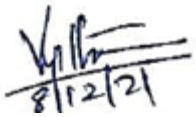

Vijitha I.

Date: 08/12/2021

Place: Thiruvananthapuram

ACKNOWLEDGEMENTS

Ph.D. life was a challenging and rewarding experience. I consider myself very lucky to have had been able to interact with many incredible scientists and friends, and I would like to take a moment to thank them for their role in this Ph.D. journey.

First of all, it is my genuine pleasure to express my sincere gratitude to my mentor, Ph.D. supervisor **Dr. Biswapriya Deb**, who was always there to help me with great patience and interest throughout these years. Throughout the Ph.D., we had great scientific and personal discussions. Several ideas in this thesis were the outcomes of these scientific discussions. Joining his lab was the best decision of my life. I thank him for introducing me to the world of material science and giving me the scientific freedom that helped me develop the confidence to move in this field.

I especially thank **Dr. C. Vijayakumar**, my Doctoral Advisory Committee (DAC) member, for his help, care, and fruitful discussions during my research at CSIR-NIIST. More than a DAC member, I want to acknowledge him as my co-guide, who has supported and encouraged me throughout these years. I am incredibly grateful for the sheer endless amount of patience and goodwill he has shown me.

I wish to thank **Dr. A. Ajayaghosh**, Director and **Dr. Gangan Pratap,** and **Dr. Suresh Das**, former Directors of the CSIR-NIIST, for providing me with the necessary facilities for carrying out the work.

I sincerely thank my other DAC members, **Dr. K.N. Narayanan Unni**, **Dr. K. P. Surendran,** and **Dr. M. Vasunthara** (former), for their support and insightful comments regarding my work and constructive criticism, which always helped me to constantly question myself and look at my work from a different perspective.

I extend my sincere thanks to **Dr. V. Karunakaran, Dr. C. H. Suresh**, **Dr. Luxmi Varma,** and **Dr. Mangalam S. Nair,** present and former AcSIR coordinators at CSIR-NIIST for their timely help and advice for the academic procedures of AcSIR.

I want to thank **Dr. K. R. Gopidas, Dr. Sujatha Devi, Dr. Joshy Joseph, Dr. V. K. Praveen, Dr. Suraj Soman, Dr. Sreejith Sankar, Dr. Rakhi R. B.,** and all other scientists of the CSIR-

NIIST for their help and support extended to me. A special thanks to former scientists **Dr. Bijitha Balan** and **Dr. Raj Sankar** for their encouragement and support.

I am very much thankful to **Dr. S.N. Potty** (C-MET), **Mr. Srinivas Deo** (CSIR-NCL), and **Mr. Visakh M.** (CUSAT) for helping in material characterization.

I thank **Dr. Saju Pillai** and **Mr. Peer Mohamed** for helping me in XPS studies.

Also, I thank **Dr. K.K. Maiti** for his help in carrying Raman Spectroscopy measurements.

My sincere thanks to **Mr. Kiran Mohan**, **Mr. Harish Raj**, **Mr. Amal Raj,** and **Mr. Vibhu Darshan** for their help in conducting TEM, SEM, XRD, and AFM analysis. I am highly indebted to the support offered by Technical Advisors **Mr. Robert Philip** and **Mr. Kiran J. S**.

I thank my previous Ph.D. colleagues, **Dr. Remya R.,** and **Dr. Gayathri Prabhu T.G.**, for the great discussions we had during the initial days of my Ph.D. I have learned a lot from both of you, and thanks for your companionship, understanding, encouragement, and personal attention, professionally and personally.

I am grateful to my dear former junior, **Arjun P.,** for sharing long workweeks as we built our thermoelectrics lab from scratch, for the long conversations, and for being with me all the time.

From the bottom of my heart, I would like to thank my fellow juniors, thermoelectrics folks **Neethi Raveendran** and **Navin Jacob,** for their words of encouragement, moments of friendship, and affection. I wish you all an excellent time ahead with a tremendous academic and personal outcome.

The rest of the Smart Materials & Devices Group, including **Dr. Sajitha Surendren**, **Shaiju S.S.**, **Ranjana Venugopal**, **Nayan Dev Madhav**, **Jiflin Das**, **Amritha P.**, **Sruthy Poovattil, Lakshmi V.K.**, **Nithin R.S.**, **Dr. Swetha S.**, **Vishnu Prasad C. V.,** and **Abhishek A. K.,** helped to create a supportive and hardworking space for good science.

I am deeply grateful to all the present and former students I've worked with within NIIST. In particular, I want to thank **Vindhya Sarumi A.**, **Dr. Sumina B.**, **Dr. Sreejith M.**, **Bamisha Balan, Dr. Silja Abraham**, **Dr. Tanwishta Ghosh**, **Dr. Jayanthi S. Panicker**, **Dr. Sankar S.** and **Dr. Rajeev V.R.**, for their love, support, and friendship.

I take this opportunity to thank my MSc project student **Anjali S.J.**, for her support in developing my teaching experience.

I acknowledge the **Gas Authority of India Limited (GAIL)** and the **Council of Scientific & Industrial Research (CSIR)** for providing research funding to complete this work. And I thank **DST-Inspire** for providing me with the fellowship.

I dedicate this thesis in memory of my beloved father, ***Late.*** **Ignatious**. I am deeply grateful to my mother, **Vimala,** and my sister, **Vibitha**, for their continued energy and unerring support in my life.

I am deeply grateful to my sweet daughter, **Nehal**, for cooperating with me during the thesis writing stage. Finally, to my husband, **Gipson**, thank you so much for all the patience, understanding, and support throughout these years- without you, this would not have been possible!

Thanks to the Almighty!

Vijitha I.

CONTENTS

LIST OF FIGURES

LIST OF TABLES

LIST OF ABBREVIATIONS

Å	Angstrom
α	Seebeck coefficient
κ	Thermal conductivity
σ	Electrical conductivity
AFM	Atomic Force Microscopy
BDT	Benzo-[1,2-b:4,5-b’]dithiophene
BE	Binding energy
CNT	Carbon nanotube
CPD	Contact potential difference
CTC	Charge transfer complex
DOS	Density of states
DOVS	Density of valance state
E_F	Fermi level
eV	Electron volt
h	Planck's constant
HOMO	Highest occupied molecular orbit
k_B	Boltzmann constant
KE	Kinetic energy
KP	Kelvin probe
LUMO	Lowest occupied molecular orbit
ME	Mobility edge

MWCNT	Multi-walled carbon nanotube
NIR	Near infra-red
OFET	Organic field-effect transistors
OSC	Organic solar cells
PF	Power factor
SEM	Scanning Electron Microscopy
SWCNT	Single-walled carbon nanotube
TE	Thermoelectrics
TEG	Thermoelectric generator
TEM	Transmission Electron Microscopy
TGA	Thermogravimetric Analysis
TTE	Theinothiophene
UPS	Ultra-Violet Photoelectron Spectroscopy
UV	Ultra-Violet
VB	Valance band
VBM	Valance band maxima
VRH	Variable range hopping
WAXS	Wide-Angle X-ray Scattering
WF	Work function
XPS	X-ray Photoelectron Spectroscopy
ZT	Figure of merit

PREFACE

With the looming energy crisis, harvesting waste heat to produce electricity has recently garnered widespread attention. Mainly, hot water released by the industries, automotive exhaust, and high-temperature industrial processing is the primary waste heat source, a conversion of which could ensure significant social benefits by producing clean energy and reducing fuel cost. Thermoelectric (TE) materials, which can convert heat energy into electric energy and vice versa, show potential for turning waste heat into power. The TE modules are solid-state devices, have no moving parts, and are silent, reliable, lightweight, and durable. Although the automobile industry has started to use TE technology for their hot gas exhaust, mainly inorganic modules, there is an enormous need for cheaper and lighter TE modules, preferably flexible and low-temperature range.

Organic-based hybrid TE materials now exhibit figure-of-merit comparable to the inorganic systems. These advances in materials progress help design superior TE devices for commercial usage while at the same time leveraging environmentally friendly and unique processing advantages. Nevertheless, to realize the utilization of such technologies, there is a fundamental need for a thorough understanding of the underlying science in these materials' TE transport and electronics properties.

The central focus of this thesis is investigating the fundamental phenomena critical to the effect of doping in conjugated thienothiophene polymer/carbon nanotube-based systems. Additionally, the carrier transport mechanisms, physics responsible for the high TE performance, and theoretical modeling of thermal transport property in these materials are studied. The design, fabrication, and simulation of TE modules prototype give insight for applications in new on-spot power generation technologies like wearable electronics and the Internet of Things.

CHAPTER 1

Thermoelectric Phenomena, Materials and Devices: An Overview

The global energy demand increases yearly, and the topic would continue to be one of the most critical issues to be mitigated by the next decade [1]. The rapid growth of population and the industrial developments demand an adequate and secure supply of energy, which must be achieved with minimal environmental detriments. Using fossil fuels to generate energy has become harmful for humankind because of its adverse impact on the atmosphere [2].

According to the International Energy Agency (IEA), the energy sector has faced more disruption due to the Covid-19 pandemic in recent history, and the impacts to be felt for years to come. Surprisingly, in 2020, the global energy demand has decreased by 5%, energy-related CO_2 emissions by 7%, and energy investment by 18%. Before the pandemic, energy demand was projected to grow by 12% between 2019 and 2030, as shown in Fig.1.1. Even during the crisis, usage of renewables proliferates and should meet ~80% of the growth in global electricity demand by 2030. There is a notable increase in global energy demand in Asia, where China and India contributed more than 40%. An increase was also recorded in Southeast Asia (8%) and Africa (6%), though per capita energy usage in these regions remains below the global average. The most considerable contribution to demand growth comes from India (30%), whose share of global energy use will rise to 11% by 2040 [3].

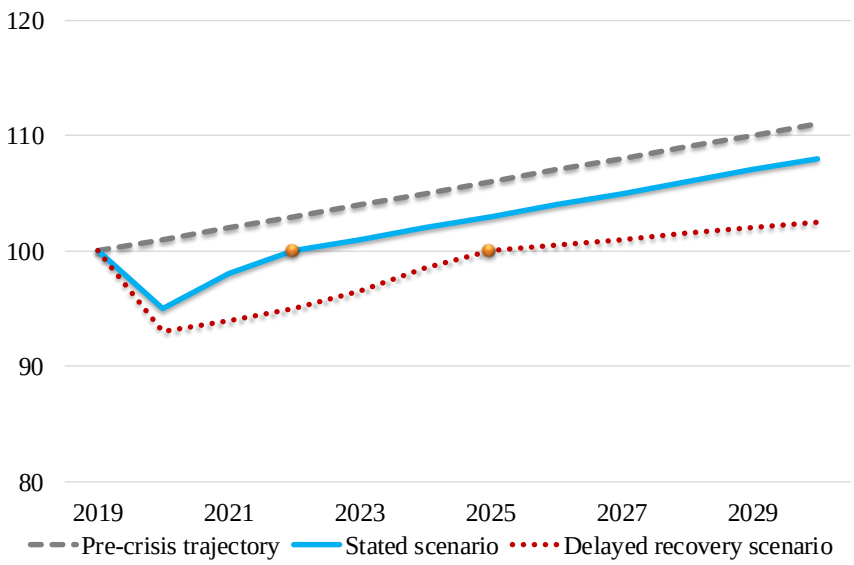

Fig. 1.1. Global primary energy demand growth by scenario 2019-2030. Adapted from Ref. [3].

It is crucial to employ safe and cheap large-scale energy alternatives to fossil fuels. Several alternative sustainable energy sources, including solar, wind, biomass, hydro, and geothermal power, are available. India is one of the countries with the largest energy production from renewable sources. There is a high potential for the generation of renewable energy from various sources- wind, solar, biomass, small hydro and cogeneration bagasse in India (Fig. 1.2). Currently, renewable sources account for up to 35.8% of India's total installed power capacity. Out of that, hydropower accounts for about 17.6%, and the other sources generate the remaining. India is also rich with agro residues, therefore having an ideal environment for biomass production for energy usage. Estimated power generation from biomass reached around 10.14 GW as of 2020. In India, wind energy development has considerably increased over the years. By 2020, wind power capacity reached 38.12 GW, accounting for 10% of the total power capacity [4]. India's cumulative efforts toward expanding renewable energy have led to a significant increase in power generation over the past few years.

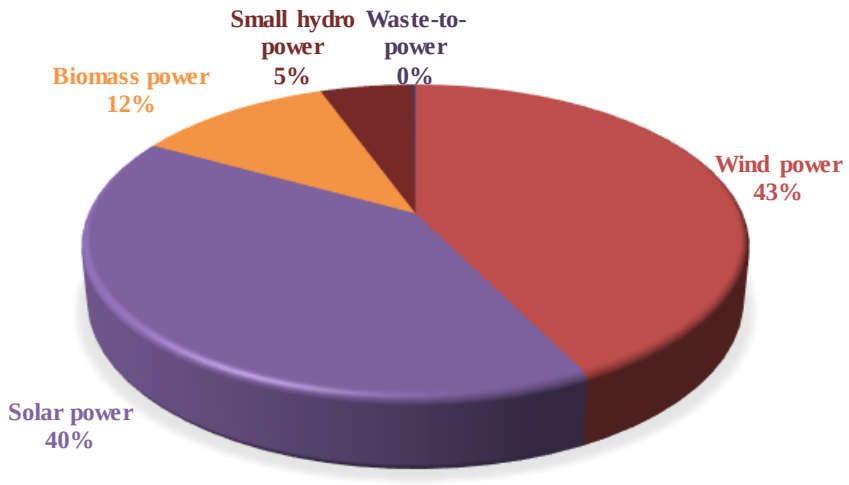

Fig. 1.2. Renewable power capacity in India as of 2020 (excluding large hydropower). Adapted from Ref.[4].

One relatively unexploited source of low-cost sustainable energy is waste heat. Without surprise, there is substantial interest in cost-effective technologies for energy generation by scavenging thermal waste. Thermoelectric generators (TEG) are the best green and sustainable waste heat recovery options. The technology is relatively inexpensive in the long run and directly generates electricity. Thermoelectric (TE) devices are meant to provide silent and long-lasting conversion that requires no moving parts. Conventional TEGs use heavy inorganic materials that are difficult to process. Therefore, there is a huge demand for lightweight TE materials that can be utilized for large-area applications and can handle low-grade heat conversion in the < 300 ºC range (covering most of the hot fluid release issues for the heavy industries).

1.1. Basic Elements of Thermoelectrics

The TE phenomenon is converting a temperature difference to electrical potential and vice-versa. The discovery of this phenomenon dates back to the 1800s, which had opened up many potential applications and a challenge to increase TE devices' performance. In the *Seebeck effect*,

a difference in temperature across a material creates a potential difference, causing charges to move from the higher temperature junction to the lower temperature junction of two dissimilar materials [5]. This fundamental TE phenomenon was Thomas Seebeck's discovery in 1821. Another related effect is the *Peltier effect*, discovered by Jean Peltier in 1934, who observed that heat absorption or rejection would occur, depending on the current direction, when an electric current goes through the junction of two dissimilar materials [6]. The factors which characterize the TE materials are unit-less Figure-of-Merit (ZT), electrical conductivity (σ), Seebeck coefficient (α), and thermal conductivity (κ) related by [7],

$$ZT = \frac{\sigma\alpha^2}{\kappa}T \tag{1.1}$$

The quantity $\sigma\alpha^2$ is called the power factor (PF). An ideal TE material comprises high σ to reduce Joule heating, low κ to block thermal shorting, and a high α to maximize the temperature to electricity conversion. However, since these three parameters are interrelated, there are challenges in maximizing ZT. The value of ZT must be at least 4 to get a device efficiency of 30% [8].

The majority carriers (electron or hole) determine the TE material types (*n* or *p*). A TE couple consists of n-type and p-type materials connected via metallic contacts called a unicouple, as shown in Fig.1.3 [9]. The TE module or device consists of a collection of these couples arranged electrically in series and thermally parallel. The TEG draws the electric power through an external circuit by employing a heat flow across a temperature gradient. The power input gives the efficiency (η) of the TE couple to the load (W) over the net heat flow rate (Q_H), where Q_H is positive for heat flow from the source to the sink [9],

$$\eta = \frac{W}{Q_H} = \frac{T_H - T_C}{T_H}\left[\frac{(1+ZT)^{1/2}-1}{(1+ZT)^{1/2}+(T_C/T_H)}\right] \tag{1.2}$$

where T_H and T_C are the hot and cold-side temperatures, respectively. Thus, η is directly proportional to $(1+ ZT)^{1/2,}$ and if ZT approaches infinity, η will reach the Carnot efficiency.

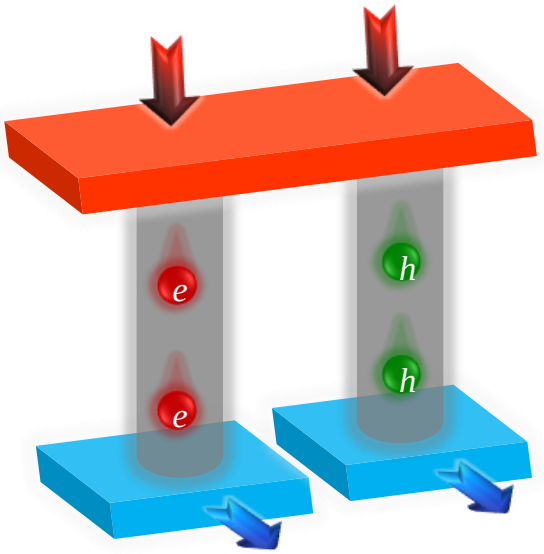

Fig. 1.3. (a) A TE couple in power generation mode. Adapted from Ref. [10].

Theoretically, α is a material's intrinsic property, developed when charge carriers move in response to a temperature gradient. In definition, α is the voltage (ΔV) induced by the temperature gradient (ΔT) across a material, measured in terms of μV/K and is given by,

$$\alpha = -\lim_{\Delta T \to 0} \frac{\Delta V}{\Delta T} \tag{1.3}$$

When a ΔT is applied across a material, the carriers from the hot side diffuse towards the cold side. The carriers on the hot side gain more kinetic energy than on the cold side, thereby accumulating the positive charge at the hot end and the negative charge at the cold side. At equilibrium, the diffusion of carriers stops, leaving opposite potential on both hot and cold ends [11].

It is necessary to have a single type of charge carrier, to ensure a considerable α value. A combination of p- and n-type conduction would lead both charge carriers to move to one end, canceling the induced Seebeck voltages [12]. Due to their low carrier concentration, materials like

insulators and semiconductors have large α. For metals or degenerate semiconductors, carrier concentration and α are interrelated by Mott's formula given by,

$$\alpha = \frac{8\pi^2 {k_B}^2}{3eh^2} m^* T \left(\frac{\pi}{3n}\right)^{2/3} \quad (1.4)$$

where n is the carrier concentration, m^* is the effective mass of the carrier, e is the elementary charge, h is the Planck's constant, and k_B is the Boltzmann constant. The α corresponds to the average of transported entropy per charge carrier; thus, increasing carrier concentration would lead to a decrease in the α value. Conversely, low carrier concentration also results in low σ. The relationship of σ and carrier concentration is commonly described using the Drude model for an electron gas given by,

$$\sigma = ne\mu \quad (1.5)$$

where n is the carrier concentration, e is the unit charge, and μ is the mobility.

Additional conflicts arise from the necessity for low κ, as κ is comprised of an electronic contribution (κ_e) and a lattice contribution (κ_L), given by,

$$\kappa = \kappa_e + \kappa_L \quad (1.6)$$

However, the Wiedemann–Franz law relates the electronic term (κ_e) directly to the σ, as,

$$\kappa_e = L\sigma T \quad (1.7)$$

where L is the Lorenz factor. Increasing the carrier concentration, κ_e increases as σ increases, resulting in the overall κ. As high σ and low κ are required to achieve high ZT, the Wiedemann–Franz law divulges an intrinsic discrepancy for high TE efficiency. This coupling between the TE properties is illustrated in Fig. 1.4 and results in a sweet spot where the ZT is maximum. This optimum occurs at carrier concentrations between 10^{19} and 10^{21} /cm^3, making heavily doped semiconductors the preferred class of TE materials [12].

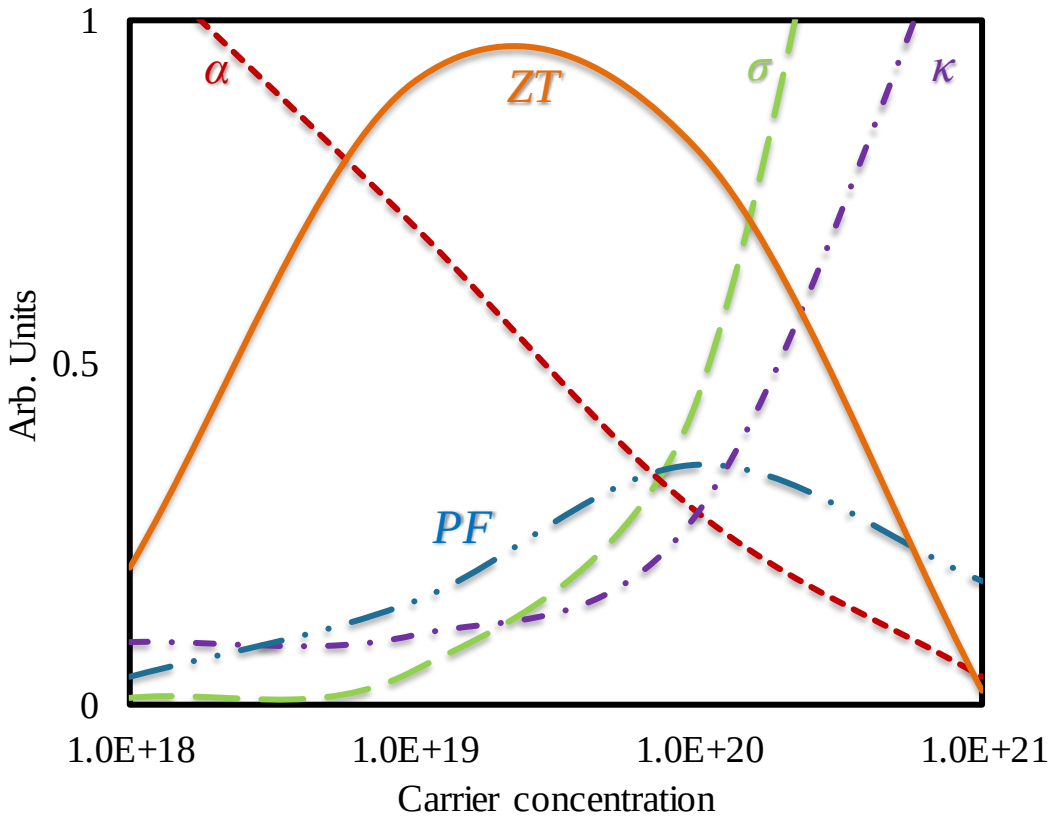

Fig. 1.4. Optimizing ZT through carrier concentration tuning. Adapted from Ref. [12].

The energy conversion efficiency of a TE material depends on its electrical/thermal transport. While electronic transport must be metal-like, phonon transport should be similar to glassy materials with low lattice thermal conductivity. Thermoelectricity, hence, requires a 'phonon glass-electron crystal' type material [13].

1.2. Towards Organic Thermoelectric Materials

The discoveries and advances in material science give life to the field of TE, which has been in slow-paced progress over the past few years. Before the 1990s, the hunt for suitable TE materials was mainly limited to bulk materials. However, over the last 30 years, broad research has been conducted in semiconductor structures [14]. The theoretical predictions suggest that

nanostructural engineering could significantly improve TE efficiency leading to efforts to demonstrate the proof-of-concept and high-efficiency materials/devices [15,16]. The inorganic TE material comprises many limitations, including the constituting elements such as bismuth, tellurium, antimony, and lead are toxic and not abundant. The fabrication of inorganic materials is costly concerning the energy and equipment needed, and hence the payback time is longer. Also, the heaviness and brittleness of most inorganic materials make them challenging to use in everyday life. All organic materials are potentially abundant, lightweight, flexible, solution-processable, and inexpensive. Hicks and Dresselhaus, in 1993, theoretically predicted that the quantum confinement of the charge carriers could effectively improve the TE efficiency [15]. After that, a sequence of first-rate scientific works was conducted mainly on nano-engineering to reduce lattice κ without changing σ [17–24]. The conducting polymers have emerged as a potential candidate due to the intrinsic advantage of having very low κ and being easily processable and scalable compared to their inorganic counterparts. The low κ is due to their comparable phonon mean free path to the minimum separation between equivalent structural units [25].

Nevertheless, due to low σ, their TE properties are still not good enough for real-world application. Many high-performance conducting polymers were developed by advancing organic synthetic techniques during the last decade, becoming an integral part of several commercial electronic devices. However, studying these materials for possible use in TE device applications is still in its infancy.

Organic semiconductors can be broadly classified into small molecules or oligomers and polymers. Over the years, various materials have been designed to transport holes or electrons in each case [26,27]. Among the organic semiconductors, conjugate polymers constitute a particular class, comprising sp^2 hybridized carbon atoms with delocalized π-orbitals that contribute to charge

transport. Typically, a conjugated polymer chain contains numerous repeating units or monomers, and functional moieties (e.g., alkyl side-chains) are added to improve the solubility, and such π-conjugated system formed by pz-orbitals overlap. Here p-electrons are localized within the molecule and make the energy gap between the highest occupied molecular orbitals (HOMO) and lowest unoccupied molecular orbitals (LUMO) relatively small, making them conducting. These materials are widely studied for organic photovoltaics such as field-effect transistors and solar cells, and their TE performance has been extensively investigated recently [7].

1.2.1. Charge transport in organic semiconductors

Understanding the transport of charge carriers is critical to improving the TE efficiency as charge carriers are the working fluid in a TE material. The dependence of σ and α in conventional TE materials, i.e., inorganic semiconductors, is well-described in the Boltzmann band transport theory,

$$\alpha = -\frac{k_B}{e}\int \frac{E-E_F}{k_B T}\frac{\sigma(E)}{\sigma}dE \tag{1.8}$$

where E_F is the Fermi level or chemical potential that can be tuned by doping.

The charge carriers in an organic semiconductor are spatially localized and disordered in nature [28]. Due to these localized states, the band-like transport model in inorganic semiconductors remains invalid for organic semiconductors. Hence a different transport framework is required to define the transport behavior of charge carriers in disordered organic materials. However, many TE models have been developed for organic semiconductors in the regime of hopping transport [29], though they lack the quantitative description for the carrier localization.

In 1987, Mott proposed the 'Mobility Edge (ME) model' (ME represents energy separating localized/non-localized states in the conduction/valence bands of a non-crystalline material) [30].

According to this model, the carriers below ME are trapped and do not affect the conduction. In contrast, the carriers above the ME freely conduct electricity (like metal). The following equations give the expression for σ and α,

$$\sigma = \sigma_0 exp\left\{-\frac{E_C - E_F}{k_B T}\right\} \tag{1.9}$$

$$\alpha = \frac{k_B}{e}\left\{\frac{E_F - E_V}{k_B T} + A\right\} \tag{1.10}$$

where σ_0 is the pre-exponential factor, E_C is the ME, E_V is the valence energy, and A relates to the density of states (DOS) dimensionless and greater than 1. However, the model does not fit the experimental data well since the model's assumptions may not be suitable for organic semiconductors.

Another approach to explain the charge transport in organic semiconductors is the hopping transport model [31,32]. Due to polymers' energetic and structural complexity, activation energy must overcome this barrier to hop from one localized site. Thermal fluctuations can provide this activation energy, and hence transport in polymers is well-explained by thermally assisted hopping [33]. There are two types of hopping transport models: nearest-neighbor hopping (NNH) and variable range hopping (VRH).

The NNH model describes a transport regime in which charge carriers have sufficient energy and the hopping rate is limited by spatial tunneling distances; then, they hop to the nearest empty neighboring site [34]. However, the nearest available site might be much higher in energy at some point. Therefore, it is more likely for the carrier to perform a hop to a non-nearest site with similar energy, referred to as VRH [34]. The VRH model assumes that charge transport occurs only around the E_F and at a constant DOS. The σ and α can be described as follows:

$$\sigma = \sigma_0 exp\left[-\left(\frac{T_0}{T}\right)^{\frac{1}{d+1}}\right] \tag{1.11}$$

$$\alpha = \frac{k_B^2}{e}(T_0 T)^{1/2} \left|\frac{dlnN}{dE}\right|_{E=E_F} \quad (1.12)$$

where σ_0 is the pre-exponential factor, T_0 is the characteristic temperature (inversely related to the hopping range), T is the temperature, d is the hopping exponent (which depends on the dimensionality of the system, d = 1/2 for two-dimensional (2D) and 1/4 for three-dimensional (3D)), and N is the DOS.

This hopping transport model could not successfully explain the charge transport in organic semiconductors. In 2015, Chabinyc *et al.* discovered the empirical power law that shows a perfect fit for the σ-α relationship over a wide range of conducting polymers [35]. The power-law relation is stated as,

$$\alpha = \frac{k_B}{e}\left(\frac{\sigma}{\sigma_\alpha}\right)^{-1/4} \quad (1.13)$$

where σ_α is a conductivity constant independent of the carrier concentration. The summary of the σ-α relationship via different transport models for organic material is illustrated in Fig. 1.5.

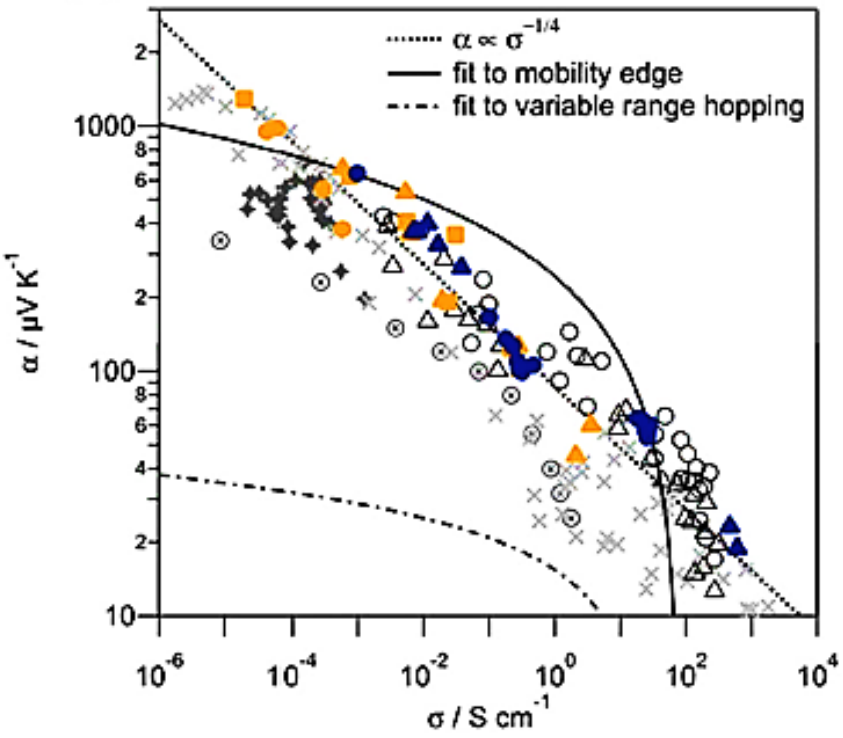

Fig. 1.5. Summary of the *σ*-*α* relationship via different transport models for organic material. The experimental data of some well-known thiophene-based polymer systems are represented in dotted shapes. Adapted from Ref. [35].

1.2.2. Doping to improve thermoelectric properties

Chemical doping is a beneficial method to adjust the *σ* of organic TE materials. The mechanism induces a charge transfer (chemical oxidation or reduction) into the molecular backbone via introducing additional charge carriers (i.e., polarons and bipolarons) [36]. For instance, in p-doping, the HOMO level of a polymer and the LUMO level of the dopant needs to be close to or higher than the latter. Thereby introducing positive polarons or bipolarons into the polymer chain via polymer to the dopant electron transfer [37].

The method of the doping process also plays a critical role in determining doping efficiency. A commonly adopted strategy is 'sequential doping', where the polymer gets exposed

to a vapor or dipped in a solution containing dopant [38]. For p-doping, the reduced dopant transforms into a negative counterion that neutralizes the positive charge on the polymer backbone. Another method is 'solution-mixed doping,' where the dopant is directly mixed with polymers in the synthesis stage [39]. Furthermore, there are strategies such as 'secondary doping' where morphological changes simultaneously improve TE properties; this provides an additional level of tuning that is not available to inorganic materials [40,41].

1.2.3. From materials to devices: Organic TEG

A TEG operates under the Seebeck effect, wherein an applied thermal gradient induces the movement of carriers in material and creates an electrical potential. An electrical current can be sourced by connecting p-type and n-type legs electrically in series and thermally in parallel. A typical inorganic TEGs (Fig. 1.3) consists of firm, pillar-like p-n legs surfaced over a ceramic substrate and required a thermal gradient incident perpendicular to the substrate. Organic TEGs (Fig 1.6) have a planar architecture patterned onto a flat substrate using low-cost, scalable printing techniques. The flat substrates for developing organic TEGs should have good electrical and thermal insulation. For organic TEGs, a thermal gradient can be applied parallel to the substrate, promoting an in-plane carrier transport along these materials [42].

Fig. 1.6. A planar organic TEG with (a) single TE leg and (b) p-n thermocouples. Adapted from Ref. [43].

1.3. State-of-Art: Organic Thermoelectric Materials Development and Device Demonstration

In recent years, state-of-the-art organic TE materials have swiftly caught up with inorganic materials, as shown in Fig. 1.7. Most organic TE materials studied are based on conducting polymers, including conjugated and coordination polymers. The conducting polymers usually show an excellent TE performance. Another efficient method is to blend these conducting polymers with nanomaterials and carbon-based materials. Progress in material research offers a unique outlook and clarifies the vital goal of establishing high-performance organic TE materials suitable for real-life applications.

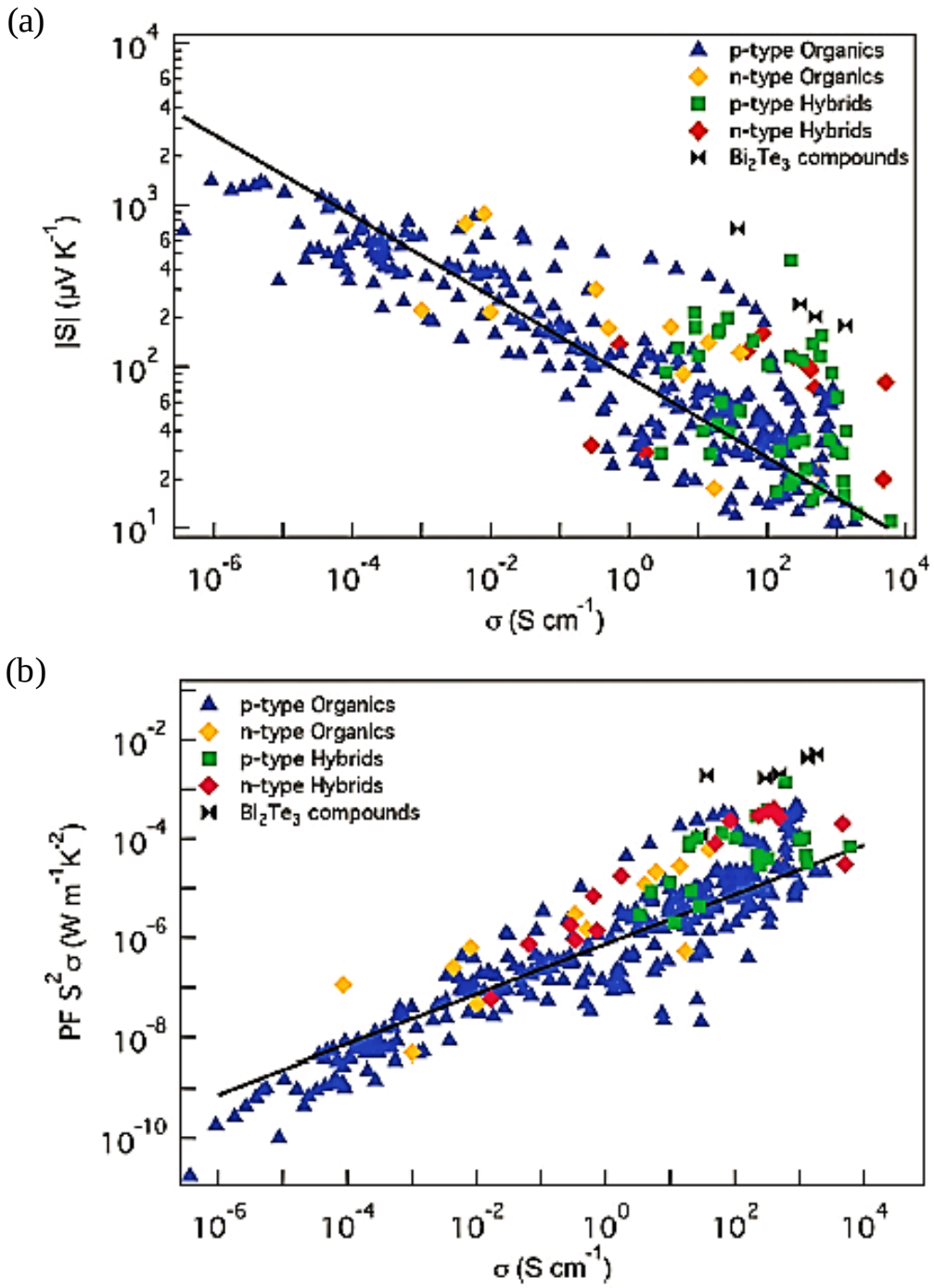

Fig. 1.7. Summary of TE properties of a wide variety of organic TE materials. High-performing Bi_2Te_3 compounds are included as the point of reference room temperature TE material. Adapted from Ref. [36].

During the last few decades, the field of p-type TE materials and dopants has shown tremendous progress, while investigations of their n-type counterparts lag far behind. The n-type materials are relatively unstable toward oxidation, limited availability of dopants, poor charge mobility, and processing difficulties in the ambient atmosphere [44]. Further sections focus on the development of p-type organic and hybrid TE materials.

1.3.1. Conducting polymers

The conducting polymers have a significant advantage of wide doping ranges, mechanical flexibility, and charge conductivity along the polymer backbone. Further increase of σ can be done by electrochemical or chemical doping of charge carriers, favoring charge transfer by hopping. Also, polymerization can be adjusted to get different microscopic and macroscopic morphologies. The highly conducting polymers which show TE properties includes polyacetylene (PA) [45], polypyrrole (PPy) [46], polyaniline (PANI) [47], polycarbazoles [48], polythiophenes [49], poly(3,4-ethylenedioxy thiophene) (PEDOT) [50] and poly(3-methylthiophene) [51], while semiconducting polymers include poly(3-octylthiophene) [52], poly(3-hexylthiophene) (P3HT) [53] and polyvinylidene fluoride [54].

An extensively explored TE material is poly(3,4-ethylenedioxythiophene):poly(styrene sulfonate) (PEDOT:PSS). Currently, different types of PEDOT:PSS as a dispersion in water is commercially available [55]. In 2002, Kim *et al.* first reported the electrical properties of PEDOT:PSS [56]. Subsequently, many studies have attempted to establish the TE properties of PEDOT:PSS. Bubnova *et al.* tried to regulate PEDOT:PSS's oxidation level by fabricating electrochemical transistors and varying the gate voltage (Fig. 1.8a). A maximum PF (=23.5 $\mu W/m.K^2$) at an oxidation level of 14.5% (corresponding to 0.8 V gate voltage) was obtained by increasing α, whereas σ decreased with reduced carrier concentration [57]. In 2013, Pipe and

coworkers achieved a ZT of 0.42 for PEDOT:PSS film by solvent-induced dedoping treatment. In this study, σ and α were increased and but κ reduced from 0.30 to 0.22 W/m.K (DMSO/PEDOT:PSS) and from 0.32 to 0.23 W/m.K (in ethylene glycol (EG)/PEDOT:PSS) (Fig.1.8b). The authors proposed an optimization scheme to minimize the dopant volume, leading to a maximum ZT value [58].

Sequential treatment with sulfuric acid (H_2SO_4) and sodium hydroxide base (NaOH) increased both the α and σ values of the PEDOT:PSS film was adapted by Ouyang *et al.* in 2017. The acid treatment enabled the charge transport with enhanced σ, and the base treatment adjusted the oxidation level, which enhanced α. By monitoring the experimental settings, the optimized PEDOT:PSS films obtained an α of 39.2 μV/K and a σ of 2170 S/cm at room temperature, and the corresponding PF is 334 $\mu W/m.K^2$ [59]. An extensive study has been done for PEDOT:PSS post-treatment and also by replacing PSS with different counterions like bistriflimide ($TFSI^-$), hexafluorophosphate (PF^{6-}), perchlorate (ClO^{4-}) [60], and tosylate (Tos) [61]. PEDOT derivatives have become the benchmark TE materials, although their shortcomings, such as their acidic properties and hygroscopic nature, have driven researchers to find new solutions.

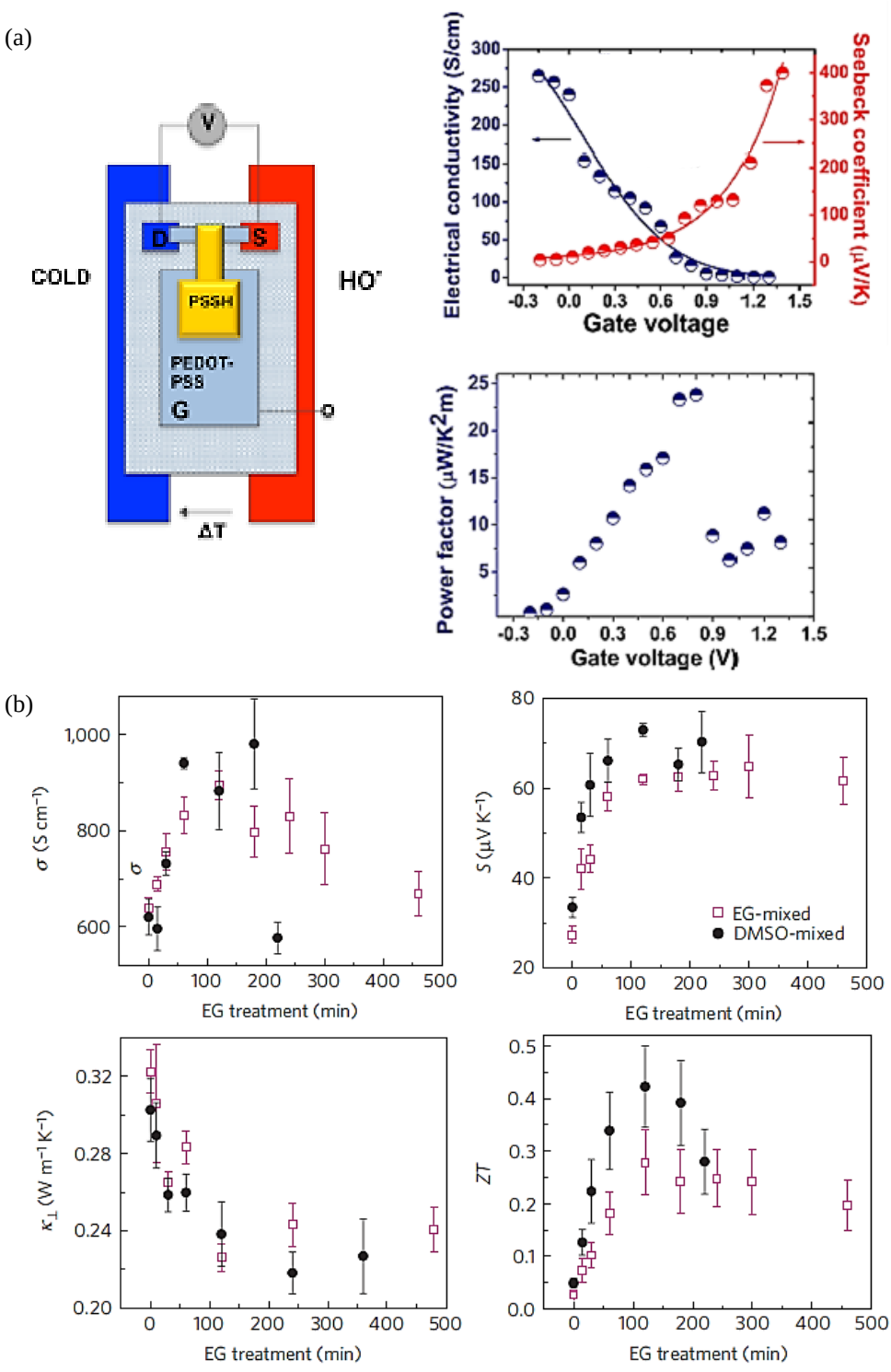

Fig. 1.8. (a) Illustration of PEDOT:PSS electrochemical transistor and the TE performance plot. Adapted from Ref. [57] and (b) TE property enhancement by doping the PEDOT:PSS film with EG or DMSO. Adapted from Ref. [58].

The TE performance of P3HT is also widely studied, and due to its regio-regular arrangement of side chains, it allows prominent charge carrier transport. Zhu *et al.* reported that P3HT doped with ferric salt of $TFSI^-$ attained a PF (=20 μW/m.K^2) at room temperature, which arises due to the higher carrier concentration [62]. Jang *et al.* studied the influence of film thickness and crystallinity of $FeCl_3$ doped P3HT films prepared by wire bar coating to improve the PF by arranging the intermolecular chain packing, which shows high σ (=254 S/cm) and a maximum PF of 35 μW/m.K^2 [63]. In 2018, Chabinyc *et al.* reported a study of morphological effects of 2,3,5,6-tetrafluoro-7,7,8,8-tetracyanoquinodimethane (F4TCNQ) doping on P3HT films. They found that the TE properties can be tuned with vapor phase doping. For solution/vapor-doped P3HT/F4TCNQ films, the α obtained were 76 μV/K and 85 μV/K, respectively [64].

The liquid crystalline nature of poly(2,5-bis(3-alkyl thiophene-2-yl)thieno[3,2-b]thiophene) (PBTTT) polymer provided designing of several high-performing TE polymers [65]. The two main reported polymers based on this kind are PBDTTT-C14 (with tetradecyl side-chains) and PBTTT-C12 (with dodecyl side-chains) with a PF of 1 μW/m.K^2 and 14 μW/m.K^2, respectively [66]. Chabinyc *et al.* investigated the TE characteristics of PBTTT-C14 via vapor and solution doping with F4TCNQ and 2,5-difluoro-7,7,8,8-tetracyanoquinodimethane (F2TCNQ). They observed the vapor-doped F2TCNQ polymer films yielded a maximum PF of 70 μW/m.K^2 while vapor-doped polymer films with F4TCNQ exhibited a maximum PF of 120 μW/m.K^2 [67]. In 2019, Brinkmann *et al.* brought the PF of PBTTT-C12 doped with $FeCl_3$ to 2 mW/m.K^2 by controlling the crystallization and orientation of polymers [68].

Recently, the TE properties of conjugated polymers based on benzo[1,2-b:4,5-b′]dithiophene (BDT) -based donor-acceptors (D-A) attracted researchers to understand the relationship between structural property and TE performance. Wang *et al.* designed three BDT-

based D-A conjugated polymers and studied their TE properties. They found that the polymer with alkylthienothiophene side chains displayed good thermal tolerance (up to 400 °C) along with the superior σ (1.519 S/cm) and α (413.79 μV/K) values [69]. Later in 2019, Wang and coworkers designed BDT-based alternative copolymers PBDT-EDOT and 2D conjugated PBDTTT-EDOT and investigated the influence of 2D conjugated structures on the TE performance conjugated polymers. The PF of doped PBDTTT-EDOT films reached 101.3 μW/m.K^2 at 350 K, which is >100x higher than PBDT-EDOT films (0.9 μW/m.K^2) [70].

1.3.2. Polymer composites with inorganic nanomaterials

The most economical and practical way to modify polymer properties is blending with inorganic nanoparticle additives. A hybrid material offers mechanical flexibility, ease of synthesis of organic components, and enhanced TE properties of inorganic materials [71]. Designing organic-inorganic TE composites presents a promising approach to overcome the low σ of organic counterparts and expensive inorganic components. Numerous strategies were adapted to prepare organic hybrid TE materials, such as physical blending, wet mixing, and in-situ polymerization [72]. Careful optimization of physical interaction between the organic and inorganic phases and intelligent design procedures to control the mechanical properties optimize TE performance. Moreover, the organic-inorganic interfaces create boundaries that scatter phonons, thus ensuring low κ [73,74]. When both components have the same charge carrier in an organic-inorganic hybrid material, they work together to improve ZT. On the other hand, if they have opposing carrier types, the blend can be either p- or n-type, depending on the relative ratio. Furthermore, the Fermi levels of both the components of a hybrid material should be matched to minimize the energy barrier between the two phases [75,76].

The inorganic materials like tellurium (Te), bismuth telluride (Bi_2Te_3), and bismuth (Bi) based alloys are potential candidates for hybrid TE materials. In 2010, See *et al.* synthesized PEDOT:PSS/Te hybrid by reducing sodium tellurite in the presence of PEDOT:PSS to form Te nanowires well dispersed in the polymer matrix as shown in Fig. 1.9. PEDOT was highly ordered at the interface with Te nanowires, and α improved from bulk PEDOT:PSS, and κ remained low to give ZT values as high as 0.1 [77]. Urban *et al.* demonstrated controlled pattering of Cu-Te alloy subphases in a PEDOT:PSS/Te hybrid system, providing up to 22% enhancement in the PF [78]. Deng *et al.* integrated Te nanowires with PANI to form PANI/Te hybrid films and achieved a PF of 105 $\mu W/m.K^2$ at room temperature with a ZT = 0.156 [79].

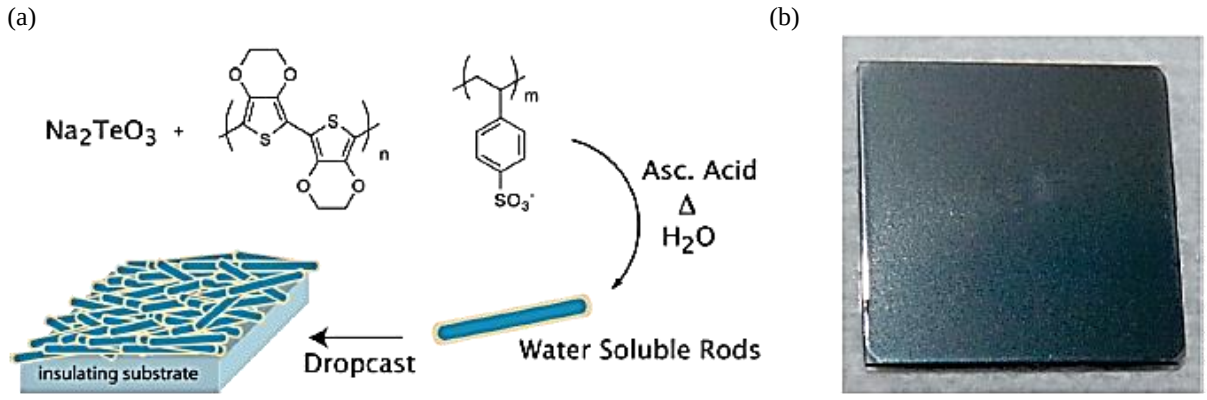

Fig. 1.9. (a) Schematic representation of PEDOT synthesis:PSS/Te nanorods hybrid and (b) Image of as-prepared hybrid film on a 1 cm^2 quartz substrate, showing good film uniformity. Adapted from Ref. [77].

Many reports have demonstrated that Bi_2Te_3 can effectively improve the α of PEDOT:PSS through the mixing method. Zhang *et al.* mixed the ball-milled Bi_2Te_3 powders into commercially purchased PEDOT:PSS (PH1000), achieving a PF of 46.57 $\mu W/m.K^2$ as shown in Fig. 1.10a [80]. Wang and coworkers reported an excellent PEDOT/Bi_2Te_3 based flexible system with a peak PF ~1350 $\mu W/m.K^2$, equivalent to ZT of 0.58 at room temperature [73]. Toshima *et al.* synthesized

PANI-Bi_2Te_3 nanohybrids and showed a higher TE value than the pure PANI because of an overall increase in the α of the composite [81]. Banerjee *et al.* prepared structurally ordered cable like PANI/Bi_2Te_3 composite with a reduced κ value by selective phonon scattering at the interfaces of the hybrid nano cable structures [82].

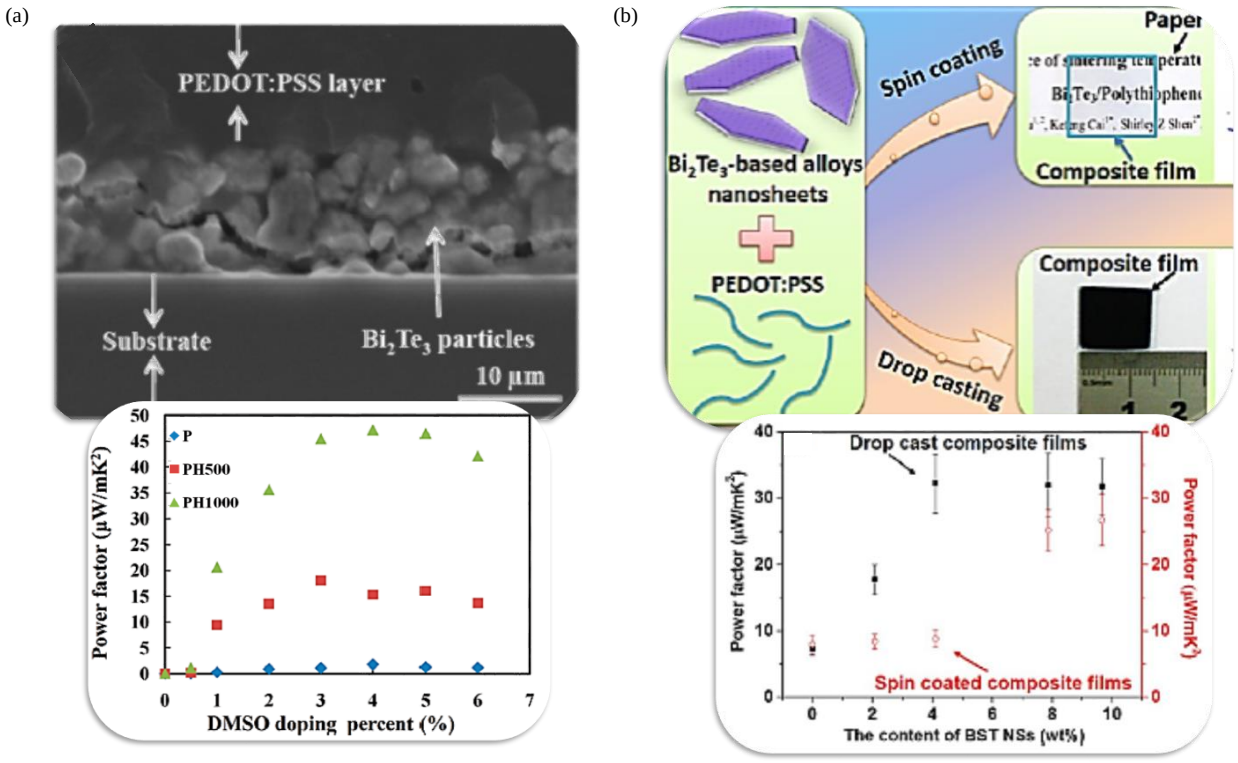

Fig. 1.10. (a) Cross-sectional SEM image of the PH1000 mixed with Bi_2Te_3 ball-milled particles and the PF of the composite film by varying DMSO doping concentration plot. Adapted from Ref. [80] and (b) Illustration of composite film and PF plot for the drop and spin-caste films vs inorganic filler content. Adapted from Ref. [83].

Lin *et al.* showed $Bi_{0.5}Sb_{1.5}Te_3$ platelets fabricated in the presence of PEDOT:PSS provided improved particle dispersion (Fig. 1.10b), an σ of 1295.21 S/cm and higher PF of 32.26µW/m.K^2 with particle loading of 4.1 wt% [83]. Liu *et al.* successfully synthesized free-standing PEDOT:PSS/$Ca_3Co_4O_9$ hybrid films via mechanical blending and casting in a flexible substrate.

The study revealed that the α of the composite could be improved by increasing the inorganic particle content; however, a decrease in PF was observed due to the decline in σ with increasing $Ca_3Co_4O_9$ content [84]. Toshima and coworkers reported the effect of gold nanoparticles (AuNP) on the TE properties of PANI and PEDOT polymers. A direct hybridization of PANI with AuNP improved the σ to as high as 330 S/cm at 323 K. They also prepared PEDOT:PSS/AuNP hybrid films revealing that a better TE performance could be obtained than the pristine polymer. The σ and ZT of the optimized film could be enhanced by ~2x and ~3x, respectively[85]. The previous work conveyed that the α of PEDOT:PSS/AuNP hybrids could be enhanced by adjusting the nanoparticle properties, and enhancement is likely to result from a reduced carrier concentration for increased AuNPs [86].

1.3.3. Polymers composite with carbon nanomaterials

Carbon nanomaterials are promising for TE because of their high carrier mobility and narrow bandgap energy. They can be effortlessly combined to fabricate flexible TE that scavenges waste heat. The polymer composite with carbon nanomaterials has received great attention for its outstanding mechanical strength and low density [87]. The majority of carbon nanoparticle composites for TE applications utilize carbon nanotubes (CNT), especially single-walled carbon nanotubes (SWCNT) or multi-walled carbon nanotubes (MWCNT), which are semiconducting and p-type due to oxygen doping [88]. Kong *et al.* demonstrated that the properties of CNTs, including DOS, σ, and α, are susceptible to the presence of oxygen [89]. Surprisingly, in 2000, Collins and coworkers found pure CNTs show n-type transport in vacuum conditions; therefore, these are intrinsically n-type [90].

Numerous approaches were experimented with to formulate the polymer/CNT nanocomposites, including in-situ polymerization, interfacial polymerization, grafting

macromolecules onto CNT, melt mixing, and dissolving polymers into organic solvents containing CNT suspensions [91–95]. Kim *et al.* prepared PEDOT:PSS/CNT composite by ultrasonication method and showed improved TE properties because of matrix-CNT electronic junctions (Fig. 1.11a). They could yield an σ of up to ~400 S/cm without significantly altering α [96]. A different study on similar composites presented a slight difference in PF depending on SWCNT content (0–85 wt%). The α remains relatively unaltered as the σ increases, leading to a maximum PF of 140 $\mu W/m.K^2$ [97]. Further studies on PEDOT:PSS/CNT hybrids were carried out by Yu and coworkers in 2011. They found that the CNT surface was decorated with PEDOT:PSS particles forming electrical junctions, shown in Fig. 1.11b. These junctions played an important role in enhancing σ keeping relatively constant α. As a result, a high PF value of 160 $\mu W/m.K^2$ was obtained at 60 wt% CNT filler. Moreover, κ remained low because the mismatched vibrational spectra between PEDOT:PSS and CNTs effectively blocked phonon transport [98].

The post-treatment also tuned PEDOT:PSS/CNT composites. For example, Lee *et al.* fabricated a PEDOT:PSS/MWCNT nanocomposite film and treated those in EG. The EG treatment mainly removed the insulating PSS molecule chains and dramatically enhanced the σ of the composites. Consequently, EG treated PEDOT:PSS/MWCNT(20 wt%) exhibited a high PF of 151 $\mu W/m.K^2$, which was much higher than the nontreated sample [99]. Hsu *et al.* reported that when the σ of PEDOT:PSS/CNT composite increases by treating with DMSO or formic acid (FA), an unaltered or increasing α was observed. After DMSO and FA treatment, large PFs of 464 and 407 $\mu W/m.K^2$ were obtained for the composites containing lower CNT loading (6.7 wt%) [100].

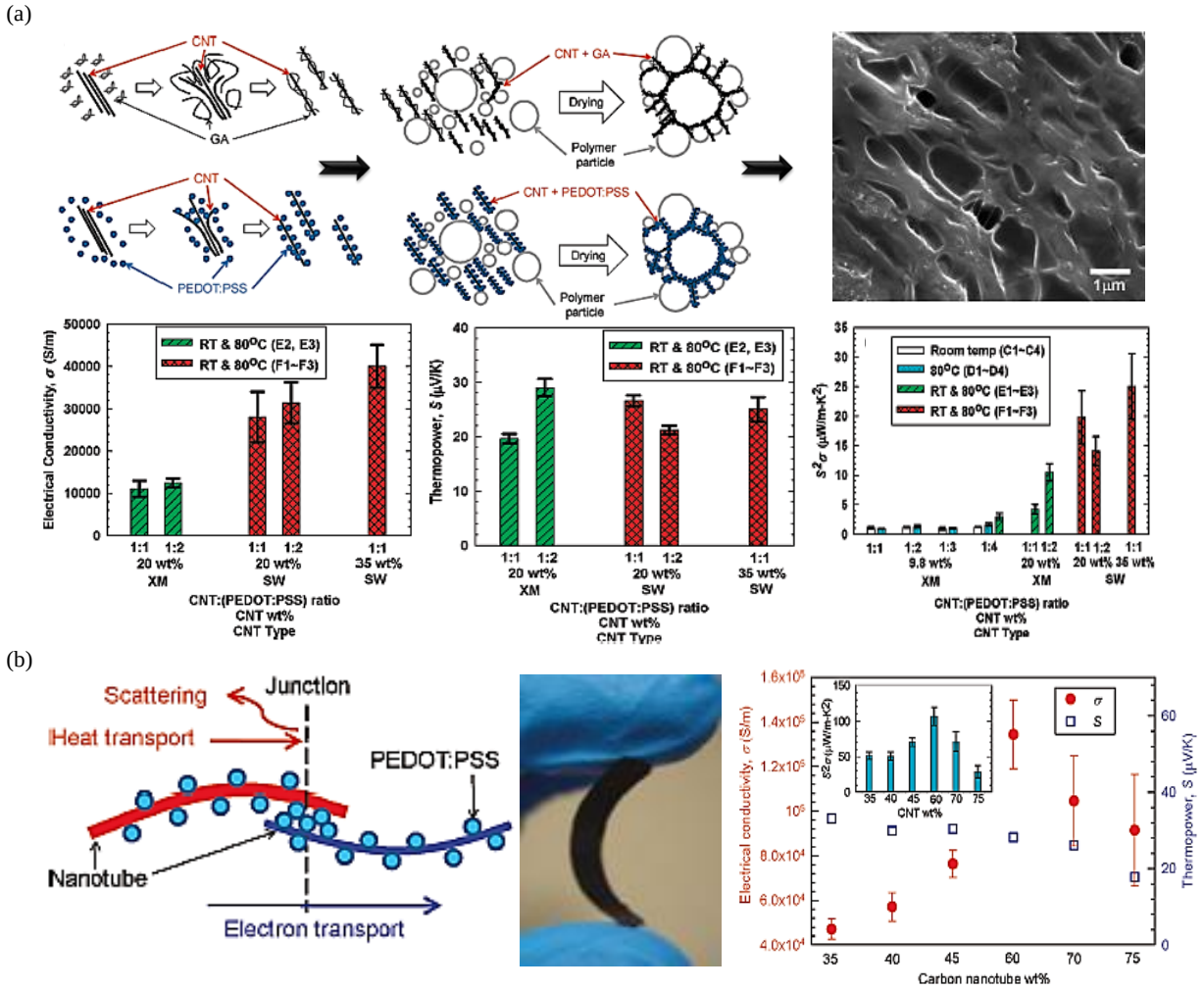

Fig. 1.11. (a) Schematic illustration of the formation of CNT-matrix junction. Cross-sectional SEM image of composite dried at room temperature and 80 °C. TE study of the composite film. Adapted from Ref. [96] and (b) Illustration of making nanotube-PEDOT:PSS-nanotube junctions, optical picture of free-standing composite material, and plot for TE properties. Adapted from Ref. [98].

Wang *et al.* prepared PANI/MWCNT composite nanofibers via in-situ polymerization and electro-spinning processes. They combined two methods that yielded both CNT and polymer nanofibers aligned and oriented along the same axis. The composite aligned in the parallel direction shows two times higher TE performance than polymer composites arranged in the

perpendicular axis [101]. Kou *et al.* prepared a bulk PANI-MWCNT/PANI composite by initially coating MWCNT over PANI by in situ polymerization, followed by incorporating it into the polymer matrix via hot pressing. They achieved a maximum σ and α of 28 S/cm and 21.6 μV/K, respectively, and ZT reached 0.001, which was more than three orders of magnitude higher than pure PANI [102]. Lin *et al.* showed a super high σ of ~ 4000 S/cm for the PANI/SWCNT composite. They suggested that the vital factor in improving the σ of composites is the presence of ordered and continuous areas on the interlayer between the SWCNT and PANI [103]. Recently, Guo *et al.* fabricated a flexible PANI/SWCNT composite via DMSO-mediated electrochemical polymerization. The optimized, flexible film shows a PF of 236.4 $\mu W/m.K^2$ at room temperature [104].

PPy/CNT composites were rarely considered despite the better stability and facile fabrication. PPy/MWCNT composites showed a steady increase in α with MWCNT contents, while σ initially showed a gradual increase and then a rapidly decreasing trend. The maximum PF value reported was 2.079 $\mu W/m.K^2$ for the 20 wt% PPy/MWCNT nanocomposite, almost 26 times as high as pure PPy [105]. In 2020, Gao *et al.* fabricated a ternary composite PANI/PPy/SWCNT and enhanced the TE properties by doping with $FeCl_3$. The doping enhances the σ of the composite by 2.9 times than before doping, increasing the PF by twofold [106].

Muller *et al.* performed the TE studies on SWCNT and MWCNT composite with P3HT. The strong π-stacking between P3HT and CNT increases σ from 1.7×10^{-5} S/cm (for P3HT) to 24 and 275 S/cm for P3HT/MWCNT and P3HT/SWCNT composites, respectively. The P3HT/SWCNT composite consistently resulted in a higher σ. The maximum value was above 10^3 S/cm with PF of 25 $\mu W/m.K^2$ for a filler content of only 8 wt% (95 $\mu W/m.K^2$ for 42–81 wt%) [107]. Rather than using the conventional immersion doping method, spin-coating the dopant over

the prepared P3HT/SWCNT produced a higher PF of 267 μW/m.K^2 [108]. Jang *et al.* suggested further improvements in these films using a spray-painting method. Spray-printed P3HT/CNT films exhibit PF ~325 μW/m.K^2 at room temperature, which is the maximum value reported for P3HT-based organic nanocomposites [109].

Nowadays, the BDT-based CNT composites have become a potential TE material. In 2017, Pan *et al.* reported that the TE behavior of PBDT-EDOT/SWCNT (30%) exhibited a high α of 82.1 μV/K at room temperature (Fig. 1.12) [110]. Later they synthesized a novel BDT- based D-A conjugated polymer PBDTDTffBT and prepared composite films with SWCNT, shown in Fig. 1.13. At room temperature, the maximum σ, α, PF, and ZT values of the composite films were 529.3 S/cm, 68.1 μV/K, 80.9 μW/m.K^2, and 0.028, respectively [111]. In 2020, Chen *et al.* designed a BDT-based D-A polymer with a carbazole segment (PBDT-C-BT) and prepared a TE composite with 50 wt% of SWCNT via ultrasonication method followed by an immersion doping with F4TCNQ. After doping, the σ increased from 120.32 S/cm to 1044.92 S/cm at room temperature and obtained a PF of 55.9 μW/m.K^2 [112].

(a)

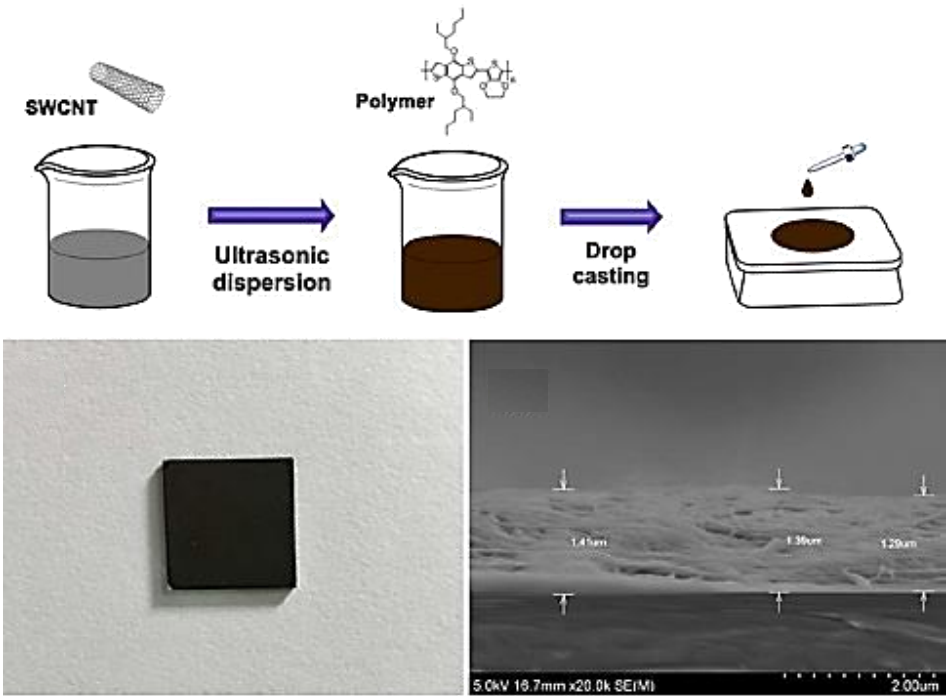

(b)

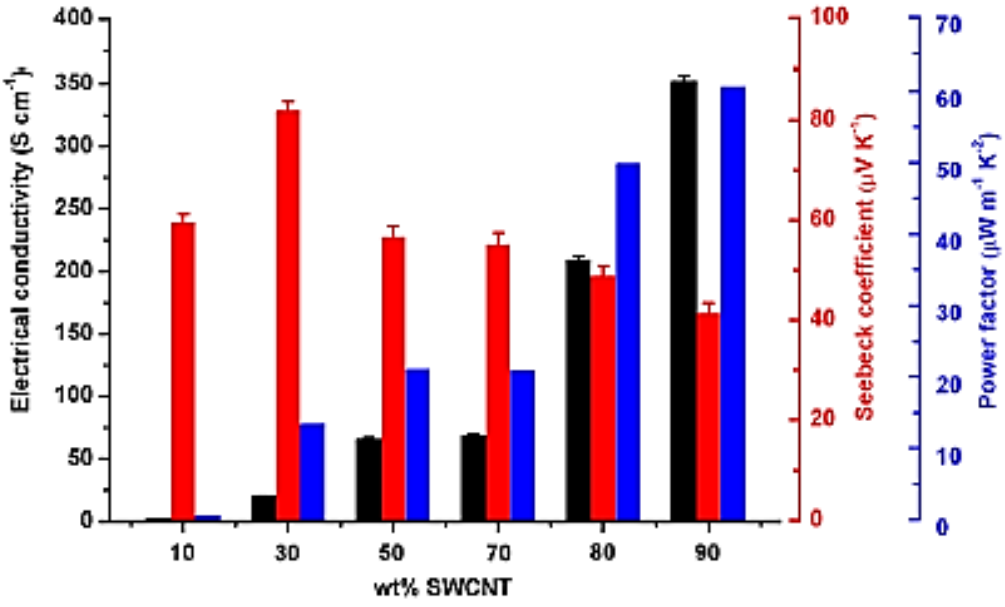

Fig. 1.12. (a) Schematic representation of the preparation method of the composite, including optical picture and cross-sectional SEM and (b) TE properties of the composite films for different SWCNT contents at room temperature. Adapted from Ref. [110].

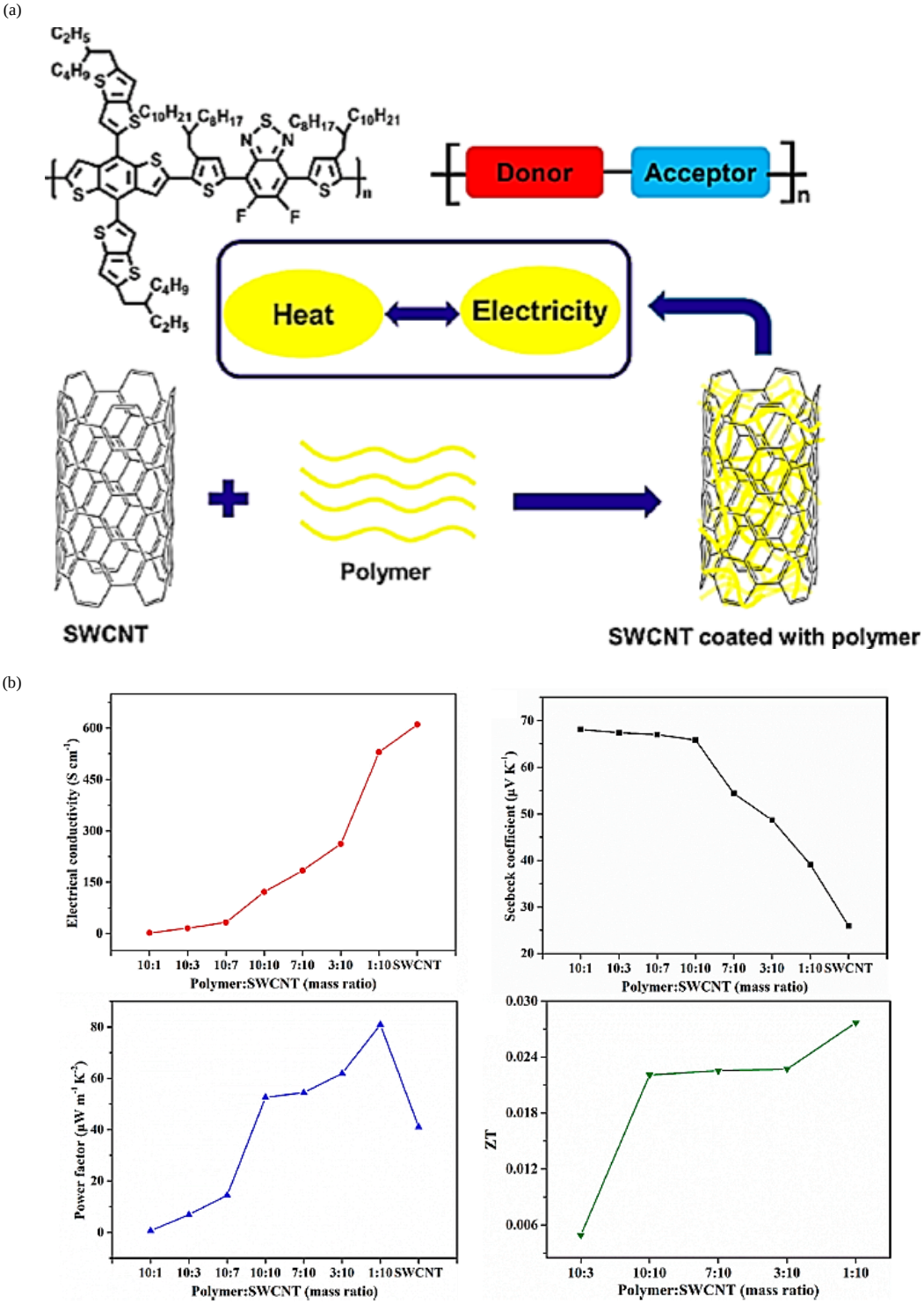

Fig. 1.13. (a) Schematics of the fabrication method of the PBDTDTffBT/SWCNT composite and (b) TE properties of composite films. Adapted from Ref. [111].

Some graphene-based 2D crystalline carbon materials show remarkably high σ and adequate TE properties. Yoo and coworkers prepared PEDOT:PSS/graphene TE composites via in-situ polymerization. After introducing 3 wt% graphenes, the composite exhibited a maximum PF value of 45.7 μW/m.K^2, 93% higher than pristine PEDOT:PSS film [113]. In 2018, Cheng *et al.* constructed a unique composite film by incorporating graphene quantum dots (GQDs) in PEDOT:PSS and reported a dramatic enhancement in the TE performance. The PF of the optimized composite was 550% higher. Due to the strong interfacial interactions between PEDOT:PSS and GQDs and the separation of PEDOT and PSS phases led to significant TE properties improvement [114]. Yao *et al.* prepared high-performance elastic TE materials with PANI and 3D tubular graphene. The distinctive PANI/3D graphene composite structure could improve energy filtering and increase TE performance [115]. Lately, a superior ZT value of 0.74 for the PANI/graphene system was conveyed by Lin and coworkers. They fabricated p-phenediamino-modified graphene (PDG) via a facile green one-step chemical route creating a unique semi-interpenetrating network. These networks provide additional pathways for transporting carriers smoothly and use less graphene to enhance the overall TE properties. The highest ZT value was calculated for the PANI/PDG samples containing only 3 wt% modified graphene [116].

1.3.4. Demonstrated thermoelectric devices

The practical realization of organic TE materials can be established by fabricating devices based on these materials. The solution processability of these materials further holds an excellent advantage in producing devices with printing technology for practical application. Also, unique device designs are essential to utilize the full promise of organic systems [117]. The interface engineering of such devices could further enhance TE performance.

In 2013, Krebs *et al.* reported a large area roll-to-roll (R2R) printed TEG (Fig. 1.14a) with 18000 serially connected junctions of silver/PEDOT:PSS/silver (Ag), and they estimated that such a configuration could produce 20 μW/cm^2 of power with a payback time of 1 year [118]. Wei and coworkers reported screen-printed TE devices using PEDOT:PSS and silver connections that produced an output power of 4 μW at ΔT=50 K (~0.1 μW/cm^2) [119]. Jang *et al.* fabricated the flexible TEG using p-type P3HT/CNT nanocomposite spray-painted on a polyimide substrate and reported a maximum output power of 32.7 nW [109]. Bae *et al.* reported a flexible TEG comprised of 32 legs arranged in two rows and printed using the Te-PEDOT:PSS solution onto polyethylene terephthalate (PET). This device had generated ~2 mV from human body heat, as shown in Fig. 1.14b [120]. A PEDOT:PSS based one-leg returned a superior power output per area of 100 μW/cm^2 for a ΔT of 30 K [121]. Zhou *et al.* prepared a flexible TE device on a PET substrate using the p-type leg as PEDOT:PSS and the n-type leg as PEDOT:PSS deposited onto indium tin oxide (ITO). Further, a 50 mm x 5 mm flexible TE module consisting of eight p-n couples was fabricated. The TE module exhibited the peak power output of 0.86 nW and 1.75 nW at a ΔT of 20 K and 30K, respectively [122].

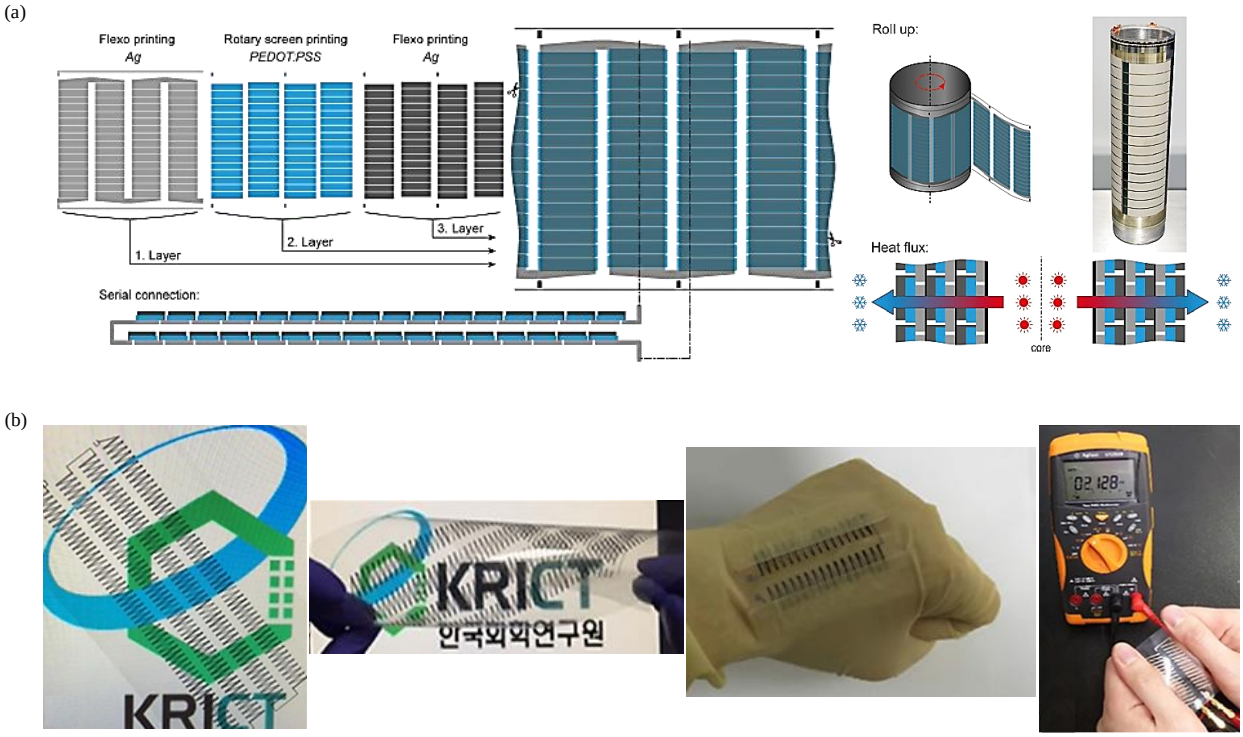

Fig. 1.14. (a) Roll-to-roll printed film-based TEG and the final device along with the heat-flow direction. Adapted from Ref. [118] and (b) Schematic diagram of the TEG geometry and demonstration of the TEG entrenched on a glove for harnessing human body heat. Adapted from Ref. [120].

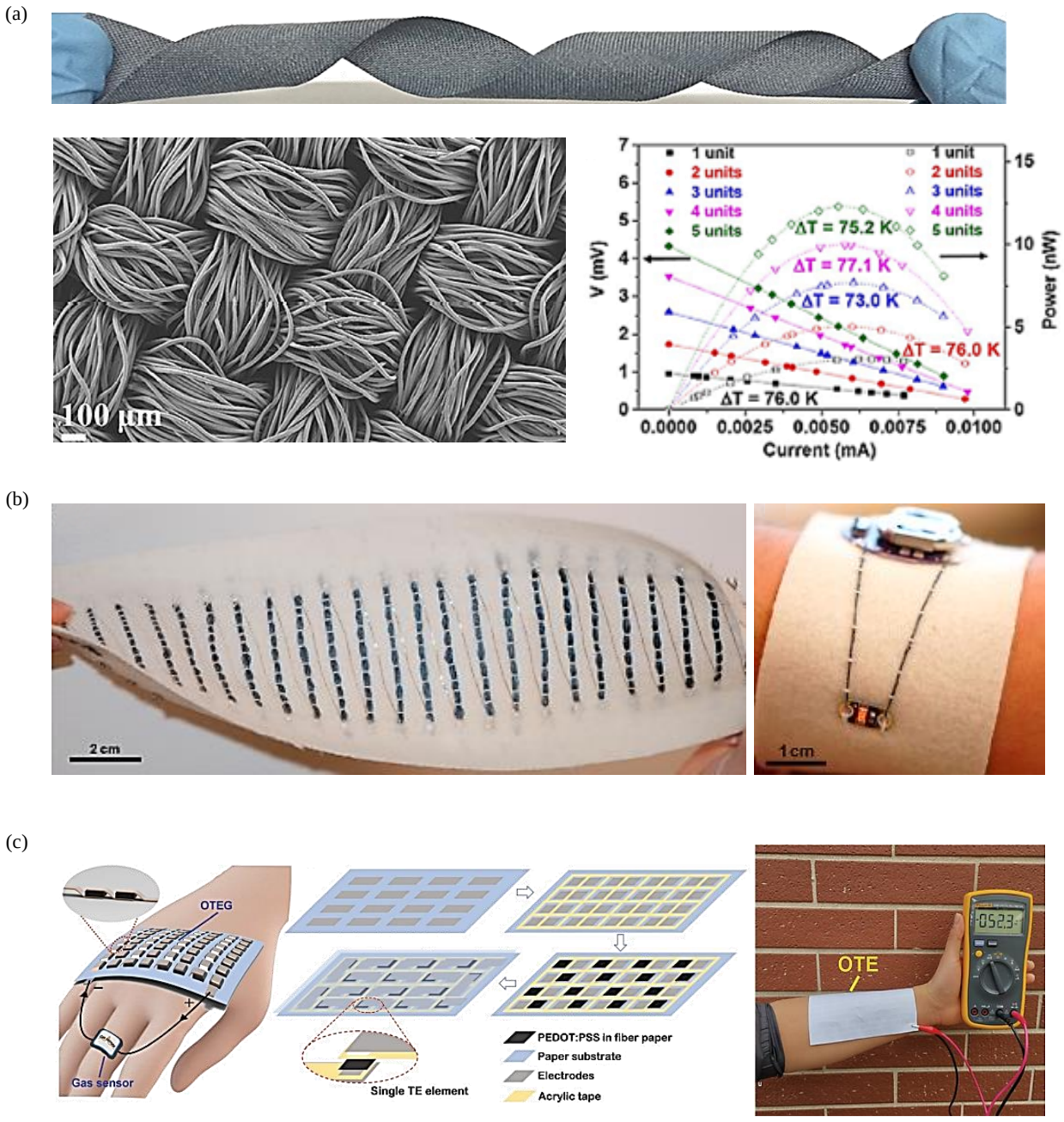

Fig. 1.15. (a) Digital image of polyester fabric after coating treatment, corresponding SEM image, and output voltage and power as a function of current. Adapted from Ref. [123]; (b) Textile TE device with 26 p-type legs using PEDOT:PSS dyed silk yarns and photograph of an LED connected with textile TE device to a battery. Adapted from Ref. [124] and (c) Organic self-

powered sensing elements integrating a flexible organic TEG with PEDOT:PSS legs on paper substrates. Adapted from Ref. [125].

Afterwards, many studies focused on more practical approaches for everyday applications and wearable fabrics. In 2015, Du *et al.* demonstrated a flexible, air-permeable TEG prepared by coating PEDOT:PSS over a polyester fabric and subsequently linked the coated strips with silver metal wires (Fig. 1.15a). The functionalized TE fabric showed excellent stability 300 K to 390 K and generated an output voltage of 4.3 mV at a ΔT of 75 K [123]. Muller *et al.* made 26 legs TE device of silk yarn coated with PEDOT:PSS, which exhibited 35 mV output voltage at ΔT ~66 K (Fig. 1.15b) [124].

The organic TE devices can be used in sensors based on the Seebeck effect to detect heat, light, bio(chemical) agents, etc. In 2019, Di *et al.* demonstrated a flexible self-powered chemical sensor by combining an OFET sensor with an organic TE device (Fig. 1.15c). The TE device was fabricated using NaOH treated PEDOT:PSS as a single TE element and silver as the electrode. The device consists of 162 legs on flexible paper, which exhibited a peak voltage and power output of 0.52 V and 0.32 μW at a ΔT= 85.5 K. Notably, this device could power OFET-based gas sensors having ultralow operating voltage [125]. This work revealed the potential of TE devices as a promising candidate for powering wearable electronics for sensing applications.

Though the flexible organic TE devices seem attractive, it is challenging to fabricate a well-performed device. Therefore, the supply of organic TE materials with much higher ZT values is critical in addition to the numerous technical issues to be addressed. Also, it is promising to integrate organic TE devices with other electronic or optoelectronic devices[126,127].

1.4. Thermoelectric Measurement Methods for Organic Materials

The commercial usage of TE materials could be possible by a better understanding the underlying physics. Organic materials for TE applications are still in their infancy, and robust device prototypes would ultimately highlight their usefulness. The structural complexity of organic materials and the diversity in processing and film fabrication techniques make the measured TE properties sample-dependent and require robust measurements to capture repeatable data. For organic TE materials, the measurement methods could be performed easily on smaller samples of micrometer scales especially prepared as films. Furthermore, since the polymers have low κ (~0.2 W/m.K), the PF is widely used to compare different materials in the literature. The details of κ measurements using 3ω, frequency-domain thermoreflectance (FDTR), and time-domain thermoreflectance (TDTR) are reported elsewhere [128–132].

The σ of the sample is determined using the standard four-point probe method, as shown in Fig. 1.16a. The sample must form a closed area of constant thickness without holes and be contacted with four spatially separated probes for a correct measurement. The outer electrodes are subjected to a high impedance current (I). The inner probes are used to sense the voltage drop (V), excluding errors related to contact resistance between the probes and the film. The slope of the V–I plot gives the material's resistance. The measured resistance and geometric factors can calculate σ [10].

Precise measurement of the α is essential to screen suitable TE materials. The α is estimated by creating a controlled temperature gradient. The experimental arrangement is shown in Fig. 1.16b, which consists of two heaters: one offers a stable ambient temperature for the whole set-up, and the second heater creates a temperature gradient (ΔT) across the material. The secondary heater is placed at one of the outer electrodes to produce ΔT across the length of the material. The

temperature at one end of the sample is varied by the secondary heater, and voltage difference (ΔV) and ΔT are measured by the inner probes. Thus, the slope of the ΔV-ΔT plot gives the α value [10].

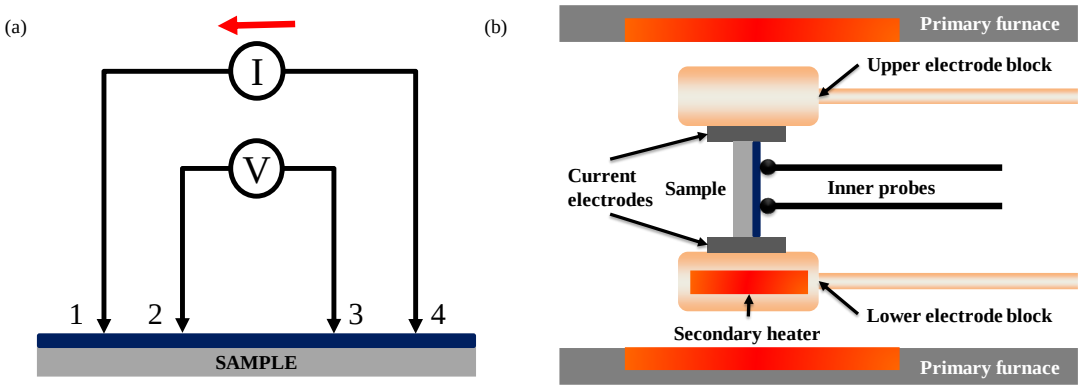

Fig. 1.16. Schematic diagram of (a) electrical conductivity measurement and (b) Seebeck coefficient measurement. Adapted from Ref. [133].

So far, several commercial instruments have been used, e.g., the ZEM-3 system from ULVAC and LSR-3 from Linseis, where both σ and α can be obtained with the same measurement set-up [133,134]. In measurements of σ and α, samples can be vertically fixed where ΔT is created linearly along with the sample, with the inner probes touching the film's surface. The films must have consistent thickness and width to maintain accuracy. Moreover, the substrate must have low σ and κ to guarantee that the current pathway is through the composite and, at the same time, avoid thermal shorting. The external electrode contacts to the film can be amended by smearing silver paste on both ends of the substrate while the inner probes directly contact the film. Notably, the electrical studies are performed along the film's length and can vary from values achieved crosswise due to anisotropy. It is most suitable and time-saving to check the film's resistance before loading it into the instrument with a multi-meter. Thereby, the film continuity along the length can be validated, and also the resistivity can be checked which should satisfy the instrumentation limits.

1.5. Outline of the thesis

The capability to convert heat into electricity of a TE device is expected to play an essential role in addressing today's global energy issues. This thesis consists of three chapters following this introduction chapter. A summary of the chapters is stated in the following,

The ***first chapter*** provided motivation and the fundamentals of the TE, and an understanding of the material properties and charge transport theories. It also reflected the current state-of-the-art organic TE materials and an examination of TE devices fabricated to date. The ***second chapter*** details our initial effort to prepare and characterize a conjugated thienothiophene polymer/MWCNT hybrid TE system. By performing post- doping treatment of films, the TE properties are enhanced simultaneously. Such enhancements show that the σ and α can be modulated in this hybrid material, making them a class of materials worth investigating for organic TE. The ***third chapter*** addresses the critical role of the p-doping mechanism in MWCNT based organic hybrids. A comparative study of the post-doping effect on the TE properties of the two conjugated thienothiophene polymer/MWCNT hybrid reveals the vital role of MWCNT in switching the Fermi level position. A systematic investigation of the doping mechanisms underlying contrary TE performance in hybrid materials is well studied. The ***fourth chapter*** extends our understanding of doping-induced TE properties of conjugated thienothiophene polymer/SWCNT composite system. The practical fabrication of a flexible TE module and its performance simulation is detailed. In ***chapter five***, the summary of the whole findings in the thesis and future scope is discussed. The materials developed in this thesis achieve some of the highest performance in organic hybrid TE to date. This work represents a step towards establishing cheaper and lighter TE materials and flexible TE modules to power new-generation electronic devices, the Internet of Things (IoT), and wearable technologies.

References

[1] British Petroleum, Energy Outlook 2020, BP Energy Outlook 2030, Stat. Rev. London Br. Pet. (2020) 81. https://www.bp.com/content/dam/bp/business-sites/en/global/corporate/pdfs/energy-economics/energy-outlook/bp-energy-outlook-2020.pdf.

[2] M. Muntean, D. Guizzardi, E. Schaaf, M. Crippa, E. Solazzo, J.G.J.G.J. Olivier, E. Vignati, Fossil CO2 emissions of all world countries - 2018 Report, 2018. https://doi.org/10.2760/30158.

[3] International Energy Agency, Global Energy Review 2020, OECD, 2020. https://doi.org/10.1787/a60abbf2-en.

[4] Government of India, Energy Statistics India 2021, (2021). www.mospi.gov.in.

[5] T.J. Seebeck, Ueber die magnetische Polarisation der Metalle und Erze durch Temperaturdifferenz, Ann. Phys. 82 (1826) 253–286. https://doi.org/10.1002/andp.18260820302.

[6] J. Peltier, Nouvelles Experiences Sur La Caloriecete Des Courans Electriques, Ann. Chem. (1834) 371–387.

[7] O. Bubnova, X. Crispin, Towards polymer-based organic thermoelectric generators, Energy Environ. Sci. 5 (2012) 9345. https://doi.org/10.1039/c2ee22777k.

[8] M. He, F. Qiu, Z. Lin, Towards high-performance polymer-based thermoelectric materials, Energy Environ. Sci. 6 (2013) 1352. https://doi.org/10.1039/c3ee24193a.

[9] T.M. Tritt, M. a. Subramanian, Thermoelectric Materials, Phenomena, and Applications: A Bird's Eye View, MRS Bull. 31 (2006) 188–198. https://doi.org/10.1557/mrs2006.44.

[10] B.T. McGrail, A. Sehirlioglu, E. Pentzer, Polymer Composites for Thermoelectric

Applications, Angew. Chemie Int. Ed. 54 (2015) 1710–1723. https://doi.org/10.1002/anie.201408431.

[11] A. Bali, R. Chetty, R.C. Mallik, Thin Film Thermoelectric Materials for Sensor Applications: An Overview, in: Thin Film Struct. Energy Appl., Springer International Publishing, Cham, 2015: pp. 215–241. https://doi.org/10.1007/978-3-319-14774-1_7.

[12] G.J. Snyder, E.S. Toberer, Complex thermoelectric materials, Nat. Mater. 7 (2008) 105–114. https://doi.org/10.1038/nmat2090.

[13] B.C. Sales, Electron Crystals and Phonon Glasses: A New Path to Improved Thermoelectric Materials, MRS Bull. 23 (1998) 15–21. https://doi.org/10.1557/S0883769400031419.

[14] G.S. Nolas, J. Poon, M. Kanatzidis, Recent Developments in Bulk Thermoelectric Materials, MRS Bull. 31 (2006) 199–205. https://doi.org/10.1557/mrs2006.45.

[15] L.D. Hicks, M.S. Dresselhaus, Effect of quantum-well structures on the thermoelectric figure of merit, Phys. Rev. B. 47 (1993) 12727–12731. https://doi.org/10.1103/PhysRevB.47.12727.

[16] L.D. Hicks, M.S. Dresselhaus, Thermoelectric figure of merit of a one-dimensional conductor, Phys. Rev. B. 47 (1993) 16631–16634. https://doi.org/10.1103/PhysRevB.47.16631.

[17] K. Biswas, J. He, I.D. Blum, C.-I. Wu, T.P. Hogan, D.N. Seidman, V.P. Dravid, M.G. Kanatzidis, High-performance bulk thermoelectrics with all-scale hierarchical architectures, Nature. 489 (2012) 414–418. https://doi.org/10.1038/nature11439.

[18] A.I. Boukai, Y. Bunimovich, J. Tahir-Kheli, J.-K. Yu, W.A. Goddard III, J.R. Heath, Silicon nanowires as efficient thermoelectric materials, Nature. 451 (2008) 168–171.

https://doi.org/10.1038/nature06458.

[19] A.I. Hochbaum, R. Chen, R.D. Delgado, W. Liang, E.C. Garnett, M. Najarian, A. Majumdar, P. Yang, Enhanced thermoelectric performance of rough silicon nanowires, Nature. 451 (2008) 163–167. https://doi.org/10.1038/nature06381.

[20] R.Y. Wang, J.P. Feser, J.-S. Lee, D. V. Talapin, R. Segalman, A. Majumdar, Enhanced Thermopower in PbSe Nanocrystal Quantum Dot Superlattices, Nano Lett. 8 (2008) 2283–2288. https://doi.org/10.1021/nl8009704.

[21] B. Poudel, Q. Hao, Y. Ma, Y. Lan, A. Minnich, B. Yu, X. Yan, D. Wang, A. Muto, D. Vashaee, X. Chen, J. Liu, M.S. Dresselhaus, G. Chen, Z. Ren, High-Thermoelectric Performance of Nanostructured Bismuth Antimony Telluride Bulk Alloys, Science (80-.). 320 (2008) 634–638. https://doi.org/10.1126/science.1156446.

[22] Y. Pei, X. Shi, A. LaLonde, H. Wang, L. Chen, G.J. Snyder, Convergence of electronic bands for high performance bulk thermoelectrics, Nature. 473 (2011) 66–69. https://doi.org/10.1038/nature09996.

[23] R. Venkatasubramanian, E. Siivola, T. Colpitts, B. O'Quinn, Thin-film thermoelectric devices with high room-temperature figures of merit, Nature. 413 (2001) 597–602. https://doi.org/10.1038/35098012.

[24] T.M. Tritt, THERMOELECTRIC MATERIALS:Holey and Unholey Semiconductors, Science (80-.). 283 (1999) 804–805. https://doi.org/10.1126/science.283.5403.804.

[25] O. Bubnova, Z.U. Khan, A. Malti, S. Braun, M. Fahlman, M. Berggren, X. Crispin, Optimization of the thermoelectric figure of merit in the conducting polymer poly(3,4-ethylenedioxythiophene), Nat. Mater. 10 (2011) 429–433. https://doi.org/10.1038/nmat3012.

[26] S. Ahmad, Organic semiconductors for device applications: current trends and future prospects, J. Polym. Eng. 34 (2014) 279–338. https://doi.org/10.1515/polyeng-2013-0267.

[27] J.D. Myers, J. Xue, Organic Semiconductors and their Applications in Photovoltaic Devices, Polym. Rev. 52 (2012) 1–37. https://doi.org/10.1080/15583724.2011.644368.

[28] S.D. Kang, G.J. Snyder, Charge-transport model for conducting polymers, Nat. Mater. 16 (2017) 252–257. https://doi.org/10.1038/nmat4784.

[29] A. V Nenashev, J.O. Oelerich, S.D. Baranovskii, Theoretical tools for the description of charge transport in disordered organic semiconductors, J. Phys. Condens. Matter. 27 (2015) 093201. https://doi.org/10.1088/0953-8984/27/9/093201.

[30] N. Mott, The mobility edge since 1967, J. Phys. C Solid State Phys. 20 (1987) 3075–3102. https://doi.org/10.1088/0022-3719/20/21/008.

[31] V. Ambegaokar, B.I. Halperin, J.S. Langer, Hopping Conductivity in Disordered Systems, Phys. Rev. B. 4 (1971) 2612–2620. https://doi.org/10.1103/PhysRevB.4.2612.

[32] P. Stallinga, Electronic Transport in Organic Materials: Comparison of Band Theory with Percolation/(Variable Range) Hopping Theory, Adv. Mater. 23 (2011) 3356–3362. https://doi.org/10.1002/adma.201101129.

[33] H. Abdalla, G. Zuo, M. Kemerink, Range and energetics of charge hopping in organic semiconductors, Phys. Rev. B. 96 (2017) 241202. https://doi.org/10.1103/PhysRevB.96.241202.

[34] N. Mott, E.A. Davis, Electronic Processes in Non-Crystalline Materials, Second, Oxford University Press, 1971.

[35] A.M. Glaudell, J.E. Cochran, S.N. Patel, M.L. Chabinyc, Impact of the Doping Method on Conductivity and Thermopower in Semiconducting Polythiophenes, Adv. Energy Mater. 5

(2015) 1401072. https://doi.org/10.1002/aenm.201401072.

[36] B. Russ, A. Glaudell, J.J. Urban, M.L. Chabinyc, R.A. Segalman, Organic thermoelectric materials for energy harvesting and temperature control, Nat. Rev. Mater. 1 (2016) 16050. https://doi.org/10.1038/natrevmats.2016.50.

[37] R. Kroon, D.A. Mengistie, D. Kiefer, J. Hynynen, J.D. Ryan, L. Yu, C. Müller, Thermoelectric plastics: from design to synthesis, processing and structure–property relationships, Chem. Soc. Rev. 45 (2016) 6147–6164. https://doi.org/10.1039/C6CS00149A.

[38] M.T. Fontana, D.A. Stanfield, D.T. Scholes, K.J. Winchell, S.H. Tolbert, B.J. Schwartz, Evaporation vs Solution Sequential Doping of Conjugated Polymers: F 4 TCNQ Doping of Micrometer-Thick P3HT Films for Thermoelectrics, J. Phys. Chem. C. 123 (2019) 22711–22724. https://doi.org/10.1021/acs.jpcc.9b05069.

[39] S.N. Patel, A.M. Glaudell, K.A. Peterson, E.M. Thomas, K.A. O'Hara, E. Lim, M.L. Chabinyc, Morphology controls the thermoelectric power factor of a doped semiconducting polymer, Sci. Adv. 3 (2017) e1700434. https://doi.org/10.1126/sciadv.1700434.

[40] S.K. Yee, N.E. Coates, A. Majumdar, J.J. Urban, R.A. Segalman, Thermoelectric power factor optimization in PEDOT:PSS tellurium nanowire hybrid composites, Phys. Chem. Chem. Phys. 15 (2013) 4024. https://doi.org/10.1039/c3cp44558e.

[41] Q. Zhang, Y. Sun, W. Xu, D. Zhu, Organic Thermoelectric Materials: Emerging Green Energy Materials Converting Heat to Electricity Directly and Efficiently, Adv. Mater. 26 (2014) 6829–6851. https://doi.org/10.1002/adma.201305371.

[42] E.W. Zaia, M.P. Gordon, P. Yuan, J.J. Urban, Progress and Perspective: Soft

Thermoelectric Materials for Wearable and Internet-of-Things Applications, Adv. Electron. Mater. 5 (2019) 1800823. https://doi.org/10.1002/aelm.201800823.

[43] Z. Fan, Y. Zhang, L. Pan, J. Ouyang, Q. Zhang, Recent developments in flexible thermoelectrics: From materials to devices, Renew. Sustain. Energy Rev. 137 (2021) 110448. https://doi.org/10.1016/j.rser.2020.110448.

[44] Y. Lu, J.-Y. Wang, J. Pei, Strategies To Enhance the Conductivity of n-Type Polymer Thermoelectric Materials, Chem. Mater. 31 (2019) 6412–6423. https://doi.org/10.1021/acs.chemmater.9b01422.

[45] R. Zuzok, A.B. Kaiser, W. Pukacki, S. Roth, Thermoelectric power and conductivity of iodine-doped ‘“new”’ polyacetylene, J. Chem. Phys. 95 (1991) 1270–1275. https://doi.org/10.1063/1.461107.

[46] L. Liang, G. Chen, C.-Y. Guo, Polypyrrole nanostructures and their thermoelectric performance, Mater. Chem. Front. 1 (2017) 380–386. https://doi.org/10.1039/C6QM00061D.

[47] L. Jun, Z. Lian-meng, H. Li, T. Xin-feng, Synthesis and thermoelectric properties of polyaniline, J. Wuhan Univ. Technol. Sci. Ed. 18 (2003) 53–55. https://doi.org/10.1007/BF02838459.

[48] I. Lévesque, P.-O. Bertrand, N. Blouin, M. Leclerc, S. Zecchin, G. Zotti, C.I. Ratcliffe, D.D. Klug, X. Gao, F. Gao, J.S. Tse, Synthesis and Thermoelectric Properties of Polycarbazole, Polyindolocarbazole, and Polydiindolocarbazole Derivatives, Chem. Mater. 19 (2007) 2128–2138. https://doi.org/10.1021/cm070063h.

[49] J. Zhang, G. Song, L. Qiu, Y. Feng, J. Chen, J. Yan, L. Liu, X. Huang, Y. Cui, Y. Sun, W. Xu, D. Zhu, Highly Conducting Polythiophene Thin Films with Less Ordered

Microstructure Displaying Excellent Thermoelectric Performance, Macromol. Rapid Commun. 39 (2018) 1800283. https://doi.org/10.1002/marc.201800283.

[50] Q. Wei, M. Mukaida, K. Kirihara, Y. Naitoh, T. Ishida, Recent Progress on PEDOT-Based Thermoelectric Materials, Materials (Basel). 8 (2015) 732–750. https://doi.org/10.3390/ma8020732.

[51] J. Li, L. Wang, X. Jia, X. Xiang, C.-L. Ho, W.-Y. Wong, H. Li, Preparation and thermoelectric properties of diphenylaminobenzylidene-substituted poly(3-methylthiophene methine)/graphite composite, RSC Adv. 4 (2014) 62096–62104. https://doi.org/10.1039/C4RA09621E.

[52] D. Wang, Y. Su, D. Chen, L. Wang, X. Xiang, D. Zhu, Preparation and characterization of poly(3-octylthiophene)/carbon fiber thermoelectric composite materials, Compos. Part B Eng. 69 (2015) 467–471. https://doi.org/10.1016/j.compositesb.2014.10.007.

[53] S. Qu, Q. Yao, L. Wang, Z. Chen, K. Xu, H. Zeng, W. Shi, T. Zhang, C. Uher, L. Chen, Highly anisotropic P3HT films with enhanced thermoelectric performance via organic small molecule epitaxy, NPG Asia Mater. 8 (2016) e292–e292. https://doi.org/10.1038/am.2016.97.

[54] S. Hu, S. Zeng, X. Li, J. Jiang, W. Yang, Y. Chen, M. Li, J. Zheng, Flexible and high performance of n-type thermoelectric PVDF composite film induced by nickel nanowires, Mater. Des. 188 (2020) 108496. https://doi.org/10.1016/j.matdes.2020.108496.

[55] Y. Wen, J. Xu, Scientific Importance of Water-Processable PEDOT-PSS and Preparation, Challenge and New Application in Sensors of Its Film Electrode: A Review, J. Polym. Sci. Part A Polym. Chem. 55 (2017) 1121–1150. https://doi.org/10.1002/pola.28482.

[56] J.Y. Kim, J.H. Jung, D.E. Lee, J. Joo, Enhancement of electrical conductivity of poly(3,4-

ethylenedioxythiophene)/poly(4-styrenesulfonate) by a change of solvents, Synth. Met. 126 (2002) 311–316. https://doi.org/10.1016/S0379-6779(01)00576-8.

[57] O. Bubnova, M. Berggren, X. Crispin, Tuning the Thermoelectric Properties of Conducting Polymers in an Electrochemical Transistor, J. Am. Chem. Soc. 134 (2012) 16456–16459. https://doi.org/10.1021/ja305188r.

[58] G.-H. Kim, L. Shao, K. Zhang, K.P. Pipe, Engineered doping of organic semiconductors for enhanced thermoelectric efficiency, Nat. Mater. 12 (2013) 719–723. https://doi.org/10.1038/nmat3635.

[59] Z. Fan, P. Li, D. Du, J. Ouyang, Significantly Enhanced Thermoelectric Properties of PEDOT:PSS Films through Sequential Post-Treatments with Common Acids and Bases, Adv. Energy Mater. 7 (2017) 1602116. https://doi.org/10.1002/aenm.201602116.

[60] M. Culebras, C.M. Gómez, A. Cantarero, Enhanced thermoelectric performance of PEDOT with different counterions optimized by chemical reduction, J. Mater. Chem. A. 2 (2014) 10109–10115. https://doi.org/10.1039/C4TA01012D.

[61] O. Bubnova, Z.U. Khan, A. Malti, S. Braun, M. Fahlman, M. Berggren, X. Crispin, Optimization of the thermoelectric figure of merit in the conducting polymer poly(3,4-ethylenedioxythiophene), Nat. Mater. 10 (2011) 429–433. https://doi.org/10.1038/nmat3012.

[62] Q. Zhang, Y. Sun, W. Xu, D. Zhu, Thermoelectric energy from flexible P3HT films doped with a ferric salt of triflimide anions, Energy Environ. Sci. 5 (2012) 9639. https://doi.org/10.1039/c2ee23006b.

[63] C.T. Hong, Y. Yoo, Y.H. Kang, J. Ryu, S.Y. Cho, K.-S. Jang, Effect of film thickness and crystallinity on the thermoelectric properties of doped P3HT films, RSC Adv. 5 (2015)

11385–11391. https://doi.org/10.1039/C4RA15681A.

[64] E. Lim, K.A. Peterson, G.M. Su, M.L. Chabinyc, Thermoelectric Properties of Poly(3-hexylthiophene) (P3HT) Doped with 2,3,5,6-Tetrafluoro-7,7,8,8-tetracyanoquinodimethane (F 4 TCNQ) by Vapor-Phase Infiltration, Chem. Mater. 30 (2018) 998–1010. https://doi.org/10.1021/acs.chemmater.7b04849.

[65] M.L. Chabinyc, M.F. Toney, R.J. Kline, I. McCulloch, M. Heeney, X-ray Scattering Study of Thin Films of Poly(2,5-bis(3-alkylthiophen-2-yl)thieno[3,2- b]thiophene), J. Am. Chem. Soc. 129 (2007) 3226–3237. https://doi.org/10.1021/ja0670714.

[66] Q. Zhang, Y. Sun, W. Xu, D. Zhu, What To Expect from Conducting Polymers on the Playground of Thermoelectricity: Lessons Learned from Four High-Mobility Polymeric Semiconductors, Macromolecules. 47 (2014) 609–615. https://doi.org/10.1021/ma4020406.

[67] S.N. Patel, A.M. Glaudell, D. Kiefer, M.L. Chabinyc, Increasing the Thermoelectric Power Factor of a Semiconducting Polymer by Doping from the Vapor Phase, ACS Macro Lett. 5 (2016) 268–272. https://doi.org/10.1021/acsmacrolett.5b00887.

[68] V. Vijayakumar, Y. Zhong, V. Untilova, M. Bahri, L. Herrmann, L. Biniek, N. Leclerc, M. Brinkmann, Bringing Conducting Polymers to High Order: Toward Conductivities beyond 10 5 S cm −1 and Thermoelectric Power Factors of 2 mW m −1 K −2, Adv. Energy Mater. 9 (2019) 1900266. https://doi.org/10.1002/aenm.201900266.

[69] L. Wang, C. Pan, Z. Chen, X. Zhou, C. Gao, L. Wang, A study of the thermoelectric properties of benzo[1,2- b :4,5- b ′]dithiophene–based donor–acceptor conjugated polymers, Polym. Chem. 9 (2018) 4440–4447. https://doi.org/10.1039/C8PY00812D.

[70] X. Zhou, C. Pan, C. Gao, A. Shinohara, X. Yin, L. Wang, Y. Li, Q. Jiang, C. Yang, L.

Wang, Thermoelectrics of two-dimensional conjugated benzodithiophene-based polymers: density-of-states enhancement and semi-metallic behavior, J. Mater. Chem. A. 7 (2019) 10422–10430. https://doi.org/10.1039/C9TA01437C.

[71] N. Toshima, Recent progress of organic and hybrid thermoelectric materials, Synth. Met. 225 (2017) 3–21. https://doi.org/10.1016/j.synthmet.2016.12.017.

[72] N. Bisht, P. More, P.K. Khanna, R. Abolhassani, Y.K. Mishra, M. Madsen, Progress of hybrid nanocomposite materials for thermoelectric applications, Mater. Adv. 2 (2021) 1927–1956. https://doi.org/10.1039/D0MA01030H.

[73] L. Wang, Z. Zhang, Y. Liu, B. Wang, L. Fang, J. Qiu, K. Zhang, S. Wang, Exceptional thermoelectric properties of flexible organic−inorganic hybrids with monodispersed and periodic nanophase, Nat. Commun. 9 (2018) 3817. https://doi.org/10.1038/s41467-018-06251-9.

[74] N.E. Coates, S.K. Yee, B. McCulloch, K.C. See, A. Majumdar, R.A. Segalman, J.J. Urban, Effect of Interfacial Properties on Polymer-Nanocrystal Thermoelectric Transport, Adv. Mater. 25 (2013) 1629–1633. https://doi.org/10.1002/adma.201203915.

[75] H. An, D. Karas, B.-W. Kim, S. Trabia, J. Moon, Flexible n-type thermoelectric composite films with enhanced performance through interface engineering and post-treatment, Nanotechnology. 29 (2018) 275403. https://doi.org/10.1088/1361-6528/aabeb6.

[76] M. He, J. Ge, Z. Lin, X. Feng, X. Wang, H. Lu, Y. Yang, F. Qiu, Thermopower enhancement in conducting polymer nanocomposites via carrier energy scattering at the organic–inorganic semiconductor interface, Energy Environ. Sci. 5 (2012) 8351. https://doi.org/10.1039/c2ee21803h.

[77] K.C. See, J.P. Feser, C.E. Chen, A. Majumdar, J.J. Urban, R.A. Segalman, Water-

Processable Polymer−Nanocrystal Hybrids for Thermoelectrics, Nano Lett. 10 (2010) 4664–4667. https://doi.org/10.1021/nl102880k.

[78] E.W. Zaia, A. Sahu, P. Zhou, M.P. Gordon, J.D. Forster, S. Aloni, Y.-S. Liu, J. Guo, J.J. Urban, Carrier Scattering at Alloy Nanointerfaces Enhances Power Factor in PEDOT:PSS Hybrid Thermoelectrics, Nano Lett. 16 (2016) 3352–3359. https://doi.org/10.1021/acs.nanolett.6b01009.

[79] Y. Wang, S.M. Zhang, Y. Deng, Flexible low-grade energy utilization devices based on high-performance thermoelectric polyaniline/tellurium nanorod hybrid films, J. Mater. Chem. A. 4 (2016) 3554–3559. https://doi.org/10.1039/C6TA01140C.

[80] B. Zhang, J. Sun, H.E. Katz, F. Fang, R.L. Opila, Promising Thermoelectric Properties of Commercial PEDOT:PSS Materials and Their Bi 2 Te 3 Powder Composites, ACS Appl. Mater. Interfaces. 2 (2010) 3170–3178. https://doi.org/10.1021/am100654p.

[81] N. Toshima, M. Imai, S. Ichikawa, Organic–Inorganic Nanohybrids as Novel Thermoelectric Materials: Hybrids of Polyaniline and Bismuth(III) Telluride Nanoparticles, J. Electron. Mater. 40 (2011) 898–902. https://doi.org/10.1007/s11664-010-1403-1.

[82] K. Chatterjee, M. Mitra, K. Kargupta, S. Ganguly, D. Banerjee, Synthesis, characterization and enhanced thermoelectric performance of structurally ordered cable-like novel polyaniline–bismuth telluride nanocomposite, Nanotechnology. 24 (2013) 215703. https://doi.org/10.1088/0957-4484/24/21/215703.

[83] Y. Du, K.F. Cai, S. Chen, P. Cizek, T. Lin, Facile Preparation and Thermoelectric Properties of Bi 2 Te 3 Based Alloy Nanosheet/PEDOT:PSS Composite Films, ACS Appl. Mater. Interfaces. 6 (2014) 5735–5743. https://doi.org/10.1021/am5002772.

[84] C. Liu, F. Jiang, M. Huang, B. Lu, R. Yue, J. Xu, Free-Standing PEDOT-PSS/Ca3Co4O9 Composite Films as Novel Thermoelectric Materials, J. Electron. Mater. 40 (2011) 948–952. https://doi.org/10.1007/s11664-010-1465-0.

[85] N. Toshima, N. Jiravanichanun, H. Marutani, Organic Thermoelectric Materials Composed of Conducting Polymers and Metal Nanoparticles, J. Electron. Mater. 41 (2012) 1735–1742. https://doi.org/10.1007/s11664-012-2041-6.

[86] N. Toshima, N. Jiravanichanun, Improvement of Thermoelectric Properties of PEDOT/PSS Films by Addition of Gold Nanoparticles: Enhancement of Seebeck Coefficient, J. Electron. Mater. 42 (2013) 1882–1887. https://doi.org/10.1007/s11664-012-2458-y.

[87] T. Ramanathan, A.A. Abdala, S. Stankovich, D.A. Dikin, M. Herrera-Alonso, R.D. Piner, D.H. Adamson, H.C. Schniepp, X. Chen, R.S. Ruoff, S.T. Nguyen, I.A. Aksay, R.K. Prud'Homme, L.C. Brinson, Functionalized graphene sheets for polymer nanocomposites, Nat. Nanotechnol. 3 (2008) 327–331. https://doi.org/10.1038/nnano.2008.96.

[88] M. Piao, J. Na, J. Choi, J. Kim, G.P. Kennedy, G. Kim, S. Roth, U. Dettlaff-Weglikowska, Increasing the thermoelectric power generated by composite films using chemically functionalized single-walled carbon nanotubes, Carbon N. Y. 62 (2013) 430–437. https://doi.org/10.1016/j.carbon.2013.06.028.

[89] J. Kong, Nanotube Molecular Wires as Chemical Sensors, Science (80-.). 287 (2000) 622–625. https://doi.org/10.1126/science.287.5453.622.

[90] P.G. Collins, Extreme Oxygen Sensitivity of Electronic Properties of Carbon Nanotubes, Science (80-.). 287 (2000) 1801–1804. https://doi.org/10.1126/science.287.5459.1801.

[91] W.-Q. Qu, C.-Y. Gao, P.-X. Zhang, X.-H. Fan, L.-M. Yang, Pseudo in situ construction of

high-performance thermoelectric composites with a dioxothiopyrone-based D–A polymer coating on SWCNTs, RSC Adv. 11 (2021) 8664–8673. https://doi.org/10.1039/D0RA10625A.

[92] W. Fan, L. Liang, B. Zhang, C.-Y. Guo, G. Chen, PEDOT thermoelectric composites with excellent power factors prepared by 3-phase interfacial electropolymerization and carbon nanotube chemical doping, J. Mater. Chem. A. 7 (2019) 13687–13694. https://doi.org/10.1039/C9TA03153G.

[93] J.U. Ha, J. Cho, S. Yoon, M.S. Jang, S.Z. Hassan, M.G. Kang, D.S. Chung, Polyvinyl alcohol covalently grafted CNT for free-standing, flexible, and high-performance thermoelectric generator film, Nanotechnology. 30 (2019) 14LT01. https://doi.org/10.1088/1361-6528/ab0121.

[94] J. Luo, B. Krause, P. Pötschke, Polymer - Carbon nanotube composites for thermoelectric applications, in: 2017: p. 030001. https://doi.org/10.1063/1.5016688.

[95] W. Fan, C.-Y. Guo, G. Chen, Flexible films of poly(3,4-ethylenedioxythiophene)/carbon nanotube thermoelectric composites prepared by dynamic 3-phase interfacial electropolymerization and subsequent physical mixing, J. Mater. Chem. A. 6 (2018) 12275–12280. https://doi.org/10.1039/C8TA04838J.

[96] D. Kim, Y. Kim, K. Choi, J.C. Grunlan, C. Yu, Improved Thermoelectric Behavior of Nanotube-Filled Polymer Composites with Poly(3,4-ethylenedioxythiophene) Poly(styrenesulfonate), ACS Nano. 4 (2010) 513–523. https://doi.org/10.1021/nn9013577.

[97] G.P. Moriarty, S. De, P.J. King, U. Khan, M. Via, J.A. King, J.N. Coleman, J.C. Grunlan, Thermoelectric behavior of organic thin film nanocomposites, J. Polym. Sci. Part B Polym. Phys. 51 (2013) 119–123. https://doi.org/10.1002/polb.23186.

[98] C. Yu, K. Choi, L. Yin, J.C. Grunlan, Light-Weight Flexible Carbon Nanotube Based Organic Composites with Large Thermoelectric Power Factors, ACS Nano. 5 (2011) 7885–7892. https://doi.org/10.1021/nn202868a.

[99] W. Lee, Y.H. Kang, J.Y. Lee, K.-S. Jang, S.Y. Cho, Improving the thermoelectric power factor of CNT/PEDOT:PSS nanocomposite films by ethylene glycol treatment, RSC Adv. 6 (2016) 53339–53344. https://doi.org/10.1039/C6RA08599G.

[100] J.-H. Hsu, W. Choi, G. Yang, C. Yu, Origin of unusual thermoelectric transport behaviors in carbon nanotube filled polymer composites after solvent/acid treatments, Org. Electron. 45 (2017) 182–189. https://doi.org/10.1016/j.orgel.2017.03.007.

[101] Q. Wang, Q. Yao, J. Chang, L. Chen, Enhanced thermoelectric properties of CNT/PANI composite nanofibers by highly orienting the arrangement of polymer chains, J. Mater. Chem. 22 (2012) 17612. https://doi.org/10.1039/c2jm32750c.

[102] H. Yan, K. Kou, Enhanced thermoelectric properties in polyaniline composites with polyaniline-coated carbon nanotubes, J. Mater. Sci. 49 (2014) 1222–1228. https://doi.org/10.1007/s10853-013-7804-9.

[103] R. Wu, H. Yuan, C. Liu, J.-L. Lan, X. Yang, Y.-H. Lin, Flexible PANI/SWCNT thermoelectric films with ultrahigh electrical conductivity, RSC Adv. 8 (2018) 26011–26019. https://doi.org/10.1039/C8RA04863K.

[104] S. Yin, W. Lu, X. Wu, Q. Luo, E. Wang, C.-Y. Guo, Enhancing Thermoelectric Performance of Polyaniline/Single-Walled Carbon Nanotube Composites via Dimethyl Sulfoxide-Mediated Electropolymerization, ACS Appl. Mater. Interfaces. 13 (2021) 3930–3936. https://doi.org/10.1021/acsami.0c19100.

[105] J. Wang, K. Cai, S. Shen, J. Yin, Preparation and thermoelectric properties of multi-

walled carbon nanotubes/polypyrrole composites, Synth. Met. 195 (2014) 132–136. https://doi.org/10.1016/j.synthmet.2014.06.003.

[106] S. Wang, Y. Zhou, Y. Liu, L. Wang, C. Gao, Enhanced thermoelectric properties of polyaniline/polypyrrole/carbon nanotube ternary composites by treatment with a secondary dopant using ferric chloride, J. Mater. Chem. C. 8 (2020) 528–535. https://doi.org/10.1039/C9TC06300E.

[107] C. Bounioux, P. Díaz-Chao, M. Campoy-Quiles, M.S. Martín-González, A.R. Goñi, R. Yerushalmi-Rozen, C. Müller, Thermoelectric composites of poly(3-hexylthiophene) and carbon nanotubes with a large power factor, Energy Environ. Sci. 6 (2013) 918. https://doi.org/10.1039/c2ee23406h.

[108] C.T. Hong, W. Lee, Y.H. Kang, Y. Yoo, J. Ryu, S.Y. Cho, K.-S. Jang, Effective doping by spin-coating and enhanced thermoelectric power factors in SWCNT/P3HT hybrid films, J. Mater. Chem. A. 3 (2015) 12314–12319. https://doi.org/10.1039/C5TA02443A.

[109] C.T. Hong, Y.H. Kang, J. Ryu, S.Y. Cho, K.-S. Jang, Spray-printed CNT/P3HT organic thermoelectric films and power generators, J. Mater. Chem. A. 3 (2015) 21428–21433. https://doi.org/10.1039/C5TA06096F.

[110] X. Zhou, C. Pan, A. Liang, L. Wang, W.-Y. Wong, Thermoelectric properties of composite films prepared with benzodithiophene derivatives and carbon nanotubes, Compos. Sci. Technol. 145 (2017) 40–45. https://doi.org/10.1016/j.compscitech.2017.03.040.

[111] L. Wang, C. Pan, Z. Chen, W. Zhou, C. Gao, L. Wang, Enhanced Thermoelectric Performance of Conjugated Polymer/Single-Walled Carbon Nanotube Composites with Strong Stacking, ACS Appl. Energy Mater. 1 (2018) 5075–5082.

https://doi.org/10.1021/acsaem.8b01126.

[112] Z. Chen, M. Lai, L. Cai, W. Zhou, D. Xie, C. Pan, Y. Qiu, Boosting the Power Factor of Benzodithiophene Based Donor–Acceptor Copolymers/SWCNTs Composites through Doping, Polymers (Basel). 12 (2020) 1447. https://doi.org/10.3390/polym12071447.

[113] D. Yoo, J. Kim, J.H. Kim, Direct synthesis of highly conductive poly(3,4-ethylenedioxythiophene):poly(4-styrenesulfonate) (PEDOT:PSS)/graphene composites and their applications in energy harvesting systems, Nano Res. 7 (2014) 717–730. https://doi.org/10.1007/s12274-014-0433-z.

[114] F.-P. Du, N.-N. Cao, Y.-F. Zhang, P. Fu, Y.-G. Wu, Z.-D. Lin, R. Shi, A. Amini, C. Cheng, PEDOT:PSS/graphene quantum dots films with enhanced thermoelectric properties via strong interfacial interaction and phase separation, Sci. Rep. 8 (2018) 6441. https://doi.org/10.1038/s41598-018-24632-4.

[115] L. Wang, H. Bi, Q. Yao, D. Ren, S. Qu, F. Huang, L. Chen, Three-dimensional tubular graphene/polyaniline composites as high-performance elastic thermoelectrics, Compos. Sci. Technol. 150 (2017) 135–140. https://doi.org/10.1016/j.compscitech.2017.07.001.

[116] Y.-H. Lin, T.-C. Lee, Y.-S. Hsiao, W.-K. Lin, W.-T. Whang, C.-H. Chen, Facile Synthesis of Diamino-Modified Graphene/Polyaniline Semi-Interpenetrating Networks with Practical High Thermoelectric Performance, ACS Appl. Mater. Interfaces. 10 (2018) 4946–4952. https://doi.org/10.1021/acsami.7b14890.

[117] M. Orrill, S. LeBlanc, Printed thermoelectric materials and devices: Fabrication techniques, advantages, and challenges, J. Appl. Polym. Sci. 134 (2017). https://doi.org/10.1002/app.44256.

[118] R.R. Søndergaard, M. Hösel, N. Espinosa, M. Jørgensen, F.C. Krebs, Practical evaluation

of organic polymer thermoelectrics by large-area R2R processing on flexible substrates, Energy Sci. Eng. 1 (2013) 81–88. https://doi.org/10.1002/ese3.8.

[119] Q. Wei, M. Mukaida, K. Kirihara, Y. Naitoh, T. Ishida, Polymer thermoelectric modules screen-printed on paper, RSC Adv. 4 (2014) 28802–28806. https://doi.org/10.1039/C4RA04946B.

[120] E. Jin Bae, Y. Hun Kang, K.-S. Jang, S. Yun Cho, Enhancement of Thermoelectric Properties of PEDOT:PSS and Tellurium-PEDOT:PSS Hybrid Composites by Simple Chemical Treatment, Sci. Rep. 6 (2016) 18805. https://doi.org/10.1038/srep18805.

[121] Z. Li, H. Sun, C. Hsiao, Y. Yao, Y. Xiao, M. Shahi, Y. Jin, A. Cruce, X. Liu, Y. Jiang, W. Meng, F. Qin, T. Ederth, S. Fabiano, W.M. Chen, X. Lu, J. Birch, J.W. Brill, Y. Zhou, X. Crispin, F. Zhang, A Free-Standing High-Output Power Density Thermoelectric Device Based on Structure-Ordered PEDOT:PSS, Adv. Electron. Mater. 4 (2018) 1700496. https://doi.org/10.1002/aelm.201700496.

[122] X. Dong, S. Xiong, B. Luo, R. Ge, Z. Li, J. Li, Y. Zhou, Flexible and Transparent Organic–Inorganic Hybrid Thermoelectric Modules, ACS Appl. Mater. Interfaces. 10 (2018) 26687–26693. https://doi.org/10.1021/acsami.8b08696.

[123] Y. Du, K. Cai, S. Chen, H. Wang, S.Z. Shen, R. Donelson, T. Lin, Thermoelectric Fabrics: Toward Power Generating Clothing, Sci. Rep. 5 (2015) 6411. https://doi.org/10.1038/srep06411.

[124] J.D. Ryan, D.A. Mengistie, R. Gabrielsson, A. Lund, C. Müller, Machine-Washable PEDOT:PSS Dyed Silk Yarns for Electronic Textiles, ACS Appl. Mater. Interfaces. 9 (2017) 9045–9050. https://doi.org/10.1021/acsami.7b00530.

[125] C. Zheng, L. Xiang, W. Jin, H. Shen, W. Zhao, F. Zhang, C. Di, D. Zhu, A Flexible Self-

Powered Sensing Element with Integrated Organic Thermoelectric Generator, Adv. Mater. Technol. 4 (2019) 1900247. https://doi.org/10.1002/admt.201900247.

[126] J.J. Lee, D. Yoo, C. Park, H.H. Choi, J.H. Kim, All organic-based solar cell and thermoelectric generator hybrid device system using highly conductive PEDOT:PSS film as organic thermoelectric generator, Sol. Energy. 134 (2016) 479–483. https://doi.org/10.1016/j.solener.2016.05.006.

[127] J.P. Jurado, B. Dörling, O. Zapata-Arteaga, A. Roig, A. Mihi, M. Campoy-Quiles, Solar Harvesting: a Unique Opportunity for Organic Thermoelectrics?, Adv. Energy Mater. 9 (2019) 1902385. https://doi.org/10.1002/aenm.201902385.

[128] K.T. Regner, S. Majumdar, J.A. Malen, Instrumentation of broadband frequency domain thermoreflectance for measuring thermal conductivity accumulation functions, Rev. Sci. Instrum. 84 (2013) 064901. https://doi.org/10.1063/1.4808055.

[129] J.P. Feser, D.G. Cahill, Probing anisotropic heat transport using time-domain thermoreflectance with offset laser spots, Rev. Sci. Instrum. 83 (2012) 104901. https://doi.org/10.1063/1.4757863.

[130] A.J. Schmidt, R. Cheaito, M. Chiesa, A frequency-domain thermoreflectance method for the characterization of thermal properties, Rev. Sci. Instrum. 80 (2009) 094901. https://doi.org/10.1063/1.3212673.

[131] D.G. Cahill, Thermal conductivity measurement from 30 to 750 K: the 3ω method, Rev. Sci. Instrum. 61 (1990) 802–808. https://doi.org/10.1063/1.1141498.

[132] J. Liu, J. Zhu, M. Tian, X. Gu, A. Schmidt, R. Yang, Simultaneous measurement of thermal conductivity and heat capacity of bulk and thin film materials using frequency-dependent transient thermoreflectance method, Rev. Sci. Instrum. 84 (2013) 034902.

https://doi.org/10.1063/1.4797479.

[133] Linseis LSR-3, (n.d.). https://www.linseis.com/en/products/thermoelectrics/lsr-3/.

[134] ULVAC ZEM-3, (n.d.). https://www.ulvac.com/components/Thermal-Instruments/Thermoelectric-Testers/ZEM-3-Series.

CHAPTER 2

Conjugated Thienothiophene Polymer/MWCNT based All-Organic Thermoelectric Composites

The world's energy demand has been increased drastically, which drives the scavenging of waste heat using thermoelectric generators (TEG) [1]. The automobile industry has already started to use thermoelectric (TE) technology to convert waste heat from the hot gas exhaust using inorganic-based TEGs. In the automobile industry, the usage of TEGs improves engine efficiency by converting the waste heat into usable power to run auxiliaries such as electronics & navigation, seat warmer, electronic braking, indoor lightings, etc. [2]. Major multinational automobile brands like BMW [3], Ford [4], Renault [5], and Honda [6] already have a strong foothold in this field, and many of their upscale models now have functional TEGs. However, significant cost reduction and other engineering challenges must be addressed to implement this technology in the mass market segment [7].

The efficiency of TEG is generally characterized by dimensionless figure-of-merit (*ZT*), defined in equation 1.1. Recent progress in the preparation and engineering of inorganic TE materials has led to remarkable improvements in device performances [8,9]. The enhancements are primarily accessed by the proper utilization of nanostructuring techniques such as creating phonon-blocking/ electron-transmitting thin-film superlattices [10–13], quantum-dot superlattices [14–17], and nanoscale inclusions in bulk materials [18,19]. However, these materials involved high temperatures, high-cost, and time-consuming fabrication processes. Moreover, most high-performance inorganic TE materials have their operation temperature above 200 °C, which is not

suitable for capturing waste heat generated at a temperature below 200 °C. In this context, there is an enormous need for cheaper and lighter TE materials, preferably flexible, and working at the low-temperature range.

Research on organic TE materials has emerged and made tremendous progress in the past few years [20–24]. Organic materials, made up of abundant and less/non-toxic elements, can be solution-processed, enabling the construction of sustainable, large area and flexible TE devices for converting low-end thermal energy into electricity. In the last decade, significant improvements in organic TE materials' performance were observed due to the development of new molecular design strategies and the fabrication of nanocomposites consisting of conducting/semiconducting polymers with various nanomaterials [25]. A clear disadvantage of TE modules consisting of composites using heavy inorganic fillers is their module weight, which reduces their overall energy efficiency and limits their large-area applications. Such modules are mainly suitable for off-site operations, where associated technology for concentrating thermal energy/heat circulation may be required. In comparison, substantial weight reduction of TEGs would enable us to fabricate flexible, portable, easily mountable systems with low processing, implementation, and maintenance costs. New application areas such as point of care sensors and IoT-based devices would immensely benefit from such power sources.

In contrast, developing an all organic-based composite such as polymer fused/reinforced with carbon nanotubes (CNT) could be a promising approach to deliver a functional ultra-lightweight TE module. The general approach would be incorporating CNT in the polymer matrix to improve σ and mechanical strength without affecting κ [26]. Kim *et al.* described the TE performance enhancement of PEDOT:PSS by CNT incorporation. The σ of the composite was enhanced up to ~400 S/cm, which is more than 100 times higher than those of the typical polymer

composite due to the formation of polymer matrix–CNT electronic junctions [27]. Another study on similar composites showed little variance in α with increased loading of single-walled CNT (0–85 wt%), but σ increases leading to a maximum power factor of 140 μW/m.K^2 [28]. This PF was in the range observed for Bi_2Te_3, one of the most explored inorganic TE materials [29].

Nevertheless, making a stable PEDOT composite is quite challenging due to the hydrophobicity of the CNT surface. The current state-of-the-art PEDOT:PSS has many disadvantages that include hygroscopicity, acidity, anisotropic charge injection, and batch-to-batch variation in physical and electrical properties. Since the PSS chains contain sulfonic acid groups with labile protons, it makes the polymer acidic in nature [30]. Moreover, in the presence of water vapors, the PSS shell, which surrounds the conducting PEDOT-rich cores, takes up water vapors and subsequently swells, making PEDOT:PSS hygroscopic [31]. Many studies have earlier been performed to suppress the acidic nature of PEDOT:PSS [32] and to reduce the hygroscopicity [33,34]. Recently, Cameron *et al.* reviewed the damaging effects of PEDOT:PSS acidic nature on semiconductor device performances [30].

In pursuit of developing a stable, ultra-lightweight, and high-performing all-organic-based TE composite, we have selected a semiconducting polymer consisting of benzo-[1,2-b:4,5-b']dithiophene (BDT) and thienothiophene (TTE) units. Conjugated polymers based on BDT have attracted significant attention in the fields of organic photovoltaics, owing to their planar conjugated structures, excellent electron-donating ability, and high oxidative stability [35–38]. To date, this class of polymers exhibited the highest hole mobility (0.25 cm^2 /V.s) and solar cell efficiency (17.3%) among semiconducting organic polymers [39,40]. However, the TE properties of such systems have been scarcely explored. Similarly, the TE properties of TTE based conjugated polymers are also not being studied even though they show good charge carrier

mobility and good capability to interact with π-structures such as CNTs yielding hybrid structures with unique properties [41]. These polymers are more adaptive to CNTs than PEDOT, and incorporation of CNTs with such polymers can enhance the σ without much effect on κ, thereby enhancing the TE performance. Among the different types of CNTs, the single-walled carbon nanotubes (SWCNT) have a higher α. However, multi-walled carbon nanotube (MWCNT) has several advantages: facile production, inexpensive, and improved chemical stability than SWCNT. These aspects enhance the realization of polymer/ MWCNT nanocomposite materials for real-world applications such as waste heat harvesting from effluent pipes in industries. In this chapter, we prepared a nanocomposite of BDT-TTE based conjugated polymer poly[4,8-bis(5-(2-ethylhexyl)thiophen-2-yl)benzo[1,2-b;4,5-b']dithiophene-2,6-diyl-alt-(4-(2-ethylhexyl)-3-fluorothieno[3,4-b]thiophene-)-2-carboxylate-2-6-diyl)] (PBDTT-FTTE) and MWCNT and studied the TE properties. The as-prepared nanocomposite was further p-doped with an oxidizing agent to improve the TE performance by realigning the Fermi level. The process is generic and could be utilized to raise the TE properties of TTE based conjugated polymer materials to a competitive level. Moreover, we demonstrate that planar TEGs could be readily prepared by the facile solution processing of PBDTT-FTTE/MWCNT nanocomposites, which is a prerequisite for the realization of flexible, large-area applications.

2.1. Experiment section

2.1.1. Chemicals

PBDTT-FTTE ($(C_{49}H_{57}FO_2S_6)_n$) was purchased from Solarmer Energy INC. MWCNT (containing >90% carbon basis, diameter ~ 110-170 nm and length ~5-9 μm) and anhydrous *ortho*-dichlorobenzene (*o*-DCB) were obtained from Sigma-Aldrich. Anhydrous ferric chloride ($FeCl_3$)

was purchased from SD Fine Chemicals, and nitromethane (CH_3NO_2) was procured from Spectrochem. No further purification of chemicals was done, and it was used as such.

2.1.2. Preparation of nanocomposite

The nanocomposites were prepared by dispersing PBDTT-FTTE and MWCNT in *o*-DCB at a concentration of 0.05 mg/µL using a bath sonicator (Elmasonic P30H Ultrasonic bath; 80 kHz and 192 watts) for 60 min. The PBDTT-FTTE/MWCNT composition was varied by adding different weight percentages of MWCNT. The homogeneity of dispersions was confirmed by visual inspection. The dispersion was drop-cast on a pre-cleaned (with extran, water, and isopropanol in that sequence by bath sonication for 15 min in each) and pre-heated (at 120 °C for 15 min) glass substrate and annealed at 120 °C for 30 min.

2.1.3. Doping of nanocomposite film

Samples were doped by immersing in 0.05 M $FeCl_3$ solution in nitromethane for 30 min, then washed with ethanol to remove excess dopant followed by annealing at 100 °C for 15 min.

2.1.4. Characterization and measurements

The present work's characterization and measurement techniques are listed in Annexure I.

2.1.5. Fabrication of TEG and testing

The TEG consists of 7 TE legs, drop cast on a glass substrate using a PBDTT-FTTE/ 45 wt% MWCNT nanocomposite solution. The drop cast TE arrays were annealed on a hotplate at 120 °C for 30 min. The metal electrodes were drop-cast using conductive silver paste (TED PELLA, Pelco ® Conductive Silver paint) to connect the TE legs. The fabricated devices were subsequently dried at 100 °C for 30 min to improve the σ of the Ag electrodes and reduce the contact resistance. Each leg was 4 mm × 2.5 cm, and the overall size of the fabricated TEG was 4.5 cm × 2.5 cm.

The fabricated TEG evaluation was carried out in a home-built setup. The setup consisted of a silicon rubber heater (TEMPSENS Instruments Pvt. Ltd.) and a Peltier device (Laird Thermal Systems, Inc.) to independently function as the hot and cold region, respectively. The exact temperature of each surface was measured using a K-type thermocouple. The temperature difference between the thermocouples was varied from 3 to 65 K. For the measurement, a Keithley 2450 source meter, a Keithley 2182A nano voltmeter, and an Aplab PPD3003-S power supply were used.

2.2. Results and discussion

2.2.1. Nanocomposite characterization and analysis

The molecular structure of PBDTT-FTTE and the sample preparation method are depicted in Fig. 2.1a and Fig. 2.1b, respectively. Fig. 2.1c shows photographs of PBDTT-FTTE and PBDTT-FTTE/MWCNT nanocomposite in *o*-DCB at a 6.5 µg/mL concentration. The photograph shows that the MWCNTs and PBDTT-FTTE formed a stable and homogeneous dispersion in *o*-DCB. It was stable for three weeks; no subsequent material settling has been observed during this period. Fig. 2.1d shows a typical SEM topography of the nanocomposite coatings on glass substrates that shows the MWCNTs were covered with PBDTT-FTTE to form a hybrid structure. In such conditions, one can expect that the electron-rich fused thiophene units promote π-stacking interactions with MWCNT leading to the hybrid structure [42,43]. To test the dispersion homogeneity, a thin film was made on a quartz substrate (2.5 × 2.5 cm^2), and absorption spectra were taken from three different regions of the film, as shown in Fig. 2.1e. As shown in Fig. 2.1f, the absorption spectra of PBDTT-FTTE reveal a characteristic sharp peak of the π-π* transition at 235.5 nm. The PBDTT-FTTE/ MWCNT nanocomposite exhibited both strong quenching of the absorbance intensity and a redshift of the absorbance peak to a broad peak centered at 245.0 nm.

The redshift in absorbance indicated the formation of ground state physical interactions of π-stacking between aromatic moieties and MWCNT [44,45]. This redshift is due to the wrapping of the conjugated polymer chains on the MWCNT surface, which increases the polymer conjugation length [45,46]. A similar absorbance intensity was observed for this peak at three different regions, revealing the homogenous dispersion of MWCNT in the polymer matrix.

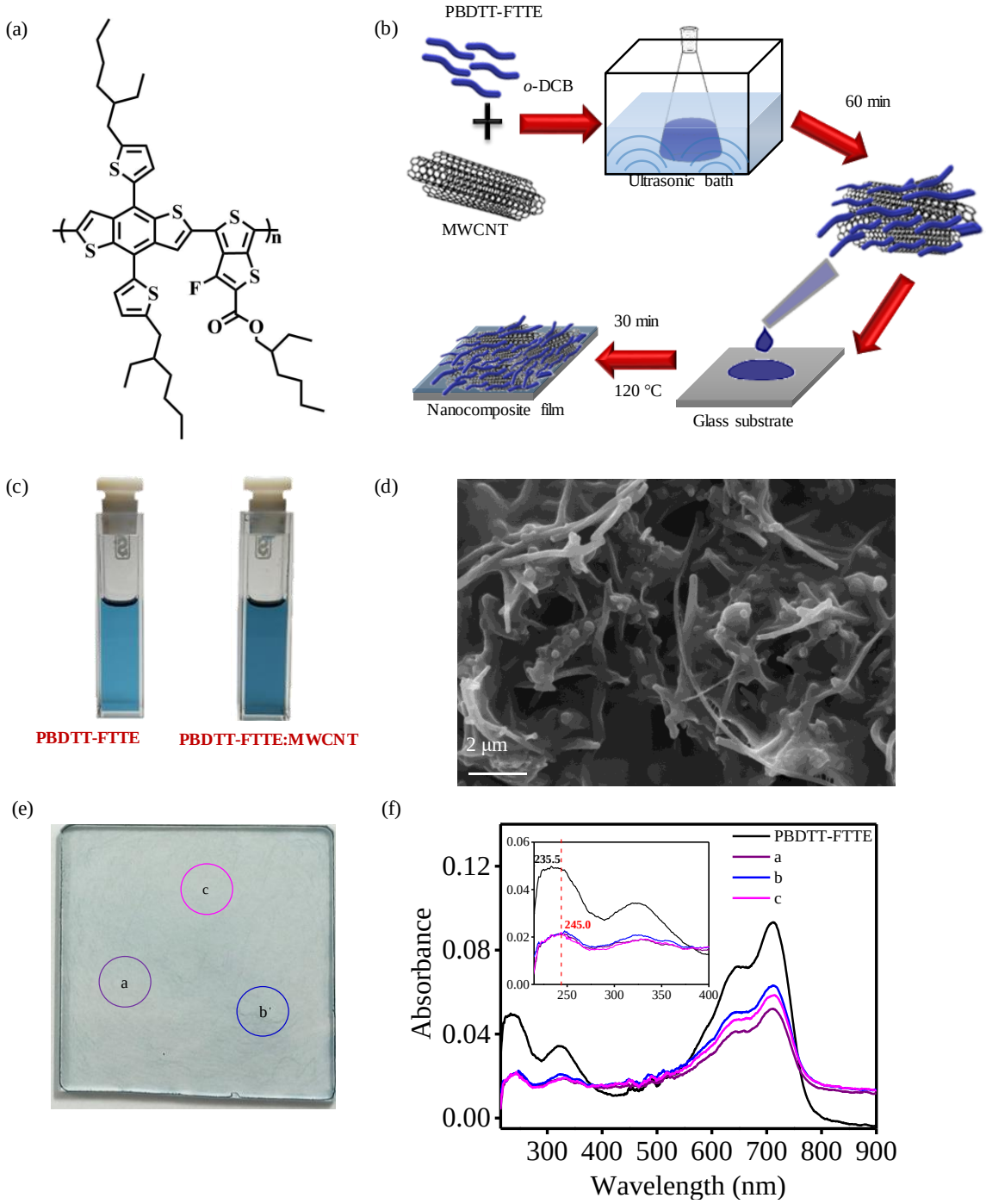

Fig. 2.1. (a) Molecular structure of PBDTT-FTTE; (b) Schematic representation of sample preparation; (c) Photographs of polymer and nanocomposite in *o*-DCB; (d) SEM image of the nanocomposite film; (e) Image of PBDTT-FTTE/45 wt% MWCNT nanocomposite thin film and (f) UV-Vis absorption spectra.

The WAXS pattern of MWCNT presented in Fig. 2.2a reveals a diffraction peak at 26.5° corresponds to the diffraction plane (002) and confirms the highly graphitic structure of the CNTs [47]. PBDTT-FTTE showed a pronounced (200) diffraction peak at 12°, arising from alkyl chain packing with a d-spacing of ~7.36 Å. A broad peak at 21.3° with the d-spacing of ~4.16 Å, corresponds to (010) plane arising from π-π stacking of thiophene rings [48]. This peak gets shifted to 22.6° with the addition of MWCNT. A decrease in the intensity of the characteristic peak of MWCNT was also observed. This implies that the walls of CNTs are distorted when the polymer is overlaid on its walls. The thermal stability of the nanocomposite was analyzed using TGA, which was done at a heating rate of 10 °C/min from 30 °C to 800 °C in a nitrogen atmosphere. The temperature at which the material loses 5% of the weight is called the T_5 value [49]. From the TGA plot (Fig. 2.2b), the T_5 value of nanocomposite was about 380 °C, while that of pure polymer is about 370 °C. This observation suggests that the thermal stability of the polymer gets better after adding MWCNT.

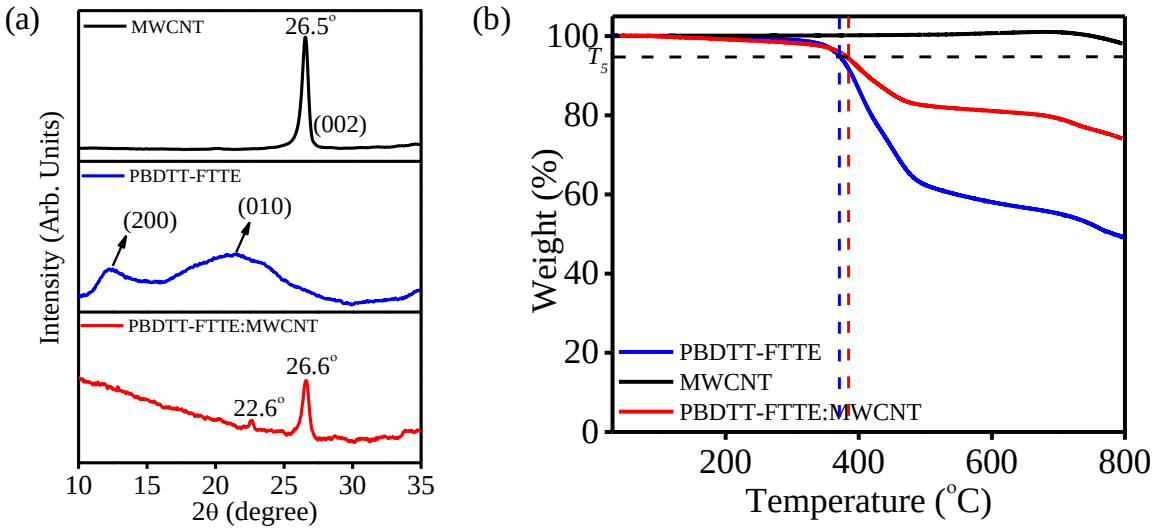

Fig. 2.2. (a) WAXS patterns and (b) TGA plot as purchased MWCNT, PBDTT-FTTE and nanocomposite with MWCNT~ 45 wt%.

2.2.2. Thermoelectric studies of undoped film

The TE behavior of nanocomposite having MWCNT weight percentage (wt%) varying from 25 to 85 has been studied using LSR. The samples were drop-casted on a glass substrate of a dimension of 14×4 mm to form a thick film of micrometer thickness. The film thickness variation with MWCNT wt% is shown in Fig. 2.3a. To understand the TE behavior of the nanocomposite film, initially, the σ and α of selected nanocomposites were measured by varying temperature from 30 °C to 260 °C. The σ of the nanocomposite films decreased with increasing temperature (Fig. 2.3b). The temperature dependence of σ mostly follows Mott variable range hopping (VRH) model as shown in equation 1.11 [50].

Mott's VRH model describes the charge transport in a disordered system in which the charge carriers hop from one localized site to another inside the network near the Fermi level [51]. The plot of ln σ as a function of $T^{-1/4}$ is shown in Fig. 2.3d, which shows two different slopes for each sample within the investigated temperature range 303 K $\leq T \leq$ 430 K. Hence the charge transport in the films follows a three-dimension (3D) VRH model, where $d = 3$ in equation 1.11 [52]. This result indicates that in the nanocomposites, the MWCNTs are densely coated with the polymer through strong π-π interfacial interactions, and the carriers in one localized MWCNT hopped to another and contributed to the conductance. The increase in temperature also shows a decrease in α value; the corresponding value of these nanocomposite films varied from 14-20 μV/K (Fig. 2.3c).

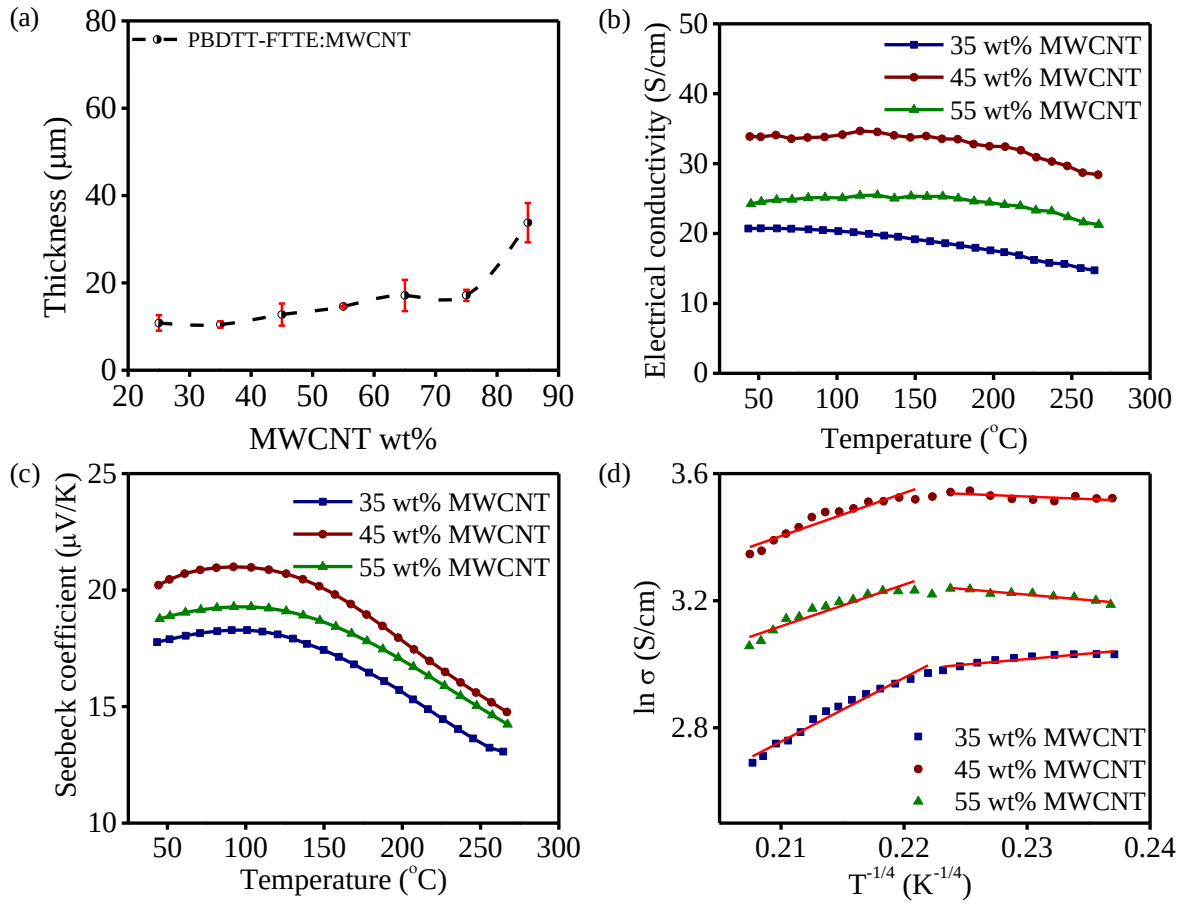

Fig. 2.3. (a) Thickness variation of nanocomposite film with MWCNT wt% before doping; Temperature-dependent changes of (b) Electrical conductivity; (c) Seebeck coefficient of nanocomposite with varying amounts of MWCNT and (d) The fitted curve of ln σ vs $T^{-1/4}$ according to Mott's VRH model.

Hence, we did the subsequent measurements at ambient temperatures. Fig. 2.4a-c shows the TE properties of the nanocomposite films by varying MWCNT wt%. We did not observe noticeable σ enhancements with a lower amount of CNT incorporation; rather, a percolation threshold is apparent beyond 25 wt% that reaches a maximum value (σ = 31.26 S/cm) at 45% of MWCNT. The improvements could be ascribed to the increase in the electrical pathways composed of inter-CNT bundle connections. The MWCNTs consist of concentric tubes; as a result,

only the outer layer will contribute to the charge transfer that gives the nanocomposite its electrical properties [53]. The uniform dispersion is essential for establishing an interconnecting filler network of MWCNTs. When the MWCNT content is low (at 35 wt%), most MWCNTs are embedded within the polymer matrix (as shown in Fig. 2.4d), which leads to a weak inter-connection between the CNTs. At 45 wt%, a well inter-connected polymer/MWCNT matrix is observed (Fig. 2.1d), creating a good channel for carrier transport.

A further rise of MWCNT wt% has resulted in a decrease in σ attributed to the breaking down of polymer stacking in the film as the percentage of MWCNT increases. At a higher concentration of 55 wt %, the network becomes thicker, and many CNTs are dragged out from the polymer matrix, as shown in Fig. 2.4e. Further increase in wt% of MWCNT, about 75 %, the MWCNT forms aggregates and gets isolated in the polymer matrix, as shown in Fig. 2.4f. This results in a decrease in σ as it loses the continuous pathway. Such a decrease in σ is also observed in other polymer/CNT composites due to the breakage of the electrical pathway [54,55]. However, the α shows an average value of 20.7 μV/K, regardless of MWCNT addition, which appears to be equivalent to the α of MWCNT, as shown in Table 2.1 [56]. The high α value, 200 μV/K (Table 2.1), of PBDTT-FTTE suddenly drops to a much lower but constant value as soon as MWCNTs are added. Since the α depends on the electronic environment that charge carriers experience [57], the polymer-coated CNT bundles are sufficiently close for tunnelling to occur when the composite is formed [58]. Thus, charge carriers select the more electrically conducting CNT environment for tunnelling. Thereby, the inherent α of MWCNTs is obtained invariant of CNT wt%. The PF of the PBDTT-FTTE/MWCNT nanocomposite followed a similar trend to that of σ.

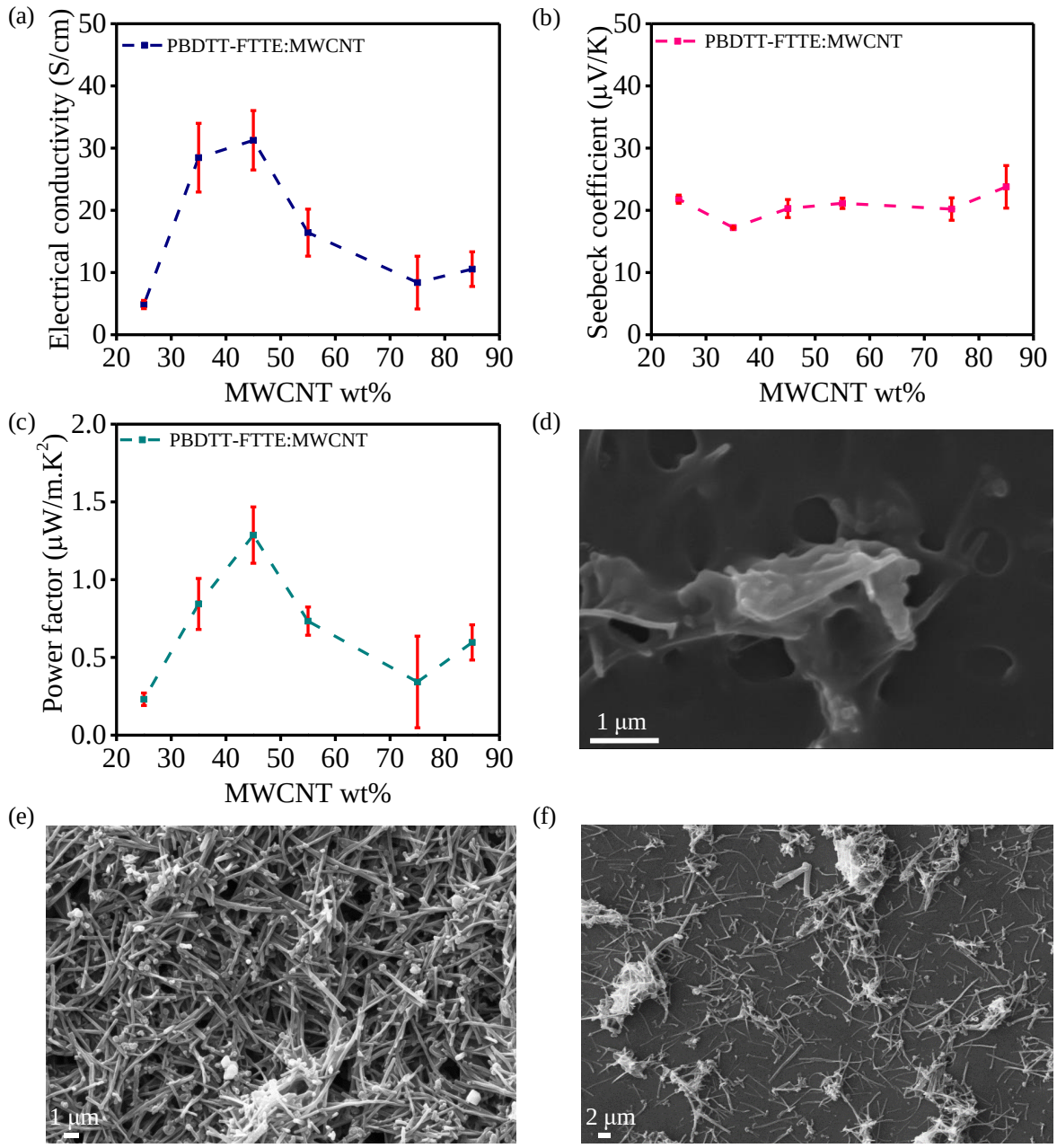

Fig. 2.4. (a) Electrical conductivity; (b) Seebeck coefficient; (c) Power factor of nanocomposite by varying MWCNT wt%; SEM image of nanocomposite at (d) 35 wt%; (e) 55wt% and (f) 75 wt % of MWCNT.

Table 2.1. The TE performance of PBDTT-FTTE and MWCNT at room temperature.

Sample	Thickness (µm)	σ (S/cm)	α (µV/K)	PF (µW/m.K^2)
PBDTT-FTTE	12.5	2.3 x 10^{-6}	200	9.2 x 10^{-6}
MWCNT	12.9	2.6	25	0.16

2.2.3. Doping of thermoelectric films

The electrical conduction of the as-prepared TE nanocomposite mainly occurs through MWCNT without any contribution from the overlaid polymer. Thus the conductivity of the polymer should be raised to metallic level for any further improvements in the nanocomposite properties. In a set of experiments, we explored the effect of p-doping in the nanocomposite and its impact on the overall TE response. In Fig. 2.5, we presented a schematic representation of the adapted doping method.

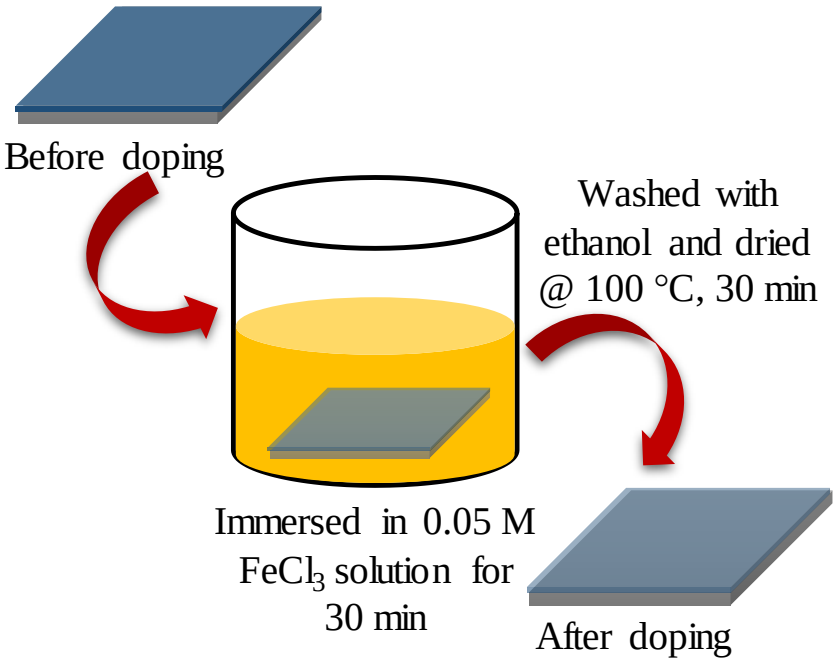

Fig. 2.5. Schematic representation of the doping method.

From a literature survey, $FeCl_3$ was used as an oxidizing agent for p-doping for PEDOT-based systems [59,60]. However, their ability to dope the present thienothiophene systems was rarely exploited. For such experiments, both dopant concentration and doping time strongly affect the resulting TE properties of the nanocomposite, as shown in Fig. 2.6a-c. The thickness of the film shows (Fig. 2.6d) a slight change after doping and within the error limit of that of before doping films.

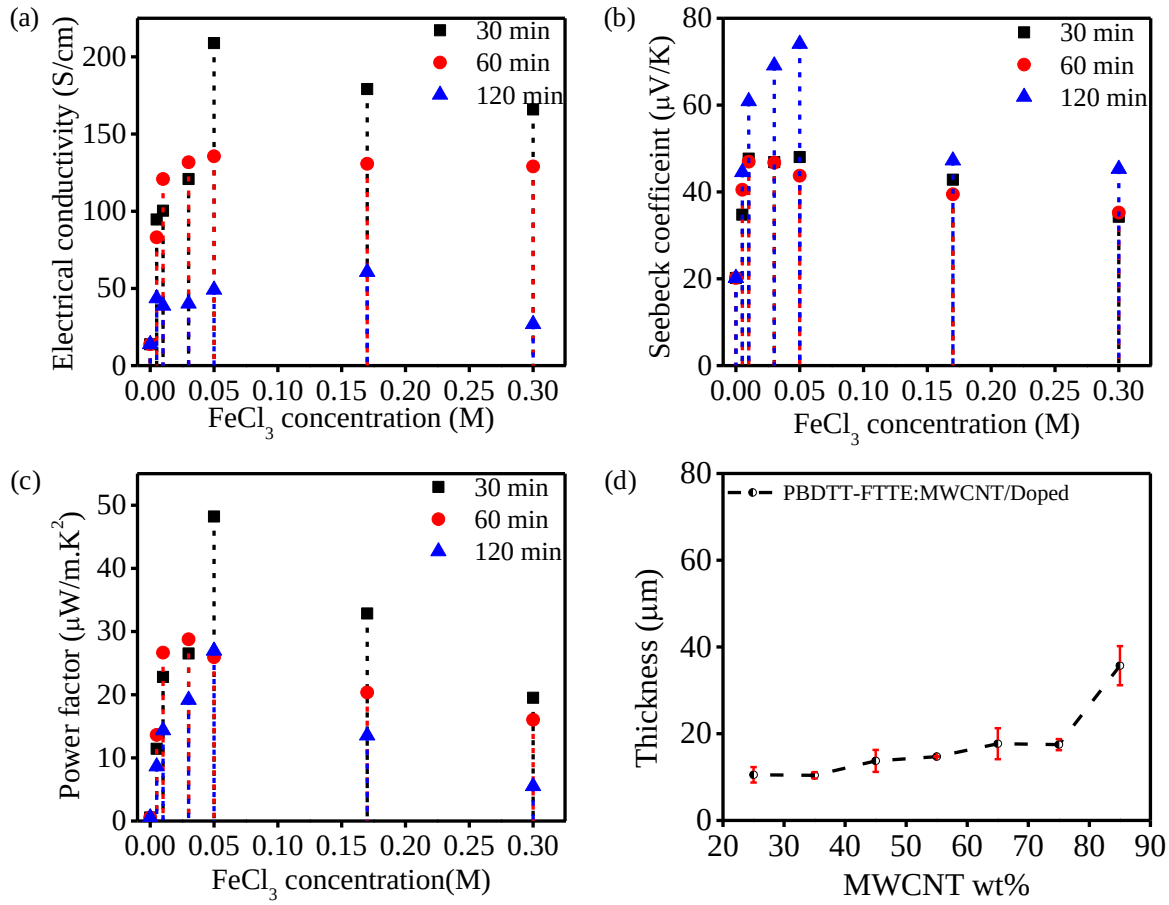

Fig. 2.6. (a) Electrical conductivity; (b) Seebeck coefficient; (c) Power factor by varying doping parameters and (d) Thickness variation of nanocomposite film with MWCNT wt% after doping.

After doping with $FeCl_3$, the nanocomposite also exhibits the same temperature tolerance as shown in Fig. 2.7a. Fig. 2.7b-c shows that after doping, there is a significant rise in both σ and

α compared to that of undoped nanocomposite films. The highest PF was obtained with MWCNT~ 45 wt%, where the σ is increased by 6.70 times (~208.9 S/cm) than the undoped nanocomposite film. The α, in contrast, exhibited a different trend from the undoped samples, and we observed a shallow drop in values with an increasing percentage of MWCNT. As the weight percentage of MWCNT becomes more than 45%, the MWCNT forms aggregates and gets isolated in the polymer matrix. Hence, the charge carriers have to move through the polymer for electrical conduction to occur. After doping, the polymer matrix is p-doped, increasing the charge carriers. The amount of polymer is lesser in 55 wt% nanocomposite than in 45 wt%, which limits the doping level and results in a decrease in active dopant species present in the polymer matrix. The increase in σ and charge transport mechanism depends on the extent of the doping level and the formation and distribution of conducting domains within the polymer matrix. However, the value of α was doubled from that of undoped film. Thus the resulting PF exhibited a whopping 37x enhancement (1.28 $\mu W/m.K^2$ in undoped nanocomposite films to 48.21 $\mu W/m.K^2$ in doped samples) for PBDTT-FTTE/ 45 wt% MWCNT nanocomposites (Fig. 2.7d).

Furthermore, the temperature-dependent TE behavior of the nanocomposite film after doping was studied at a varying temperatures from 30 °C to 260 °C. After doping, the σ of nanocomposite film increases up to 126 °C (Fig. 2.7e), followed by a decreasing slope up to 188 °C and a sustained value beyond this point. In the same way, α of the doped nanocomposite also exhibited an increasing trend by increasing temperature and a steep decreasing slope afterward (Fig. 2.7f). For doped nanocomposite films, the gradual decrease of σ and α as the temperature enhances may be due to the de-doping process of $FeCl_3$ [61,62].

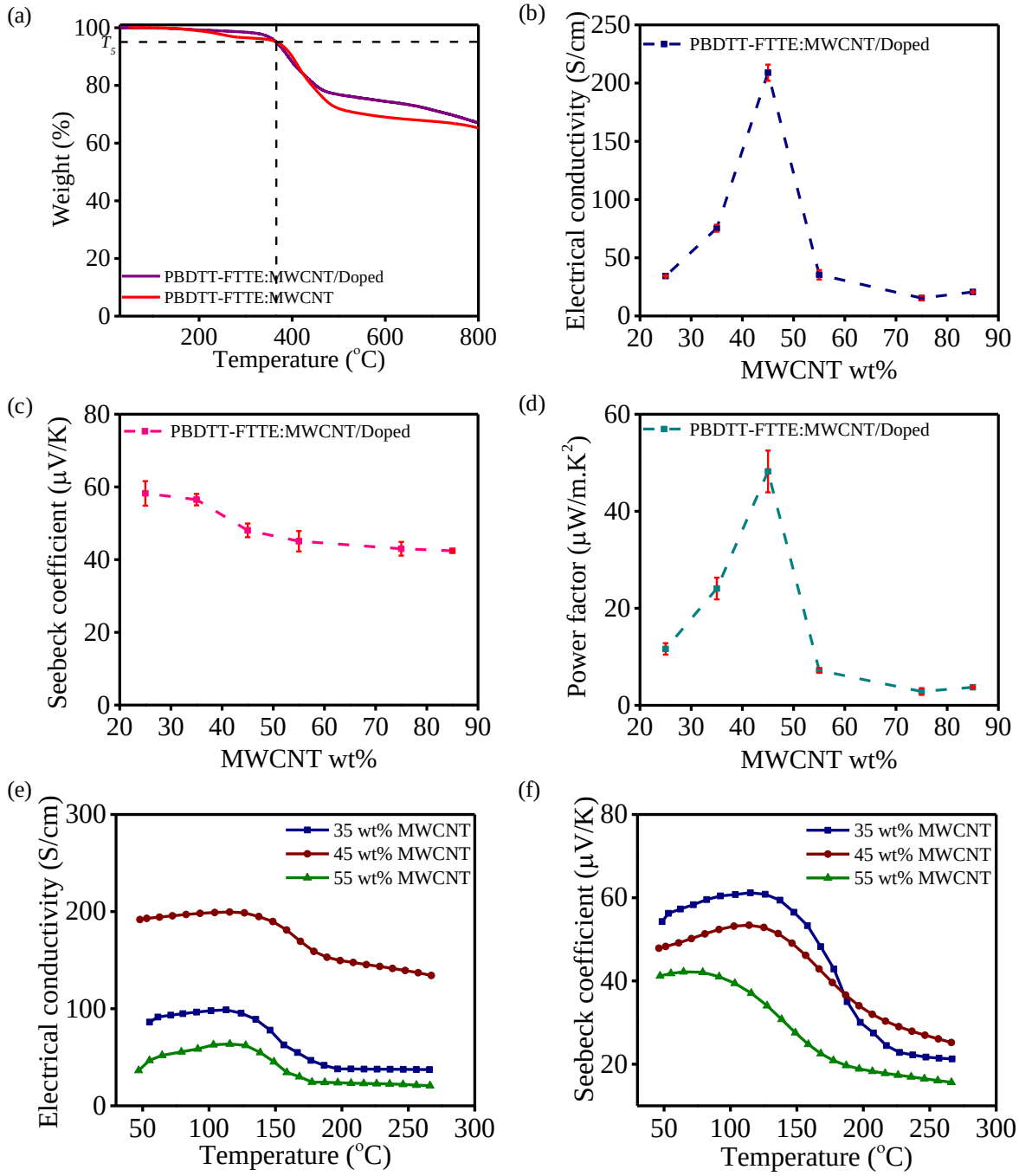

Fig. 2.7. (a) TGA plot; (b) Electrical conductivity; (c) Seebeck coefficient; (d) Power factor; Temperature-dependent changes of (e) Electrical conductivity and (c) Seebeck coefficient of nanocomposite after doping by varying MWCNT wt%.

Besides, we compared the TE properties of PBDTT-FTTE/MWCNT and other conjugated polymers/MWCNT composites and thienothiophene polymers, as shown in Table 2.2. We found that PBDTT-FTTE/MWCNT nanocomposites show good TE performance compared to other MWCNT composite systems.

Table 2.2. The TE performance for some conjugated polymer/MWCNT composites at room temperature.

Polymer	**Inorganic/ Dopant**	**Loading (wt %)**	**σ (S/cm)**	**α (μV/K)**	**PF (μW/m.K^2)**	**Ref.**
PANI/ HCl	MWCNT	1	14.1	79.8	8.98	[63]
PANI	MWCNT	84.2	50	28	5	[56]
PANI	MWCNT	40	17.1	10	0.17	[64]
PANI	MWCNT	30	159	25	0.1	[65]
PEDOT:PSS/Graphene	MWCNT	5	689	23.2	37.08	[66]
PPy	MWCNT	20	32	25	2.1	[67]
P3HT/ $FeCl_3$	MWCNT	10	71.3	29	6	[68]
PBDTTT-TEO	DDQ	25	2.84×10^{-3}	418	0.049	[69]
PBDTTT-TEO	F4TCNQ	25	2.13×10^{-3}	376	0.028	[69]
PBDT-EDOT	$FeCl_3$	20	0.81	67.60	0.37	[70]
PBDTTT-EDOT	$FeCl_3$	20	1.64	115.58	2.19	[70]
PBDTT-FTTE / $FeCl_3$	MWCNT	45	208.9	48.03	48.21	This work

The concept of doping of organic polymers is generally accomplished by the charge-transfer process between the polymer and dopant (oxidizing or reducing agent). The p-doping of conducting polymers refers to the partial oxidation of the polymer, where a counter-ion is provided to maintain electrical neutrality [71]. The doping of PBDTT-FTTE has been achieved by using $FeCl_3$ (oxidant) involving the electron transfer between the two, resulting in the formation of PBDTT-FTTE:$FeCl_3$ charge-transfer complex. The concurrent improvements in σ and α in the PBDTT-FTTE:$FeCl_3$ complex could have resulted from the so-called "hole-doping" effect, where the Fermi level of the system is pinned below the valance band due to the presence of Fe^{3+} [72]. To confirm the presence of the charge transfer complex, we conducted XPS measurement and valance band maxima (VBM) analysis. Fig. 2.8 shows a typical broad scan survey spectrum of pristine polymer, nanocomposite before and after doping. The peaks of the survey spectra mirror the major elements present in the sample, e.g., S, F, O, and C. The $Fe2p_1$, $Fe2p_3$, and Cl2p peaks confirm the presence of intercalated dopant species.

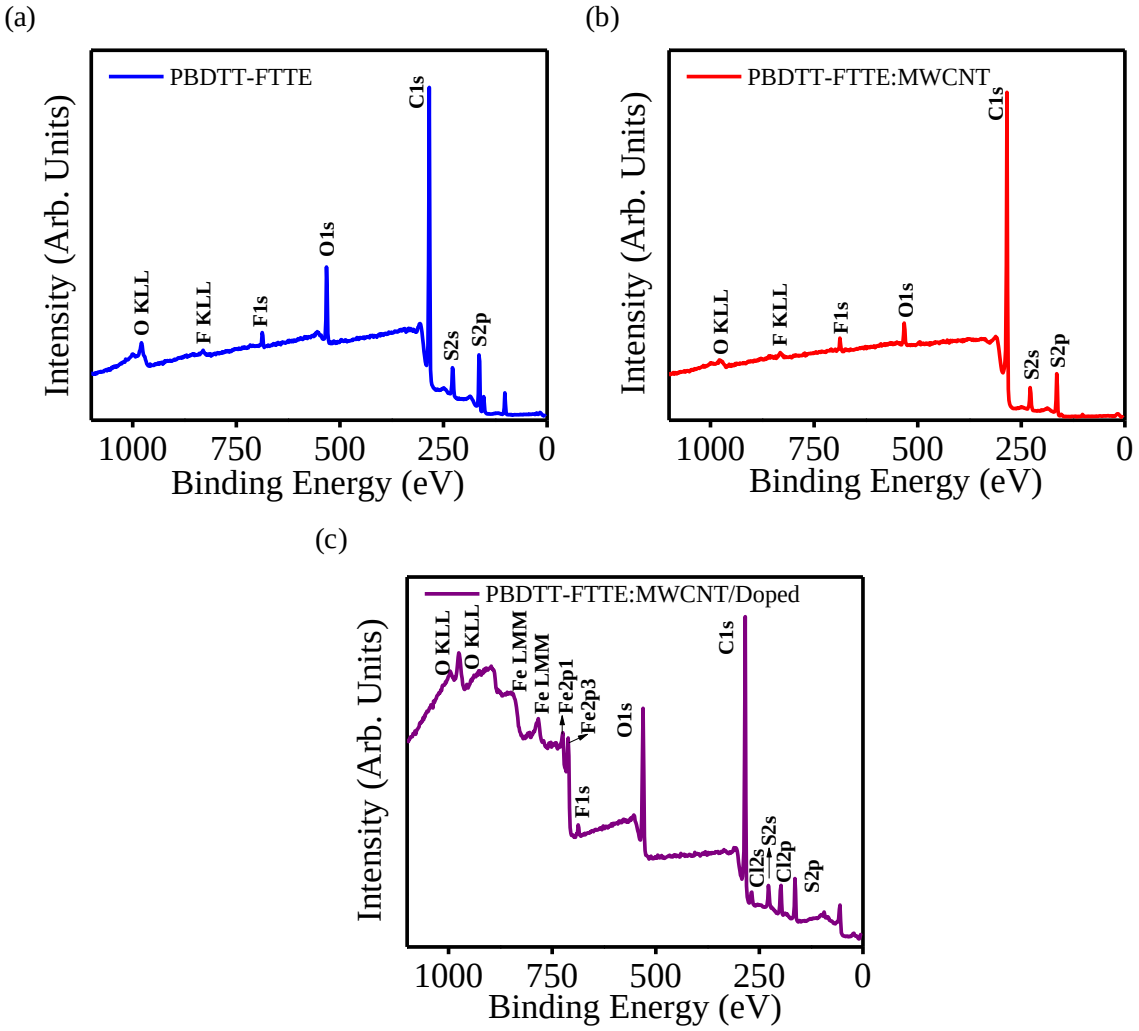

Fig. 2.8. XPS survey spectra of (a) pristine polymer; (b) nanocomposite with MWCNT~ 45 wt% before doping and (c) after doping.

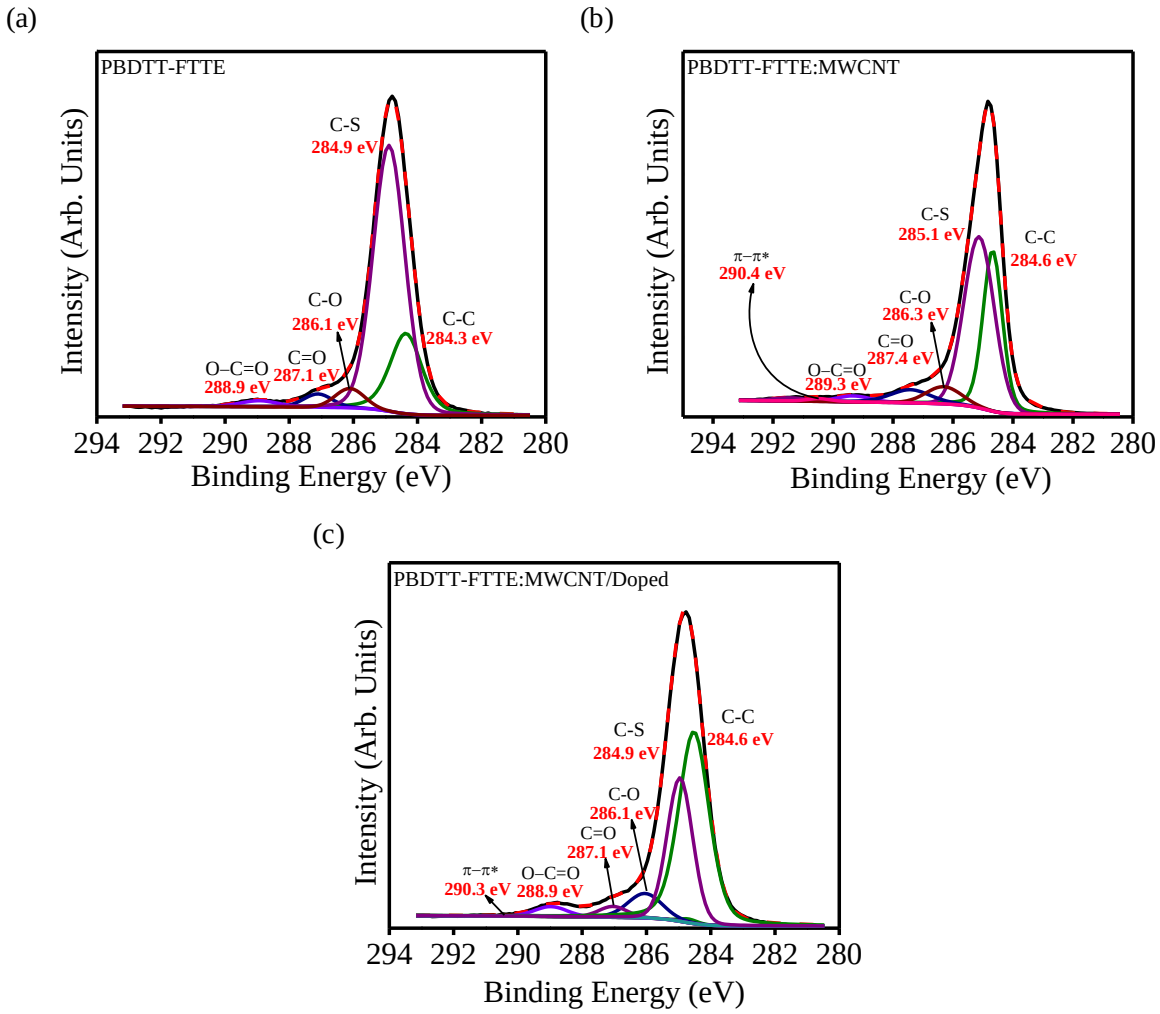

Fig. 2.9. C1s XPS spectra of (a) pristine polymer; (b) nanocomposite with MWCNT~ 45 wt% before doping and (c) after doping.

The Fig. 2.9 and Fig. 2.10 show the high resolution of C1s and O1s XPS results and the deconvoluted peaks (bonding components) for pristine polymer, nanocomposite before and after doping, respectively. The C1s XPS spectrum (Fig. 2.9a) represents the three oxygen functional groups of PBDTT-FTTE at 286.1, 287.1, and 288.9 eV, which are assigned to the C–O, C=O and O–C=O bonds, respectively [73,74]. The addition of MWCNT marginally shifts these functional group peaks to higher binding energies (Fig. 2.9b). The peak at 290.4 eV is related to the π-π* bonds that arise from the sp^2 carbon atom of MWCNT. However, after doping, the functional

group peaks returned to the pristine polymer that confirmed the presence of strained bonds due to MWCNT-polymer interaction and their subsequent relaxation after doping (Fig. 2.9c). The O1s XPS spectrum of PBDTT-FTTE (Fig. 2.10a) and nanocomposite (Fig. 2.10b) exhibits the oxygen peak arising from C=O (~532.1 eV) and C–O–C (~533.4 eV). The intensity of the C–O–C peak increases by adding MWCNT, as MWCNTs were oxidized by ozone and hydroxyl radicals from the ambient [75]. The peak at 529.8 eV in Fig. 2.10c corresponds to C–O–Fe due to the charge transfer complex after doping. The S2p and F1s XPS spectra are shown in Fig. 2.11a-b that showed a negligible change.

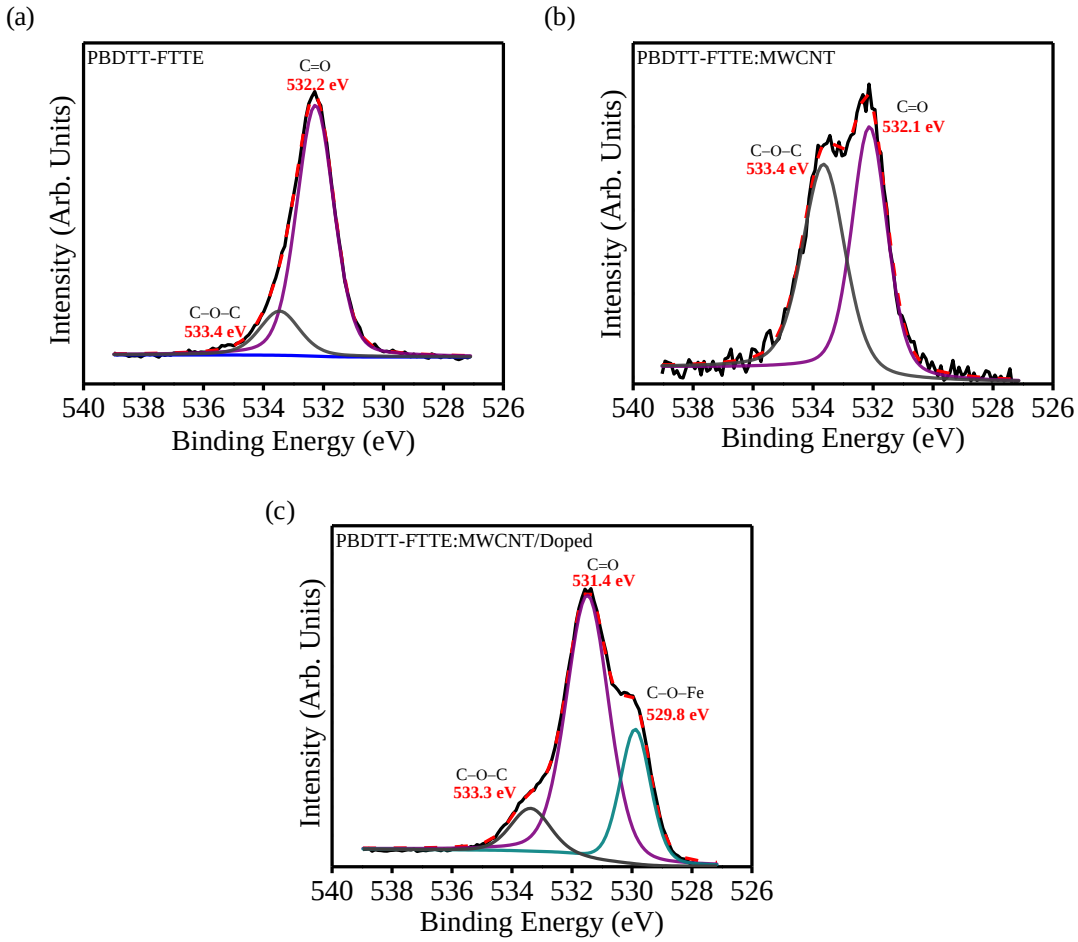

Fig. 2.10. O1s XPS spectra of (a) pristine polymer; (b) nanocomposite with MWCNT~ 45 wt% before doping and (c) after doping.

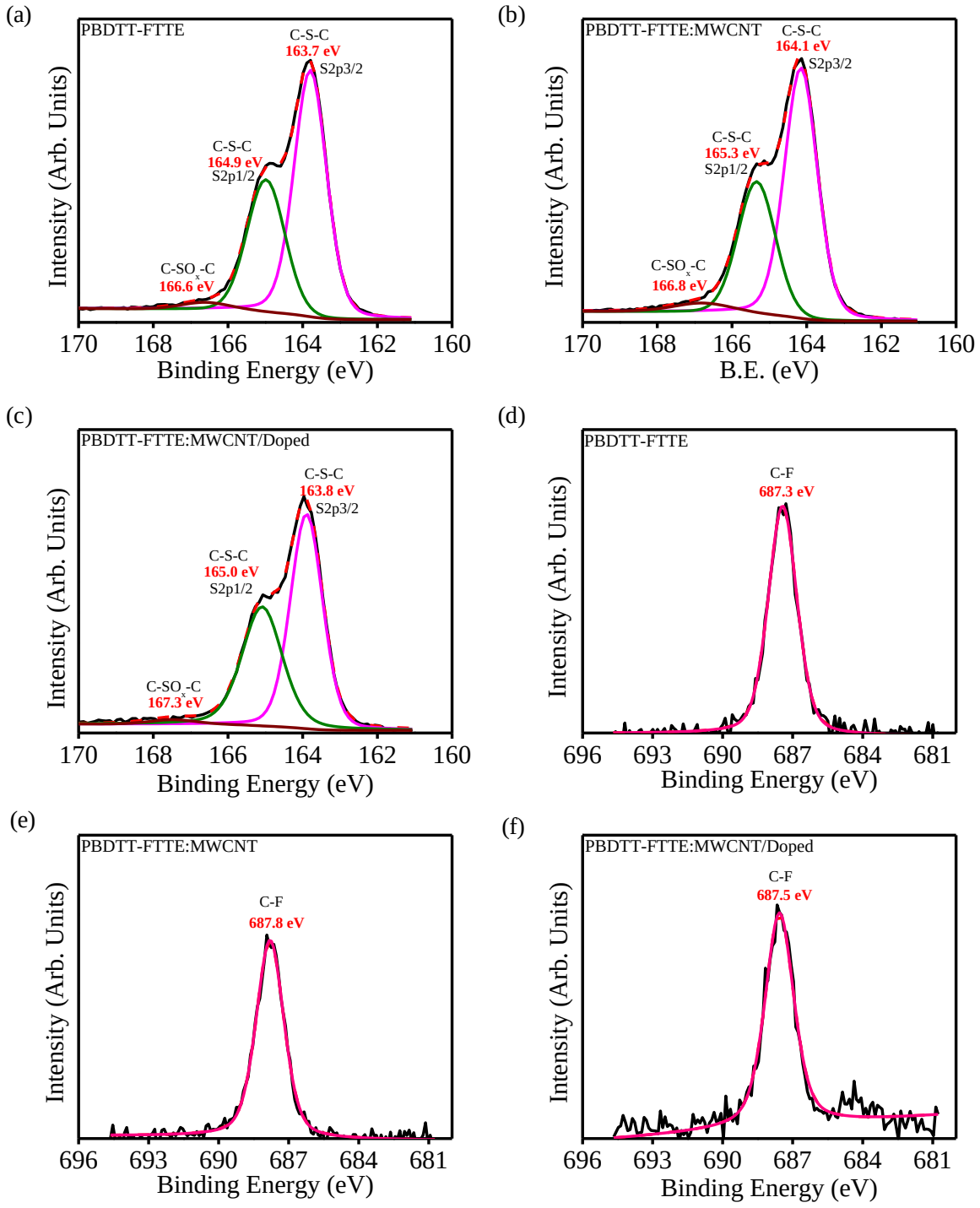

Fig. 2.11. S2p XPS spectra of (a) pristine polymer; (b) nanocomposite with MWCNT~ 45 wt% before doping and (c) after doping; F1s XPS spectra of (d) pristine polymer; (e) nanocomposite with MWCNT~ 45 wt% before doping and (f) after doping.

The high-resolution Fe2p spectra were measured to evaluate the electronic nature of iron after doping. The Fe2p core level spectra are shown in Fig. 2.12a. The $Fe2p_{3/2}$ and $Fe2p_{1/2}$ peaks binding energies are located at 711.2 eV and 724.7 eV respectively corresponded to Fe^{3+} (oxide). The observed energy value for $Fe2p_{3/2}$ core level matches to the value found for Fe^{3+} in $(Et_4N)FeCl_4$ salt. Shake-up satellite value at 719.0 eV, which is ~7.8 eV from the main $Fe2p_{3/2}$ peak, supports that Fe is presented in Fe^{3+} ionic state. The Fe2p energy value suggests the presence of Fe^{3+} in the form of $FeCl_4^-$. In Fig. 2.12b, the Cl2p core level signal gives two $Cl2p_{3/2}$ unresolved doublets with their maxima respectively at ~ 198.2 eV and ~ 200.0 eV on the binding energy scale. The peak at low energy that shows the similar energy value observed for $Cl2p_{3/2}$ in $(Et_4N)FeCl_4$ salt can be assigned as being due to $FeCl_4^-$ species [76–81].

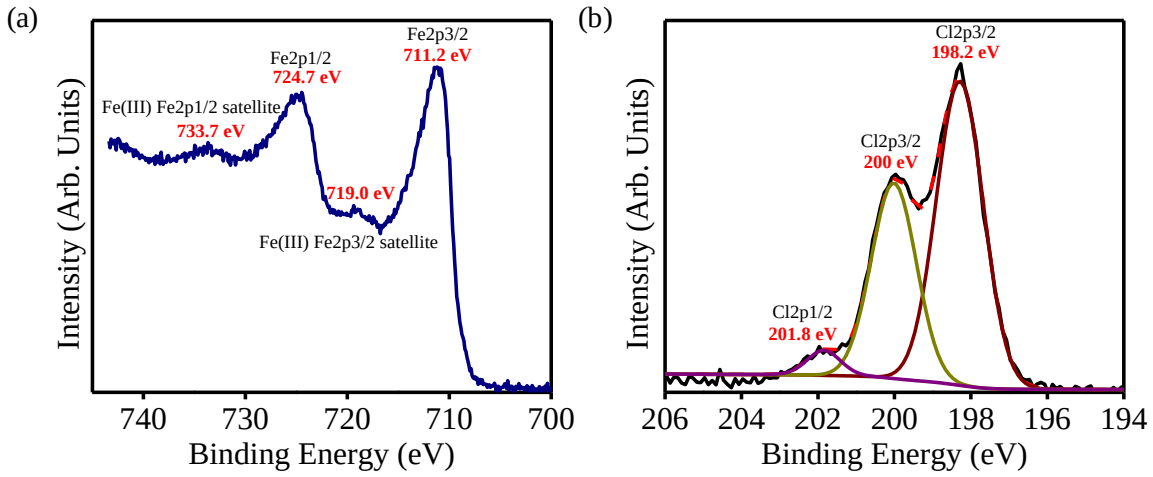

Fig. 2.12. (a) Fe2p XPS spectra and (b) Cl2p XPS spectra of nanocomposite with MWCNT~ 45 wt% after doping.

The XPS valence band (VB) spectra for pristine polymer, nanocomposite before doping and after doping on a gold substrate are shown in Fig. 2.13a. The VBM position is determined by linear extrapolation of the low binding energy edge of the valence band spectrum shown in the inset. The spectra exhibit a steep rise in the density of states (DOS) after doping that is primarily

responsible for the massive increase in σ. The position of VBM is also shifted (from ~ 2.12 eV to ~1.78 eV) towards the reference Fermi level after doping that could cause overlap with its internal Fermi level. The work function (WF) of the nanocomposite is investigated by regulating the obtained contact potential difference (CPD) from the tip WF using a Kelvin probe (KP) setup (Fig. 2.13b). With reference to the vacuum level, the work functions of the nanocomposite are estimated at 4.845 eV before doping and 4.969 eV after doping. Thus, the increase in WF after doping also suggests shifting the Fermi level towards the valence band.

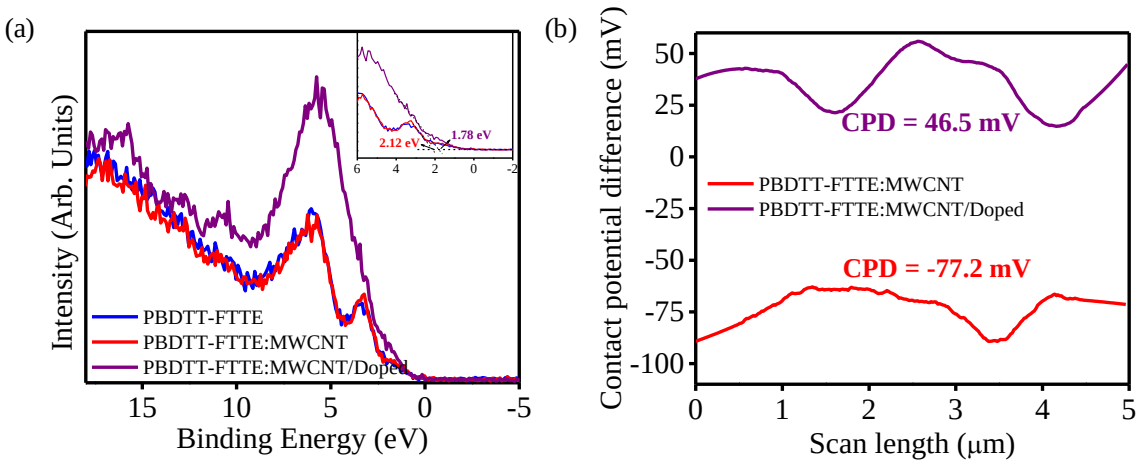

Fig. 2.13. (a) XPS VB spectra and (b) Contact potential difference of nanocomposite with MWCNT~ 45 wt% before and after doping.

Table 2.3. Mobility and carrier concentration of PBDTT-FTTE nanocomposite with 45 wt% of MWCNT before and after doping.

Particulars	**Before doping**	**After doping**
Bulk concentration (/cm^3)	3.767E+20	3.133E+20
Sheet concentration (/cm^2)	3.940E+17	3.277E+17
Mobility (cm^2/Vs)	3.415E-1	5.614E-1

The dependence of carrier concentration and α could be explained by Mott's relation [82],

$$\alpha = \frac{8\pi^2 k_B^2 T}{3eh^2} m^* \left(\frac{\pi}{3n}\right)^{2/3} \quad (2.1)$$

where k_B, T, m^*, and n are the Boltzmann constant, absolute temperature, carrier effective mass, and carrier concentration, respectively. The Hall measurement studies suggest that the mobility of the charge carrier increases after doping, with a decrease in carrier concentration (Table 2.3). Depending on the molecular architecture, incorporating dopants into a p-type polymer matrix may create carrier traps that reduces the carrier concentration [83–85]. Along with the realignment of the Fermi level, the reduction in carrier concentration results in a significant increase in α.

Finally, a practical TE application using these all-organic composites does not solely depend on its PF values but requires prevention from thermal shorting. The actual κ determination is beyond the scope of this work, as we need specialized systems to evaluate a polymer composite coating. Since the percolation threshold and peak PF values in the described system required ≤ 25 wt% of MWCNT usage, the existing theories are not applicable as these were developed lower wt% of the fillers [86–88]. However, literature reports suggest that the π- conjugated polymers as well as polymer/MWCNT composites exhibited a low κ value, which is a prerequisite for TE devices. The π- conjugated polymers like P3HT and PEDOT shows a low κ value of 0.2 W/m.K [89] and 0.16 W/m.K [90], respectively, at room temperature. Cola *et al.* studied the conductivity property of P3HT/MWCNT composite nanofibers, where nanofiber κ peaks at 4.7 ± 1.1 W/m.K for 24 wt % MWCNT [91]. In 2017, Hsiao *et al.* prepared a thermally conductive polymeric composite incorporating MWCNT/PEDOT:PSS scaffolds and reported a κ value of 1.16 W/m.K [92]. Voit and co-workers studied the TE properties of melt-mixed polycarbonate/MWCNT composites and reported κ of 0.29 ± 0.01 W/m.K [93]. An indirect assessment of κ is possible by

fabricating an actual device and evaluating its TE output [94–96]. The fabrication of TEG and geometry adapted for measurement are shown in Fig. 2.14.

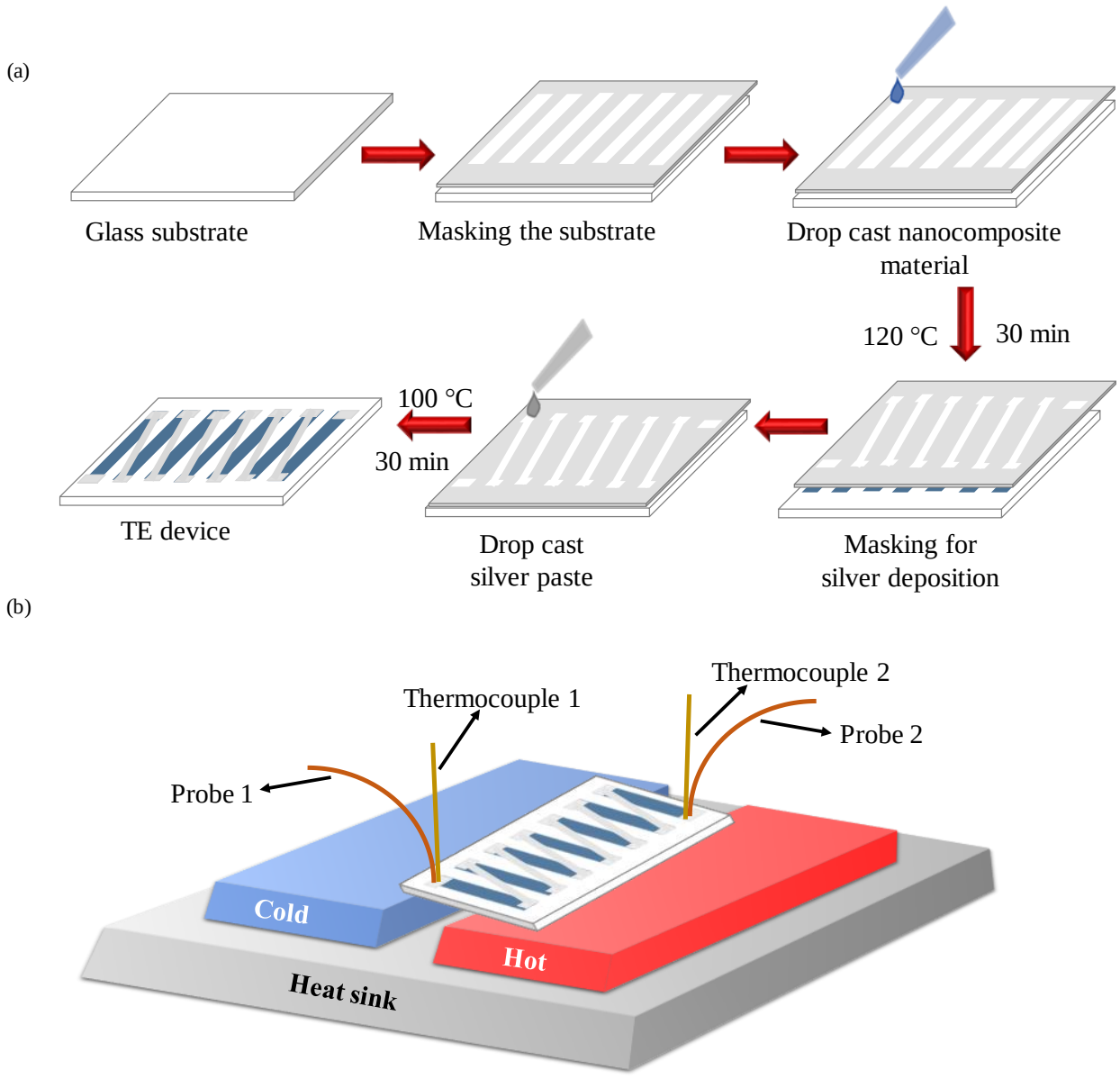

Fig. 2.14. (a) Fabrication of planar TEG consisting of 7 legs and (b) Schematic diagram of geometry of TEG measurement.

The proposed device configuration in Fig 2.14a is a planar-type TEG. Such TEG devices were fabricated by a conventional drop casting method. However, literature shows that the planar

TE segment can be miniaturized into micrometre-scale using nanolithography and printing techniques like screen printing, inkjet printing and dispenser printing [97–100].

Herein, we fabricated a TEG comprising seven legs arranged on a glass substrate using PBDTT-FTTE/ 45 wt% MWCNT solution, as shown in Fig. 2.15a. Fig. 2.15b shows the device's measured voltage, current, and output power as a function of temperature difference (ΔT). The fabricated TEG shows a moderate output voltage of 9.12 mV and output power of 6.92 nW at ΔT = 65 K with a load resistance of 1 kΩ. Furthermore, α determined by the open-circuit voltage and ΔT of the TEG is approximately 22 ± 2 μV/K, which corresponds to that of the PBDTT-FTTE/MWCNT thin film. The maximum power was observed at a load resistance range ~15 Ω, as shown in Fig. 2.15c, which indicates that the TEG have relatively low internal resistances providing a chance to connect more legs serially to achieve higher power output.

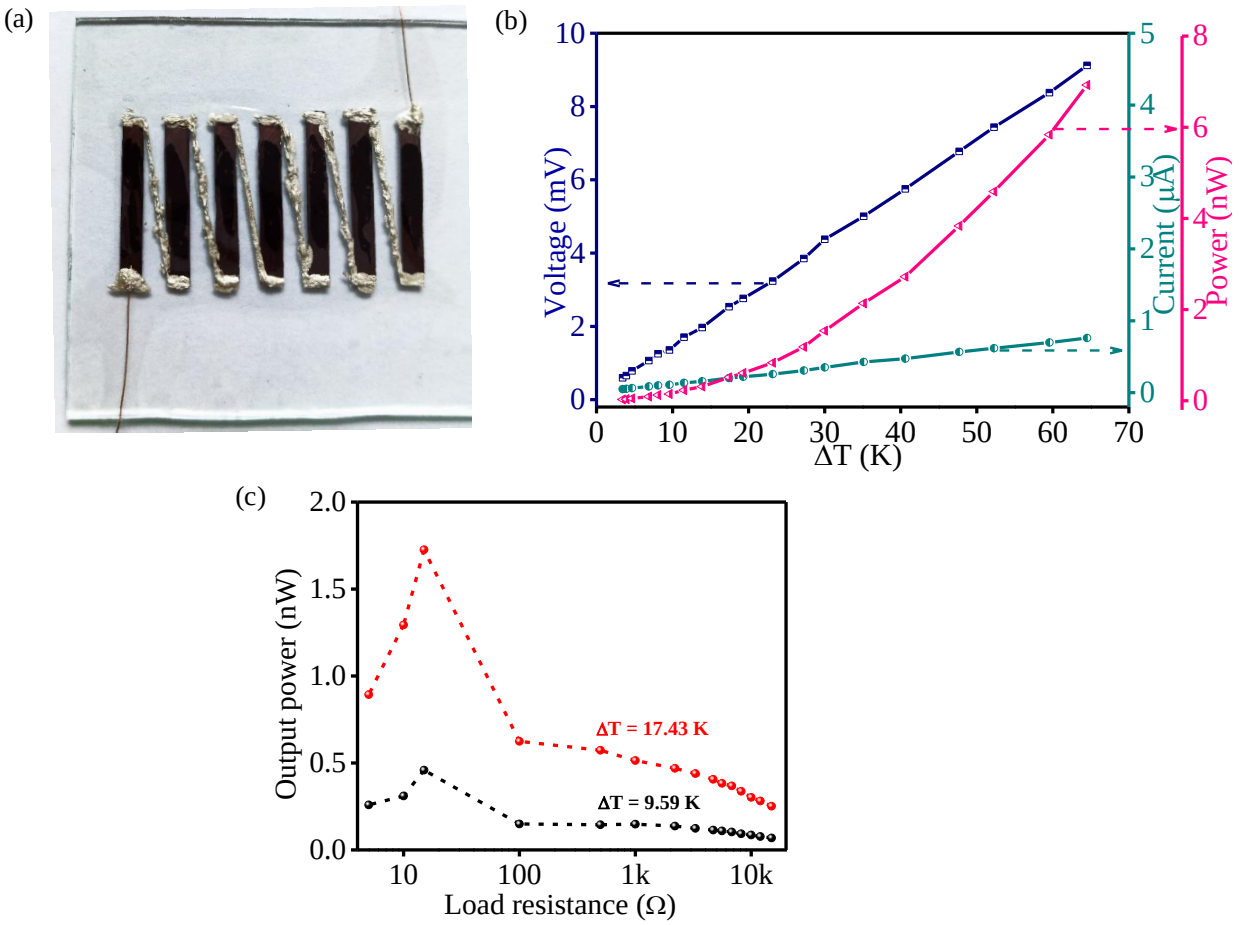

Fig. 2.15. (a) Image of planar TEG consisting of 7 legs; (b) The output voltage, short circuit current, and output power of TEG versus ΔT and (c) The output power curves according to different load resistance at ΔT = 9.59 K and 17.43 K.

2.3. Conclusion

In summary, we prepared and characterized BDT-TTE-based polymer nanocomposite films hybridizing with MWCNT that exhibited p-type TE response. Further enhancement of TE properties was achieved by doping with an oxidizing agent, $FeCl_3$, which increases both σ and α. The doping mechanism increases the DOS and results in the alignment of the Fermi level by introducing a charge-transfer complex. From this perspective, our work provides an insight into the relationship between doping mechanism and enhancement in thermoelectric properties. At room temperature, for doped PBDTT-FTTE/45 wt% MWCNT, the σ is enhanced up to 6.7x compared to the as-prepared samples. At the same time, the α exhibited ~2.5x improvement. Thus, the power factor raised from 1.28 $\mu W/m.K^2$ to 48.21 $\mu W/m.K^2$, leading to the highest value for the thienothiophene-based conjugated polymer/MWCNT nanocomposite. TGA verifies that the nanocomposite is stable up to ~350 °C, which boosts the nanocomposite application as a low-temperature TE material. Organic-based TE devices typically function >350 °C and could be used for point-of-care sustainable power generation from thermal sources.

References

[1] R. Freer, A. V. Powell, Realising the potential of thermoelectric technology: a Roadmap, J. Mater. Chem. C. 8 (2020) 441–463. https://doi.org/10.1039/C9TC05710B.

[2] N. Jaziri, A. Boughamoura, J. Müller, B. Mezghani, F. Tounsi, M. Ismail, A comprehensive review of Thermoelectric Generators: Technologies and common applications, Energy Reports. 6 (2020) 264–287. https://doi.org/10.1016/j.egyr.2019.12.011.

[3] D.T. Crane, J.W. Lagrandeur, Progress report on BSST-led US Department of Energy Automotive Waste Heat Recovery Program, J. Electron. Mater. 39 (2010) 2142–2148. https://doi.org/10.1007/s11664-009-0991-0.

[4] Q.E. Hussain, D.R. Brigham, C.W. Maranville, Thermoelectric exhaust heat recovery for hybrid vehicles, SAE Tech. Pap. 2 (2009) 1132–1142. https://doi.org/10.4271/2009-01-1327.

[5] N. Espinosa, M. Lazard, L. Aixala, H. Scherrer, Modeling a thermoelectric generator applied to diesel automotive heat recovery, J. Electron. Mater. 39 (2010) 1446–1455. https://doi.org/10.1007/s11664-010-1305-2.

[6] M. Mori, T. Yamagami, M. Sorazawa, T. Miyabe, S. Takahashi, T. Haraguchi, Simulation of Fuel Economy Effectiveness of Exhaust Heat Recovery System Using Thermoelectric Generator in a Series Hybrid, SAE Int. J. Mater. Manuf. 4 (2011) 1268–1276. https://doi.org/10.4271/2011-01-1335.

[7] B. Orr, A. Akbarzadeh, M. Mochizuki, R. Singh, A review of car waste heat recovery systems utilising thermoelectric generators and heat pipes, Appl. Therm. Eng. 101 (2016) 490–495. https://doi.org/10.1016/j.applthermaleng.2015.10.081.

[8] P. Ren, Y. Liu, J. He, T. Lv, J. Gao, G. Xu, Recent advances in inorganic material thermoelectrics, Inorg. Chem. Front. 5 (2018) 2380–2398. https://doi.org/10.1039/C8QI00366A.

[9] D. Li, Y. Gong, Y. Chen, J. Lin, Q. Khan, Y. Zhang, Y. Li, H. Zhang, H. Xie, Recent Progress of Two-Dimensional Thermoelectric Materials, Nano-Micro Lett. 12 (2020) 36. https://doi.org/10.1007/s40820-020-0374-x.

[10] I. Chowdhury, R. Prasher, K. Lofgreen, G. Chrysler, S. Narasimhan, R. Mahajan, D. Koester, R. Alley, R. Venkatasubramanian, On-chip cooling by superlattice-based thin-film thermoelectrics, Nat. Nanotechnol. 4 (2009) 235–238. https://doi.org/10.1038/nnano.2008.417.

[11] R. Venkatasubramanian, Lattice thermal conductivity reduction and phonon localizationlike behavior in superlattice structures, Phys. Rev. B. 61 (2000) 3091–3097. https://doi.org/10.1103/PhysRevB.61.3091.

[12] P. Hyldgaard, G.D. Mahan, Phonon superlattice transport, Phys. Rev. B. 56 (1997) 10754–10757. https://doi.org/10.1103/PhysRevB.56.10754.

[13] H. Böttner, G. Chen, R. Venkatasubramanian, Aspects of Thin-Film Superlattice Thermoelectric Materials, Devices, and Applications, MRS Bull. 31 (2006) 211–217. https://doi.org/10.1557/mrs2006.47.

[14] J.P. Heremans, C.M. Thrush, D.T. Morelli, Thermopower enhancement in lead telluride nanostructures, Phys. Rev. B. 70 (2004) 115334. https://doi.org/10.1103/PhysRevB.70.115334.

[15] R.Y. Wang, J.P. Feser, J.-S. Lee, D. V. Talapin, R. Segalman, A. Majumdar, Enhanced Thermopower in PbSe Nanocrystal Quantum Dot Superlattices, Nano Lett. 8 (2008)

2283–2288. https://doi.org/10.1021/nl8009704.

[16] P. Trocha, J. Barnaś, Large enhancement of thermoelectric effects in a double quantum dot system due to interference and Coulomb correlation phenomena, Phys. Rev. B. 85 (2012) 085408. https://doi.org/10.1103/PhysRevB.85.085408.

[17] Z. Quan, Z. Luo, W.S. Loc, J. Zhang, Y. Wang, K. Yang, N. Porter, J. Lin, H. Wang, J. Fang, Synthesis of PbSeTe Single Ternary Alloy and Core/Shell Heterostructured Nanocubes, J. Am. Chem. Soc. 133 (2011) 17590–17593. https://doi.org/10.1021/ja207763p.

[18] J.P.A. Makongo, D.K. Misra, X. Zhou, A. Pant, M.R. Shabetai, X. Su, C. Uher, K.L. Stokes, P.F.P. Poudeu, Simultaneous Large Enhancements in Thermopower and Electrical Conductivity of Bulk Nanostructured Half-Heusler Alloys, J. Am. Chem. Soc. 133 (2011) 18843–18852. https://doi.org/10.1021/ja206491j.

[19] J.W. Simonson, D. Wu, W.J. Xie, T.M. Tritt, S.J. Poon, Introduction of resonant states and enhancement of thermoelectric properties in half-Heusler alloys, Phys. Rev. B. 83 (2011) 235211. https://doi.org/10.1103/PhysRevB.83.235211.

[20] G. Zuo, H. Abdalla, M. Kemerink, Conjugated Polymer Blends for Organic Thermoelectrics, Adv. Electron. Mater. 5 (2019) 1800821. https://doi.org/10.1002/aelm.201800821.

[21] H. Jin, J. Li, J. Iocozzia, X. Zeng, P.-C. Wei, C. Yang, N. Li, Z. Liu, J.H. He, T. Zhu, J. Wang, Z. Lin, S. Wang, Hybrid Organic–Inorganic Thermoelectric Materials and Devices, Angew. Chemie Int. Ed. 58 (2019) 15206–15226. https://doi.org/10.1002/anie.201901106.

[22] G. Chen, W. Xu, D. Zhu, Recent advances in organic polymer thermoelectric composites, J. Mater. Chem. C. 5 (2017) 4350–4360. https://doi.org/10.1039/C6TC05488A.

[23] M. Culebras, K. Choi, C. Cho, Recent Progress in Flexible Organic Thermoelectrics, Micromachines. 9 (2018) 638. https://doi.org/10.3390/mi9120638.

[24] L.M. Cowen, J. Atoyo, M.J. Carnie, D. Baran, B.C. Schroeder, Review—Organic Materials for Thermoelectric Energy Generation, ECS J. Solid State Sci. Technol. 6 (2017) N3080–N3088. https://doi.org/10.1149/2.0121703jss.

[25] C.-J. Yao, H.-L. Zhang, Q. Zhang, Recent Progress in Thermoelectric Materials Based on Conjugated Polymers, Polymers (Basel). 11 (2019) 107. https://doi.org/10.3390/polym11010107.

[26] T. Ramanathan, A.A. Abdala, S. Stankovich, D.A. Dikin, M. Herrera-Alonso, R.D. Piner, D.H. Adamson, H.C. Schniepp, X. Chen, R.S. Ruoff, S.T. Nguyen, I.A. Aksay, R.K. Prud'Homme, L.C. Brinson, Functionalized graphene sheets for polymer nanocomposites, Nat. Nanotechnol. 3 (2008) 327–331. https://doi.org/10.1038/nnano.2008.96.

[27] D. Kim, Y. Kim, K. Choi, J.C. Grunlan, C. Yu, Improved Thermoelectric Behavior of Nanotube-Filled Polymer Composites with Poly(3,4-ethylenedioxythiophene) Poly(styrenesulfonate), ACS Nano. 4 (2010) 513–523. https://doi.org/10.1021/nn9013577.

[28] G.P. Moriarty, S. De, P.J. King, U. Khan, M. Via, J.A. King, J.N. Coleman, J.C. Grunlan, Thermoelectric behavior of organic thin film nanocomposites, J. Polym. Sci. Part B Polym. Phys. 51 (2013) 119–123. https://doi.org/10.1002/polb.23186.

[29] G.J. Snyder, E.S. Toberer, Complex thermoelectric materials, Nat. Mater. 7 (2008) 105–114. https://doi.org/10.1038/nmat2090.

[30] J. Cameron, P.J. Skabara, The damaging effects of the acidity in PEDOT:PSS on semiconductor device performance and solutions based on non-acidic alternatives, Mater. Horizons. 7 (2020) 1759–1772. https://doi.org/10.1039/C9MH01978B.

[31] B. Sarkar, M. Jaiswal, D.K. Satapathy, Swelling kinetics and electrical charge transport in PEDOT:PSS thin films exposed to water vapor, J. Phys. Condens. Matter. 30 (2018) 225101. https://doi.org/10.1088/1361-648X/aabe51.

[32] B. Xu, S.-A. Gopalan, A.-I. Gopalan, N. Muthuchamy, K.-P. Lee, J.-S. Lee, Y. Jiang, S.-W. Lee, S.-W. Kim, J.-S. Kim, H.-M. Jeong, J.-B. Kwon, J.-H. Bae, S.-W. Kang, Functional solid additive modified PEDOT:PSS as an anode buffer layer for enhanced photovoltaic performance and stability in polymer solar cells, Sci. Rep. 7 (2017) 45079. https://doi.org/10.1038/srep45079.

[33] K. Norrman, M. V. Madsen, S.A. Gevorgyan, F.C. Krebs, Degradation Patterns in Water and Oxygen of an Inverted Polymer Solar Cell, J. Am. Chem. Soc. 132 (2010) 16883–16892. https://doi.org/10.1021/ja106299g.

[34] S. Shao, J. Liu, J. Bergqvist, S. Shi, C. Veit, U. Würfel, Z. Xie, F. Zhang, In Situ Formation of MoO 3 in PEDOT:PSS Matrix: A Facile Way to Produce a Smooth and Less Hygroscopic Hole Transport Layer for Highly Stable Polymer Bulk Heterojunction Solar Cells, Adv. Energy Mater. 3 (2013) 349–355. https://doi.org/10.1002/aenm.201200609.

[35] Q. Peng, X. Liu, D. Su, G. Fu, J. Xu, L. Dai, Novel Benzo[1,2- b :4,5- b ′]dithiophene-Benzothiadiazole Derivatives with Variable Side Chains for High-Performance Solar Cells, Adv. Mater. 23 (2011) 4554–4558. https://doi.org/10.1002/adma.201101933.

[36] C. Wang, H. Dong, W. Hu, Y. Liu, D. Zhu, Semiconducting π-conjugated systems in field-effect transistors: A material odyssey of organic electronics, Chem. Rev. 112 (2012) 2208–2267. https://doi.org/10.1021/cr100380z.

[37] J. Kim, S. Park, S. Lee, H. Ahn, S. Joe, B.J. Kim, H.J. Son, Low-Temperature Processable High-Performance D-A-Type Random Copolymers for Nonfullerene Polymer Solar Cells

and Application to Flexible Devices, Adv. Energy Mater. 8 (2018) 1801601. https://doi.org/10.1002/aenm.201801601.

[38] X. Guo, H.N. Tsao, P. Gao, D. Xia, C. An, M.K. Nazeeruddin, M. Baumgarten, M. Grätzel, K. Müllen, Dithieno[2,3-d;2′,3′-d′]benzo[1,2-b;4,5-b′]dithiophene based organic sensitizers for dye-sensitized solar cells, RSC Adv. 4 (2014) 54130–54133. https://doi.org/10.1039/C4RA11873A.

[39] H. Pan, Y. Li, Y. Wu, P. Liu, B.S. Ong, S. Zhu, G. Xu, Low-Temperature, Solution-Processed, High-Mobility Polymer Semiconductors for Thin-Film Transistors, J. Am. Chem. Soc. 129 (2007) 4112–4113. https://doi.org/10.1021/ja067879o.

[40] L. Meng, Y. Zhang, X. Wan, C. Li, X. Zhang, Y. Wang, X. Ke, Z. Xiao, L. Ding, R. Xia, H.-L. Yip, Y. Cao, Y. Chen, Organic and solution-processed tandem solar cells with 17.3% efficiency, Science (80-.). 361 (2018) 1094–1098. https://doi.org/10.1126/science.aat2612.

[41] H. Luo, C. Yu, Z. Liu, G. Zhang, H. Geng, Y. Yi, K. Broch, Y. Hu, A. Sadhanala, L. Jiang, P. Qi, Z. Cai, H. Sirringhaus, D. Zhang, Remarkable enhancement of charge carrier mobility of conjugated polymer field-effect transistors upon incorporating an ionic additive, Sci. Adv. 2 (2016) e1600076. https://doi.org/10.1126/sciadv.1600076.

[42] P. Imin, F. Cheng, A. Adronov, Supramolecular complexes of single walled carbon nanotubes with conjugated polymers, Polym. Chem. 2 (2011) 411–416. https://doi.org/10.1039/C0PY00286K.

[43] A.W. Musumeci, G.G. Silva, J.-W. Liu, W.N. Martens, E.R. Waclawik, Structure and conductivity of multi-walled carbon nanotube/poly(3-hexylthiophene) composite films, Polymer (Guildf). 48 (2007) 1667–1678. https://doi.org/10.1016/j.polymer.2007.01.027.

[44] W. Feng, A. Fujii, M. Ozaki, K. Yoshino, Perylene derivative sensitized multi-walled carbon nanotube thin film, Carbon N. Y. 43 (2005) 2501–2507. https://doi.org/10.1016/j.carbon.2005.05.014.

[45] E. Cohen, H. Dodiuk, A. Ophir, S. Kenig, C. Barry, J. Mead, Evidences for π-interactions between pyridine modified copolymer and carbon nanotubes and its role as a compatibilizer in poly(methyl methacrylate) composites, Compos. Sci. Technol. 79 (2013) 133–139. https://doi.org/10.1016/j.compscitech.2013.02.012.

[46] B.K. Kuila, S. Malik, S.K. Batabyal, A.K. Nandi, In-situ synthesis of soluble poly(3-hexylthiophene)/multiwalled carbon nanotube composite: Morphology, structure, and conductivity, Macromolecules. 40 (2007) 278–287. https://doi.org/10.1021/ma061548e.

[47] R. Das, S. Hamid, M. Ali, S. Ramakrishna, W. Yongzhi, Carbon Nanotubes Characterization by X-ray Powder Diffraction – A Review, Curr. Nanosci. 11 (2014) 23–35. https://doi.org/10.2174/15734137106661408182100 43.

[48] W. Li, B. Guo, C. Chang, X. Guo, M. Zhang, Y. Li, Efficient polymer solar cells based on a copolymer of meta-alkoxy-phenyl-substituted benzodithiophene and thieno[3,4-b]thiophene, J. Mater. Chem. A. 4 (2016) 10135–10141. https://doi.org/10.1039/C6TA04030F.

[49] C. Vijayakumar, B. Balan, M.-J. Kim, M. Takeuchi, Noncovalent Functionalization of SWNTs with Azobenzene-Containing Polymers: Solubility, Stability, and Enhancement of Photoresponsive Properties, J. Phys. Chem. C. 115 (2011) 4533–4539. https://doi.org/10.1021/jp111248r.

[50] K. Matsuda, W. Norimatsu, J. Bao, H. Kawarada, M. Kusunoki, In-plane electrical conduction mechanisms of highly dense carbon nanotube forests on silicon carbide, J.

Appl. Phys. 123 (2018) 045104. https://doi.org/10.1063/1.5004507.

[51] H. Peng, Aligned Carbon Nanotube/Polymer Composite Films with Robust Flexibility, High Transparency, and Excellent Conductivity, J. Am. Chem. Soc. 130 (2008) 42–43. https://doi.org/10.1021/ja078267m.

[52] M. Goswami, A. Mukherjee, A.K. Das, R. Ghosh, A.K. Meikap, Synthesis, characterization and electrical property of MWCNT-ZnS nanocomposite embedded in polyaniline, Adv. Nat. Sci. Nanosci. Nanotechnol. 8 (2017) 025018. https://doi.org/10.1088/2043-6254/aa71ec.

[53] M.N. Norizan, M.H. Moklis, S.Z. Ngah Demon, N.A. Halim, A. Samsuri, I.S. Mohamad, V.F. Knight, N. Abdullah, Carbon nanotubes: functionalisation and their application in chemical sensors, RSC Adv. 10 (2020) 43704–43732. https://doi.org/10.1039/D0RA09438B.

[54] C. Yu, K. Choi, L. Yin, J.C. Grunlan, Light-Weight Flexible Carbon Nanotube Based Organic Composites with Large Thermoelectric Power Factors, ACS Nano. 5 (2011) 7885–7892. https://doi.org/10.1021/nn202868a.

[55] D. Kim, Y. Kim, K. Choi, J.C. Grunlan, C. Yu, Improved Thermoelectric Behavior of Nanotube-Filled Polymer Composites with Poly(3,4-ethylenedioxythiophene) Poly(styrenesulfonate), ACS Nano. 4 (2010) 513–523. https://doi.org/10.1021/nn9013577.

[56] C. Meng, C. Liu, S. Fan, A Promising Approach to Enhanced Thermoelectric Properties Using Carbon Nanotube Networks, Adv. Mater. 22 (2010) 535–539. https://doi.org/10.1002/adma.200902221.

[57] X. Zhang, Y. Pei, Manipulation of charge transport in thermoelectrics, Npj Quantum Mater. 2 (2017) 68. https://doi.org/10.1038/s41535-017-0071-2.

[58] C. Bounioux, P. Díaz-Chao, M. Campoy-Quiles, M.S. Martín-González, A.R. Goñi, R. Yerushalmi-Rozen, C. Müller, Thermoelectric composites of poly(3-hexylthiophene) and carbon nanotubes with a large power factor, Energy Environ. Sci. 6 (2013) 918–925. https://doi.org/10.1039/c2ee23406h.

[59] D. Kelkar, A. Chourasia, Structural, Thermal and Electrical Properties of Doped Poly(3,4 ethylenedioxythiophene), Chem. Chem. Technol. 10 (2016) 395–400. https://doi.org/10.23939/chcht10.04.395.

[60] S. He, M. Mukaida, K. Kirihara, L. Lyu, Q. Wei, Reversible protonic doping in poly(3,4-ethylenedioxythiophene), Polymers (Basel). 10 (2018). https://doi.org/10.3390/polym10101065.

[61] S.A. Gregory, A.K. Menon, S. Ye, D.S. Seferos, J.R. Reynolds, S.K. Yee, Effect of Heteroatom and Doping on the Thermoelectric Properties of Poly(3-alkylchalcogenophenes), Adv. Energy Mater. 8 (2018) 1802419. https://doi.org/10.1002/aenm.201802419.

[62] G. Gustafsson, O. Inganäs, J.O. Nilsson, Thermal instability of doped poly(3-alkylthiophenes), Synth. Met. 28 (1989) 427–434. https://doi.org/10.1016/0379-6779(89)90555-9.

[63] K. Zhang, M. Davis, J. Qiu, L. Hope-Weeks, S. Wang, Thermoelectric properties of porous multi-walled carbon nanotube/polyaniline core/shell nanocomposites, Nanotechnology. 23 (2012). https://doi.org/10.1088/0957-4484/23/38/385701.

[64] Q. Wang, Q. Yao, J. Chang, L. Chen, Enhanced thermoelectric properties of CNT/PANI composite nanofibers by highly orienting the arrangement of polymer chains, J. Mater. Chem. 22 (2012) 17612. https://doi.org/10.1039/c2jm32750c.

[65] F. Paquin, J. Rivnay, A. Salleo, N. Stingelin, C. Silva-Acuña, Multi-phase microstructures drive exciton dissociation in neat semicrystalline polymeric semiconductors, J. Mater. Chem. C. 3 (2015) 10715–10722. https://doi.org/10.1039/C5TC02043C.

[66] D. Yoo, J. Kim, S.H. Lee, W. Cho, H.H. Choi, F.S. Kim, J.H. Kim, Effects of one- and two-dimensional carbon hybridization of PEDOT:PSS on the power factor of polymer thermoelectric energy conversion devices, J. Mater. Chem. A. 3 (2015) 6526–6533. https://doi.org/10.1039/C4TA06710J.

[67] J. Wang, K. Cai, S. Shen, J. Yin, Preparation and thermoelectric properties of multi-walled carbon nanotubes/polypyrrole composites, Synth. Met. 195 (2014) 132–136. https://doi.org/10.1016/j.synthmet.2014.06.003.

[68] C. Bounioux, P. Díaz-Chao, M. Campoy-Quiles, M.S. Martín-González, A.R. Goñi, R. Yerushalmi-Rozen, C. Müller, Thermoelectric composites of poly(3-hexylthiophene) and carbon nanotubes with a large power factor, Energy Environ. Sci. 6 (2013) 918. https://doi.org/10.1039/c2ee23406h.

[69] C. Pan, L. Wang, T. Liu, X. Zhou, T. Wan, S. Wang, Z. Chen, C. Gao, L. Wang, Polar Side Chain Effects on the Thermoelectric Properties of Benzo[1,2-b:4,5-b′]Dithiophene-Based Conjugated Polymers, Macromol. Rapid Commun. 40 (2019) 1900082. https://doi.org/10.1002/marc.201900082.

[70] X. Zhou, C. Pan, C. Gao, A. Shinohara, X. Yin, L. Wang, Y. Li, Q. Jiang, C. Yang, L. Wang, Thermoelectrics of two-dimensional conjugated benzodithiophene-based polymers: density-of-states enhancement and semi-metallic behavior, J. Mater. Chem. A. 7 (2019) 10422–10430. https://doi.org/10.1039/C9TA01437C.

[71] A.G. MacDiarmid, R.J. Mammone, R.B. Kaner, S.J. Porter, R. Pethig, A.J. Heeger, D.R.

Rosseinsky, The Concept of `Doping' of Conducting Polymers: The Role of Reduction Potentials [and Discussion], Philos. Trans. R. Soc. A Math. Phys. Eng. Sci. 314 (1985) 3–15. https://doi.org/10.1098/rsta.1985.0004.

[72] P. Mangelis, P. Vaqueiro, J.C. Jumas, I. da Silva, R.I. Smith, A. V. Powell, The effect of electron and hole doping on the thermoelectric properties of shandite-type Co3Sn2S2, J. Solid State Chem. 251 (2017) 204–210. https://doi.org/10.1016/j.jssc.2017.04.028.

[73] J. Beuvelot, C. Bergeret, R. Mallet, V. Fernandez, J. Cousseau, M.F. Baslé, D. Chappard, In vitro calcification of chemically functionalized carbon nanotubes, Acta Biomater. 6 (2010) 4110–4117. https://doi.org/10.1016/j.actbio.2010.05.011.

[74] B. Singh, L. Murad, F. Laffir, C. Dickinson, E. Dempsey, Pt based nanocomposites (mono/bi/tri-metallic) decorated using different carbon supports for methanol electro-oxidation in acidic and basic media, Nanoscale. 3 (2011) 3334–3349. https://doi.org/10.1039/c1nr10273g.

[75] T. Du, A.S. Adeleye, T. Zhang, N. Yang, R. Hao, Y. Li, W. Song, W. Chen, Effects of ozone and produced hydroxyl radicals on the transformation of graphene oxide in aqueous media, Environ. Sci. Nano. 6 (2019) 2484–2494. https://doi.org/10.1039/C9EN00361D.

[76] A. Furlani, M. V. Russo, G. Polzonetti, K. Martin, H.H. Wang, J.R. Ferraro, Spectroscopic Studies of FeCl 3 -Doped Polymers of Polyphenylacetylene, Appl. Spectrosc. 44 (1990) 331–334. https://doi.org/10.1366/0003702904085688.

[77] T. Yamashita, P. Hayes, Analysis of XPS spectra of Fe2+ and Fe3+ ions in oxide materials, Appl. Surf. Sci. 254 (2008) 2441–2449. https://doi.org/10.1016/j.apsusc.2007.09.063.

[78] M. V. Russo, G. Polzonetti, A. Furlani, A. Bearzotti, I. Fratoddi, P. Altamura, X-ray

photoelectron spectroscopy and scanning electron microscopy characterization of novel poly(monosubstituted) acetylenes containing doping species, J. Vac. Sci. Technol. A Vacuum, Surfaces, Film. 16 (1998) 35–44. https://doi.org/10.1116/1.581006.

[79] A. Abidov, B. Allabergenov, J. Lee, H.-W. Jeon, S.-W. Jeong, S. Kim, X-Ray Photoelectron Spectroscopy Characterization of Fe Doped TiO2 Photocatalyst, Int. J. Mater. Mech. Manuf. 1 (2013) 294–296. https://doi.org/10.7763/IJMMM.2013.V1.63.

[80] B.W. Veal, A.P. Paulikas, Final-state screening and chemical shifts in photoelectron spectroscopy, Phys. Rev. B. 31 (1985) 5399–5416. https://doi.org/10.1103/PhysRevB.31.5399.

[81] M.V. Russo, G. Polzonetti, A. Furlani, XPS and IR investigations of FeCl3-doped polyphenylacetylene: the solvent effect, Synth. Met. 39 (1991) 291–301. https://doi.org/10.1016/0379-6779(91)91755-Y.

[82] Y.H. Kang, U.-H. Lee, I.H. Jung, S.C. Yoon, S.Y. Cho, Enhanced Thermoelectric Performance of Conjugated Polymer/CNT Nanocomposites by Modulating the Potential Barrier Difference between Conjugated Polymer and CNT, ACS Appl. Electron. Mater. 1 (2019) 1282–1289. https://doi.org/10.1021/acsaelm.9b00224.

[83] H.F. Haneef, A.M. Zeidell, O.D. Jurchescu, Charge carrier traps in organic semiconductors: a review on the underlying physics and impact on electronic devices, J. Mater. Chem. C. 8 (2020) 759–787. https://doi.org/10.1039/C9TC05695E.

[84] W. Zhao, J. Ding, Y. Zou, C. Di, D. Zhu, Chemical doping of organic semiconductors for thermoelectric applications, Chem. Soc. Rev. 49 (2020) 7210–7228. https://doi.org/10.1039/D0CS00204F.

[85] C. Gayner, Y. Amouyal, Energy Filtering of Charge Carriers: Current Trends, Challenges,

and Prospects for Thermoelectric Materials, Adv. Funct. Mater. 30 (2020) 1901789. https://doi.org/10.1002/adfm.201901789.

[86] A.M. Almasri, Predicting the thermal conductivity of polypropylene-multiwall carbon nanotubes using the Krenchel model, IEEE J. Sel. Top. Quantum Electron. 25 (2018) 383–388. https://doi.org/10.1515/secm-2016-0032.

[87] C.W. Nan, Z. Shi, Y. Lin, A simple model for thermal conductivity of carbon nanotube-based composites, Chem. Phys. Lett. 375 (2003) 666–669. https://doi.org/10.1016/S0009-2614(03)00956-4.

[88] C.W. Nan, R. Birringer, D.R. Clarke, H. Gleiter, Effective thermal conductivity of particulate composites with interfacial thermal resistance, J. Appl. Phys. 81 (1997) 6692–6699. https://doi.org/10.1063/1.365209.

[89] Y.-J. Lee, K.-S. Jeng, J.-T. Chen, K.W. Sun, Exceptionally low thermal conductivity of poly(3-hexylthiophene) single nanowires, RSC Adv. 5 (2015) 90847–90851. https://doi.org/10.1039/C5RA09977C.

[90] P.M. Smith, L. Su, W. Gong, N. Nakamura, B. Reeja-Jayan, S. Shen, Thermal conductivity of poly(3,4-ethylenedioxythiophene) films engineered by oxidative chemical vapor deposition (oCVD), RSC Adv. 8 (2018) 19348–19352. https://doi.org/10.1039/C8RA03302A.

[91] M.K. Smith, V. Singh, K. Kalaitzidou, B.A. Cola, Poly(3-hexylthiophene) Nanotube Array Surfaces with Tunable Wetting and Contact Thermal Energy Transport, ACS Nano. 9 (2015) 1080–1088. https://doi.org/10.1021/nn5027406.

[92] C.-W. Chang-Jian, E.-C. Cho, K.-C. Lee, J.-H. Huang, P.-Y. Chen, B.-C. Ho, Y.-S. Hsiao, Thermally conductive polymeric composites incorporating 3D MWCNT/PEDOT:PSS

scaffolds, Compos. Part B Eng. 136 (2018) 46–54. https://doi.org/10.1016/j.compositesb.2017.10.004.

[93] M. Liebscher, T. Gärtner, L. Tzounis, M. Mičušík, P. Pötschke, M. Stamm, G. Heinrich, B. Voit, Influence of the MWCNT surface functionalization on the thermoelectric properties of melt-mixed polycarbonate composites, Compos. Sci. Technol. 101 (2014) 133–138. https://doi.org/10.1016/j.compscitech.2014.07.009.

[94] D. Yoo, J. Kim, J.H. Kim, Direct synthesis of highly conductive poly(3,4-ethylenedioxythiophene):Poly(4-styrenesulfonate) (PEDOT:PSS)/graphene composites and their applications in energy harvesting systems, Nano Res. 7 (2014) 717–730. https://doi.org/10.1007/s12274-014-0433-z.

[95] E. Jin Bae, Y. Hun Kang, K.-S. Jang, S. Yun Cho, Enhancement of Thermoelectric Properties of PEDOT:PSS and Tellurium-PEDOT:PSS Hybrid Composites by Simple Chemical Treatment, Sci. Rep. 6 (2016) 18805. https://doi.org/10.1038/srep18805.

[96] F. Jiao, C. Di, Y. Sun, P. Sheng, W. Xu, D. Zhu, Inkjet-printed flexible organic thin-film thermoelectric devices based on p- and n-type poly(metal 1,1,2,2-ethenetetrathiolate)s/polymer composites through ball-milling, Philos. Trans. R. Soc. A Math. Phys. Eng. Sci. 372 (2014) 20130008. https://doi.org/10.1098/rsta.2013.0008.

[97] R. Yanagisawa, N. Tsujii, T. Mori, P. Ruther, O. Paul, M. Nomura, Nanostructured planar-type uni-leg Si thermoelectric generators, Appl. Phys. Express. 13 (2020) 095001. https://doi.org/10.35848/1882-0786/aba5c4.

[98] W. Shin, T. Nakashima, M. Nishibori, N. Izu, T. Itoh, I. Matsubara, Planar-type thermoelectric micro devices using ceramic catalytic combustor, Curr. Appl. Phys. 11 (2011) S36–S40. https://doi.org/10.1016/j.cap.2011.01.051.

[99] N. Nandihalli, C.-J. Liu, T. Mori, Polymer based thermoelectric nanocomposite materials and devices: Fabrication and characteristics, Nano Energy. 78 (2020) 105186. https://doi.org/10.1016/j.nanoen.2020.105186.

[100] Z. Fan, Y. Zhang, L. Pan, J. Ouyang, Q. Zhang, Recent developments in flexible thermoelectrics: From materials to devices, Renew. Sustain. Energy Rev. 137 (2021) 110448. https://doi.org/10.1016/j.rser.2020.110448.

CHAPTER 3

Role of p- Doping in Thermoelectric Properties of Conjugated Thienothiophene Polymer/MWCNT Hybrids

The growing energy usage in the present world demands improving the efficiency of energy conversion and saving technologies. In recent years, thermoelectric (TE) devices have proved to be a promising sustainable energy source that directly converts waste heat into electricity. TE devices are robust, silent, and solid-state energy conversion systems that convert thermal energy to electrical energy and vice versa. They are widely used in many fields such as in aerospace [1,2], automobile industry [3,4], consumer electronic devices [5,6], point-care devices [7–9], micro-self powered wireless platforms [10,11], and air conditioning appliances for particular targets [12,13]. Body heat can act as sustainable energy and can be exploited to power up emerging wearable medical devices allowing applications ranging from health monitoring and tracking systems to sports and fitness devices [7,8,14,15]. TE devices have become an area of interest in energy harvesting for large and even small applications throughout the last years due to their attractive features, such as long life, easy maintenance, and energy efficiency. The energy conversion efficiency of a TE material is linked to its dimensionless figure of merit (ZT), electrical conductivity (σ), Seebeck coefficient (α), and thermal conductivity (κ), as defined in equation 1.1.

Conventionally, some low-bandgap/degenerate inorganic semiconductors or semimetals were used as TE materials. Well-known examples include bismuth chalcogenides for low to mid-temperature ranges and silicon for high-temperature applications. Lately, organic-based materials/composites/hybrids are being pursued because of their intrinsic advantages over

traditional TE materials [16,17]. These factors are substantial functionality multipliers for TE applications and must be prioritized along with the maximum-*ZT* hunt.

Prior studies on organic TE materials were primarily focused on conducting polymers such as polythiophene, polyaniline, polyfluorene, polypyrrole, and their derivatives by preparing organic/inorganic hybrids/composites [18,19]. Recently, significant progress has been made in studying the relationship between polymer structure and TE properties [20,21]. Wang *et al.* designed and synthesized donor-acceptor (D–A) type conjugated polymers and effectively enhanced their TE properties through side-chain engineering [22]. They reported that the polymer backbone structure significantly affects the TE properties, and the inclusion of thiophene/carbazole units can advance the conversion efficiency of the polymers. Zhou *et al.* tailored the density of states (DOS) of two-dimensional conjugated polymers with different side-chain groups, leading to a dramatic PF improvement [23]. At 350 K, the PF of the doped film with alkylthienothiophene side-chain reached 101.3 μW/m.K^2, which is more than two orders higher than that of the undoped film (0.9 μW/m.K^2). Carbon nanotube (CNT) based organic TE materials were also of great importance for fabricating stable and lightweight modules [14,24]. However, detailed insight on the role of the doping mechanism of CNT-based hybrids is still lacking.

In recent years, benzo[1,2-b:4,5-b′]dithiophene (BDT) based conjugated polymers were found to be an excellent candidate for optoelectronic devices such as solar cells, field effect transistors (FET), and fluorescence sensors [25,26]. The BDT units are common organic semiconducting units with a planar backbone and high oxidative stability, effectively improving the charge carrier mobility [27]. Furthermore, the central benzene core of BDT can be anchored to different substituents for tuning the energy levels, solubility, absorption spectra, and thermal stability [28]. These polymers are more adaptive to π-structures like CNTs resulting in hybrid

structures with unique properties [29]. Since the BDT-based conjugated polymers have rarely been explored in TE, a detailed study linking their structure with TE performance is essential for improving ZT. Furthermore, very few studies have analyzed the effect of doping on the strutuctre-property relation of TE materials.

In the present study, we used two conjugated benzodithiophene-thienothiophene (BDT-TTE) polymers, poly[(4,8-bis-(2-ethylhexyloxy)-benzo(1,2-b:4,5-b′)dithiophene)-2,6-diyl-alt-(4-(2-ethylhexanoyl)-thieno[3,4-b]thiophene-)-2-6-diyl)] (PBDTTT-C) and poly[[4,8-bis[5-(2-ethylhexyl)-2-thienyl]benzo[1,2-*b*:4,5-*b*′]dithiophene-2,6-diyl][2-(2-ethyl-1-oxohexyl)thieno[3,4-*b*]thiophenediyl]] (PBDTTT-C-T). These two polymers have identical conjugated backbones but different side-chain; alkoxy and alkylthiophene groups are attached to the BDT units in PBDTTT-C and PBDTTT-C-T, respectively. Several scientific papers documented the excellent ambient stability and charge transport for organic photovoltaics [30,31], and their structure-property correlation for solar cells [32]. Such properties could be favorable for TE applications with a judicious tuning of σ, α, and κ. Herein, we formed hybrids of these polymers with multi-walled carbon nanotube (MWCNT) and systematically investigated their TE properties and the effect of p-doping (with $FeCl_3$). A concurrent increase of σ and α is achieved for the hybrid consisting of alkylthiophene side-chain polymer after doping, while α remained unchanged for the hybrids fabricated using the polymer with alkoxy side-chain group although it showed a slight increase in σ. This chapter presents a universal understanding of the doping mechanism and the underlying physics to design high-performance organic-based TE hybrids.

3.1. Experiment section

3.1.1. Chemicals

PBDTTT-C ($(C_{40}H_{52}O_3S_4)_n$) and PBDTTT-C-T ($(C_{48}H_{56}OS_6)_n$) were purchased from Solarmer Energy INC. MWCNT (containing >90% carbon basis, diameter ~ 110-170 nm and length ~5-9 μm) and anhydrous *ortho*-dichlorobenzene (*o*-DCB) were obtained from Sigma-Aldrich. Anhydrous ferric chloride ($FeCl_3$) was purchased from SD Fine Chemicals, and nitromethane (CH_3NO_2) was procured from Spectrochem. No further purification of chemicals was done, and it was used as such.

3.1.2. Preparation of organic hybrids

The polymers PBDTTT-C and PBDTTT-C-T along with MWCNT) were dispersed in *o*-DCB to produce 0.05 mg/μL of solutions of each. A bath sonicator (Elmasonic P30H Ultrasonic bath; 80 kHz and 192 W) is used for 60 min for the sample preparation. The hybrid composition was tuned by different wt% of MWCNT addition. The subsequent mixture showed good stability over three weeks, with no material settling. The dispersion was drop-cast on a pre-cleaned (with extran, water, and isopropanol in that sequence by bath sonication for 15 min in each) and pre-heated (at 120 °C for 15 min) glass substrate and annealed at 120 °C for 30 min.

3.1.3. Doping of organic hybrid film

The hybrid films were immersed into 0.05 M $FeCl_3$ solution in nitromethane for 30 min and washed with ethanol to remove the excess dopants, then annealed at 100 °C for 15 min.

3.1.4. Characterization and measurements

The present work's characterization and measurement techniques are listed in Annexure I.

3.2. Results and discussion

3.2.1. Characterization and analysis of hybrids

The molecular structures of two BDT-based polymers, PBDTTT-C and PBDTTT-C-T, are shown in Fig. 3.1a. Both polymers have identical conjugated backbones but different side-chain groups. The alkoxy and alkylthiophene groups are at the 4 and 8 positions of the BDT units in PBDTTT-C and PBDTTT-C-T, respectively. The PBDTTT-C/MWCNT (OH1) and PBDTTT-C-T/MWCNT (OH2) hybrids preparation processes are schematically shown in Fig. 3.1b.

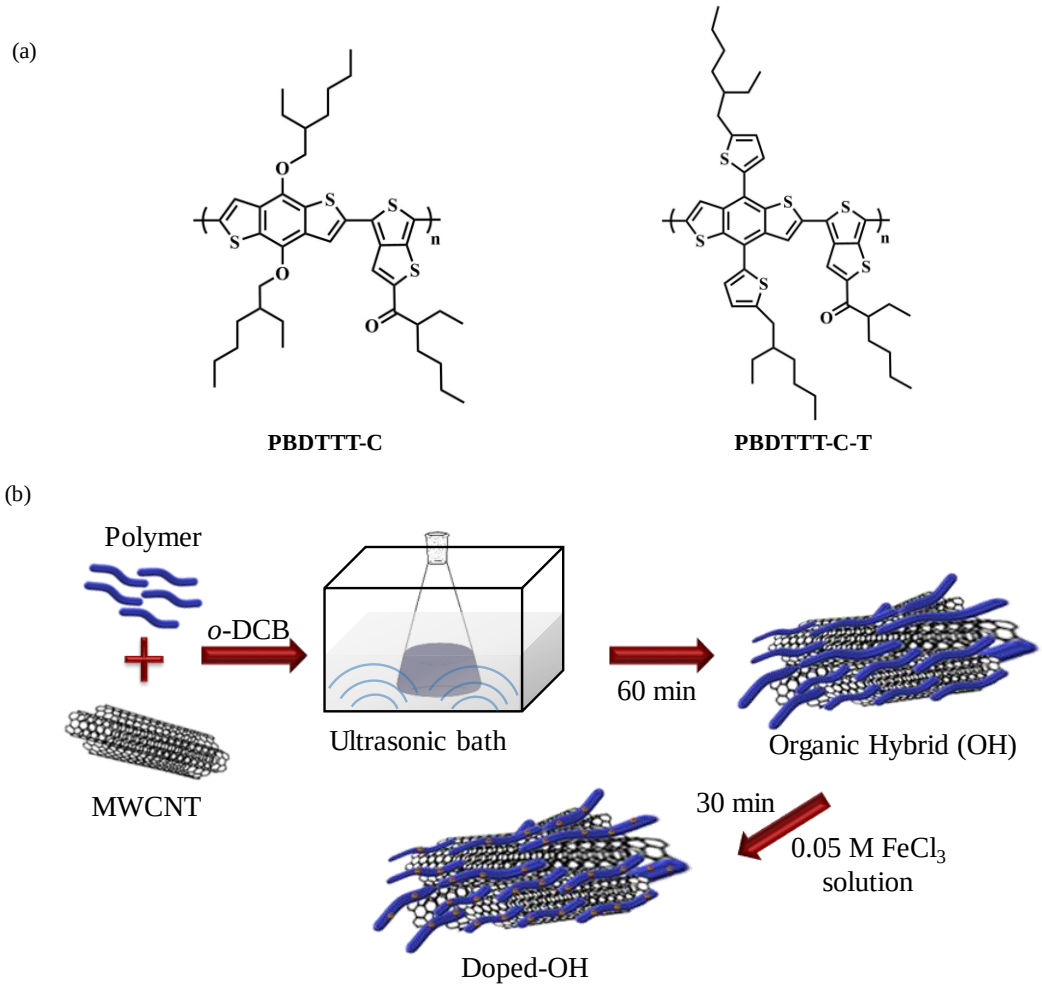

Fig. 3.1. (a) Molecular structures of PBDTTT-C and PBDTTT-C-T and (b) Schematic diagram of the preparation of hybrid films.

As shown in Fig. 3.2a, both hybrids displayed an embedded network of MWCNT in polymer matrices. Such MWCNT-reinforced networks are expected to establish π-stacking interactions of the electron-rich fused thiophene units while enhancing mechanical strength [33,34]. The topographic morphology of the hybrids was unaffected by doping, and the corresponding SEM images are given in Fig. 3.2b.

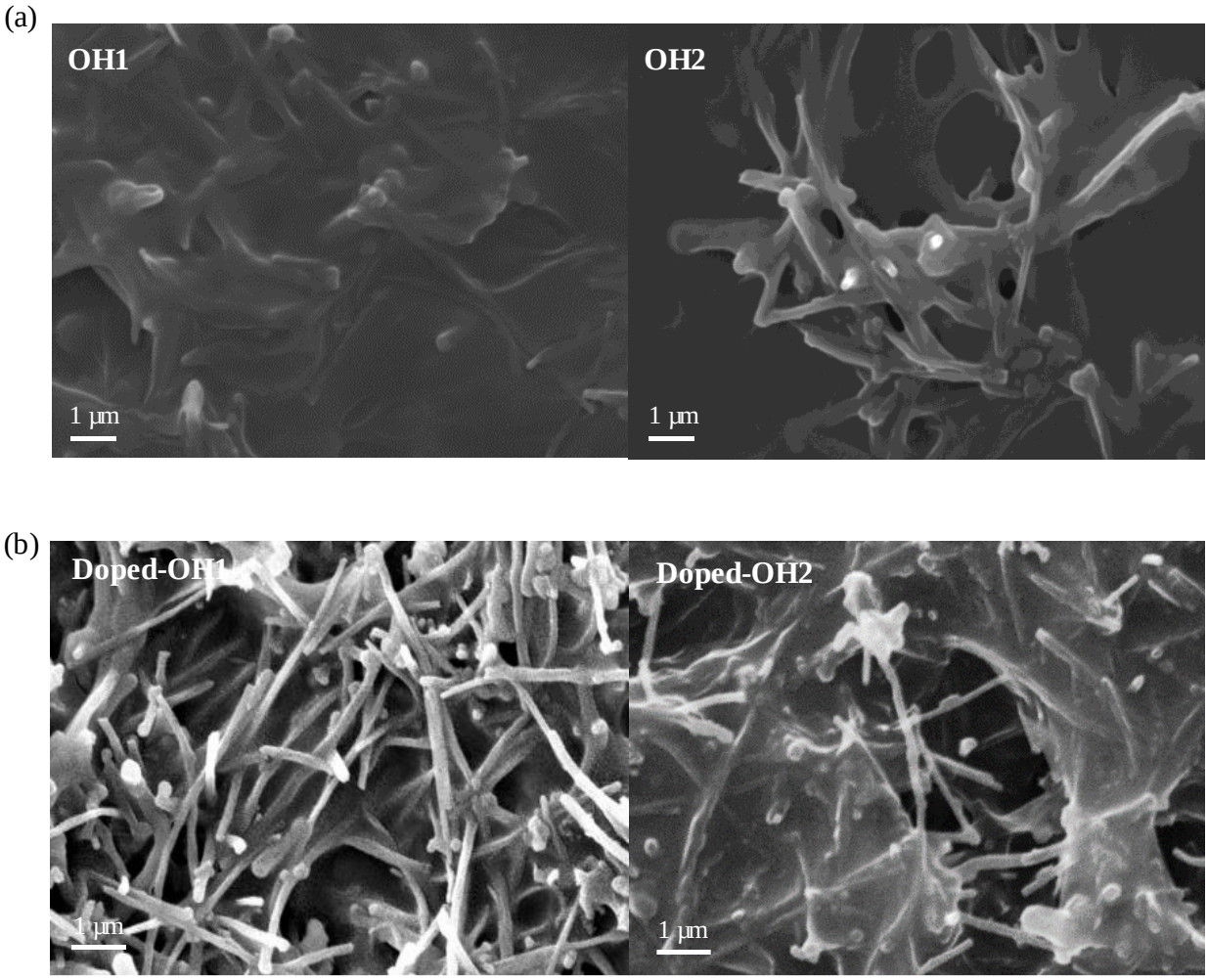

Fig. 3.2. SEM images of (a) OH1 and OH2 hybrids and (b) Doped-OH1 and Doped-OH2 hybrids.

The UV-visible spectra of the pure polymer and their hybrid films are shown in Fig. 3.3a. The intramolecular donor-acceptor copolymers commonly show a relatively strong absorption peak in 550 to 700 nm and a weak absorption peak in the shorter 300 to 500 nm range [35,36]. The

long-wavelength absorption peak is due to intramolecular charge transfer between the acceptor and the donor, while the short-wavelength peak originates from the π-π* transition [37]. Here, the short-wavelength absorption peaks of PBDTTT-C and PBDTTT-C-T appeared at 343 and 350 nm and were redshifted to ~344 nm (OH1) and ~356 nm (OH2) upon hybrid formation. The shift is due to the elongation of the effective conjugation length upon incorporating CNT, which would enhance intermolecular orbital overlap [38]. As the hybrid forms, the polymer gets adsorbed on the MWCNT surface through physical interaction, and the polymer backbone structure becomes more planar after interacting with the MWCNT surface, thereby increasing the effective conjugation length [39–41]. The absorption peak maxima of PBDTTT-C and PBDTTT-C-T were observed at 579 and 636 nm, which broadened after the hybrid formation with a small energy blueshift (OH1~576 and OH2 ~634 nm). The shift indicates a change in intra-chain and inter-chain hybrid connections due to the interaction between CNT and polymer [42]. Post-doping (Fig. 3.3b), the absorption maxima of OH1 and OH2 films were redshifted to 613 and 643 nm, indicating the enhancement of intermolecular π-π interaction between the CNT and polymer [23]. The doped OH2 films showed a more prominent absorption shoulder towards the longer wavelength due to more robust intermolecular π-π stacking.

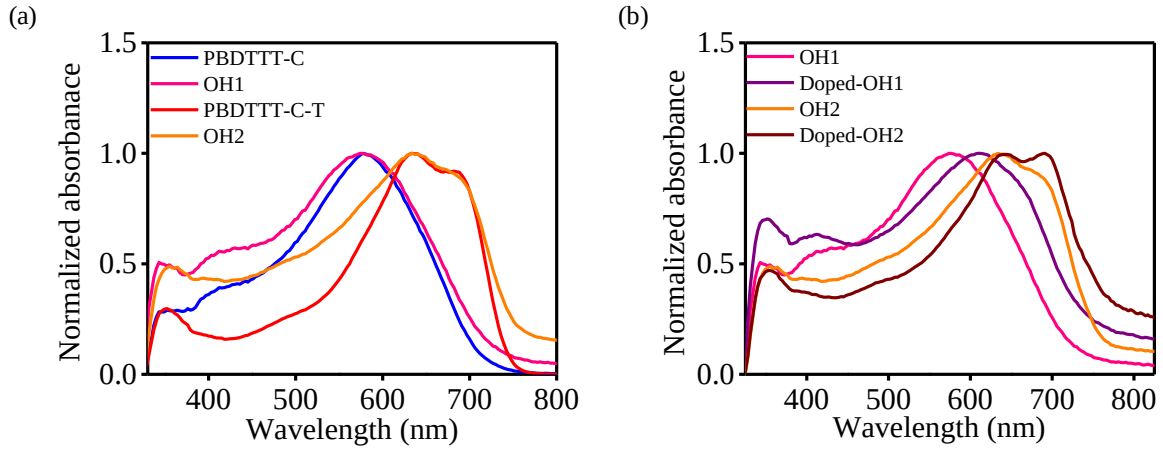

Fig. 3.3. (a) & (b) UV-vis absorption spectra of pristine polymers, hybrid films, and doped hybrid films.

The crystal structure analysis exhibited a redshift in lamellar peak (100) of both the polymer after hybrid formation (Fig. 3.4a), indicating an excellent local ordering [43]. The WAXS spectrum of pristine polymers shows a peak at 22.03° (for PBDTTT-C) and 21.19° (for PBDTTT-C-T), representing d_{010} spacing for the π-π stacking of thiophene rings [44]. Also, MWCNT shows a diffraction peak at 26.3°, corresponding to the characteristic graphitic peak (002) having a d-spacing of 3.4 Å. Upon hybrid formation, the (010) peak of polymer shifted towards a lower 2θ, and (002) peak of MWCNT shifted towards the higher value. A decrease in intensity is noted due to the overlaying of polymer on the surface of MWCNT. This observation confirmed a successful hybrid formation of the components. Post-doping (Fig. 3.4b), a shift towards lower 2θ in the (100) peak of both hybrids were observed (OH1: 4.77°→ 4.67°; OH2: 4.20° → 4.04°) due to the elongation of lamellar stacking. A reduction of the peak intensity was observed for both the hybrid films, suggesting a decrease in the local order after doping [45]. The (010) peak intensity faded, and the peak at $2\theta = 26.37°$ shifted to 26.55° after doping due to the stronger interchain coupling between components. For the pristine polymers, hybrids, and doped hybrids, the variation of d-

spacing for (100) and (002) peaks are plotted in Fig. 3.4c and Fig. 3.4d. The d-value assigned to the lamellar-stacking direction is bigger for the doped- OH2 hybrid than the OH1. In OH1 and OH2, the d- spacing corresponding to π-stacking direction reduces upon hybrid formation and doping, implying a stronger π-π intermolecular interaction. These observations suggest that the doped-OH2 hybrid has a larger conjugated plane and better interchain π-π overlap post-doping, leading to higher carrier mobility and better charge transport properties.

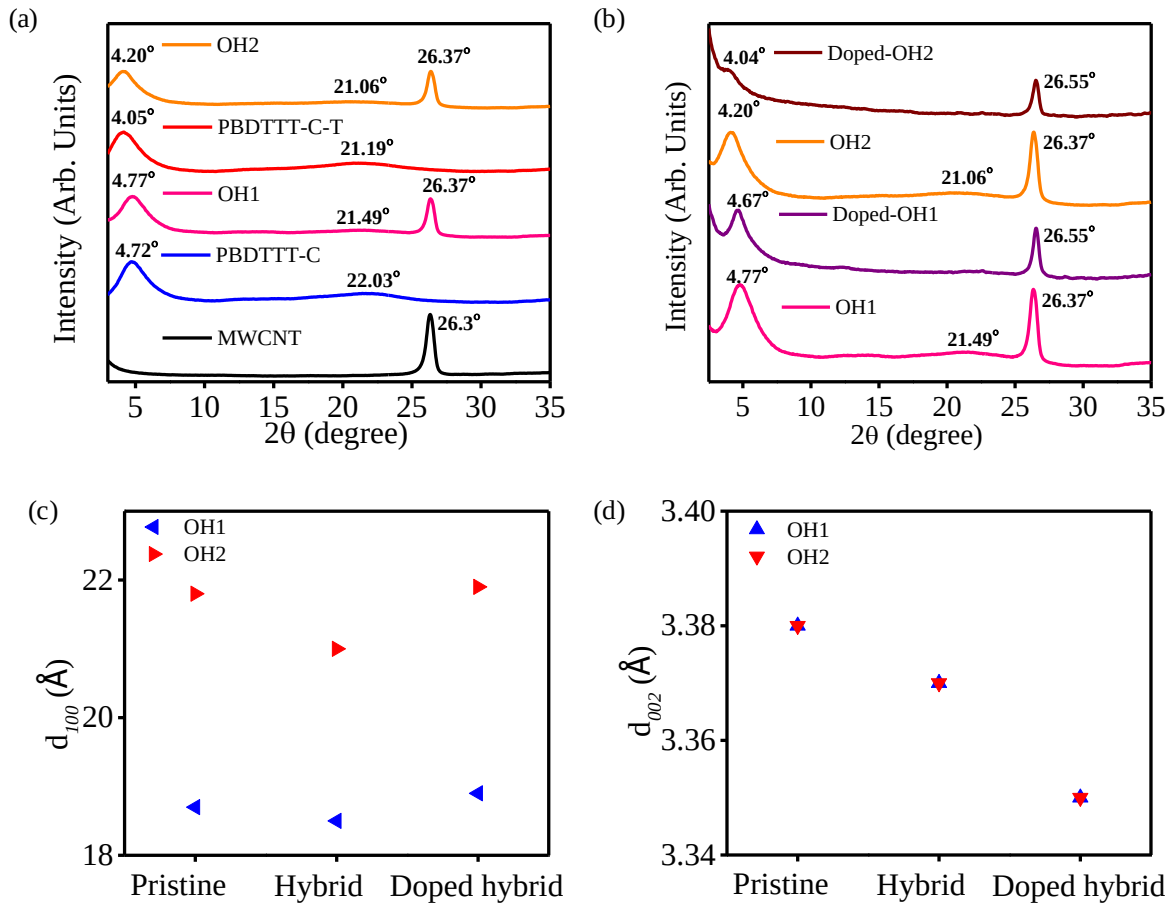

Fig. 3.4. (a) & (b) WAXS plot and (c) & (d) d-spacing of the pristine polymers, hybrid films, and doped hybrid.

3.2.2. Thermoelectric studies of hybrid films

The TE parameters of hybrid films with different MWCNT weight percentages (wt%) at room temperature (~28-30 °C) were studied. The samples were drop-cast on a 16 × 4 mm glass substrate to form thick films. The average film thickness was obtained as ~25 ± 5 μm. The significant thickness measurement error was due to the high roughness in surface topography. Fig. 3.5a and Fig. 3.6a shows the variation of film thickness with MWCNT wt% for OH1 and OH2, respectively. We noted minor thickness changes in the film thicknesses after doping, which lies in the relatively large thickness assessment error as stated before. With the addition of a lower amount of MWCNT, the undoped hybrids showed an imperceptible improvement in σ value. Beyond 15 wt%, a percolation threshold in σ value was observed that peaks at 45 wt% of MWCNT for both the hybrids, as plotted in Fig. 3.5b and Fig. 3.6b. Such conductivity enhancement could be attributed to forming an inter-CNT bundle that creates new electrical pathways through the hybrid. Beyond this optimum level, a further increase in MWCNT wt% led to a decrease in σ, probably because of aggregates forming at higher MWCNT wt%, which eventually separate from the polymer support leading to a breakdown in the electrical network. However, α remained almost unaffected regardless of MWCNT addition, with an average value of ~19.36 μV/K and 19.46 μV/K for OH1 and OH2, respectively (Fig. 3.5c and Fig. 3.6c). The α is essentially linked to the thermally activated charge carrier transport [46,47]. Beyond the percolation threshold, the energetic charge carriers primarily travel through the embedded CNT network. Therefore, the α value of these hybrids remains more or less constant and similar to that of MWCNT [48]. Accordingly, the PF also peaks with the σ, as shown in Fig. 3.5d and Fig. 3.6d.

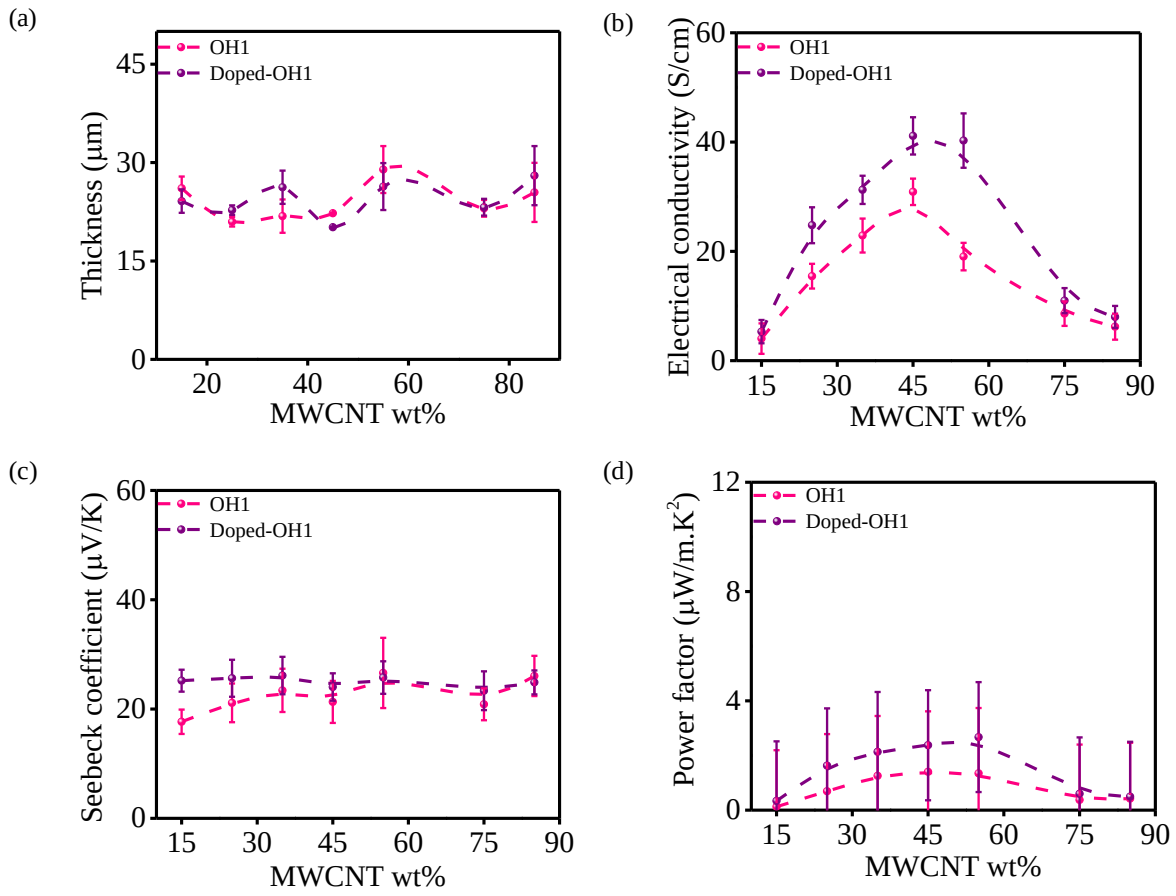

Fig. 3.5. The variation of (a) thickness; (b) electrical conductivity; (c) Seebeck coefficient and (c) power factor with MWCNT wt% for OH1 hybrids.

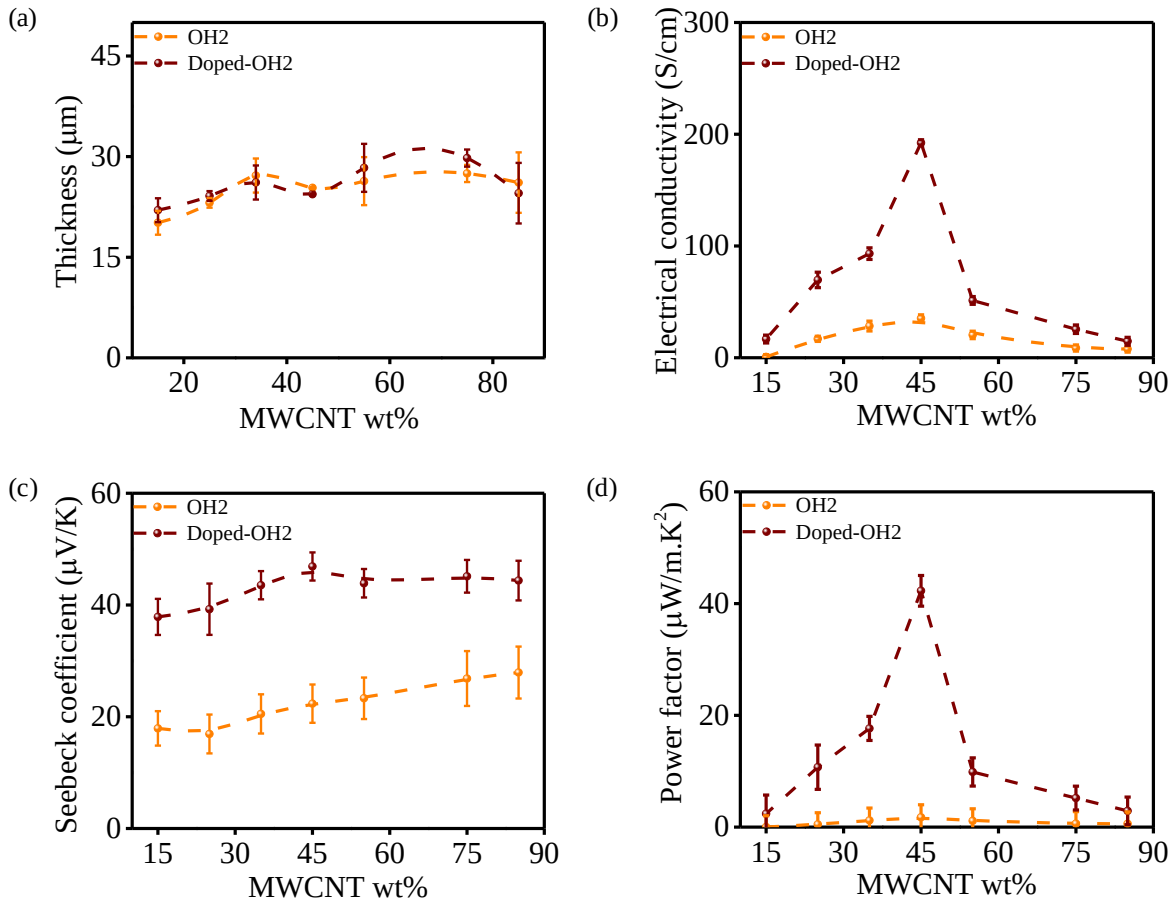

Fig. 3.6. The variation of (a) thickness; (b) electrical conductivity; (c) Seebeck coefficient and (c) power factor with MWCNT wt% for OH2 hybrids.

To further confirm the percolation behavior of MWCNT wt%, the temperature-dependent TE properties of selected organic hybrids were measured from 30 °C to 260 °C (Fig. 3.7 & Fig. 3.8). The highest σ for both OH1 and OH2 hybrids is obtained at 45 wt% MWCNT content. As the temperature increases, the σ and α of OH1 and OH2 film decreases (Fig. 3.7a & b and Fig. 3.8a & b). Post doping, an increase in σ value is observed initially for both hybrids, followed by a decreasing slope, and after a specific temperature attains a constant value (Fig. 3.7c & Fig. 3.8c). Correspondingly, α of the doped hybrids also showed an increasing trend by increasing temperature and a steep decreasing slope afterward (Fig. 3.7d & Fig. 3.8d). Fig. 3.9 shows the

SEM image of hybrid films with 55 and 75 wt% of MWCNT. As the CNT content increases, the MWCNT networks are dragged out from the polymer matrix (Fig. 3.9a) and eventually form aggregates and get isolated in the polymer matrix, as shown in Fig. 3.9b. This results in a decrease in σ as it loses the continuous pathway. Such a decrease in σ is also observed in other polymer/CNT composites due to the breakage of the electrical pathway [49,50].

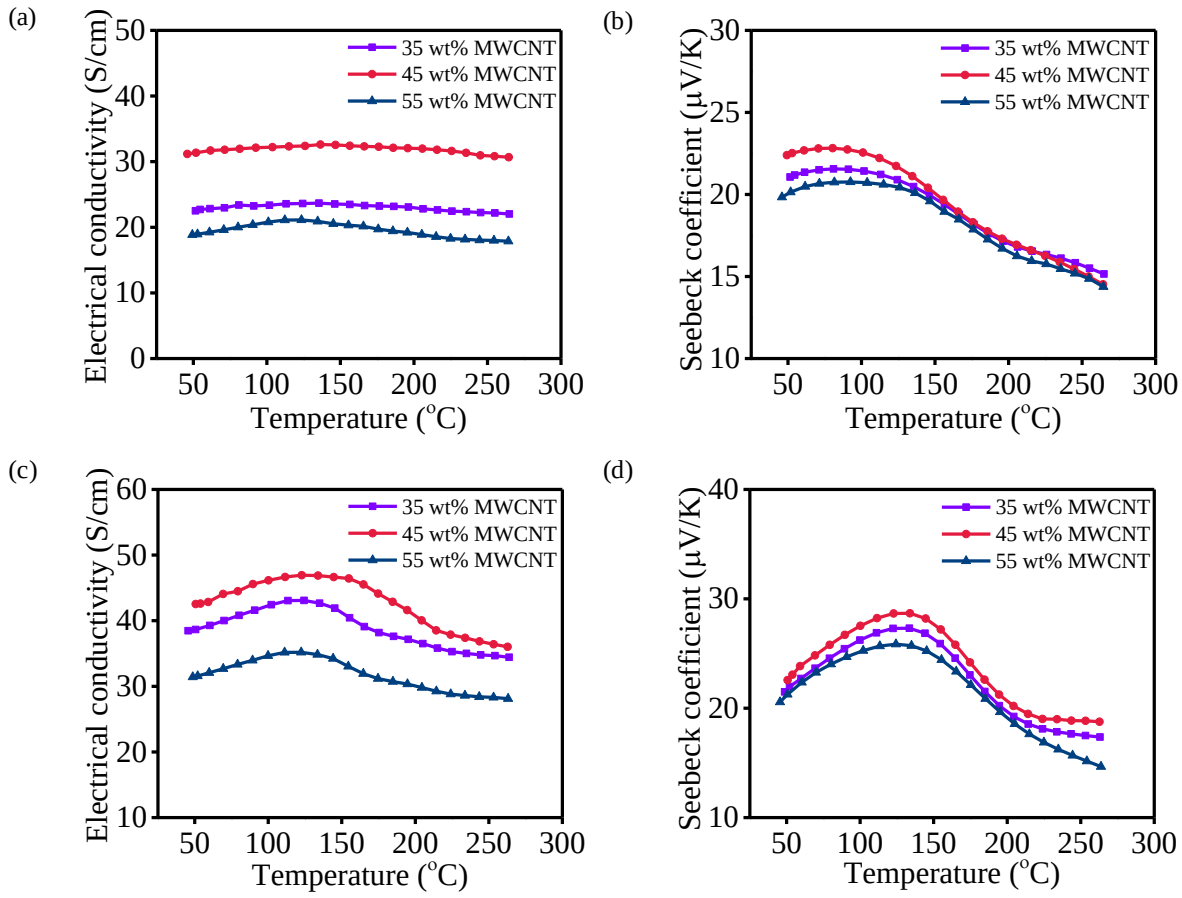

Fig. 3.7. Temperature-dependent changes of (a) Electrical conductivity and (b) Seebeck coefficient of OH1; (c) Electrical conductivity and (d) Seebeck coefficient of Doped-OH1.

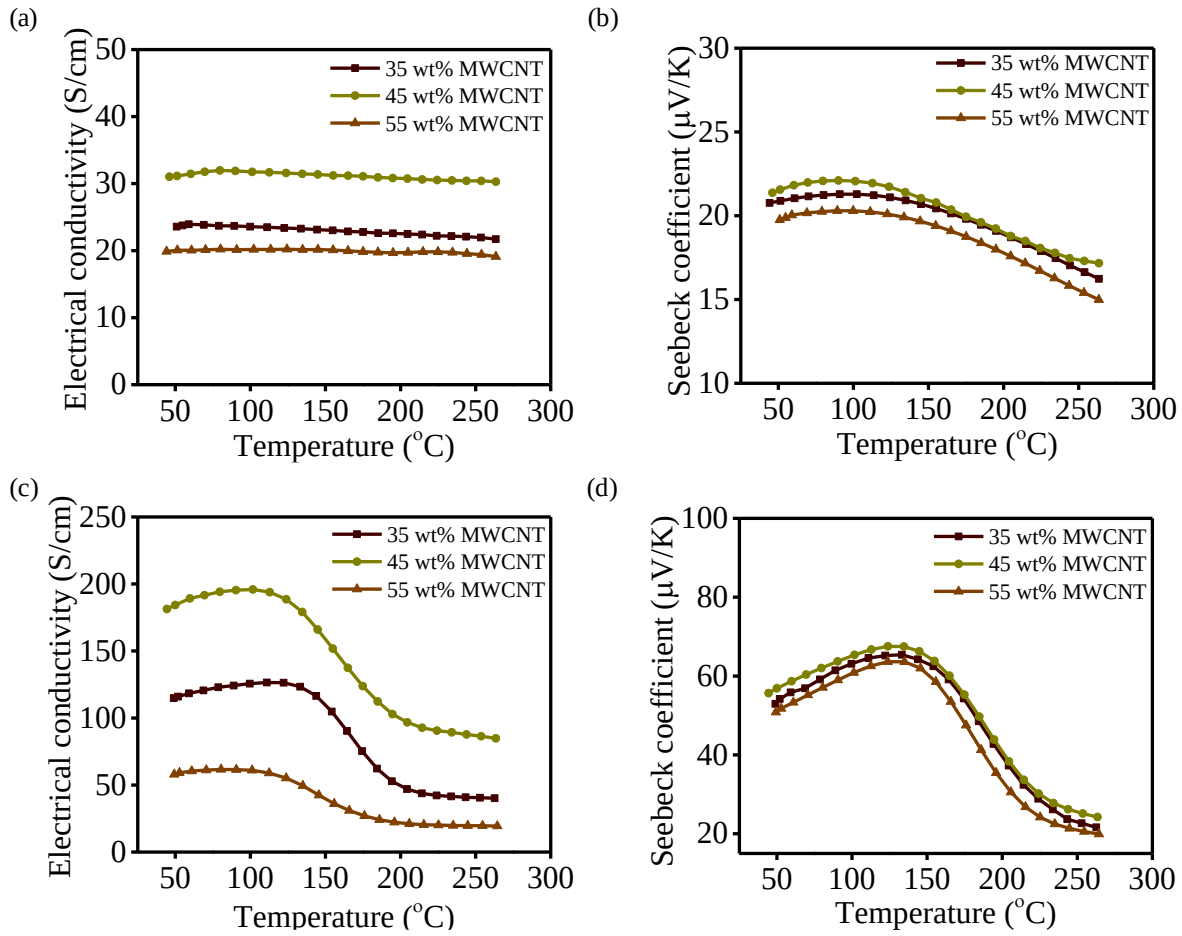

Fig. 3.8. Temperature-dependent changes of (a) Electrical conductivity and (b) Seebeck coefficient of OH2; (c) Electrical conductivity and (d) Seebeck coefficient of Doped-OH2.

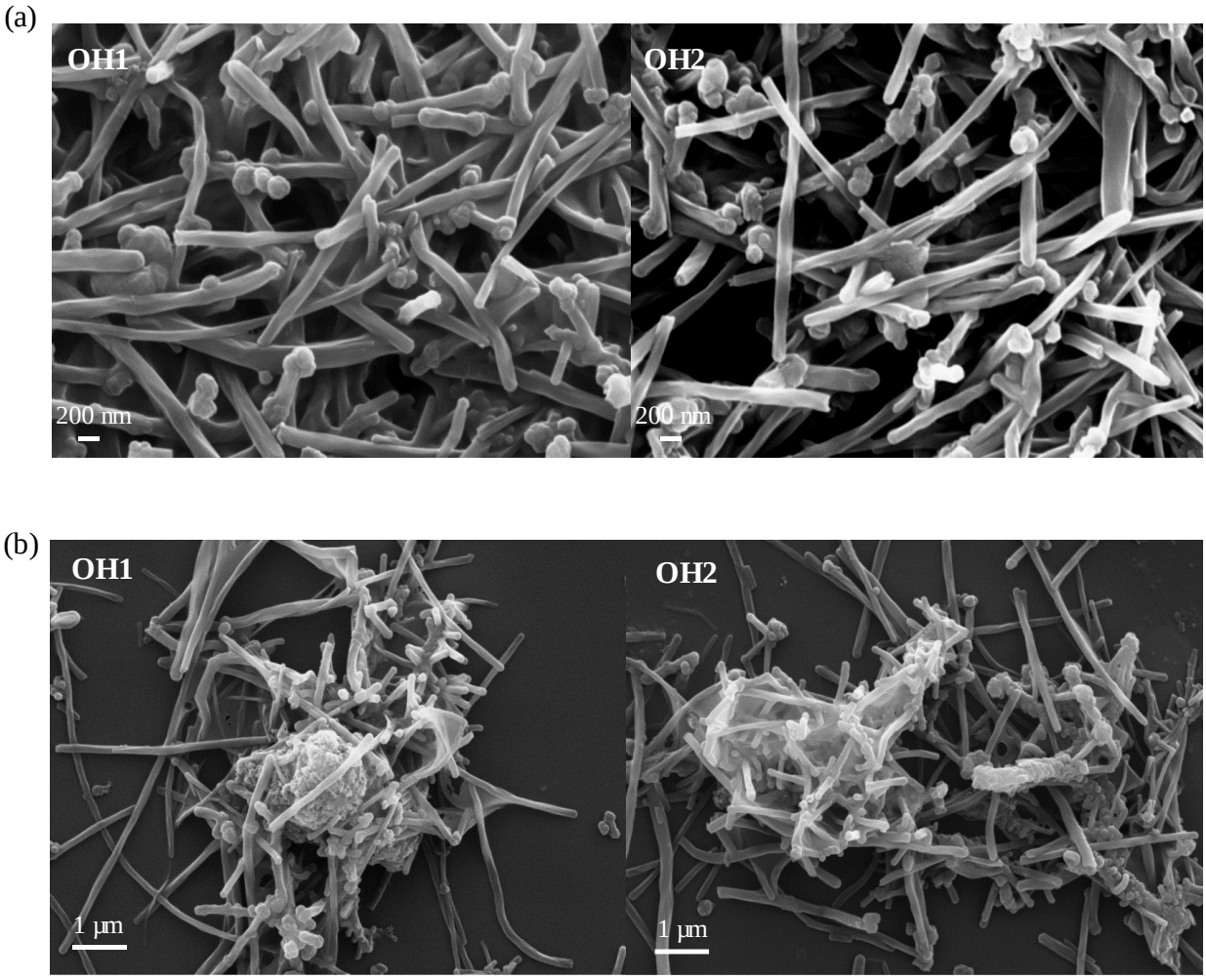

Fig. 3.9. SEM images of (a) 55 wt% MWCNT hybrids and (b) 75 wt% MWCNT hybrids.

There are prominent dissimilarities in the properties of OH1 and OH2 hybrids after $FeCl_3$ doping. The variation of σ, α, and PF with different wt% of MWCNT followed a similar trend for doped and undoped OH1 hybrids. The peak σ-value showed ~1.3x enhancement, but α remained almost unaltered. Contrastingly, there was a substantial enhancement in both σ and α values of OH2 hybrids post-doping. The peak σ exhibited up to ~5.45x increment (35.25 S/cm → 192.28 S/cm) after doping, and parallelly, α almost doubled from the undoped hybrids. Overall, a ~24x enhancement in the PF (1.76 $\mu W/m.K^2$ → 42.25 $\mu W/m.K^2$) could be obtained from a doped-OH2 hybrid. Typical reasons for such post-doping enhancements may include formations of charge-

transfer-complexes (CTC) that augments polaron/bipolaron transports in the system, shortening the π-stacking distance, structural changes, etc. [51]. The apparent shift in weak absorption band observed in the 400-500 nm range (Fig. 3.3b) could be attributed to the existence of polaron/bipolarons [52]. Moreover, reducing inter-chain distance post-doping (Fig. 3.4d) could overlap the π-electronic density of adjacent chains, creating a polaron/bipolaron network [53]. The formation of CTC and its interaction with the hybrids are detailed in the next section.

3.2.3. Doping mechanism of hybrid films

The XPS survey spectrum of the pristine polymers, hybrids, and doped hybrids indicates the characteristic C1s, O1s, and S2p peaks, shown in Fig. 3.10. Table 3.1 presents the obtained chemical composition of the surface region in atomic percent (atomic %). Fe2p and Cl2p in doped-OH2 are higher than OH1, indicating that stronger doping of $FeCl_3$ is achieved with the OH2 hybrid.

Table 3.1. Chemical composition in atomic %.

Sample	**C1s**	**O1s**	**S2p**	**Fe2p**	**Cl2p**
PBDTTT-C	83.53	10.06	6.41	0	0
OH1	90.68	4.66	4.66	0	0
Doped-OH1	89.45	5.52	4.11	0.5	0.41
PBDTTT-C-T	86.06	5.19	8.75	0	0
OH2	92.18	2.45	5.37	0	0
Doped-OH2	87.35	5.63	4.38	1.79	0.84

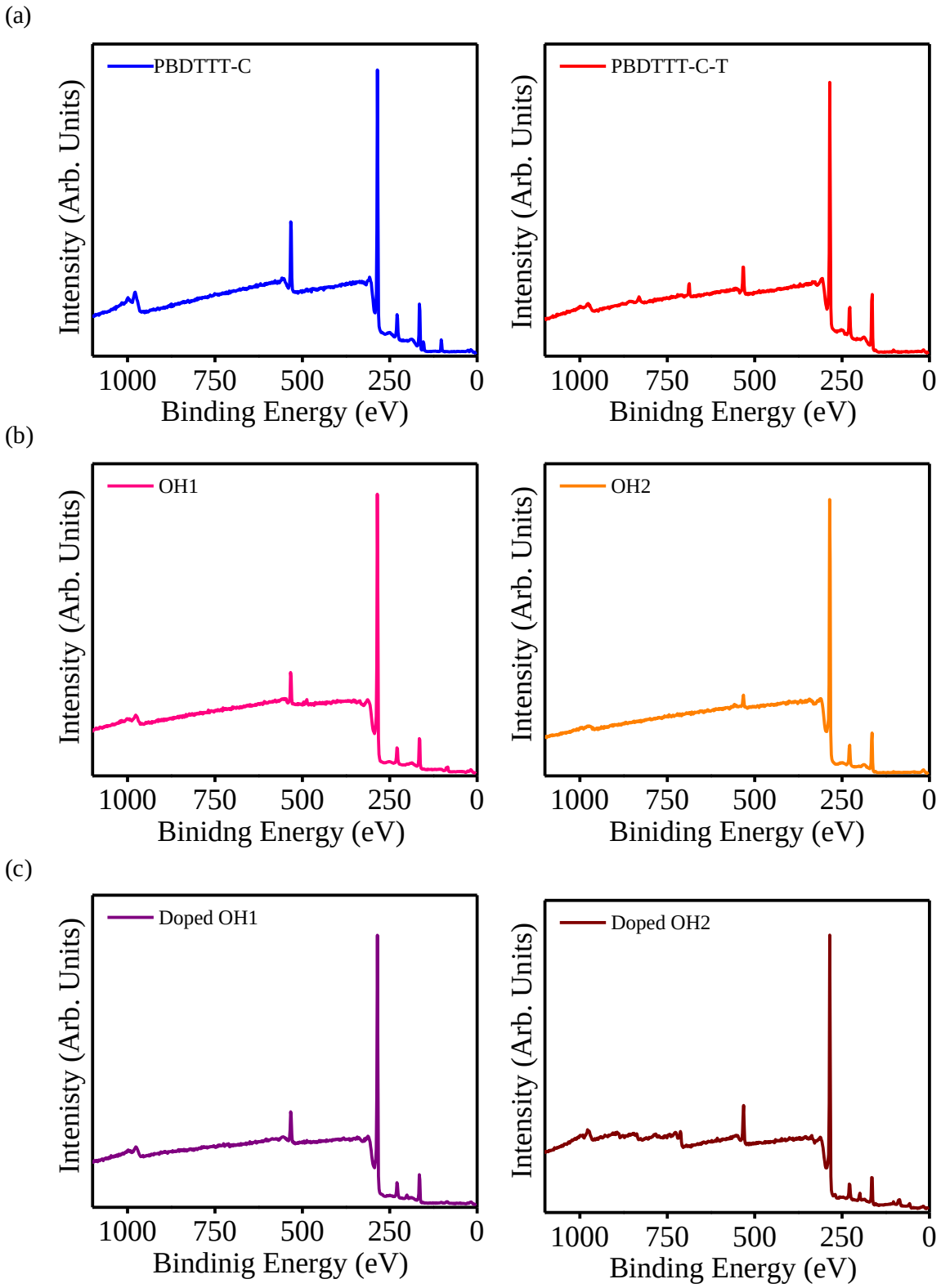

Fig. 3.10. XPS survey spectra of (a) pristine polymer; (b) organic hybrids and (c) doped hybrids.

The core-level O1s and S2p peaks (Fig. 3.11) of both polymers were shifted to higher binding energies (BE) with the addition of MWCNT due to the polymer-MWCNT interactions. As shown in Fig. 3.11a, the peaks in the OH1 hybrid shifted towards the higher BE after $FeCl_3$ doping. However, the peaks of doped-OH2 hybrids shift towards the lower BE side (Fig. 3.11b). The BE shift could be attributed to the relative electronegativity of the dopant compared to the base elements [54]. Post $FeCl_3$ doping, the electron density around the OH1 hybrid decreases while that around OH2 increases. Such variations lead to the Fermi energy repositioning, i.e., the Fermi energy moving away or close to the valance band maxima (VBM) [23,55]. The peak positions of high-resolution O1s and S2p spectra are listed in Table 3.2.

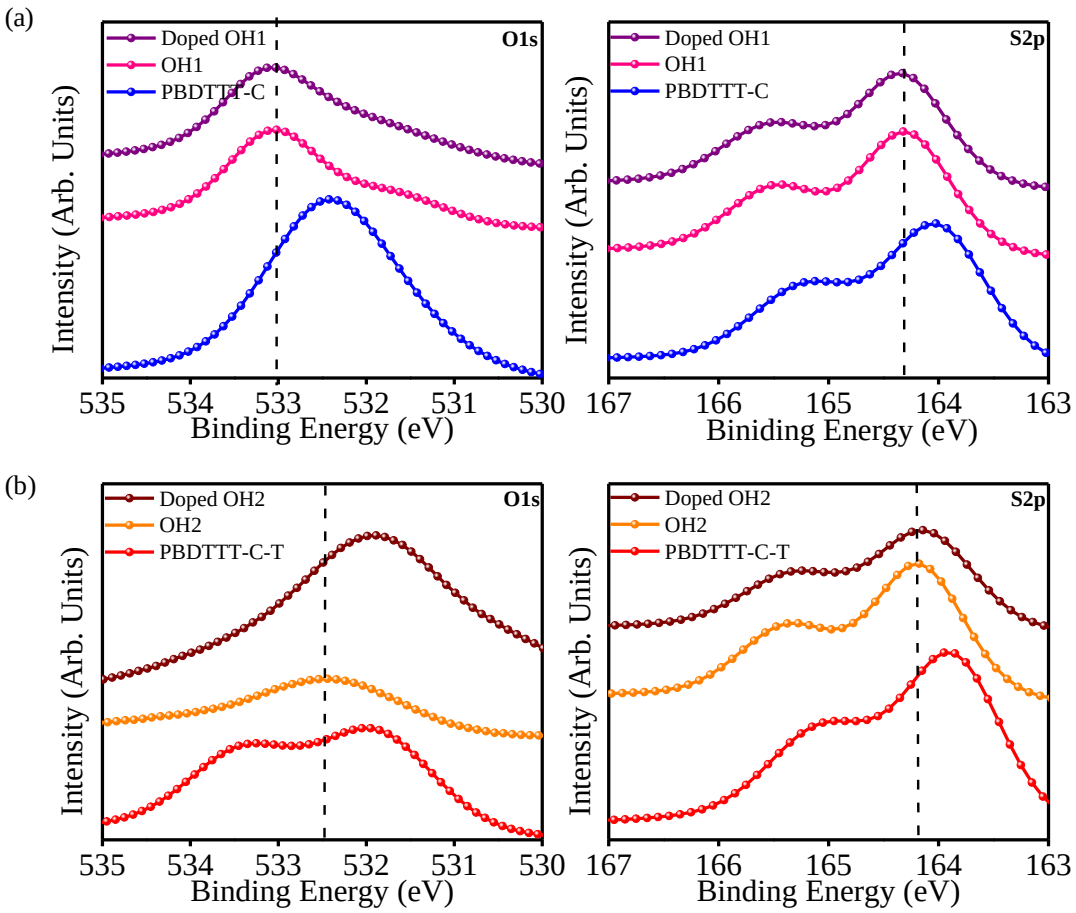

Fig. 3.11. XPS core-level spectra of (a) OH1 and (b) OH2 hybrids before and after doping.

Table 3.2. XPS peak positions of O1s and S2p core level spectra.

	PBDTTT-C	**OH1**	**Doped-OH1**	**PBDTTT-C-T**	**OH2**	**Doped-OH2**
O1s (eV)	532.41	533.02	533.13	532.03	532.48	531.88
S2p (eV)	164.02	164.31	164.36	163.91	164.21	164.14

The CTC formation was investigated by the high-resolution Fe2p and Cl2p core level spectra of doped-OH1 and OH2 hybrids. Fig. 3.12a shows that for the doped-OH1, the Fe2p region exhibits characteristic peaks of Fe2p3/2 and Fe2p1/2 with associated broad satellites at ~711.34 eV and ~725.46 eV. Graat *et al.* described that for iron oxide films, Fe^{3+} shows two distinguishing peaks at ~711.2 eV and ~724.3 eV attributed to Fe2p3/2 and Fe2p1/2, with corresponding satellites at ~719.5 eV and ~733.6 eV [56]. For the Fe^{2+} cation, the distinctive peaks are located at ~709.8 eV and ~722.8 eV, with satellites at ~716.4 eV and ~730.0 eV, respectively. Our experimental observations confirm the presence of Fe^{3+} cations, as evident from Fig. 3.12a. A close examination of the Cl2p spectrum provided further information on the CTC. As seen in Fig. 3.12b, the spectra consist of Cl2p3/2 spin-orbit doublets peaked at ~198.79 eV, and ~200.61 eV and Cl2p1/2 peaked at ~202.26 eV. The higher BE peak (200.61 eV) of Cl2p3/2 dominates with an area ratio of 2:3 that corresponds well to chlorine atoms covalently bonded to sp^2 carbon [57–59].

For doped-OH2, as shown in Fig. 3.12c, the Fe2p peaks are located at ~711.32 eV (Fe2p3/2) and ~725.36 eV (Fe2p1/2) with shakeup satellite peak offset by ~7.9 eV from the main Fe2p3/2 peak. Ferraro and co-workers reported from the study of $FeCl_3$-doped polymers of polyphenylacetylene that post-doping, the Fe2p3/2 core level peak appears at ~711.2 − 711.3 eV,

consistent with the value for Fe^{3+} ions found in reference compound $(Et_4N)FeCl_4$ salt [60]. The Fe^{3+} shakeup satellite energies are usually found at ~7 eV offset from the main 2p3/2 peak for $FeCl_3$ [61]. The observed satellite energy value for doped-OH2 remains close to that, supporting the presence of Fe^{3+} state. The Cl2p core level emission spectrum (Fig. 3.12d) doublet showed the highest intensity at ~ 198.71 eV, followed by a weaker ~200.30 eV peak. The more intense peak at the lower BE region of Cl2p3/2 doublet could be assigned to the presence of Cl^- ions, leading to the formation of the $FeCl_4^-$ complex [33,62,63].

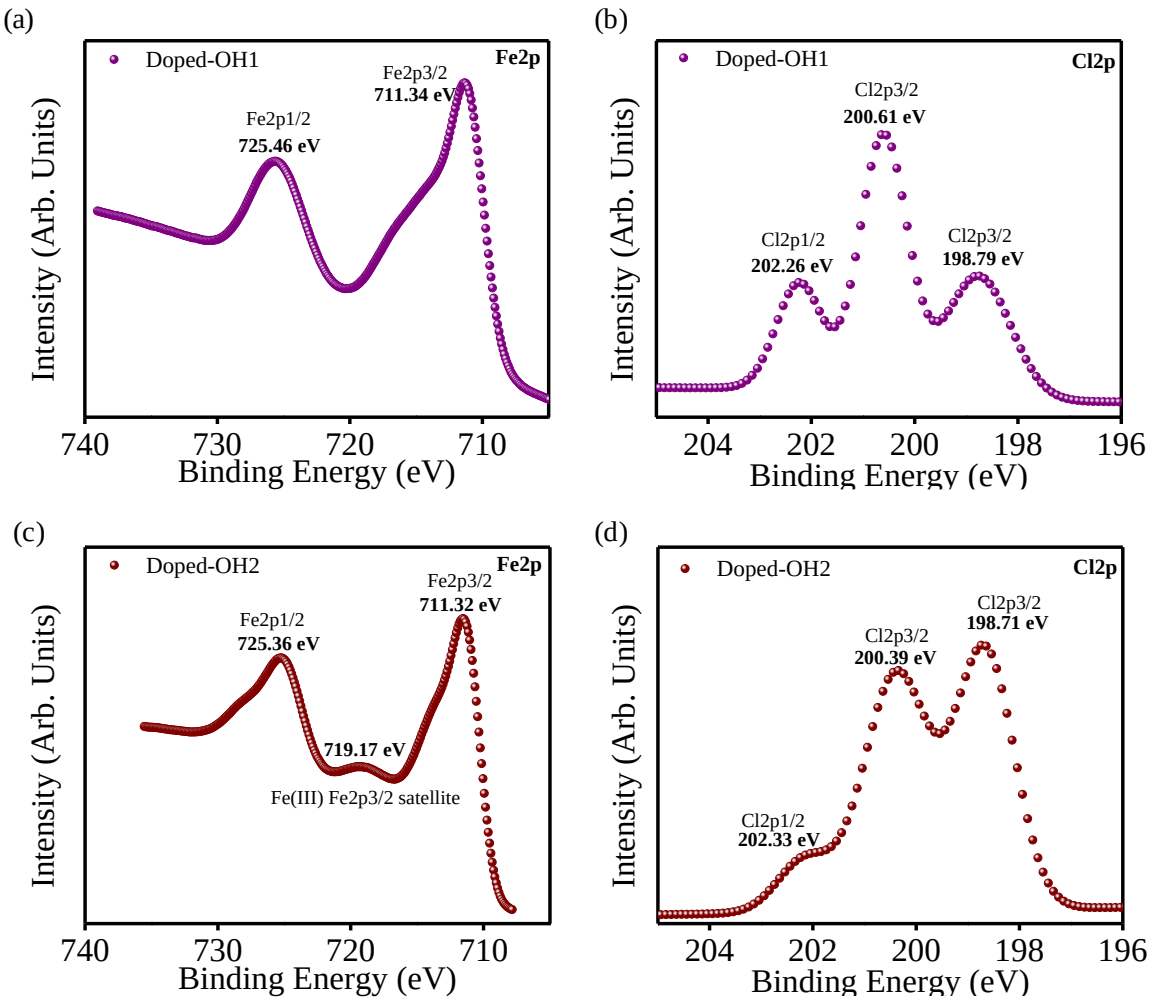

Fig. 3.12. (a) Fe2p and (b) Cl2p core level spectra of doped-OH1; (c) Fe2p and (d) Cl2p core level spectra of doped-OH2.

The XPS observation suggests that both hybrids possibly form Fe^{3+} species after doping, with OH1 forming a Cl-C bond and OH2 forming a Cl^- ion. It can be reasoned that the CTC created in two doped hybrids would attach at two different coordination sites. Further evidence of CTC formation could be obtained with a careful analysis of C1s and O1s spectra. Fig. 3.13a shows the high-resolution spectrum for C1s of PBDTTT-C. Four definite peaks were observed due to the different bonding environments of carbon atoms. The incorporation of MWCNT led to the formation of π-π^* bonds due to the sp^2 carbon atoms of MWCNT [64]. A similar peak appears in the OH2 hybrid and the other characteristic peaks of PBDTTT-C-T, as shown in Fig. 3.13d. However, in doped-OH1 (Fig. 3.13c), an additional C-Cl bond was observed at ~286.46 eV, confirming the presence of the CTC coordination site. The deconvoluted S2p XPS spectra of the pristine polymer, hybrids, and doped hybrids are shown in Fig. 3.14.

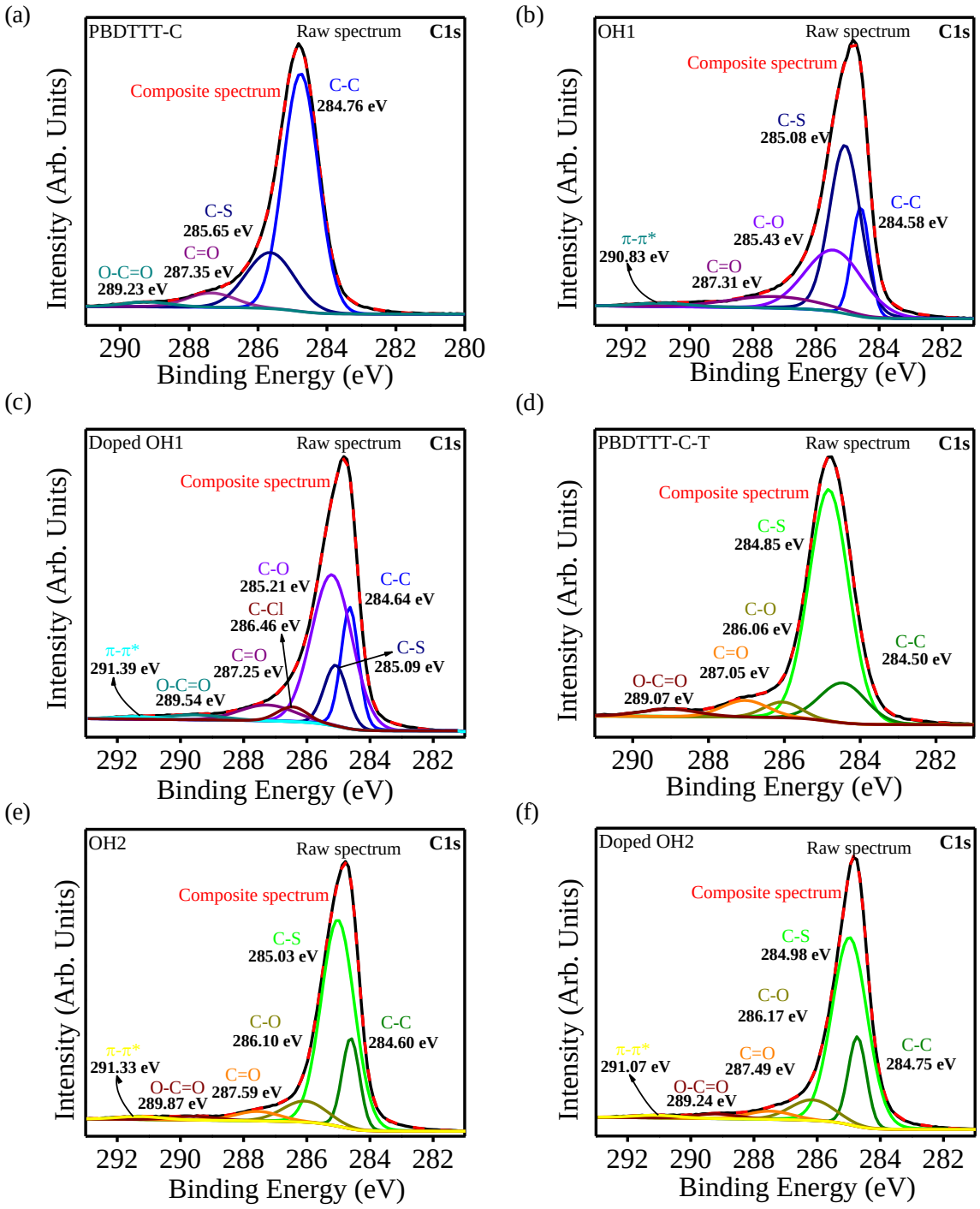

Fig. 3.13. C1s core level spectra of (a) PBDTTT-C; (b) OH1; (c) doped-OH1; (d) PBDTTT-C-T; (e) OH2 and (f) doped-OH2.

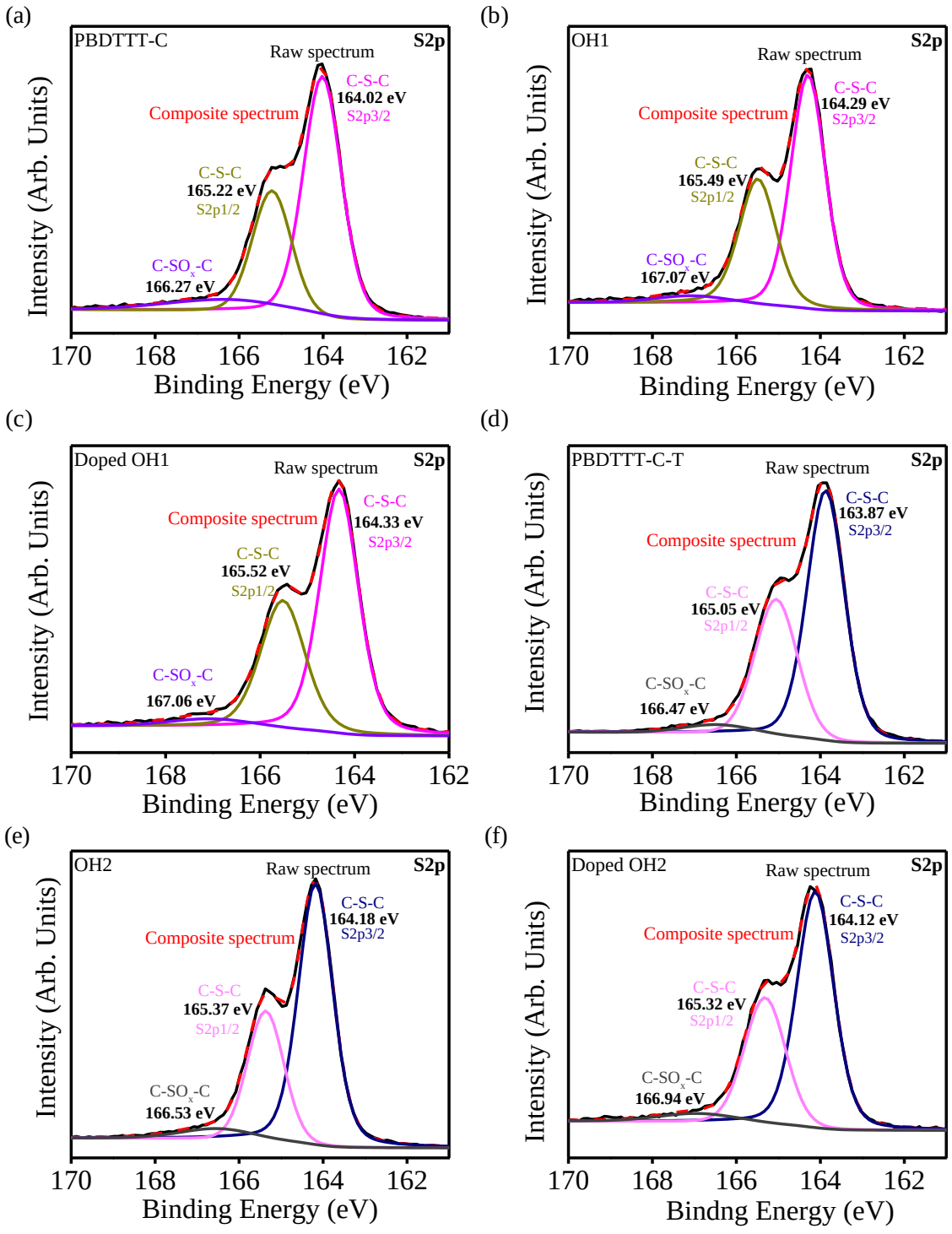

Fig. 3.14. Core level S2p XPS spectra of (a) PBDTTT-C; (b) OH1; (c) doped-OH1; (d) PBDTTT-C-T; (e) OH2 and (f) doped-OH2.

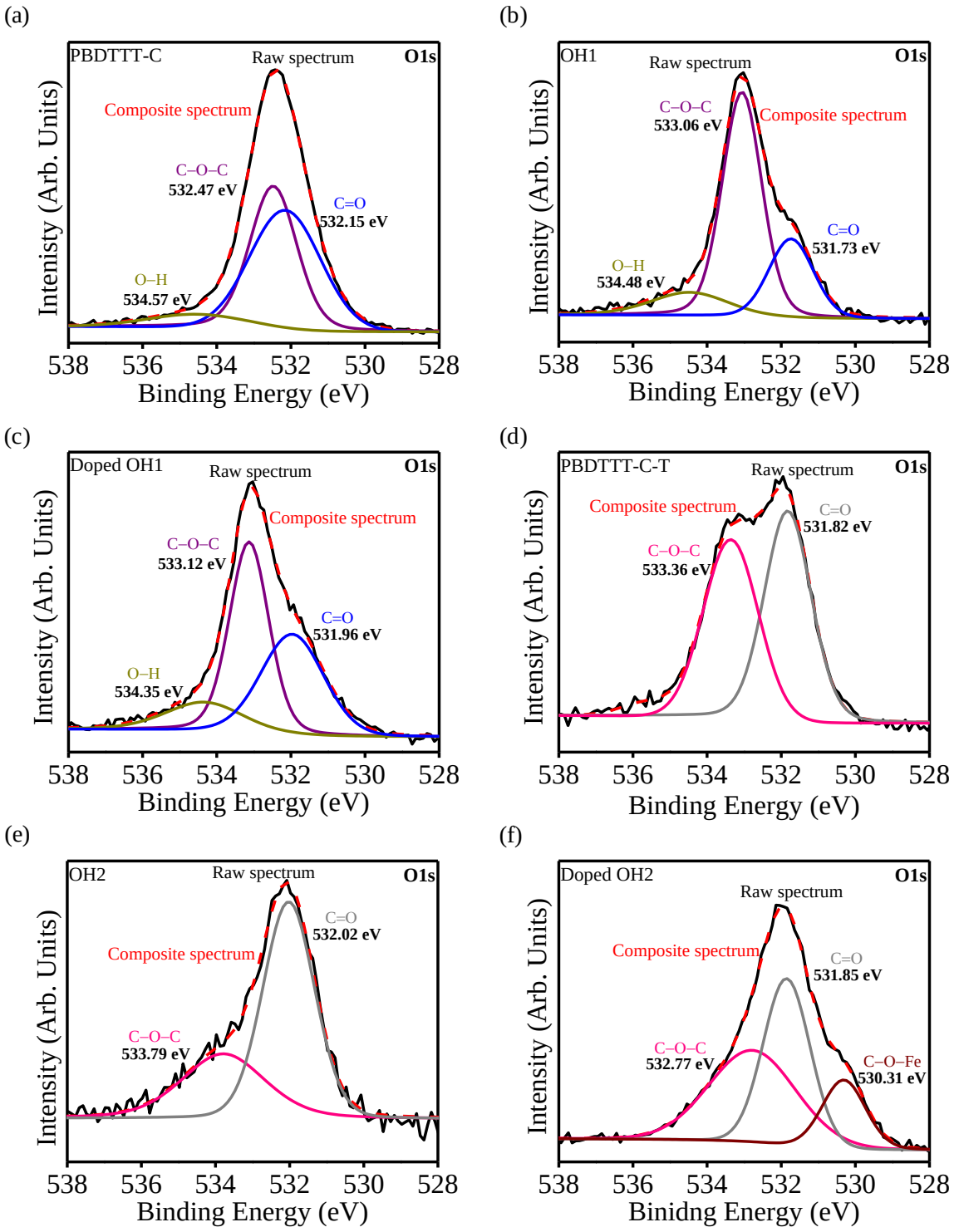

Fig. 3.15. O1s core level spectra of (a) PBDTTT-C; (b) OH1; (c) doped-OH1; (d) PBDTTT-C-T; (e) OH2 and (f) doped-OH2.

Fig. 3.15a, b & c shows the core level O1s spectra of the PBDTTT-C, OH1, and doped-OH, respectively. Each spectrum consists of three peaks corresponding to C=O, C-O-C, and O-H bonds, with BE shifts related to the hybrid formation and doping. The O1s spectra of the undoped (Fig. 3.15e) and doped-OH (Fig. 3.15f) show an additional peak at ~530.31 eV that may be ascribed to the C-O-Fe bond formation [65]. Therefore, it is reasonable to conclude that the CTC coordination sites in doped-OH2 differ from the doped-OH1.

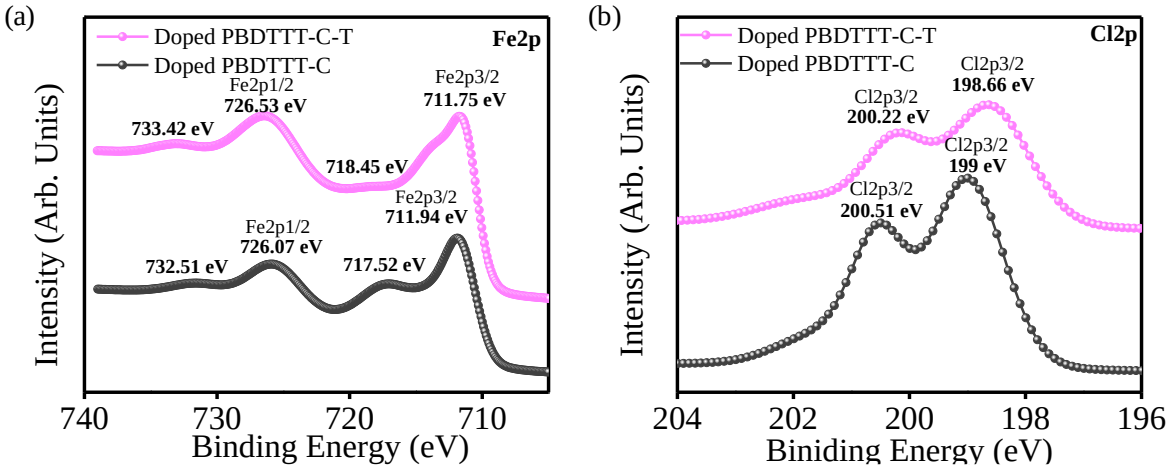

Fig. 3.16. Core level (a) Fe2p and (b) Cl2p XPS spectra.

The Fe2p and Cl2p spectra of the doped PBDTTT-C/PBDTTT-C-T are shown in Fig. 3.16. Both the polymers exhibited the presence of Fe^{3+} and Cl^- ions upon doping with $FeCl_3$. The deconvoluted high-resolution O1s spectra (Fig. 3.17) revealed the occurrence of C-O-Fe bonds in the doped-polymers, confirming $FeCl_4^-$ complex formation. This observation differs from the earlier results as the $FeCl_4^-$ complex was not observed in OH1, suggesting that the presence of MWCNT hinders the formation of coordination sites in PBDTTT-C. It is reasonable to state that the wrapping of π-conjugated polymers over the surface of the MWCNT differs and results in the availability of different coordination sites for doping in hybrids. Both polymers have identical

BDT backbone conjugated with TTE moiety but consist of different side-chain groups; PBDTTT-C has alkoxy, and PBDTTT-C-T has an alkylthiophene group.

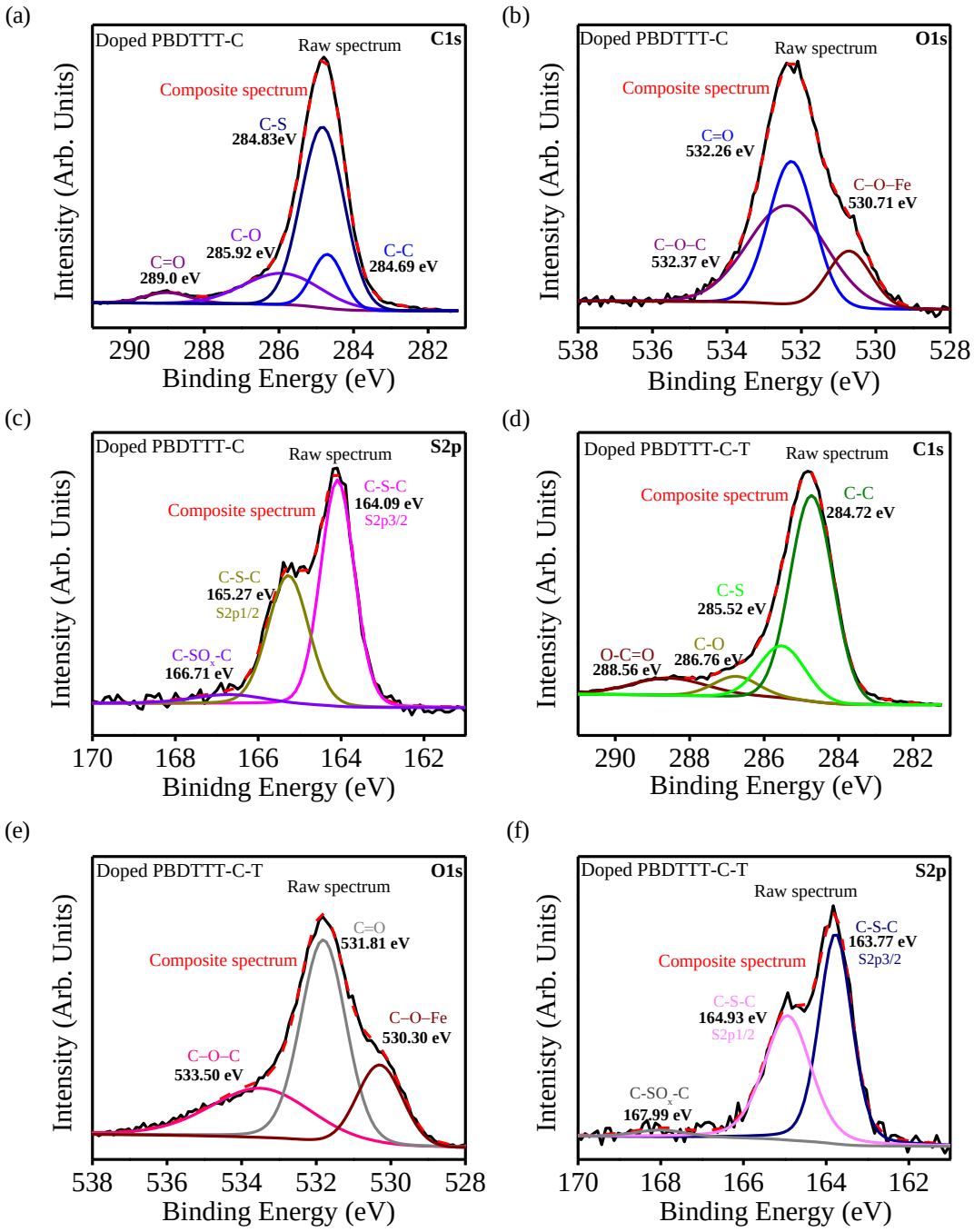

Fig. 3.17. Core level (a) C1s; (b) O1s; (c) S2p XPS spectra of doped PBDTTT-C and core level (d) C1s; (e) O1s; (f) S2p XPS spectra of doped PBDTTT-C-T.

It should be noted that the presence of =O in TTE moiety coordinates the formation of the C-O-Fe bond in doped polymers. During the hybrid formation, the presence of a more electron-rich alkylthiophene group in PBDTTT-C-T enhances the π-π interaction with the surface of MWCNT, providing the =O available for doping. On the other hand, the PBDTTT-C wraps around the surface of MWCNT to offer π-π interaction, resulting in a different coordination site for doping.

3.2.4. Fermi level repositioning

The UPS characterization of the hybrids revealed their relative positioning of the VBM and the work function (φ). The full range UPS plots in BE scale of the hybrids are given in Fig. 3.18a.

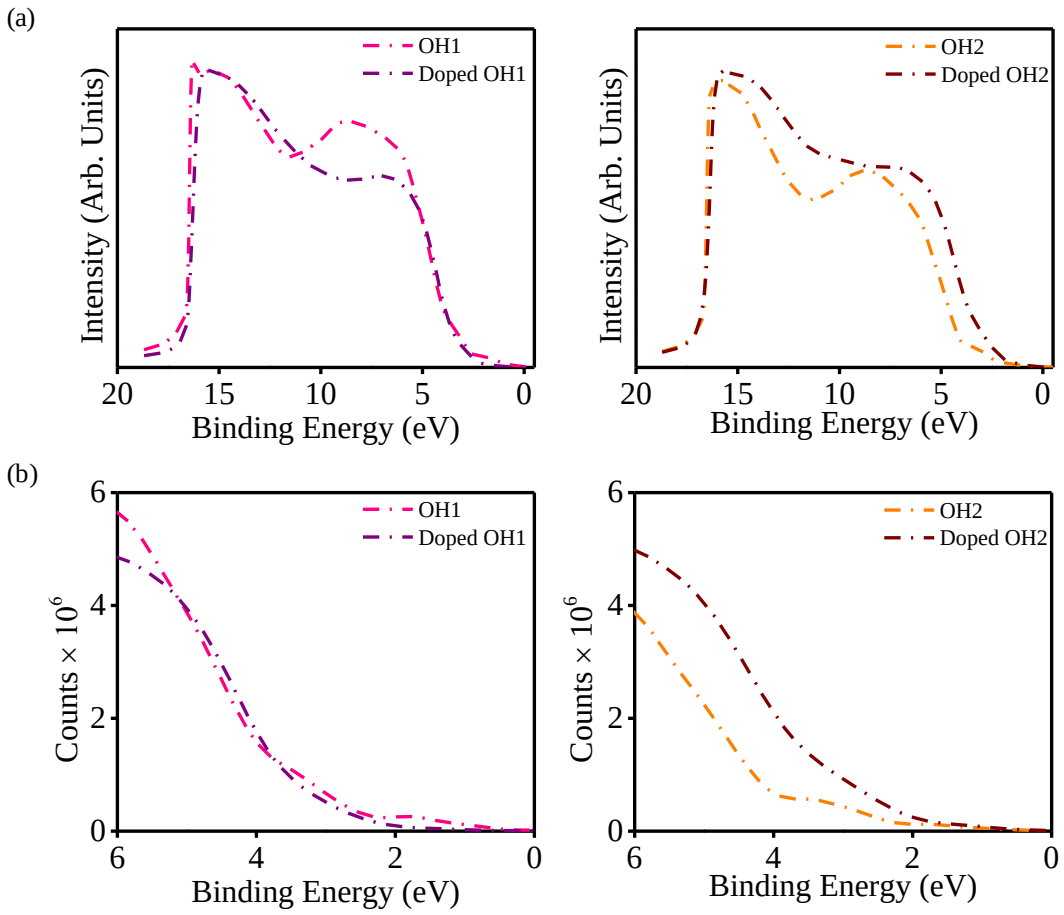

Fig. 3.18. (a) UPS valence band spectra (He I radiation) of OH1 and OH2 in pristine and doped conditions and (b) A magnified view of the low BE region showing the DOVS.

The φ is obtained from the secondary cut-off region, plotted in kinetic energy (KE) scale as shown in Fig. 3.19a. The VBM is estimated through the linear extrapolation of the low BE edge, as shown in Fig. 3.19b. The VBM position shifts to a higher BE for the doped-OH1, while in contrast, the doped-OH2 exhibited a lower BE. Also, φ of OH1 and OH2 is estimated to be 4.62 eV and 4.52 eV, respectively. After doping, φ shifted to 4.58 eV and 4.63 eV in OH1 and OH2. A schematic energy band diagram depicting these complementary behaviors of the two hybrids in consideration is shown in Fig. 3.19c.

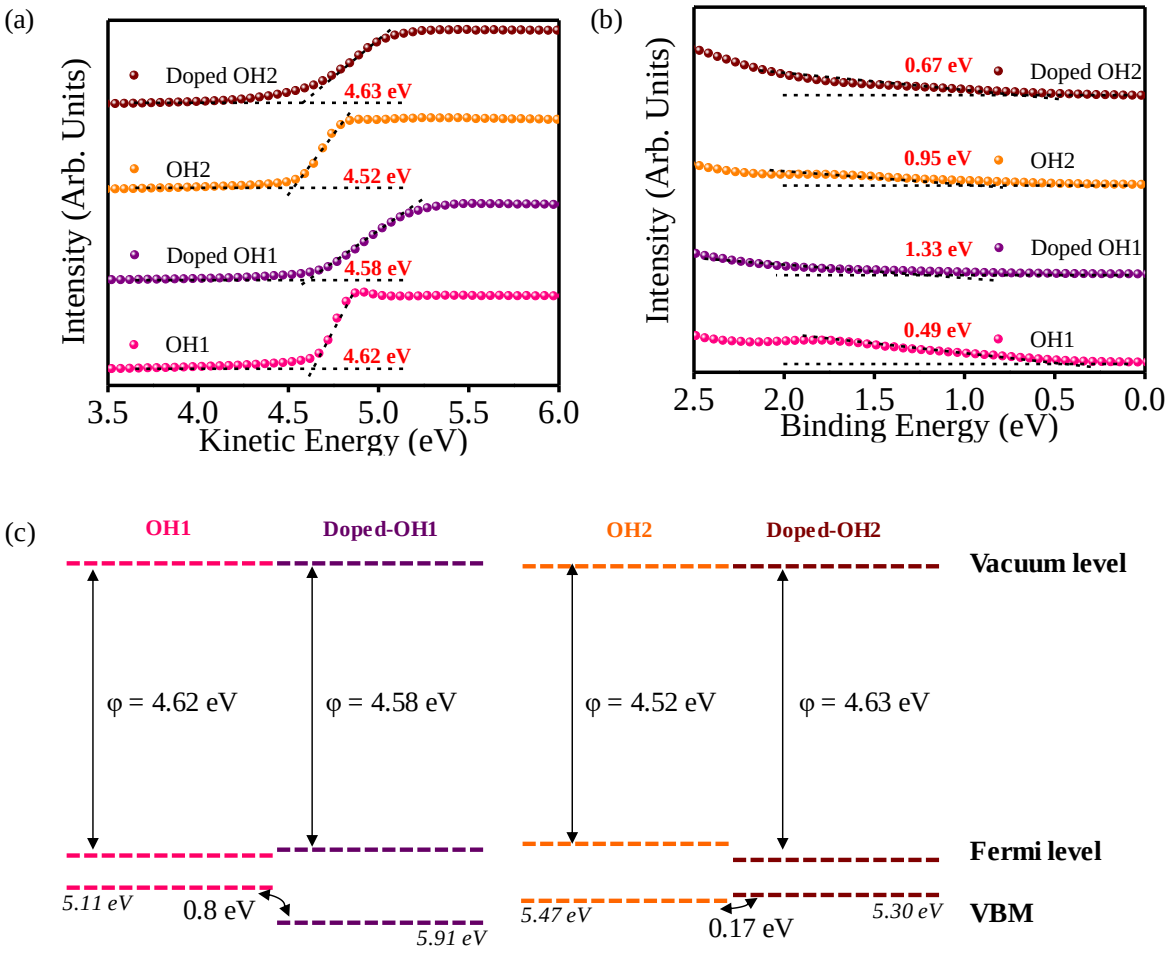

Fig. 3.19. UPS spectra of the (a) secondary cut-off region & (b) low BE region and (c) Energy band diagram of OH1 and OH2 hybrids before and after doping.

As per Mott's formula, the α can be considered as the contribution of a 'mobility' term and a 'density of states (DOS)' term, given by [23],

$$\alpha = \frac{\pi^2}{3}\frac{k_B^2 T}{e}\left(\frac{\partial \ln \mu}{\partial E} + \frac{\partial \ln N}{\partial E}\right)_{E_f} \quad (3.1)$$

where k_B, T, e, and μ are the Boltzmann constant, absolute temperature, electron charge, and carrier mobility, respectively. The latter term in equation 3.1, $N(E_f)$, relates to DOS and its slope at the Fermi level. The density of valence electronic states (DOVS) of doped OH1 and OH2 were investigated by UPS (Fig. 3.18b). For the doped-OH1, the apparent decoupling of σ and α (i.e., increasing σ without affecting α) is due to the slight upward shift of the Fermi level from VBM with the DOVS remaining close to the undoped hybrids. However, for doped-OH2, the Fermi level moved closer to the VBM, increasing σ considerably. At the same time, a steep rise in DOVS is responsible for the concurrent enhancement of α. The Table 3.3 shows the Hall measurement studies of the hybrid films before and after doping.

Table 3.3. Mobility and carrier concentration values of OH1 and OH2 (before and after doping) with 45 wt% of MWCNT.

Particulars	**OH1**	**Doped-OH1**	**OH2**	**Doped-OH2**
Bulk concentration (/cm^3)	1.57 E+20	2.56 E+20	3.66 E+20	3.01 E+20
Mobility (cm^2/Vs)	3.14 E-1	4.80 E-1	2.50 E-1	4.85 E-1

For OH1 hybrids, the carrier concentration and mobility increase after doping, thereby increasing σ. For doped-OH2 hybrids, there is a decrease in the carrier concentration due to post-doping carrier trap-state formation, which contributes to enhancing the α through Mott's relation given in equation 2.1 [66]. The increased mobility effectively compensates for the reduction in

carrier concentration due to the post-doping dielectric environment change in the composite (Table 3.3). The repositioning of the Fermi level and the enhanced mobility result in the independent rise of σ and α for doped-OH2.

3.3. Conclusion

In summary, two p-type organic hybrids, OH1 and OH2, were prepared using BDT-TTE based polymers PBDTTT-C and PBDTTT-C-T with MWCNT fillers. Both hybrids show a percolation threshold in σ value beyond 15 wt% of MWCNT incorporation, with the peak value at 45 wt%. After doping, a sharp increase in σ and α is observed for OH2 while OH1 exhibited an unaltered α with a minor rise in σ. Such post-doping enhancements are due to the formation of CTC that augments polaron/bipolaron transports in the system, shortening the π-stacking distance and inducing structural changes. The doping increased DOVS of the OH2 hybrid that led to the Fermi level shift towards the VBM. However, doping of OH1 exhibited the Fermi level shifting away from the VBM with an almost unchanged DOVS pattern. A detailed spectroscopic investigation revealed that the π-π interaction with the surface of MWCNT is strengthened by the more electron-rich alkylthiophene group in PBDTTT-C-T and =O is available for doping. In contrast, PBDTTT-C wraps around the surface of MWCNT to offer π-π interaction, resulting in a different coordination site for doping. These results highlight some salient features of the $FeCl_3$ doping mechanism for polymer/MWCNT hybrids that could be utilized for designing high-performing materials in the future.

References

[1] Z. Yuan, X. Tang, Z. Xu, J. Li, W. Chen, K. Liu, Y. Liu, Z. Zhang, Screen-printed radial structure micro radioisotope thermoelectric generator, Appl. Energy. 225 (2018) 746–754. https://doi.org/10.1016/j.apenergy.2018.05.073.

[2] K. Liu, Y. Liu, Z. Xu, Z. Zhang, Z. Yuan, X. Guo, Z. Jin, X. Tang, Experimental prototype and simulation optimization of micro-radial milliwatt-power radioisotope thermoelectric generator, Appl. Therm. Eng. 125 (2017) 425–431. https://doi.org/10.1016/j.applthermaleng.2017.07.022.

[3] S.A. Mostafavi, M. Mahmoudi, Modeling and fabricating a prototype of a thermoelectric generator system of heat energy recovery from hot exhaust gases and evaluating the effects of important system parameters, Appl. Therm. Eng. 132 (2018) 624–636. https://doi.org/10.1016/j.applthermaleng.2018.01.018.

[4] J. Yang, F.R. Stabler, Automotive Applications of Thermoelectric Materials, J. Electron. Mater. 38 (2009) 1245–1251. https://doi.org/10.1007/s11664-009-0680-z.

[5] S. Qing, A. Rezania, L.A. Rosendahl, A.A. Enkeshafi, X. Gou, Characteristics and parametric analysis of a novel flexible ink-based thermoelectric generator for human body sensor, Energy Convers. Manag. 156 (2018) 655–665. https://doi.org/10.1016/j.enconman.2017.11.065.

[6] Y.-W. Chen, C.-C. Wu, C.-C. Hsu, C.-L. Dai, Fabrication and Testing of Thermoelectric CMOS-MEMS Microgenerators with CNCs Film, Appl. Sci. 8 (2018) 1047. https://doi.org/10.3390/app8071047.

[7] M. Thielen, L. Sigrist, M. Magno, C. Hierold, L. Benini, Human body heat for powering wearable devices: From thermal energy to application, Energy Convers. Manag. 131 (2017) 44–54. https://doi.org/10.1016/j.enconman.2016.11.005.

[8] A. Amar, A. Kouki, H. Cao, Power Approaches for Implantable Medical Devices, Sensors. 15 (2015) 28889–28914. https://doi.org/10.3390/s151128889.

[9] A. Proto, L. Peter, M. Cerny, M. Penhaker, D. Bibbo, S. Conforto, M. Schmid, Human Body Energy Harvesting Solutions for Wearable Technologies, in: 2018 IEEE 20th Int. Conf. e-Health Networking, Appl. Serv., IEEE, 2018: pp. 1–5. https://doi.org/10.1109/HealthCom.2018.8531189.

[10] M. Guan, K. Wang, D. Xu, W.-H. Liao, Design and experimental investigation of a low-voltage thermoelectric energy harvesting system for wireless sensor nodes, Energy Convers. Manag. 138 (2017) 30–37. https://doi.org/10.1016/j.enconman.2017.01.049.

[11] B. Iezzi, K. Ankireddy, J. Twiddy, M.D. Losego, J.S. Jur, Printed, metallic thermoelectric generators integrated with pipe insulation for powering wireless sensors, Appl. Energy. 208 (2017) 758–765. https://doi.org/10.1016/j.apenergy.2017.09.073.

[12] X. Li, C. Xie, S. Quan, L. Huang, W. Fang, Energy management strategy of thermoelectric generation for localized air conditioners in commercial vehicles based on 48 V electrical system, Appl. Energy. 231 (2018) 887–900. https://doi.org/10.1016/j.apenergy.2018.09.162.

[13] X. Li, Z. Zhong, J. Luo, Z. Wang, W. Yuan, G. Zhang, C. Yang, C. Yang, Experimental Investigation on a Thermoelectric Cooler for Thermal Management of a Lithium-Ion

Battery Module, Int. J. Photoenergy. 2019 (2019) 1–10. https://doi.org/10.1155/2019/3725364.

[14] C. Bounioux, P. Díaz-Chao, M. Campoy-Quiles, M.S. Martín-González, A.R. Goñi, R. Yerushalmi-Rozen, C. Müller, Thermoelectric composites of poly(3-hexylthiophene) and carbon nanotubes with a large power factor, Energy Environ. Sci. 6 (2013) 918–925. https://doi.org/10.1039/c2ee23406h.

[15] M. Wahbah, M. Alhawari, B. Mohammad, H. Saleh, M. Ismail, Characterization of Human Body-Based Thermal and Vibration Energy Harvesting for Wearable Devices, IEEE J. Emerg. Sel. Top. Circuits Syst. 4 (2014) 354–363. https://doi.org/10.1109/JETCAS.2014.2337195.

[16] M. Lindorf, K.A. Mazzio, J. Pflaum, K. Nielsch, W. Brütting, M. Albrecht, Organic-based thermoelectrics, J. Mater. Chem. A. 8 (2020) 7495–7507. https://doi.org/10.1039/C9TA11717B.

[17] H. Jin, J. Li, J. Iocozzia, X. Zeng, P.-C. Wei, C. Yang, N. Li, Z. Liu, J.H. He, T. Zhu, J. Wang, Z. Lin, S. Wang, Hybrid Organic–Inorganic Thermoelectric Materials and Devices, Angew. Chemie Int. Ed. 58 (2019) 15206–15226. https://doi.org/10.1002/anie.201901106.

[18] R. Tian, C. Wan, Y. Wang, Q. Wei, T. Ishida, A. Yamamoto, A. Tsuruta, W. Shin, S. Li, K. Koumoto, A solution-processed TiS2/organic hybrid superlattice film towards flexible thermoelectric devices, J. Mater. Chem. A. 5 (2017) 564–570. https://doi.org/10.1039/c6ta08838d.

[19] H.J. Lee, G. Anoop, H.J. Lee, C. Kim, J.W. Park, J. Choi, H. Kim, Y.J. Kim, E. Lee, S.G. Lee, Y.M. Kim, J.H. Lee, J.Y. Jo, Enhanced thermoelectric performance of

PEDOT:PSS/PANI-CSA polymer multilayer structures, Energy Environ. Sci. 9 (2016) 2806–2811. https://doi.org/10.1039/c5ee03063c.

[20] C. Pan, L. Wang, T. Liu, X. Zhou, T. Wan, S. Wang, Z. Chen, C. Gao, L. Wang, Polar Side Chain Effects on the Thermoelectric Properties of Benzo[1,2-b:4,5-b′]Dithiophene-Based Conjugated Polymers, Macromol. Rapid Commun. 40 (2019) 1–9. https://doi.org/10.1002/marc.201900082.

[21] L. Wang, C. Pan, Z. Chen, W. Zhou, C. Gao, L. Wang, Enhanced Thermoelectric Performance of Conjugated Polymer/Single-Walled Carbon Nanotube Composites with Strong Stacking, ACS Appl. Energy Mater. 1 (2018) 5075–5082. https://doi.org/10.1021/acsaem.8b01126.

[22] L. Wang, C. Pan, A. Liang, X. Zhou, W. Zhou, T. Wan, L. Wang, The effect of the backbone structure on the thermoelectric properties of donor-acceptor conjugated polymers, Polym. Chem. 8 (2017) 4644–4650. https://doi.org/10.1039/c7py01005b.

[23] X. Zhou, C. Pan, C. Gao, A. Shinohara, X. Yin, L. Wang, Y. Li, Q. Jiang, C. Yang, L. Wang, Thermoelectrics of two-dimensional conjugated benzodithiophene-based polymers: density-of-states enhancement and semi-metallic behavior, J. Mater. Chem. A. 7 (2019) 10422–10430. https://doi.org/10.1039/C9TA01437C.

[24] M. Tonga, L. Wei, P.S. Taylor, E. Wilusz, L. Korugic-Karasz, F.E. Karasz, P.M. Lahti, Thermoelectric Enhancement by Compositing Carbon Nanotubes into Iodine-Doped Poly[2-methoxy-5-(2-ethylhexyloxy)-1,4-phenylenevinylene], ACS Appl. Mater. Interfaces. 9 (2017) 8975–8984. https://doi.org/10.1021/acsami.6b14695.

[25] J. Kim, S. Park, S. Lee, H. Ahn, S. Joe, B.J. Kim, H.J. Son, Low-Temperature Processable High-Performance D-A-Type Random Copolymers for Nonfullerene Polymer Solar Cells and Application to Flexible Devices, Adv. Energy Mater. 8 (2018) 1801601. https://doi.org/10.1002/aenm.201801601.

[26] L. Meng, Y. Zhang, X. Wan, C. Li, X. Zhang, Y. Wang, X. Ke, Z. Xiao, L. Ding, R. Xia, H.-L. Yip, Y. Cao, Y. Chen, Organic and solution-processed tandem solar cells with 17.3% efficiency, Science (80-.). 361 (2018) 1094–1098. https://doi.org/10.1126/science.aat2612.

[27] H. Luo, C. Yu, Z. Liu, G. Zhang, H. Geng, Y. Yi, K. Broch, Y. Hu, A. Sadhanala, L. Jiang, P. Qi, Z. Cai, H. Sirringhaus, D. Zhang, Remarkable enhancement of charge carrier mobility of conjugated polymer field-effect transistors upon incorporating an ionic additive, Sci. Adv. 2 (2016) e1600076. https://doi.org/10.1126/sciadv.1600076.

[28] L. Huo, X. Guo, S. Zhang, Y. Li, J. Hou, PBDTTTZ: A broad band gap conjugated polymer with high photovoltaic performance in polymer solar cells, Macromolecules. 44 (2011) 4035–4037. https://doi.org/10.1021/ma200743b.

[29] H. Luo, C. Yu, Z. Liu, G. Zhang, H. Geng, Y. Yi, K. Broch, Y. Hu, A. Sadhanala, L. Jiang, P. Qi, Z. Cai, H. Sirringhaus, D. Zhang, Remarkable enhancement of charge carrier mobility of conjugated polymer field-effect transistors upon incorporating an ionic additive, Sci. Adv. 2 (2016). https://doi.org/10.1126/sciadv.1600076.

[30] P. Adhikary, S. Venkatesan, N. Adhikari, P.P. Maharjan, O. Adebanjo, J. Chen, Q. Qiao, Enhanced charge transport and photovoltaic performance of PBDTTT-C-T/PC70BM solar cells via UV–ozone treatment, Nanoscale. 5 (2013) 10007.

https://doi.org/10.1039/c3nr03355d.

[31] A. Zusan, B. Gieseking, M. Zerson, V. Dyakonov, R. Magerle, C. Deibel, The Effect of Diiodooctane on the Charge Carrier Generation in Organic Solar Cells Based on the Copolymer PBDTTT-C, Sci. Rep. 5 (2015) 8286. https://doi.org/10.1038/srep08286.

[32] Y.J. Kim, W. Jang, D.H. Wang, C.E. Park, Structure–Property Correlation: A Comparison of Charge Carrier Kinetics and Recombination Dynamics in All-Polymer Solar Cells, J. Phys. Chem. C. 119 (2015) 26311–26318. https://doi.org/10.1021/acs.jpcc.5b08367.

[33] V. Ignatious, N. Raveendran, A. Prabhakaran, Y. Tanjore Puli, V. Chakkooth, B. Deb, MWCNT/Thienothiophene based All-Organic thermoelectric composites: Enhanced performance by realigning of the Fermi level through doping, Chem. Eng. J. 409 (2021) 128294. https://doi.org/10.1016/j.cej.2020.128294.

[34] A.W. Musumeci, G.G. Silva, J.-W. Liu, W.N. Martens, E.R. Waclawik, Structure and conductivity of multi-walled carbon nanotube/poly(3-hexylthiophene) composite films, Polymer (Guildf). 48 (2007) 1667–1678. https://doi.org/10.1016/j.polymer.2007.01.027.

[35] A. Ajayaghosh, Donor–acceptor type low band gap polymers: polysquaraines and related systems, Chem. Soc. Rev. 32 (2003) 181–191. https://doi.org/10.1039/B204251G.

[36] J.-L. Brédas, D. Beljonne, V. Coropceanu, J. Cornil, Charge-Transfer and Energy-Transfer Processes in π-Conjugated Oligomers and Polymers: A Molecular Picture, Chem. Rev. 104 (2004) 4971–5004. https://doi.org/10.1021/cr040084k.

[37] Z. Ma, W. Sun, S. Himmelberger, K. Vandewal, Z. Tang, J. Bergqvist, A. Salleo, J.W. Andreasen, O. Inganäs, M.R. Andersson, C. Müller, F. Zhang, E. Wang, Structure–

property relationships of oligothiophene–isoindigo polymers for efficient bulk-heterojunction solar cells, Energy Environ. Sci. 7 (2014) 361–369. https://doi.org/10.1039/C3EE42989J.

[38] E. Cohen, H. Dodiuk, A. Ophir, S. Kenig, C. Barry, J. Mead, Evidences for π-interactions between pyridine modified copolymer and carbon nanotubes and its role as a compatibilizer in poly(methyl methacrylate) composites, Compos. Sci. Technol. 79 (2013) 133–139. https://doi.org/10.1016/j.compscitech.2013.02.012.

[39] A. Ikeda, K. Nobusawa, T. Hamano, J. Kikuchi, Single-Walled Carbon Nanotubes Template the One-Dimensional Ordering of a Polythiophene Derivative, Org. Lett. 8 (2006) 5489–5492. https://doi.org/10.1021/ol062187q.

[40] B.K. Kuila, S. Malik, S.K. Batabyal, A.K. Nandi, In-Situ Synthesis of Soluble Poly(3-hexylthiophene)/Multiwalled Carbon Nanotube Composite: Morphology, Structure, and Conductivity, Macromolecules. 40 (2007) 278–287. https://doi.org/10.1021/ma061548e.

[41] D.W. Steuerman, A. Star, R. Narizzano, H. Choi, R.S. Ries, C. Nicolini, J.F. Stoddart, J.R. Heath, Interactions between Conjugated Polymers and Single-Walled Carbon Nanotubes, J. Phys. Chem. B. 106 (2002) 3124–3130. https://doi.org/10.1021/jp014326l.

[42] P. Rathore, C.M.S. Negi, A. Yadav, A.S. Verma, S.K. Gupta, Influence of MWCNT doping on performance of polymer bulk heterojunction based devices, Optik (Stuttg). 160 (2018) 131–137. https://doi.org/10.1016/j.ijleo.2018.01.092.

[43] S. Sahare, N. Veldurthi, S. Datar, T. Bhave, Photon assisted conducting atomic force microscopy study of nanostructured additives in P3HT:PCBM, RSC Adv. 5 (2015) 102795–102802. https://doi.org/10.1039/c5ra20266c.

[44] W. Li, B. Guo, C. Chang, X. Guo, M. Zhang, Y. Li, Efficient polymer solar cells based on a copolymer of meta-alkoxy-phenyl-substituted benzodithiophene and thieno[3,4-b]thiophene, J. Mater. Chem. A. 4 (2016) 10135–10141. https://doi.org/10.1039/C6TA04030F.

[45] L. Hrostea, L. Leontie, M. Dobromir, C. Doroftei, M. Girtan, On the electrical and optical properties stability of P3HT thin films sensitized with nitromethane ferric chloride solutions, Coatings. 10 (2020) 1–8. https://doi.org/10.3390/coatings10111072.

[46] Y.S. Kim, D. Kim, K.J. Martin, C. Yu, J.C. Grunlan, Influence of Stabilizer Concentration on Transport Behavior and Thermopower of CNT-Filled Latex-Based Composites, Macromol. Mater. Eng. 295 (2010) 431–436. https://doi.org/10.1002/mame.200900243.

[47] Y. Choi, Y. Kim, S.-G. Park, Y.-G. Kim, B.J. Sung, S.-Y. Jang, W. Kim, Effect of the carbon nanotube type on the thermoelectric properties of CNT/Nafion nanocomposites, Org. Electron. 12 (2011) 2120–2125. https://doi.org/10.1016/j.orgel.2011.08.025.

[48] C. Meng, C. Liu, S. Fan, A promising approach to enhanced thermoelectric properties using carbon nanotube networks, Adv. Mater. 22 (2010) 535–539. https://doi.org/10.1002/adma.200902221.

[49] D. Kim, Y. Kim, K. Choi, J.C. Grunlan, C. Yu, Improved Thermoelectric Behavior of Nanotube-Filled Polymer Composites with Poly(3,4-ethylenedioxythiophene) Poly(styrenesulfonate), ACS Nano. 4 (2010) 513–523. https://doi.org/10.1021/nn9013577.

[50] C. Yu, K. Choi, L. Yin, J.C. Grunlan, Light-Weight Flexible Carbon Nanotube Based Organic Composites with Large Thermoelectric Power Factors, ACS Nano. 5 (2011)

7885–7892. https://doi.org/10.1021/nn202868a.

[51] E. Bilotti, O. Fenwick, B.C. Schroeder, M. Baxendale, P. Taroni-Junior, T. Degousée, Z. Liu, 6.14 Organic Thermoelectric Composites Materials, in: Compr. Compos. Mater. II, Elsevier, 2018: pp. 408–430. https://doi.org/10.1016/B978-0-12-803581-8.10024-4.

[52] T.R. Naveen Kumar, P. Karthik, B. Neppolian, Polaron and bipolaron induced charge carrier transportation for enhanced photocatalytic H 2 production, Nanoscale. 12 (2020) 14213–14221. https://doi.org/10.1039/D0NR02950E.

[53] O. Bubnova, Z.U. Khan, H. Wang, S. Braun, D.R. Evans, M. Fabretto, P. Hojati-Talemi, D. Dagnelund, J.-B. Arlin, Y.H. Geerts, S. Desbief, D.W. Breiby, J.W. Andreasen, R. Lazzaroni, W.M. Chen, I. Zozoulenko, M. Fahlman, P.J. Murphy, M. Berggren, X. Crispin, Semi-metallic polymers, Nat. Mater. 13 (2014) 190–194. https://doi.org/10.1038/nmat3824.

[54] P.S. Bagus, F. Illas, G. Pacchioni, F. Parmigiani, Mechanisms responsible for chemical shifts of core-level binding energies and their relationship to chemical bonding, J. Electron Spectros. Relat. Phenomena. 100 (1999) 215–236. https://doi.org/10.1016/S0368-2048(99)00048-1.

[55] Y. Zou, D. Huang, Q. Meng, C. an Di, D. Zhu, Correlation between Seebeck coefficient and transport energy level in poly(3-hexylthiophene), Org. Electron. 56 (2018) 125–128. https://doi.org/10.1016/j.orgel.2018.02.008.

[56] P.C.J. Graat, M.A.J. Somers, Simultaneous determination of composition and thickness of thin iron-oxide films from XPS Fe 2p spectra, Appl. Surf. Sci. 100–101 (1996) 36–40. https://doi.org/10.1016/0169-4332(96)00252-8.

[57] S. Yuan, J. Gu, Y. Zheng, W. Jiang, B. Liang, S.O. Pehkonen, Purification of phenol-contaminated water by adsorption with quaternized poly(dimethylaminopropyl methacrylamide)-grafted PVBC microspheres, J. Mater. Chem. A. 3 (2015) 4620–4636. https://doi.org/10.1039/c4ta06363e.

[58] E. Papirer, R. Lacroix, J.-B. Donnet, Chemical modifications and surface properties of carbon blacks, Carbon N. Y. 34 (1996) 1521–1529. https://doi.org/10.1016/S0008-6223(96)00103-0.

[59] A.F. Pérez-Cadenas, F.J. Maldonado-Hódar, C. Moreno-Castilla, On the nature of surface acid sites of chlorinated activated carbons, Carbon N. Y. 41 (2003) 473–478. https://doi.org/10.1016/S0008-6223(02)00353-6.

[60] A. Furlani, M. V. Russo, G. Polzonetti, K. Martin, H.H. Wang, J.R. Ferraro, Spectroscopic Studies of FeCl 3 -Doped Polymers of Polyphenylacetylene, Appl. Spectrosc. 44 (1990) 331–334. https://doi.org/10.1366/0003702904085688.

[61] B.W. Veal, A.P. Paulikas, Final-state screening and chemical shifts in photoelectron spectroscopy, Phys. Rev. B. 31 (1985) 5399–5416. https://doi.org/10.1103/PhysRevB.31.5399.

[62] H. Piao, K. Adib, M.A. Barteau, A temperature-programmed X-ray photoelectron spectroscopy (TPXPS) study of chlorine adsorption and diffusion on Ag(111), Surf. Sci. 557 (2004) 13–20. https://doi.org/10.1016/j.susc.2004.03.063.

[63] I. Pełech, U. Narkiewicz, D. Moszyński, R. Pełech, Simultaneous purification and functionalization of carbon nanotubes using chlorination, J. Mater. Res. 27 (2012) 2368–

2374. https://doi.org/10.1557/jmr.2012.243.

[64] D. Puentes-Camacho, E.F. Velázquez, D.E. Rodríguez-Félix, M. Castillo-Ortega, R.R. Sotelo-Mundo, T. del Castillo-Castro, Functionalization of multiwalled carbon nanotubes by microwave irradiation for lysozyme attachment: comparison of covalent and adsorption methods by kinetics of thermal inactivation, Adv. Nat. Sci. Nanosci. Nanotechnol. 8 (2017) 045011. https://doi.org/10.1088/2043-6254/aa8b3c.

[65] Y. Pang, K. Luo, L. Tang, X. Li, Y. Song, C. Li, L. Wang, Preparation and application of magnetic nitrogen-doped rGO for persulfate activation, Environ. Sci. Pollut. Res. 25 (2018) 30575–30584. https://doi.org/10.1007/s11356-018-2974-2.

[66] Y.H. Kang, U.-H. Lee, I.H. Jung, S.C. Yoon, S.Y. Cho, Enhanced Thermoelectric Performance of Conjugated Polymer/CNT Nanocomposites by Modulating the Potential Barrier Difference between Conjugated Polymer and CNT, ACS Appl. Electron. Mater. 1 (2019) 1282–1289. https://doi.org/10.1021/acsaelm.9b00224.

CHAPTER 4

Optimizing the Thermoelectric Performance of Conjugated Thienothiophene Polymer/SWCNT Composites

Portable and lightweight power generators are immensely attractive for self-powered electronic devices, including wearables, sensors/actuators, IoT (internet of things) devices, and round-the-clock health/environmental monitoring systems [1]. Printable polymer nanocomposites with acceptable TE conversion efficiency are ideal for sustainable power generation from various low-grade heat sources. The past decade witnessed rapid progress in this area, mainly due to its portability, low cost, solution processability, and environment-friendly characteristics [2]. Among the various organic TE materials, conjugated polymers such as polyaniline (PANI) [3], poly(3,4-ethylene dioxythiophene) (PEDOT) [4,5], polypyrrole (PPy) [6], and poly(3-hexylthiophene) (P3HT) [7,8] showed good potential for TE applications. In addition, these materials could be printed to fabricate lightweight thermoelectric generators (TEGs) by conventional ink-jet or dispensing process, retaining good efficiency and power output [1,9–11]. Recently, benzo-[1,2-b:4,5-b']dithiophene (BDT) based conjugated polymers made tremendous progress in this field [12,13]. Generally, the TE performance is gauged by a dimensionless figure-of-merit, ZT = PF × T/ κ (T is temperature), and power factor (PF) = $\alpha^2\sigma$. High α and σ with low κ are favorable for achieving excellent conversion efficiency in TE materials.

Since conjugated polymers possess low κ and large α, the facile route of achieving a high TE performance is to improve the σ without sacrificing the former two parameters. Researchers attempted to enhance σ by adopting strategies such as molecular doping, hybridizing with electrically conducting fillers, multi-layered composite structure formation, etc. [1,14,15]. A

rational approach to significantly improving TE performance is using single-walled carbon nanotubes (SWCNTs) as fillers due to their exceptional electrical conductivity and flexibility [16–21]. Strong interfacial interactions between conjugated polymers and SWCNTs enhance the charge carrier mobility in the composites [22]. On the other hand, the presence of polymers provides a low κ value (< 1 W/m.K) for the composites, which is generally independent of the concentration of CNTs [23,24]. Recently, Liu *et al.* reported a PF of ~526 μW/m.K^2 for PEDOT:PSS/SWCNT nanocomposite by improving the charge carrier concentration via base treatment [25]. Although many PEDOT:PSS-based composites show the state of the art TE performance, their practical application is challenging due to the lack of stability, acidic nature, and hygroscopicity [26–28] which leads to device degradation [28]. Wang *et al.* designed and synthesized a novel donor-acceptor-type BDT-based conjugated polymer (PBDTDTffBT) and prepared composite films containing SWCNTs with a mass ratio of 1:10, which exhibited the highest PF =116.7 μW/m.K^2 at ~95 °C [29].

Chemical doping is the performance modifier for many conjugated polymer/SWCNT composites. Muller *et al.* p-doped a P3HT/CNT composite film, resulting in a PF of 95 ± 12 μW/m.K^2 [30]. Jang *et al.* studied the influence of the method of doping in P3HT/SWCNT films. Hybrid films doped by spin-coating exhibited PF of 267 ± 38 μW/m.K^2, which is an enhancement over that of hybrid films doped by the conventional immersion method (103 ± 24 μW/m.K^2) [31]. Side-chain engineering of conjugated polymers is another efficient method to improve TE performance. For example, Pan and co-workers compared the TE properties of the composites of SWCNT and two kinds of polythiophenes bearing different side-chains, namely P3HT and poly(thiophene-3-[2-(2-methoxy-ethoxy)ethoxy]-2,5-diyl) (PMEET). The latter showed a two-times higher PF (121 μW/m.K^2) compared to P3HT/SWCNT composite (65 μW/m.K^2) [32].

In this work, we have prepared a composite of BDT-TTE based conjugated polymer, poly[4,8-bis(5-(2-ethylhexyl)thiophene-2-yl)benzo[1,2-b;4,5-b']dithiophene-2,6-diyl-alt-(4-(2-ethylhexyl)-3-fluorothieno[3,4-b]thiophene-)-2-carboxylate-2-6-diyl)] (PBDTT-FTTE) and SWCNT, p-doped with an oxidizing agent and studied the TE properties. The temperature-dependent TE characteristics revealed the charge transport mechanism in the composite. Besides, we have estimated the *ZT* value by theoretically calculating the κ value using the DIGIMAT-MF material modelling platform. We have demonstrated the performance of flexible TEG and simultaneously predicted the output characteristics with COMSOL Multiphysics software. Along with the experimental results, theoretical modelling provides a good understanding of the underlying science.

4.1. Experiment section

4.1.1. Chemicals

PBDTT-FTTE ($(C_{49}H_{57}FO_2S_6)_n$, M_w > 40,000, PDI ~ 1.8-2.0) was procured from Solarmer Energy Inc. SWCNT (containing ≥89% carbon basis (≥99% as CNT), a diameter of ~ 0.7-1.3 nm and length of ~1 μm), anhydrous *ortho*-dichlorobenzene (*o*-DCB), and anhydrous ferric chloride ($FeCl_3$) were obtained from Sigma-Aldrich. Nitromethane (CH_3NO_2) was procured from TCI Chemicals (India) Pvt. Ltd.

4.1.2. Preparation of composite

The polymer and SWCNT are dispersed in *o*-DCB at 2 mg/mL concentration using a probe sonicator (VCX-750 Vibra-Cell, Sonics & Materials) for 60 min in an ice bath, followed by stirring for 60 min at room temperature (~ 303 K). The composition was varied by adding different weight percentages (wt%) of SWCNT. The dispersion was drop-cast on a pre-cleaned (with extran, water,

and isopropanol in that sequence by bath sonication for 15 min in each) and pre-heated (at 120 °C for 15 min) glass substrate and annealed at 120 °C for 30 min.

4.1.3. Doping of composite film

Samples were doped by immersing in 0.05 M $FeCl_3$ solution in nitromethane for 30 min, then washed with ethanol to remove excess dopant followed by annealing at 100 °C for 15 min.

4.1.4. Characterization and measurement techniques

The present work's characterization and measurement techniques are listed in Annexure I. The thermal and electronic properties were simulated using the DIGIMAT-MF© 2020 material modelling platform, and the TEG was modelled and studied using COMSOL Multiphysics® 5.6 software package.

4.1.5. Density measurement of the composite

Density (ρ) is the measurement of the amount of mass (M) per unit volume (V). The density is given by,

$$\rho = \frac{M}{V} \tag{4.1}$$

It is usually easy to find the mass in equation 4.1 while measuring volume can be tricky. However, the volume formula can be used for regular shapes like a cube, sphere, or brick. For irregular shapes, the easiest way is to measure volume displaced by placing the object in a liquid.

In the present study, the PBDTT-FTTE polymer solution was drop cast on a rectangular glass plate of dimensions 25 x 15 mm and annealed at 120 °C for 30 min. The obtained film had a thickness of 52 μm. For a cubical shape, the volume is given by,

$$\text{V= length x breadth x thickness} \tag{4.2}$$

Thus the volume of the as-casted film, $V_p = 19.5\ mm^3$

The film was then peeled off from the substrate and measured the mass as $M_p = 34.8$ mg

Hence, density of PBDTT-FTTE, ρ (polymer) = 1784.6 kg/m^3

Similarly, the density of PBDTT-FTTE:55wt% SWCNT/doped is calculated. The solution was drop cast on a rectangular glass plate of dimensions 25 x 15 mm and annealed at 120 °C for 30 min. The film was immersed in 0.05 M $FeCl_3$ solution for 30 min, washed with ethanol, and then annealed at 100 °C for 30 min. The obtained film had a thickness of 50 μm. The volume of the doped film, V_c = 18.75 mm^3

The mass of the peeled off film from the substrate was measured as M_c = 33.6 mg

Hence, density of PBDTT-FTTE:55 wt% SWCNT/doped, ρ (composite) = 1792 kg/m^3

4.1.6. Fabrication of flexible TEG and testing

Flexible TEGs were fabricated on a polyimide substrate (DuPont Kapton® HN50) using a formulation of PBDTT-FTTE:55wt% SWCNT composite. An automated 3D dispenser needle valve (Nordson EFD 741) is used for dispensing, and the resulting films were annealed on a hot plate at 120 °C for 30 min. For interconnection of the TE legs, silver screen ink (Novacentrix Metalon® HPS-FG777) was dispensed using an automated 3D dispenser jet valve (Nordson PICO Pμlse). TEGs were subsequently annealed at 120 °C for 30 min on a hot plate. Each leg had dimensions of 4 mm × 40 mm × 2.5 μm with a spacing of 4 mm and silver interconnection with a thickness of 500 μm. The overall size of the fabricated flexible TEG was 16.8 cm × 4 cm. The fabricated TEGs were analyzed in a home-built setup adopting a previously devised method [28]. The temperature gradient (Δ*T*) across the TEGs varied from 3 to 65 K. The output voltage and current were measured using a Keithley 6510 DAQ system.

4.2. Results and discussion

4.2.1. Thermoelectric properties of the composite film

A schematic illustration of the composite preparation process is presented in Fig. 4.1. We varied the SWCNT content from 25 − 95 wt%, as below 25% SWCNT, the coating resistance became too high to extract a stable output from LSR-3. The formulation used for subsequent drop-casting was stable for several weeks without any phase segregation or precipitation traces.

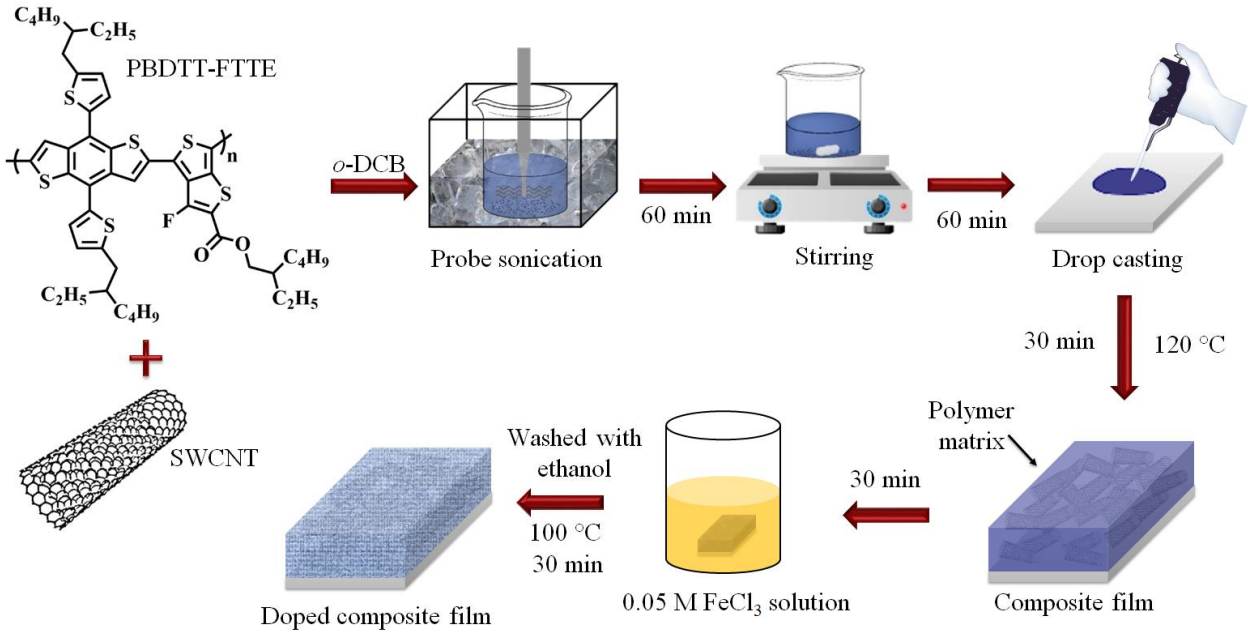

Fig. 4.1. Schematic illustration of the composite preparation process.

The variation of coating thickness with SWCNT content is obtained using the stylus profilometer (Fig. 4.2a). The slight difference in the observed pre- and post-doping thickness values largely falls within the experimental error limit. The TE properties of the doped and undoped films against SWCNT wt% are compared in Fig. 4.2b & 2c. All composites exhibited a p-type conductivity with positive α values. Fig. 4.2b shows a minor drop in the α values (35 μV/K @ 25% − 28 μV/K @ 95%) with varying SWCNT amounts in the composites, and all values remained unchanged after doping. This observation is distinctly different from our earlier work

with nanocomposites of PBDTT-FTTE with multi-walled carbon nanotube (MWCNT), where the α values showed ~2.25× enhancement (from 20 μV/K to >45 μV/K) post-doping with $FeCl_3$ [28]. Such simultaneous enhancement in σ and α were also observed in the PEDOT:PSS/SWCNT system by treating it with a base [25]. However, in the present study, we observe an enhancement in σ without altering the α value after doping. This may be due to the trade-off between carrier concentration, mobility and Fermi-level discussed in the latter section.

Fig. 4.2c shows a perceptible σ enhancement with increasing SWCNT incorporation beyond 25 wt% as new electrical pathways open up in the PBDTT-FTTE matrix. Between 45 and 70 wt%, σ values show a steeper increase, and a percolation-like behavior is observed with further SWCNT addition with a peak value of ~ 795 S/cm at 85 wt%. After doping with $FeCl_3$, two different maxima appear for σ at 55% and 85% SWCNT, again strikingly deviating from our previous observation with PBDTT-FTTE:MWCNT system that exhibited a single conductivity peak at 45% MWCNT [28]. The SEM morphologies presented in the insets show that a mat-like network of SWCNT with diameters in the range of 10-30 nm is formed at 55 wt%, which appeared to be more compacted and smoothed after $FeCl_3$ treatment. TEM observations confirmed that the CNTs are coated fully with the polymer species (Fig. 4.3), and possibly the doped polymer and CNT combinedly contributed to the composite's electrical conductivity [28,32,33]. At the first maxima, the σ yielded a value of ~575 S/cm, 18% enhancement from the undoped film. The reduction of σ between 55 and 70 wt% SWCNT could be linked to the reduced polymer amount and thereby reduced σ contribution that outweighs SWCNT increase in the composite. Beyond ~70 wt%, the polymer contribution becomes less significant, and the composite closely follows the trend exhibited by the undoped sample with the peak σ = 1187 S/cm (67% enhancement) at 85

wt%. Since α retained almost the same value, the PF vs. SWCNT wt% trend closely followed the σ variation exhibiting PF = 57 and ~81 μW/m.K^2 for 55 and 85 wt%.

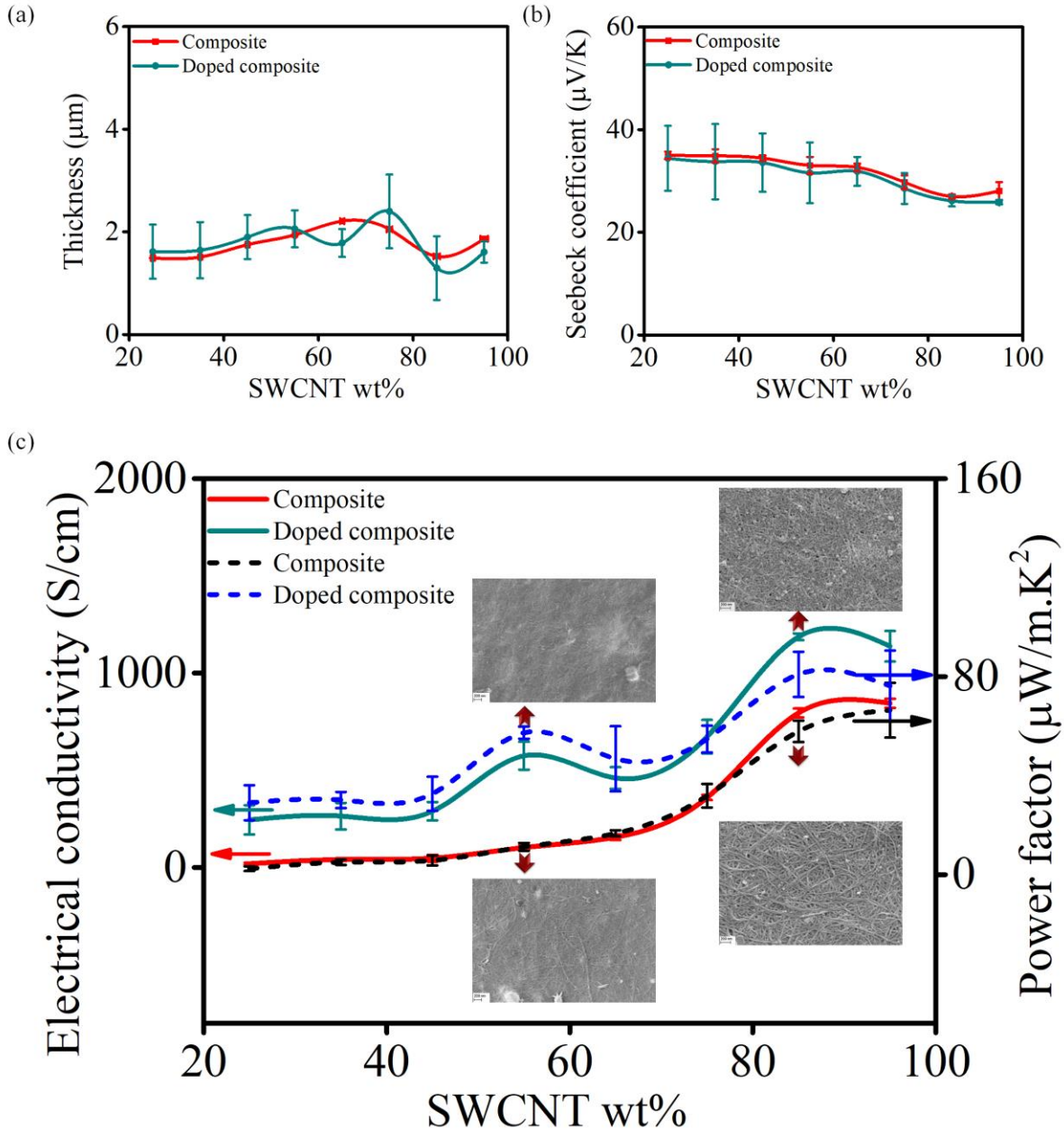

Fig. 4.2. The variation of (a) thickness; (b) Seebeck coefficient and (b) electrical conductivity and PF of the composite and doped composite vs. SWCNT wt%. The SEM morphology of the composite and doped composite at 55 and 85 wt% SWCNT is shown in the inset.

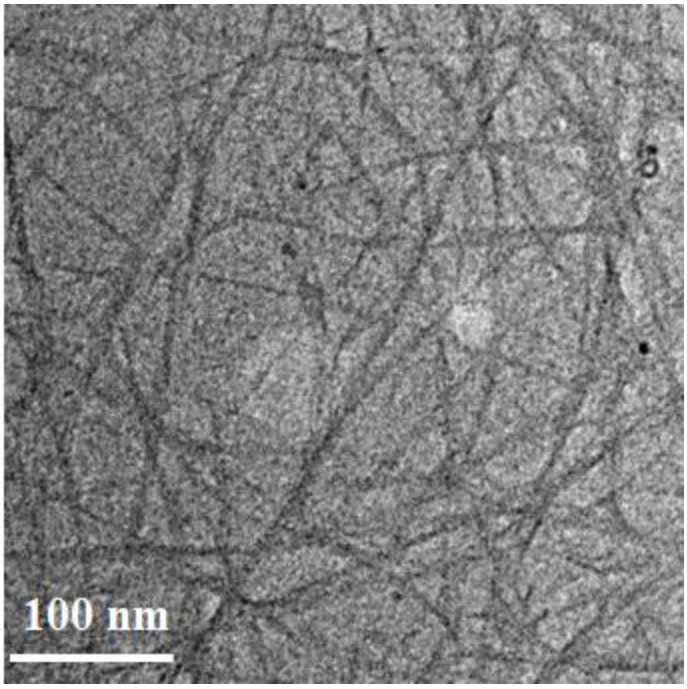

Fig. 4.3. The TEM image of composite with 55 wt% SWCNT.

4.2.2. Characterization of the composites

UV-vis-NIR absorption plots (Fig. 4.4a) of pristine PBDTT-FTTE and the composite containing 55 wt% SWCNT (both precursors were dissolved in *o*-DCB) revealed the interactions between different ingredients. PBDTT-FTTE spectrum shows the absorption maximum (λ_{max}) at 703 nm for interband transitions and an associated strong shoulder at 632 nm, confirming significant π-conjugation and molecular packing. PBDTT-FTTE:SWCNT composite exhibited a decrease in absorbance intensity and a nominal blue-shift in λ_{max} (~699 nm) along with the quenching of the shoulder. The characteristic van Hove singularities for SWCNTs were evident in the NIR region, with additional polymer peaks in the shorter wavelengths [34]. The blue-shift could be attributed to the reduction in effective conjugation of the polymer upon functionalization with SWCNT, altering the electronic interactions [26,27]. A PBDTT-FTTE characteristic peak at 322 nm corresponding to the π-π* transition also is blue-shifted (301 nm) in the composite due to

the interfacial interactions between SWCNT and the polymer. Fig. 4.4b shows the normalized UV-vis-NIR absorption spectra of the polymer, undoped- and doped (with $FeCl_3$)-composite in the film state. Similar to our observation for the solution-state, the λ_{max} gets blue-shifted (700 nm → 682 nm) upon hybrid formation with a diminishing shoulder peak. π-π interactions between the polymer interface and SWCNT in the film state are furthermore confirmed by ~14 nm blue-shift of the polymer absorption peak at 324 nm. Post-doping, the λ_{max} exhibits a further shift to 669 nm and a rapid decrease in intensity, signifying effective hole doping of the polymer by $FeCl_3$ [30]. Further the optical bandgap was determined from the film-state absorption onset wavelength and is listed in Table 4.1.

Table 4.1. Optical bandgap of pristine polymer, composite and doped composite.

Particulars	λ_{onset} (nm)	E_g (eV)
PBDTT-FTTE	752.4	1.65
Composite	779.8	1.59
Doped composite	779.8	1.59

The interfacial interactions in the composites were investigated using Raman spectroscopy. Fig. 4.4c shows the Raman spectrum of pure polymer and Fig. 4.4d presents that of SWCNT, composite, and composite doped with $FeCl_3$. The polymer showed two prominent fingerprint peaks: the stretching vibrations of the benzene ring of BDT units at 1579 cm^{-1} and the C-C stretching vibration of the π–π conjugated backbone at 1332 cm^{-1}, respectively [29]. The spectrum of SWCNT showed characteristic peaks of the G band of sp^2 carbon at 1545 and 1585 cm^{-1}, where the splitting originates from the E_{2g} stretching mode of graphite [35,36]. The SWCNT Raman spectrum also consisted of a D band (1304 cm^{-1}) of sp^3 carbon and a G' band (2591 cm^{-1}) of

graphite [37]. For the composite, the intensity ratio of the G band (I_G) to D band (I_D) gradually decreased, and these peaks showed ~4 and 7 cm^{-1} shifts, which ensued from strong π-π interfacial interactions between the polymer and SWCNT [38]. After doping, the I_G/I_D ratio is notably enhanced, indicating a better crystalline packing [37]. The observed data are listed in Table 4.2. The peaks were shifted to lower wavenumbers (~1-2 cm^{-1}), which is attributed to the strong interaction and charge transfer between the polymer and SWCNT [29,39].

Table 4.2. I_G/I_D ratio of SWCNT, composite and doped composite.

Particulars	I_G (a.u.)	I_D (a.u.)	I_G/I_D
SWCNT	9877.79	253.33	38.99
Composite	6975.06	467.84	14.91
Doped composite	12918.75	563.53	22.92

Fig. 4.4e shows the WAXS plot of SWCNT, pristine polymer, composite and doped composite. A broad peak is visible in the SWCNTs WAXS pattern, at 2θ = 25.8°, which could be indexed as the C (002) reflection of graphite [40]. The PBDTT-FTTE showed a pronounced (010) diffraction peak at 2θ = 21.9°, arising from π-π stacking of thiophene rings [41]. A peak shift to 22.3° is observed after introducing SWCNT to the polymer matrix. This shift is due to decreased interplanar spacing caused by the interfacial interaction between PBDTT-FTTE and SWCNT [42]. Post-doping, a further shift towards higher 2θ is observed (22.8°), indicating an additional enhancement in π-π stacking between CNT and polymer [43]. The analysis of thermal stability by TGA (Fig. 4.4f) indicated that both undoped- and doped-composite have good thermal stability (5% weight loss temperature (T_5): 542 K (composite), 603 K (doped composite)).

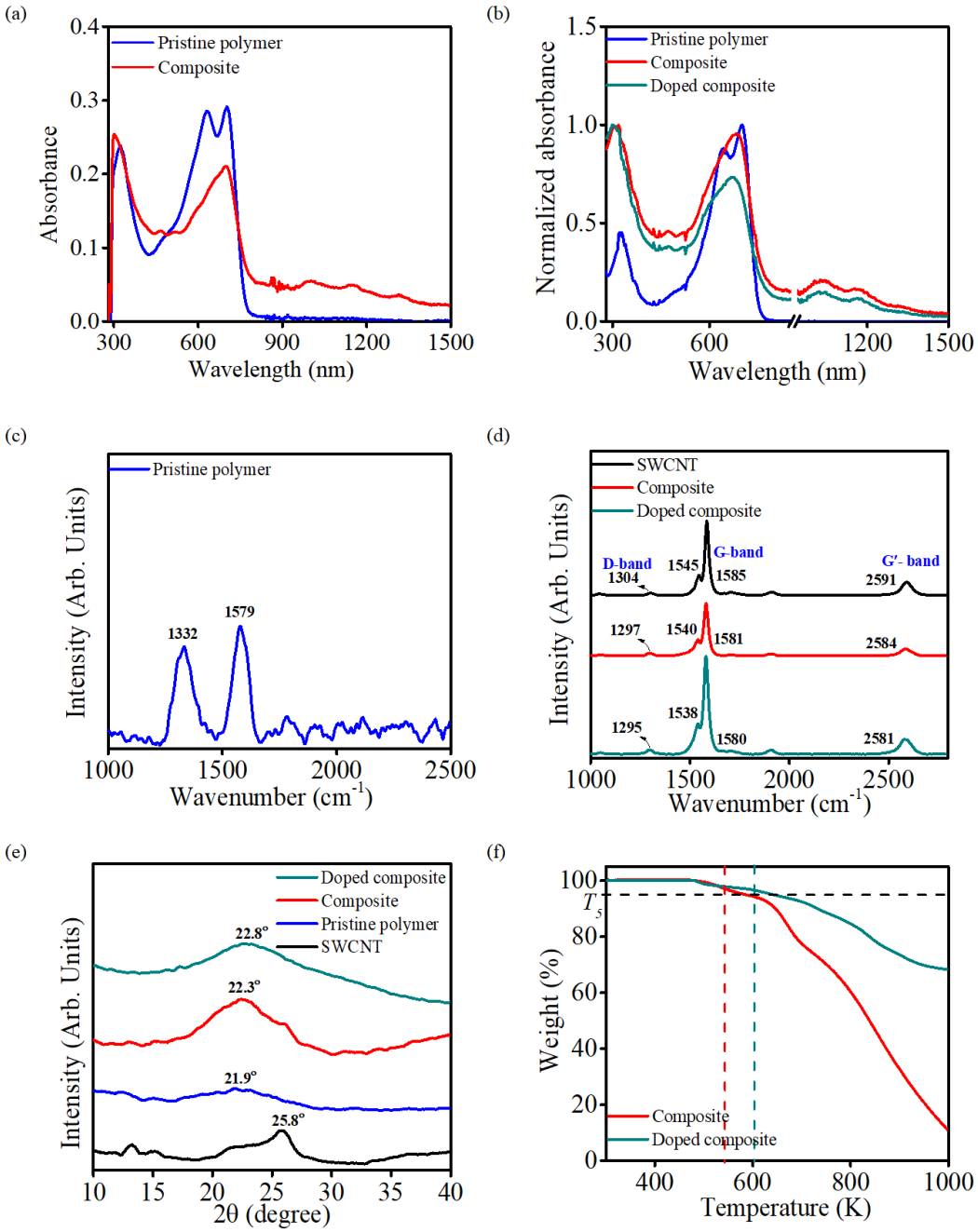

Fig. 4.4. UV-vis-NIR absorption spectra of the polymer and composite in (a) solution and (b) film state; Raman spectra of (c) pristine polymer and (d) SWCNT, composite with 55 wt% SWCNT and doped composite; (e) WAXS plot of SWCNT, pristine polymer, composite with 55 wt% SWCNT and doped composite and (f) TGA plot of composite with 55 wt% SWCNT and doped composite.

4.2.3. Temperature-dependent thermo-electric transport

Fig. 4.5 shows the TE parameters' temperature dependence plots by taking the composite with 55 wt% SWCNT content as a representing example. The temperature varied from 313−523 K with a 10 K incremental step. The σ of the undoped composite remains unchanged till 400 K (~104 S/cm) and gradually decreases with further temperature rise (Fig. 4.5a). For doped films, σ sustains up to 350 K (~ 591 S/cm), followed by a shallow decreasing slope up to 400 K and a swift downturn beyond this point. The temperature dependence of α before and after doping is shown in Fig. 4.5b. While α of the undoped composite exhibited a single increasing slope, a steep enhancement of α is observed between 400 K to 450 K after doping, portraying the classic tradeoff with σ. The enhancement could be due to the hot carrier filtering at the interface that arose from the Fermi level repositioning. The PF values peak at 420 K for both undoped (19 $\mu W/m.K^2$) and doped (60 $\mu W/m.K^2$, 32% enhancement) films, as shown in Fig. 4.5c.

Mott's variable range hopping (VRH) model reveals the disordered system's transport behavior, assuming that inside a network, electrons hop between the localized sites near the Fermi level [44,45]. The model is expressed as in equation 1.11. Here, both undoped and doped composite films exhibited a linear fit between ln σ and $T^{-1/2}$ (Fig. 4.5d). The charge transport, therefore, follows the one-dimensional VRH (1D-VRH) model, where d = 1. Clearly, in such a disordered system, a strong π-π interfacial interaction exists between polymer and SWCNT, and the carriers can hop from one SWCNT to another through the 1-D channel [29].

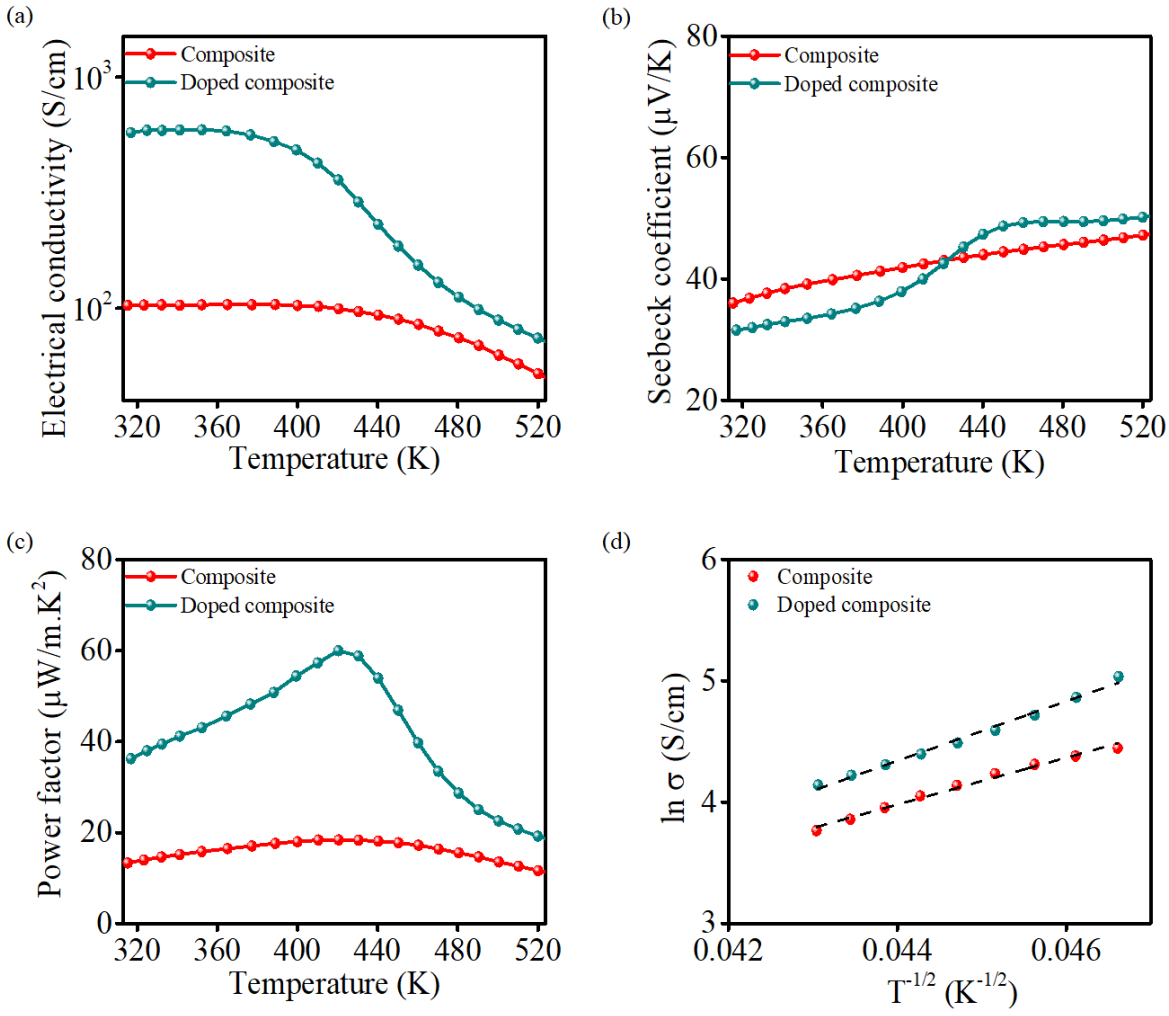

Fig. 4.5. Temperature dependency of (a) electrical conductivity; (b) Seebeck coefficient; (c) PF and (d) ln σ vs. $T^{-1/2}$ fitting plot according to the VRH model before and after doping.

The temperature-dependent TE studies of undoped and doped composites for 25-95 wt% SWCNT are shown in Fig. 4.6. A peak PF of 98 μW/m.K^2 is achieved at 387 K for 85 wt% SWCNT. The TE performance trend of these composites is expectedly similar to the earlier reported semi-metallic systems [12].

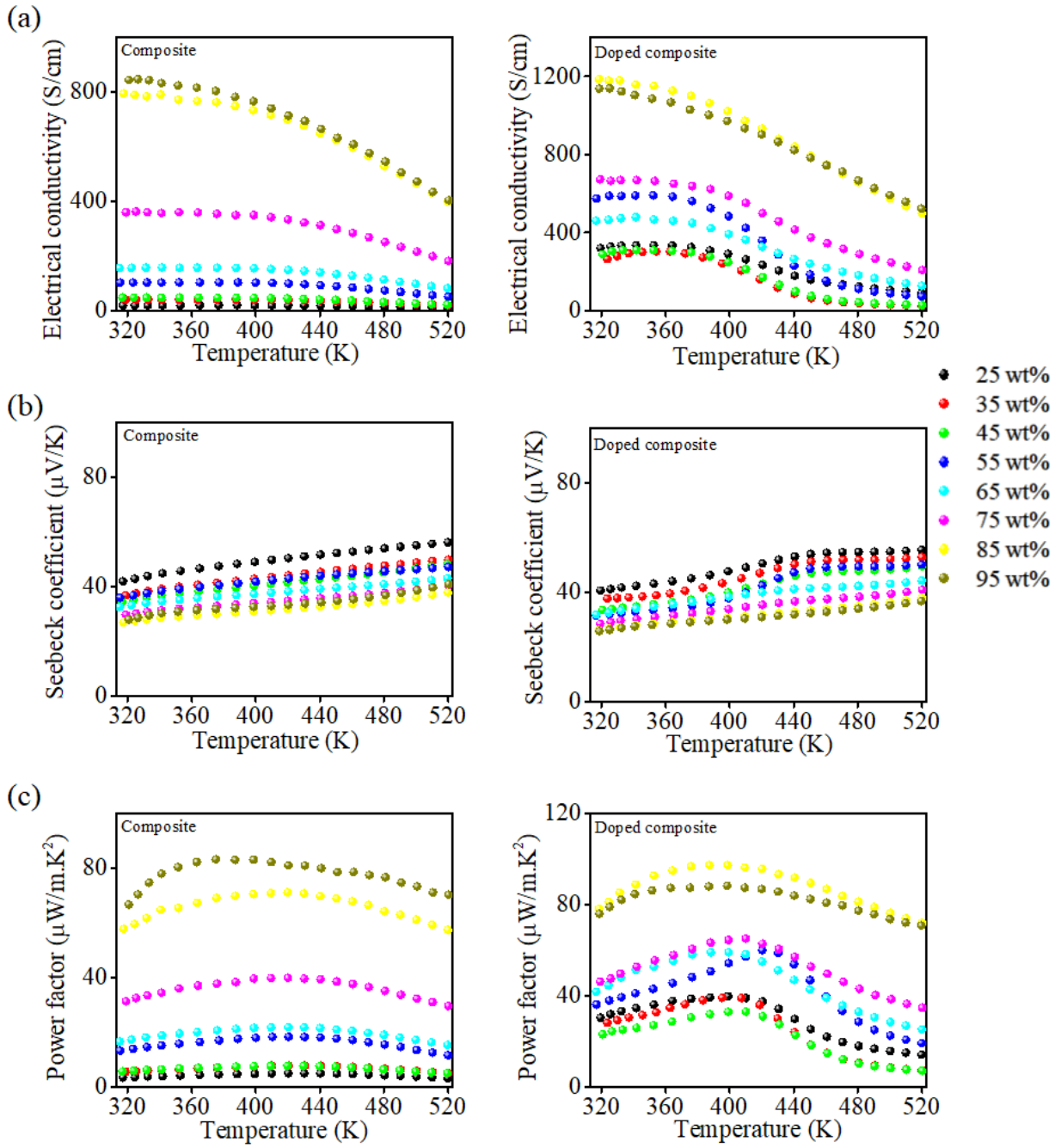

Fig. 4.6. Temperature dependence (a) electrical conductivity; (b) Seebeck coefficient and (c) PF of composite and doped composite by varying SWCNT wt%.

4.2.4. Effect of doping in thermoelectric performance

The hole-doping using $FeCl_3$ essentially exhibits a decoupling between α and σ, as evident from Fig. 4.2. Unlike the pristine polymer or CNT systems, several additional factors contribute to the thermoelectric output after composite formation, requiring first-principle thinking to reveal the underlying mechanism. Although the better crystalline packing (revealed in Fig. 4.4d) and decreasing coating roughness (AFM image, Fig. 4.7) after doping enhanced σ value [46], the predominant contribution was from post-doping hole mobility (μ_h) enhancement caused by decreasing barrier height of the traps and resulting dielectric changes in the sample (Table 4.3) [28,33,47]. From the SEM images (Fig. 4.2 inset), it is evident that due to immersion doping, the surface of the composite becomes more compacted, and the polymer in the top surface gets connected, which fills the gap between the CNTs to form a uniform smoother outer surface. Thus the surface roughness value decreases [48,49].

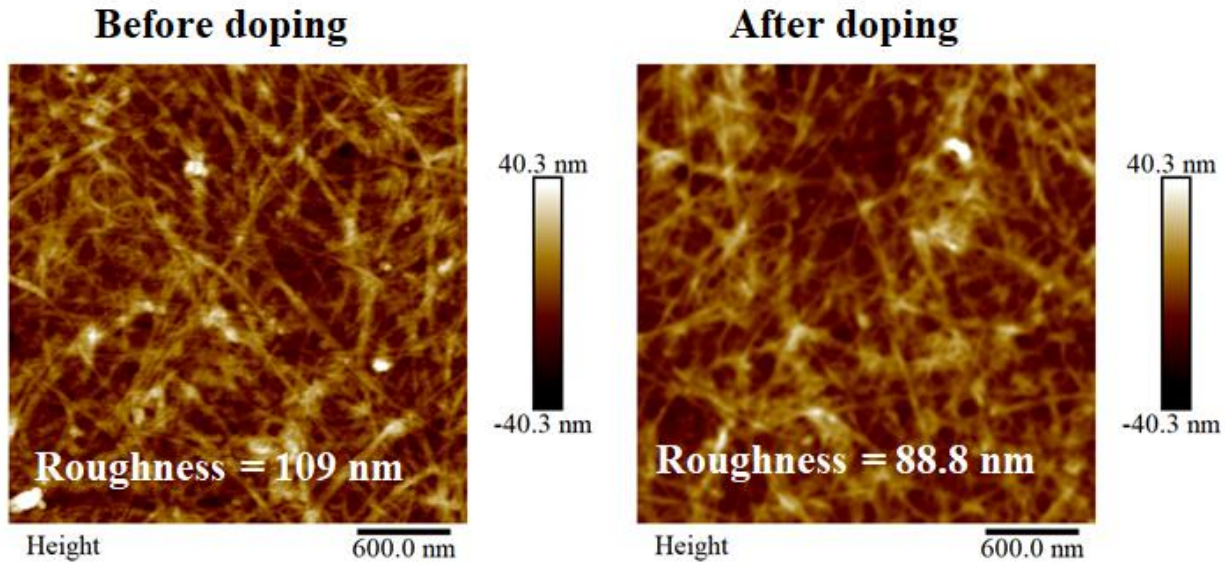

Fig. 4.7. AFM image of composite and doped composite at 55 wt% SWCNT.

Table 4.3. Concentration and mobility of charge carriers in the composite and doped composite.

Particulars	Composite	Doped composite
Bulk concentration (/cm^3)	4.953E+22	1.302E+21
Sheet concentration (/cm^2)	1.28E+19	3.073E+17
Mobility (cm^2/Vs)	1.196E-2	6.528E-1

According to the Boltzmann transport equation, α is a function of the density of states (DOS) of a material, described as [50],

$$\alpha = \frac{k_B}{e}\left[\left(\frac{E_F - E_{trans}}{k_B T}\right) - A\right] \quad (4.3)$$

k_B, $E_{trans,}$ and A are the Boltzmann constant, transport energy level, and a term for the heat of transport, respectively. Fermi level (E_F) and valance band maxima (VBM) positioning in the samples were tracked by UPS studies. The full range UPS plots for pristine polymer, 55 wt% SWCNT composite, and doped composite are shown in Fig. 4.8a. In Fig. 4.8b (i), the work function (φ) is obtained from the secondary cut-off region, plotted in the kinetic energy (KE) scale, and the VBM is extrapolated from the low binding energy (BE) edge (BE scale is used for convenience) in Fig. 4.8b (ii). The VBM (HOMO) position and φ of PBDTT-FTTE were estimated to be 5.12 and 4.96 eV which matches well with the reported values [51]. After composite formation, the overall φ shifted to 4.87 eV, closer to the literature-reported value of SWCNT work function (4.7-4.9 eV) [52–55], implying strong Fermi level pinning for the polymer in the system. The reduction in the carrier concentration post-doping is due to low-energy carrier filtering through barrier formation in the CNT-polymer interfaces [56]. Similar to the previously reported MWCNT composites [28][33], the carrier mobility of the system is significantly enhanced to compensate for the overall electrical conductivity.

Nevertheless, even after doping the PBDTT-FTTE:SWCNT composite, the Fermi level remained pinned with the DOS distribution near the Fermi edge remaining indistinguishable, leading to an unchanged α value. Fig. 4.8c shows the flat band diagram for the polymer and undoped/doped composite.

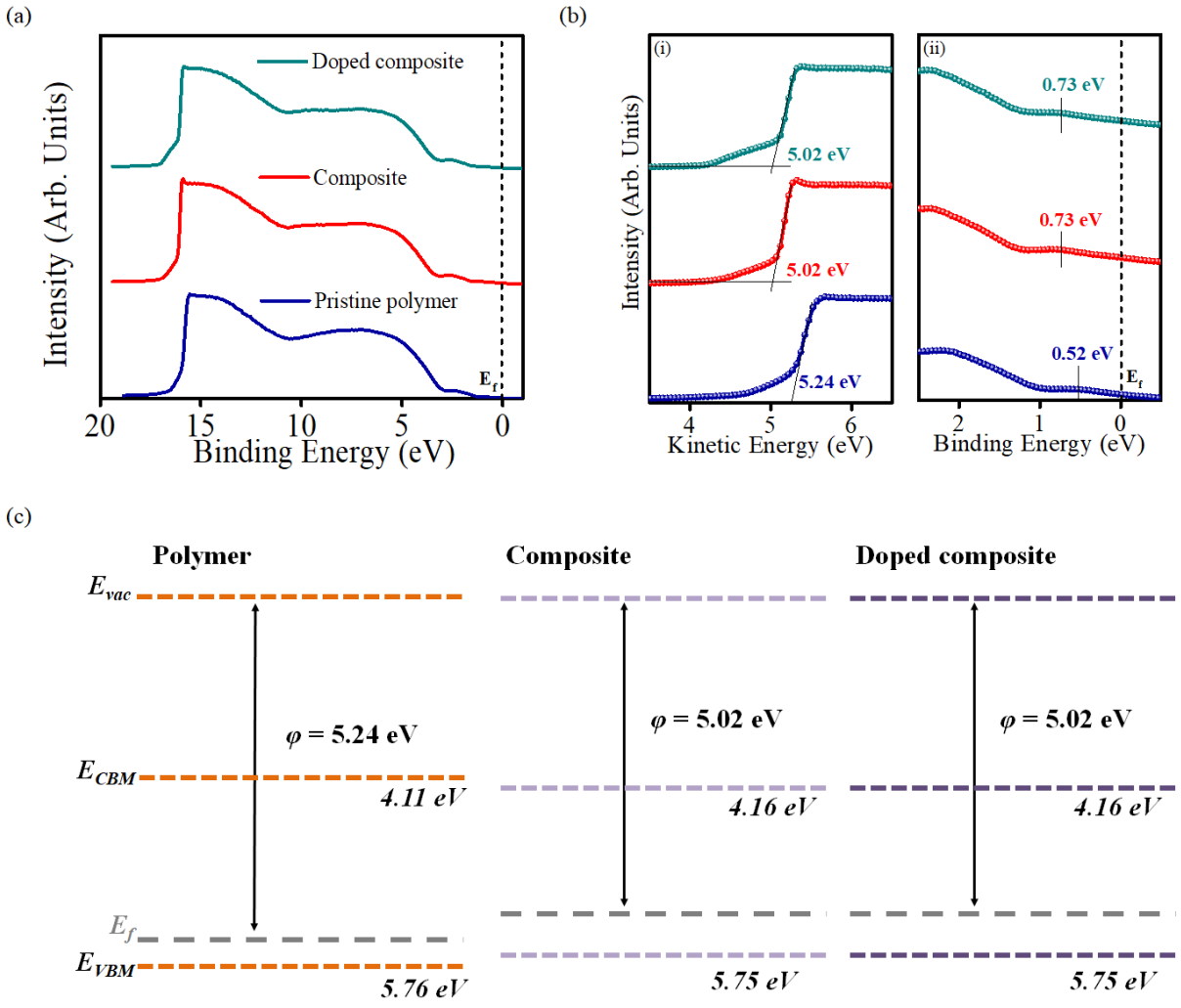

Fig. 4.8. (a) UPS spectra of the pristine polymer, composite and doped composite; (b) (i) secondary cut-off region in KE scale and (ii) low BE region and (c) band diagram.

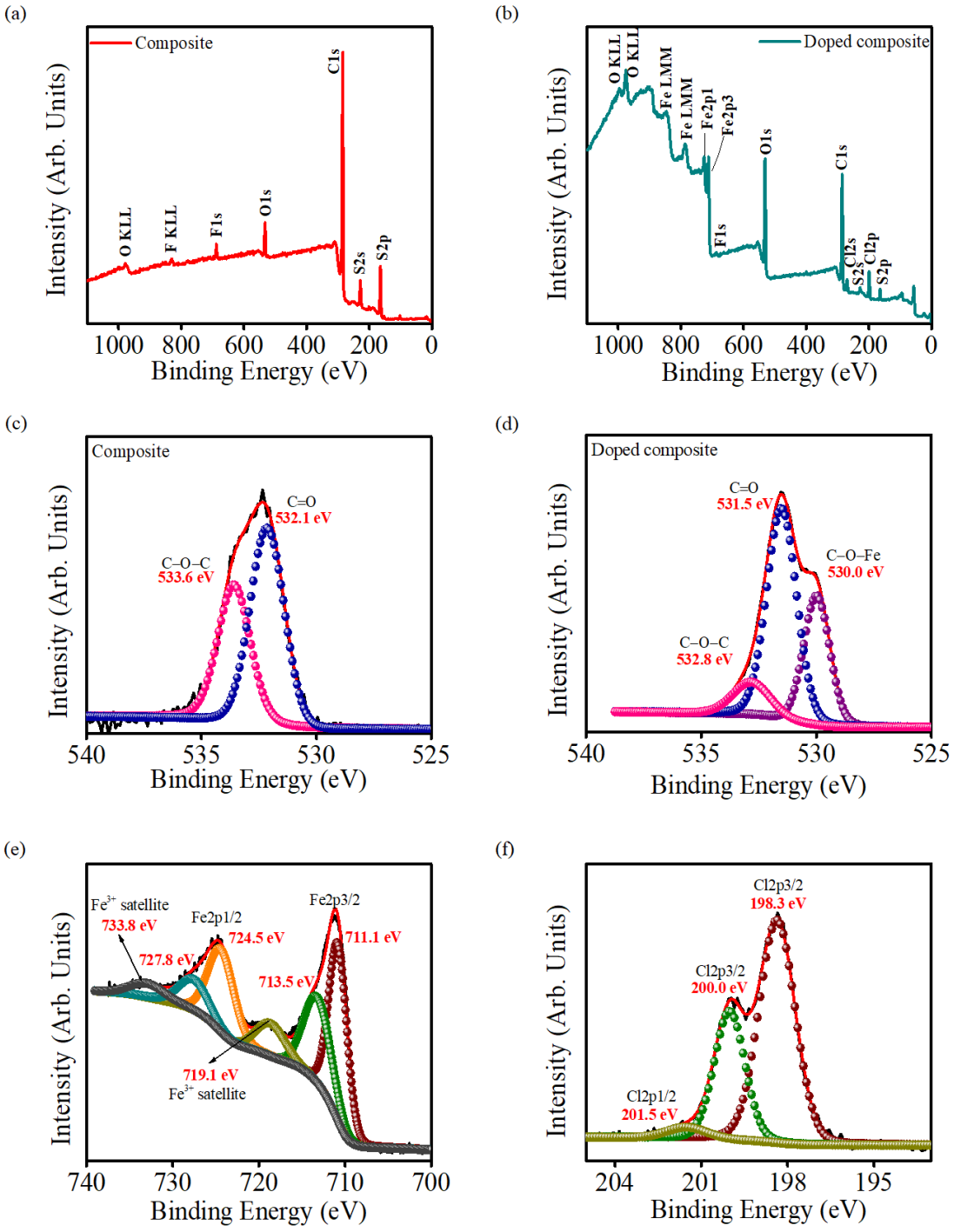

Fig. 4.9. XPS survey spectrum of (a) composite and (b) doped composite containing 55 wt% SWCNT. Core-level O1s XPS spectra of (c) undoped and (d) doped composite; (e) Fe2p and (f) Cl2p XPS spectra of composite with SWCNT~ 55 wt% after doping.

Fig. 4.9a & 4.9b show the XPS survey spectrum of the composite before and after doping. The spectra exhibited carbon, oxygen, sulfur, and fluorine peaks from the undoped composite. Additional characteristic peaks of iron and chlorine could be observed in the doped samples. The O1s core-level spectrum of the composite (Fig. 4.9c) exhibits the oxygen peak arising from C=O (~532.1 eV) and C–O–C (~533.6 eV). Doping induced an additional peak at 530 eV (Fig. 4.9d) corresponding to C–O–Fe due to the formation of a charge-transfer complex (CTC).

The high-resolution Fe2p spectra, shown in Fig. 4.9e, consist of characteristic peaks of Fe2p3/2 and Fe2p1/2. The Fe2p3/2 envelope from the doped composite is deconvoluted into two multiplets (711.1 and 713.5 eV) and a shake-up-related satellite peak (719.1 eV). Similarly, Fe2p1/2 contains multiplets at 724.5 and 727.8 eV, with a satellite peak at 733.8 eV. The observed energy value of Fe2p and satellite peak position supports the composite containing Fe^{3+} cations [57]. In Fig. 4.9f, the Cl2p core level signal exhibits two spin-orbit doublets at 198.3 eV and 200.0 eV, which is attributed to Cl^- ions [58,59]. According to the literature, $(Et_4N)FeCl_4$ salt developed an analogous spectral feature, and hence the charge-transfer complex presented in the composite can be assigned as being due to $FeCl_4^-$ species [60,61].

The deconvoluted high-resolution C1s, F1s, and S2p spectra are shown in Fig. 4.10. The peaks showed a small red-shift in BE post-doping due to the enhanced electron density around the composite caused by the lower electronegativity of the $FeCl_4^-$ species [62].

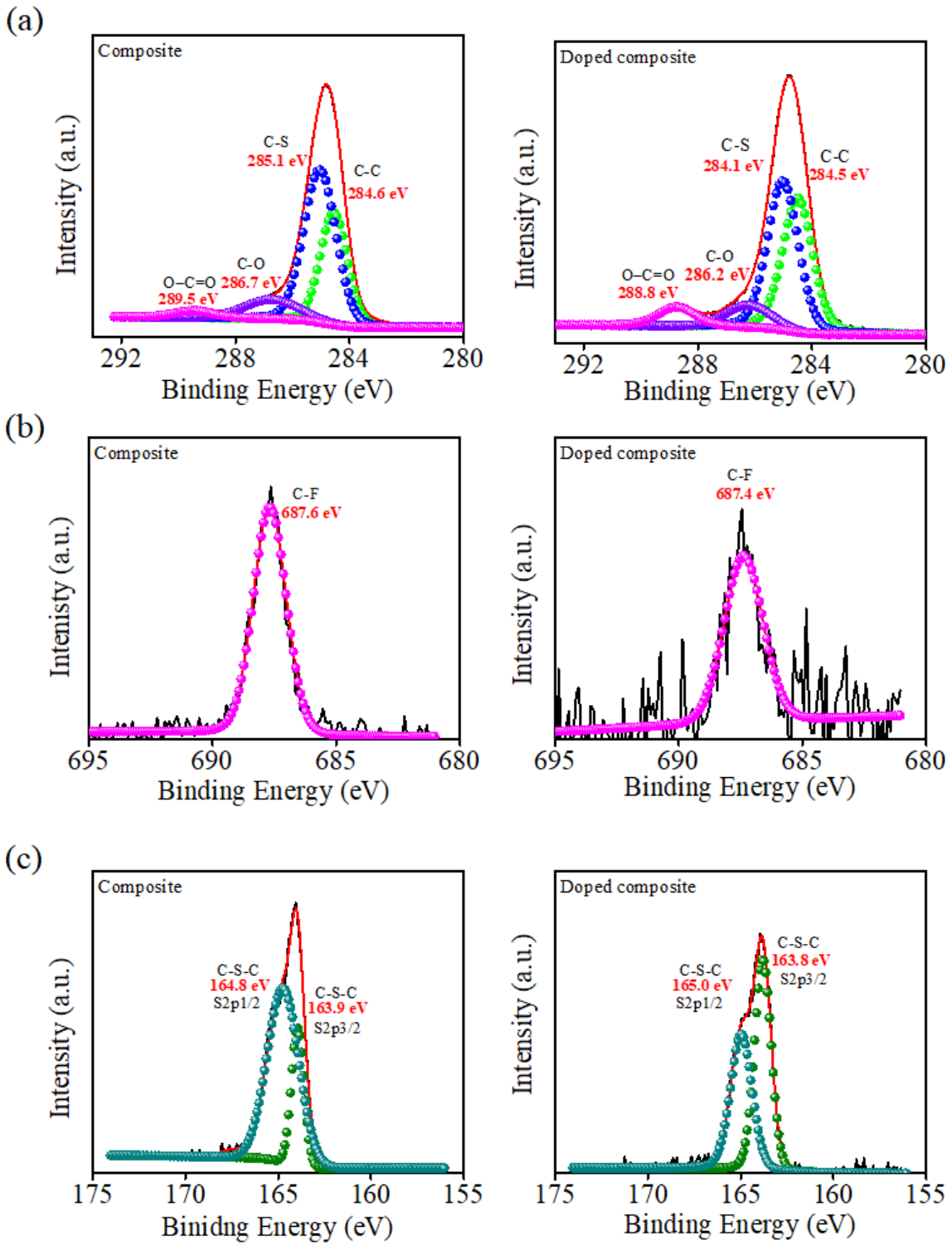

Fig. 4.10. Core level (a) C1s; (b) F1s and (c) S2p XPS spectra of composite and doped composite at 55 wt% SWCNT.

4.2.5. Simulation of thermal conductivity and the projected ZT

The κ (and therefore the projected *ZT* values) was simulated using DIGIMAT-MF, the mean-field homogenization module of DIGIMAT. The platform defines the material's local behavior as a function of the matrix and inclusion phases using the composite microstructure morphology (including weight, shape, and size) [63]. The composites were assumed to contain SWCNT embedded in the polymeric matrix in this investigation. The SWCNTs have been modelled as straight and curved cylinders. This parametric study considered various geometrical characteristics and processing parameters, such as CNT volume fraction, aspect ratio, curvature, and the interphase. We simulated the curvature using the tortuosity factor setting, and the interphases of one or more CNTs were considered interpenetrated. The aspect ratio and the average CNT diameter (0.8 nm) were used as inputs for the Mori Tanaka analytical method [64,65]. The CNTs were assumed to take a random 3D orientation of trihedron type, as shown in Fig. 4.11a. In addition, a percolation model has been developed in DIGIMAT-MF to simulate the percolation effect accurately, which strongly influences the σ of the composite when the volume fraction of filler is more significant than the percolation threshold [63,66]. Adding a small percentage of SWCNT tends to increase the σ of the composite. Also, it is observed that a sharp increase in the σ value was achieved at 15 wt% of SWCNT and further addition exponentially increased the σ. Thus in the present simulation, the composite percolation threshold was set to a value of 0.15 with an exponent value of 2.

The inputs of individual component properties were fed into the software to simulate the composite. The density (ρ) of polymer was measured per the procedure detailed in experiment section 4.1.5, while SWCNT density was manufacturer-provided. The σ of the polymer and SWCNT were measured in Linseis LSR. Though the κ value for the polymer is unknown at this

point, we used the reported value of P3HT films since the conjugated polymers in the pure form mostly show similar κ values. The thermal properties of the components were taken from the literature and are listed in Table 4.4.

Table 4.4. Material properties used in DIGIMAT.

Particulars	**Matrix (PBDTT-FTTE)**	**Inclusion (SWCNT)**
ρ (kg/m^3)	1784.6	1800
σ (S/cm)	2.3E-6	3000
κ (W/m.K)	0.158 [67]	0.8 [68]
Specific heat capacity, C_p (J/g.K)	1.32 [67]	0.72 [68]

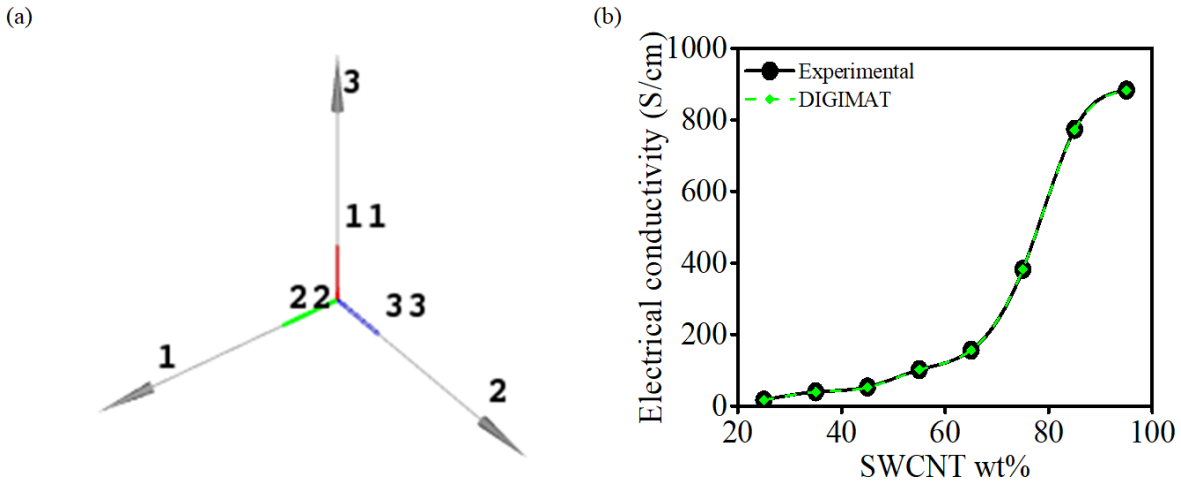

Fig. 4.11. (a) 3D random orientation tensor and (b) Simulated electrical conductivity.

We attempted fitting the experimental σ value to validate the computational model. It is observed that an aspect ratio distribution modulation leads to a perfect agreement with the experimental σ data, as shown in Fig. 4.11b. Fig. 4.12 shows the aspect ratio distribution by

varying SWCNT loading. The aspect ratio distribution increases with the SWCNT wt%, which is rational as increasing CNT content offers better mechanical reinforcement in the composites.

(a)

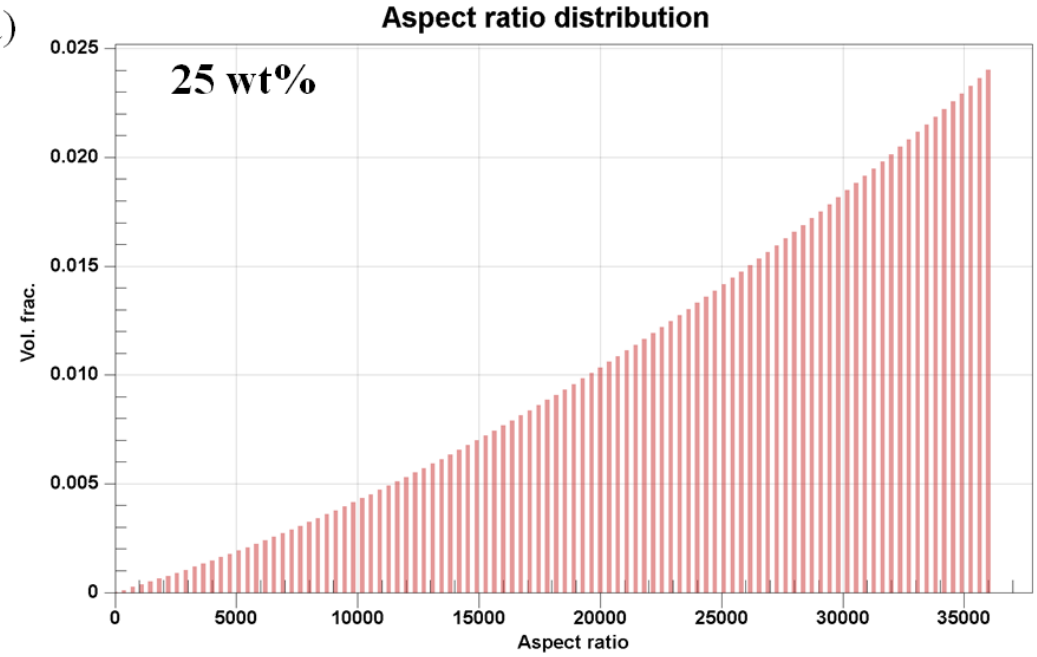

(b)

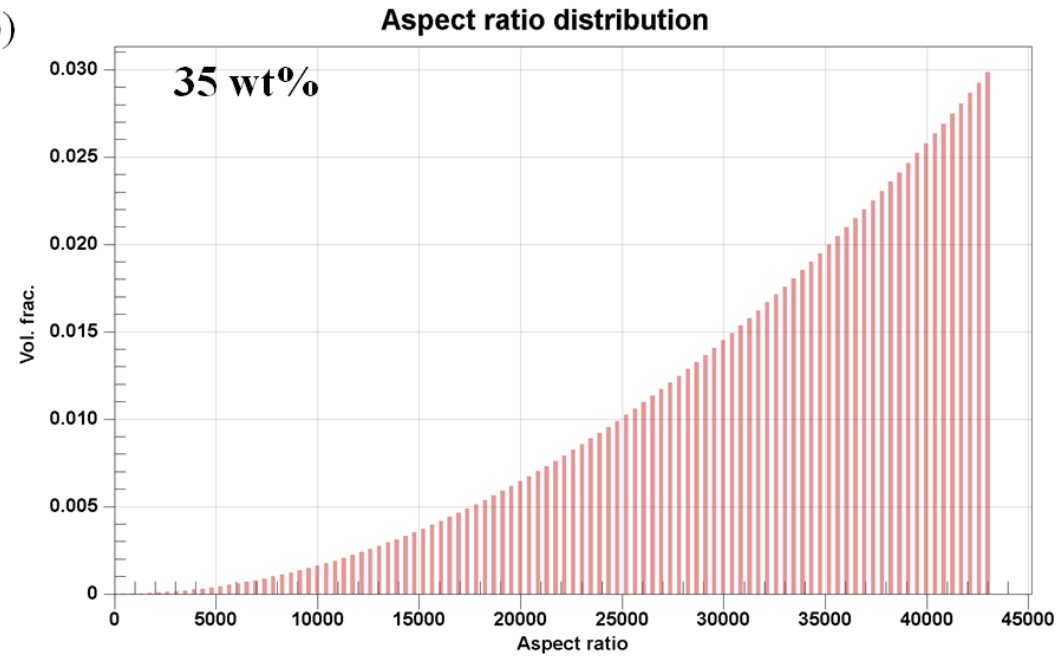

(c)

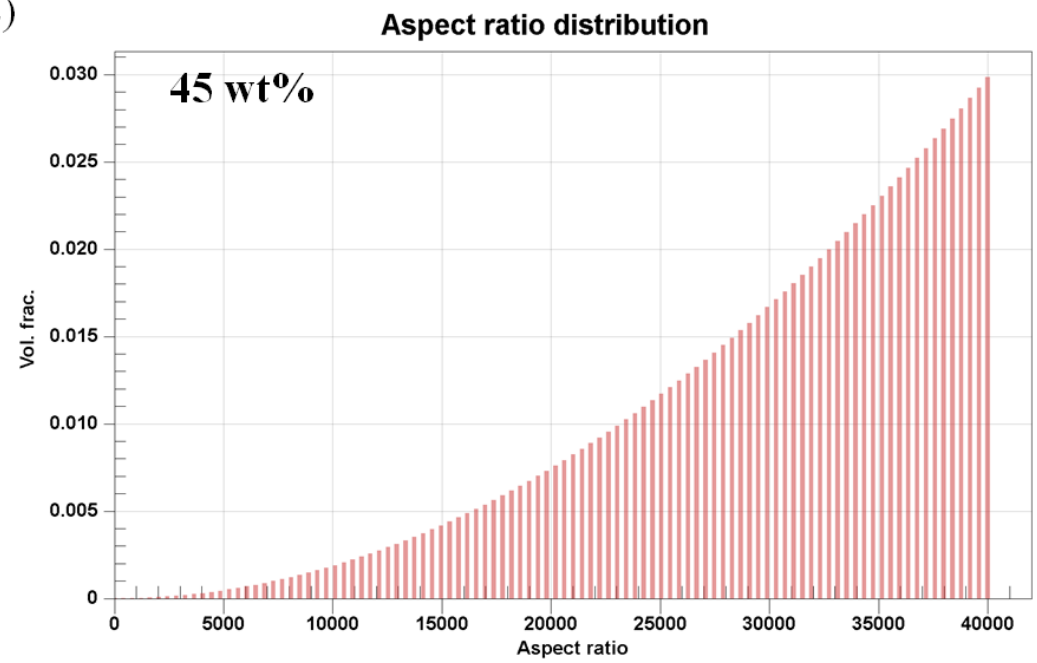
Aspect ratio distribution
45 wt%
Vol. frac.
0.030
0.025
0.020
0.015
0.010
0.005
0
0
5000
10000
15000
20000
25000
30000
35000
40000
Aspect ratio

(d)

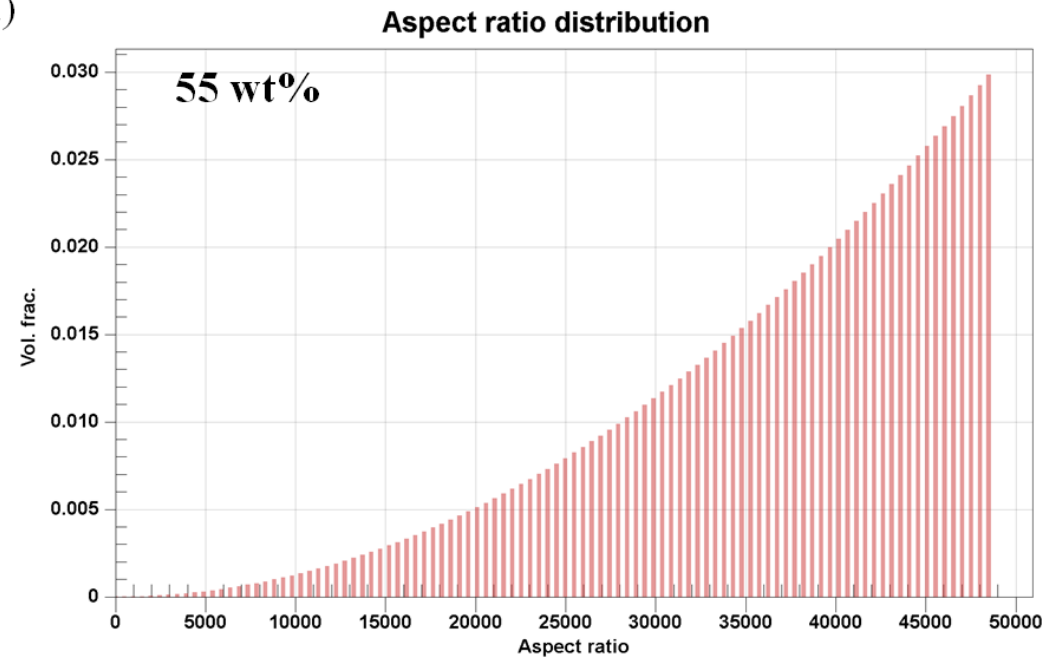
Aspect ratio distribution
55 wt%
Vol. frac.
0.030
0.025
0.020
0.015
0.010
0.005
0
0
5000
10000
15000
20000
25000
30000
35000
40000
45000
50000
Aspect ratio

(e)

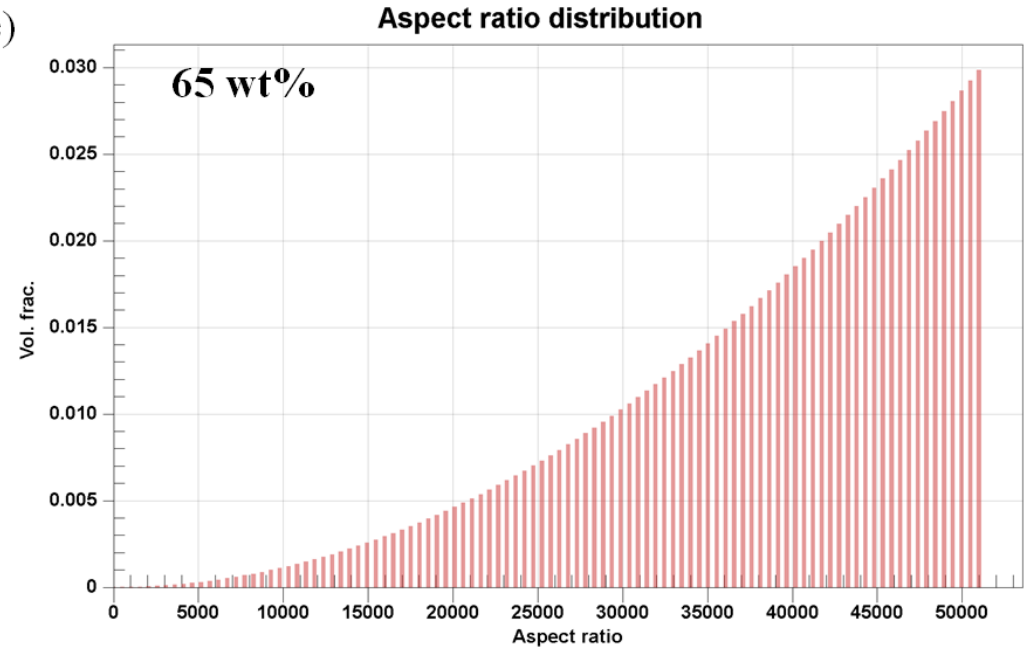
Aspect ratio distribution
65 wt%
Vol. frac.
0.030
0.025
0.020
0.015
0.010
0.005
0
0
5000
10000
15000
20000
25000
30000
35000
40000
45000
50000
Aspect ratio

(f)

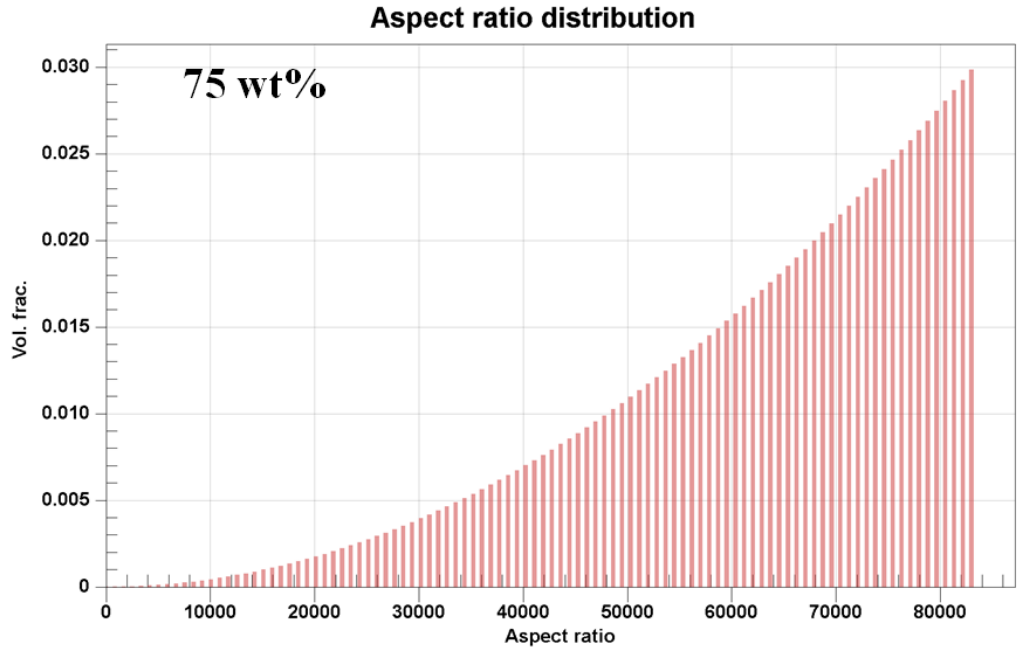
Aspect ratio distribution
75 wt%
Vol. frac.
0.030
0.025
0.020
0.015
0.010
0.005
0
0
10000
20000
30000
40000
50000
60000
70000
80000
Aspect ratio

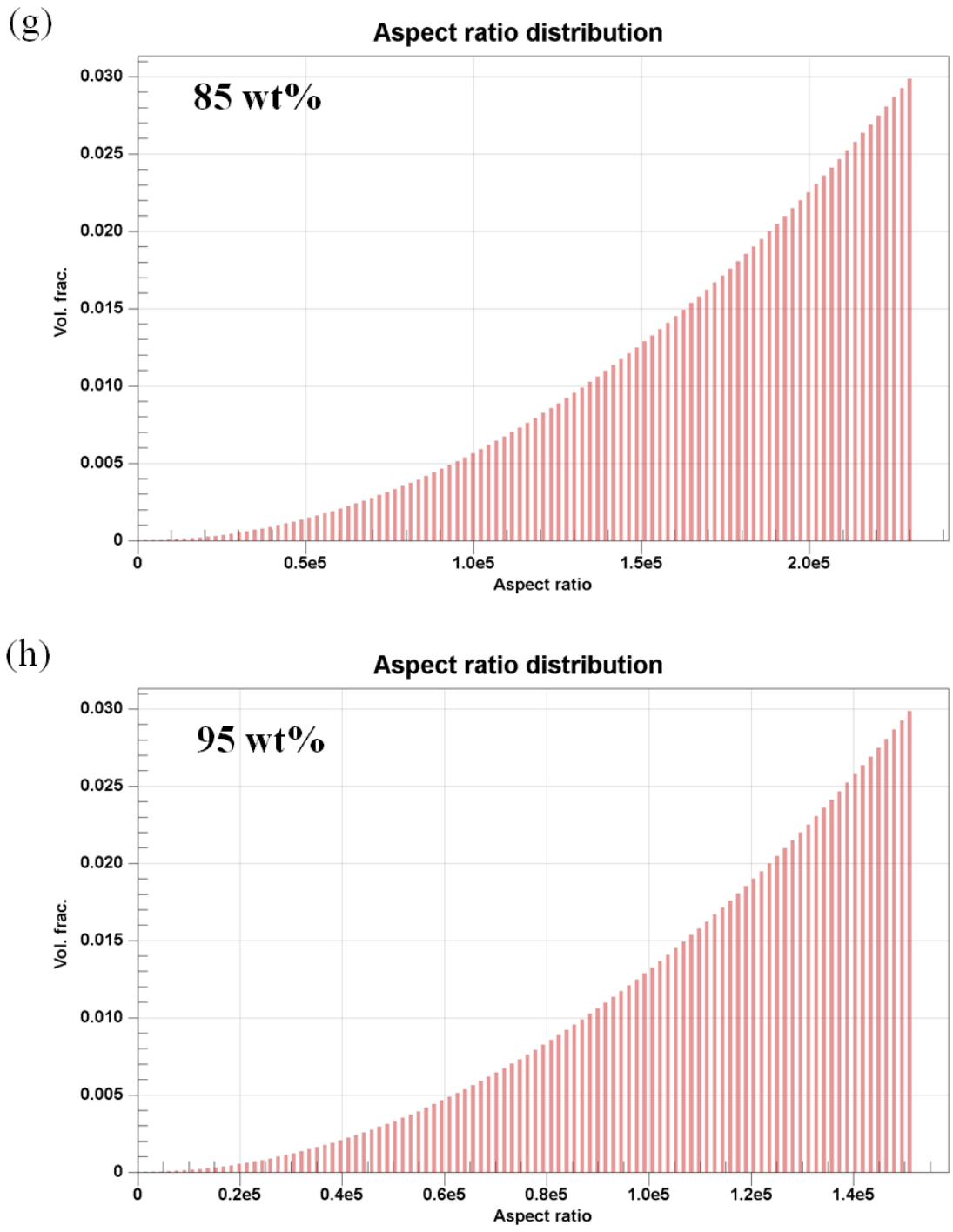

Fig. 4.12. Aspect ratio distribution at (a) 25 wt%; (b) 35 wt%; (c) 45 wt%; (d) 55 wt%; (e) 65 wt%; (f) 75 wt%; (g) 85 wt% and (h) 95 wt% of SWCNT loading.

The result proposed that the curved SWCNTs with large aspect ratio distribution formed a good network and excellent electronic channels for the composites, leading to a nonlinear rise in σ. With the optimized microstructure and aspect ratio distribution, the κ value of composite is simulated by varying SWCNT wt%, as presented in Fig.4.13a. Understandably, κ rises with increasing CNT content as the electronic contribution to thermal conductivity (κ_e) follows Wiedemann-Franz law and linearly increases with σ.

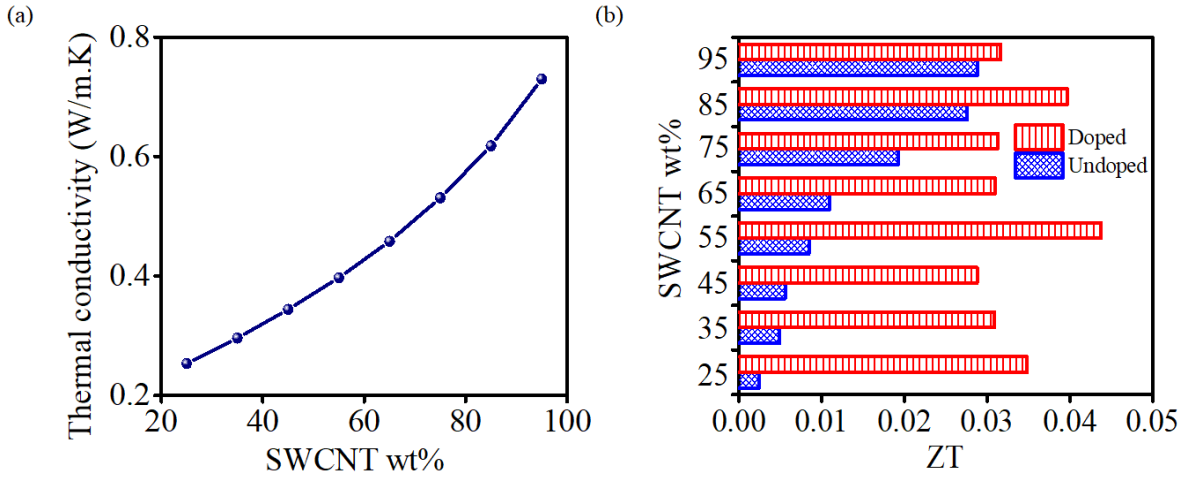

Fig. 4.13. Simulated (a) thermal conductivity and (b) *ZT* of composite by varying SWCNT wt%.

However, the simulation becomes more intricate for doped composites by adding $FeCl_3$ and corresponding CTC formation. Adaptation of a dynamic simulation model is required, which is beyond the scope of the present work. *ZT* of the undoped and doped composites at room temperature is calculated using the simulated κ values assuming that doping primarily affects σ rather than κ [69]. A maximum *ZT* of 0.044 at 303 K is obtained for the doped composite with 55 wt% of SWCNT (Fig. 4.13b). The observation confirms that although we achieved the highest PF with a higher CNT content because of its 2D thin film morphology, it would be less useful as a TE generator (TEG) for higher thermal shorting between the hot and cold junctions.

4.2.6. *Flexible TEG prototype*

A practical disadvantage in using conventional TEGs to harvest heat waste is that they are uneconomical where the heat source has moving parts or has a curved surface. In such a scenario, the fabrication of flexible and lightweight TEGs is proposed as a solution to harvest energy. The preparation scheme of flexible TEGs and measurement geometry are shown in Fig. 4.14.

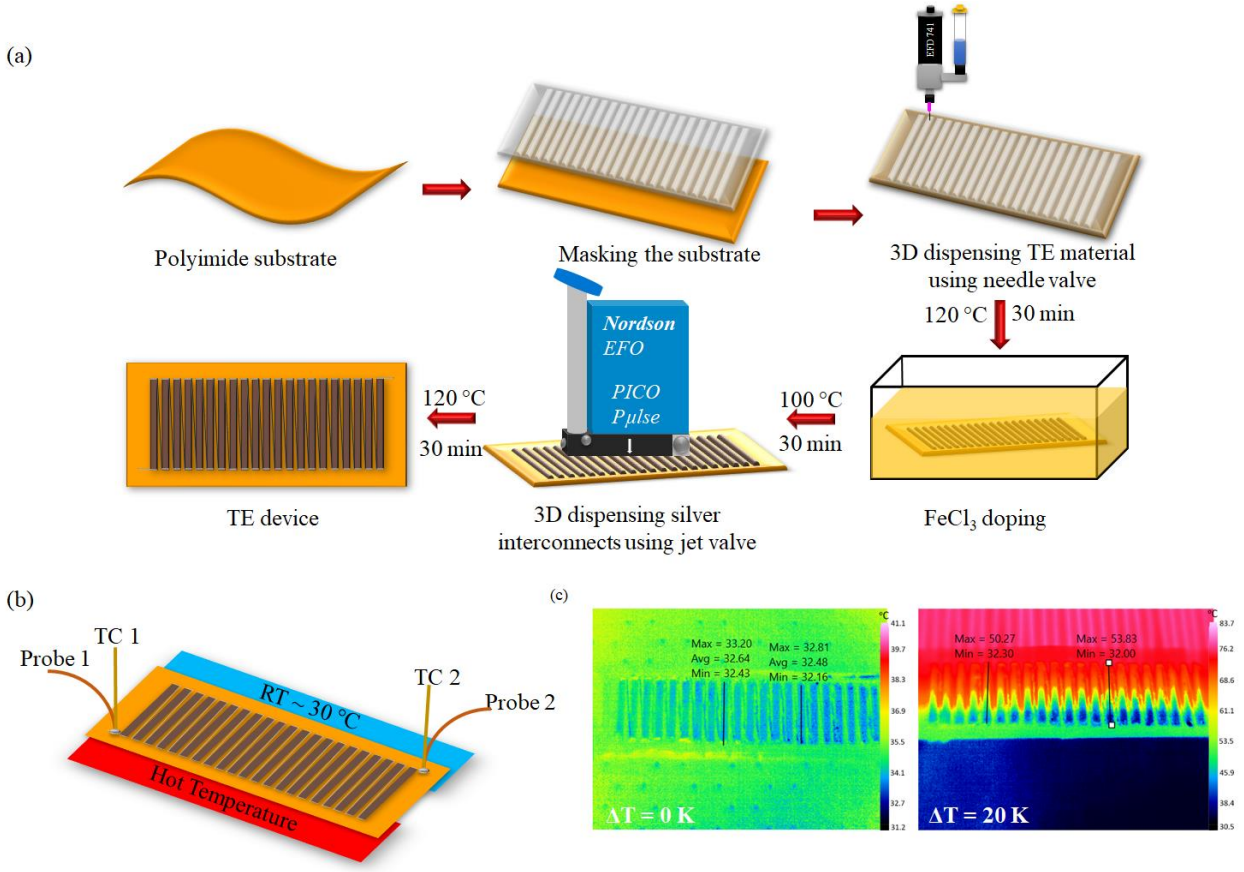

Fig. 4.14. (a) Fabrication of flexible TEG consisting of 21 legs; (b) Schematic diagram of geometry of TEG measurement and (c) Thermal image of temperature distribution at ΔT= 0 K and 20 K.

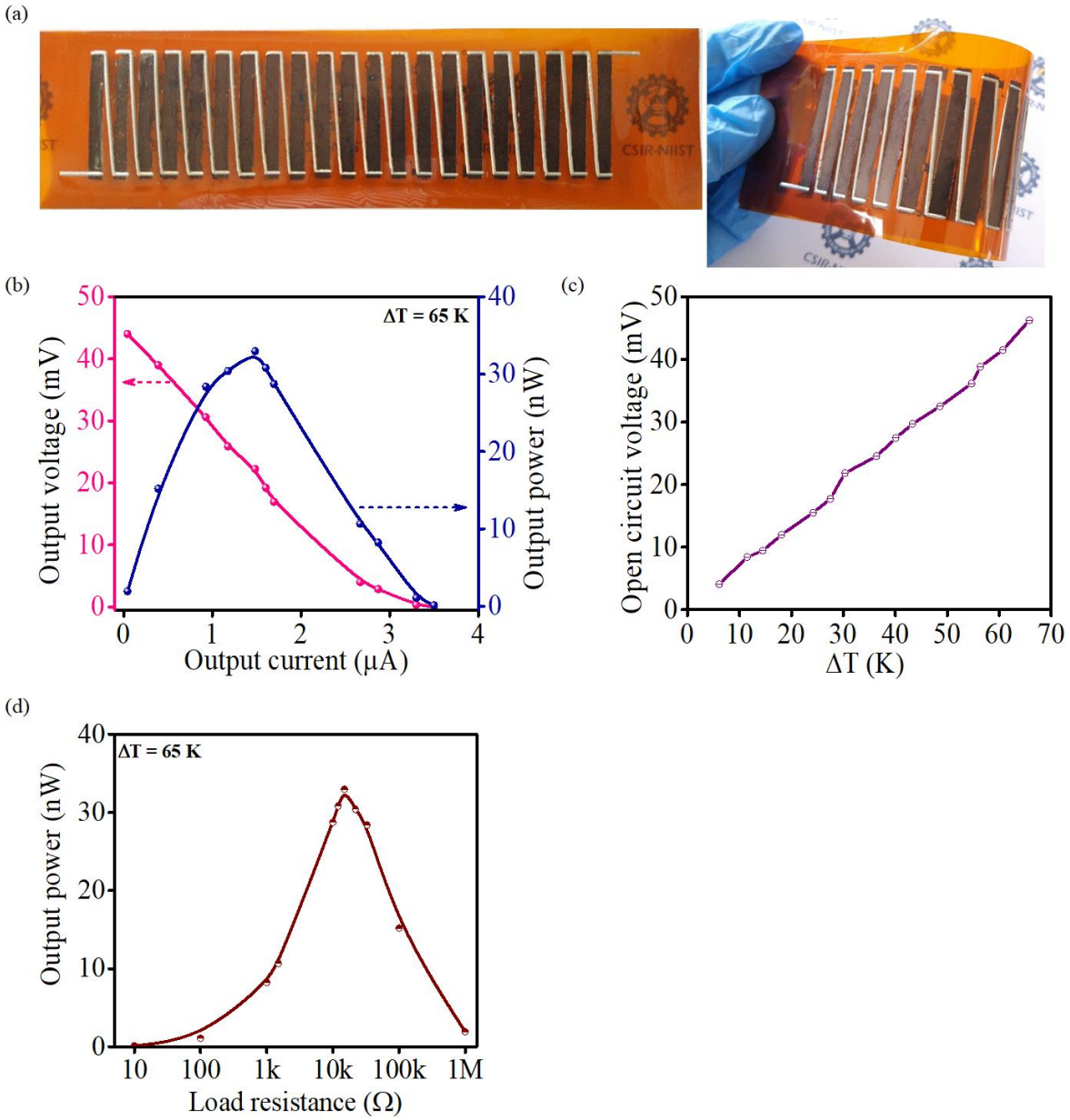

Fig. 4.15. (a) Photograph of a 21-legged flexible TEG; (b) The output current - voltage and current -power plots; (c) The open-circuit voltage by varying Δ*T* and (d) The output power by varying load resistance at a Δ*T* of 65 K.

A representative device prototype comprising 21 TE legs arranged on a polyimide flexible substrate using the doped composite (55 wt% SWCNT) is fabricated, and highly conducting (HPS-FG777) silver lines were used as the interconnects (Fig. 4.15a). Fig. 4.15b shows the output

current-voltage and current-power plots of the TEG at ΔT = 65 K. The internal resistance of the TEG was ~15 kΩ, and we obtained a peak power output of 32.9 nW (ΔT= 65 K) around that resistance range due to the impedance matching. The open-circuit voltage as a function of ΔT is plotted in Fig. 4.15c. Fig. 4.15d shows the power output at an applied ΔT of 65 K by varying load resistance.

4.2.7. TEG prototype simulation using COMSOL

Calculating the maximum extractable power from a TEG is crucial for understanding the engineering limitations in device fabrications and identifying the pathways for performance loss. We modelled a 21-legged TEG prototype, identical to the previously-mentioned device, using COMSOL Multiphysics®-thermoelectric effect module. The module simultaneously solves the equations for the coupled heat transfer in solids and electric currents to predict the output power generated in the TE device [70]. A detailed explanation of the governing equations and the theory can be found in previous literature [71,72].

The model is developed by mimicking the geometry of the experimental setup. The accuracy of the geometry was found to be the critical success requirement, as any variations would result in significant output deviations. The TE legs consisted of doped composite (55 wt% of SWCNT) with a dimension of 4 mm × 40 mm × 2.5 μm. Table 4.5 shows the material properties used for the model development, where the substrate and interconnect materials properties were taken from the manufacturer-provided datasheet. The complete geometry developed for the model is illustrated in Fig. 4.16a. The 'Normal' mesh option, one of the pre-defined choices, is suitable for this test as using a smaller mesh leads only to a higher computation time without any accuracy benefit. Fig. 4.16b shows the mesh size adopted for the current simulation. The output of this experimental test cell is simulated in Multiphysics using an electrical circuit module with 15 kΩ

load resistance. Various inbuilt simulation modules were used in the model to account for the heat transfer in solids, electric current, thermos-electric effects, and electromagnetic heating.

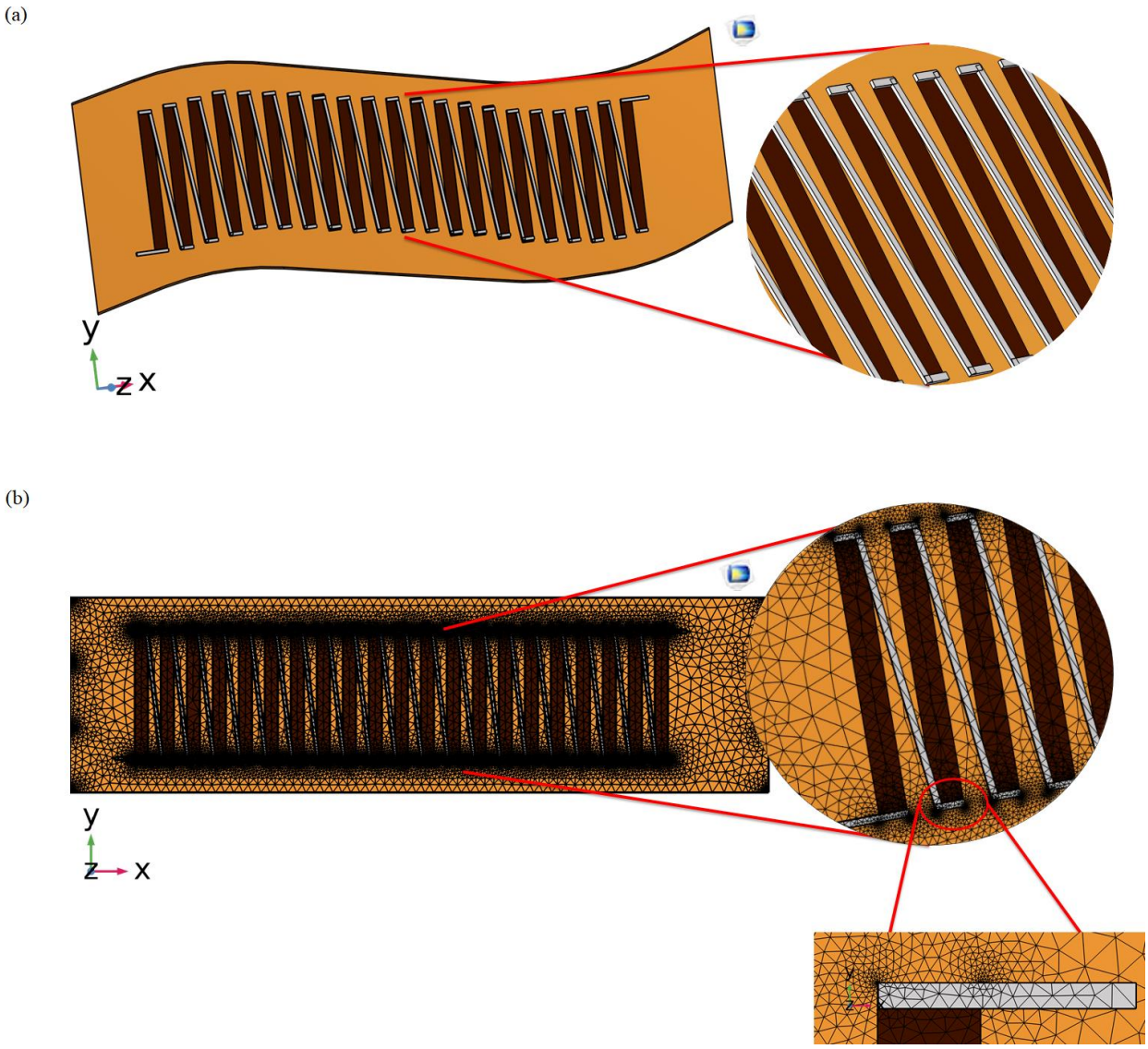

Fig. 4.16. (a) The complete geometry of the flexible TEG model and (b) The developed model showing the mesh used for the simulation with a zoomed-in part.

Table 4.5. Material properties used in COMSOL.

Particulars	**Substrate (Polyimide KAPTON 50 HN)**	**TE material (Doped composite with 55 wt% SWCNT)**	**Interconnection (Silver)**
ρ (kg/m^3)	1420	1792	10490
σ (S/cm)	6.66E-18	421	7.69E4
κ (W/m.K)	0.2	0.377	9.1
C_p (J/g.K)	1.09	0.99	0.233
α (μV/K)	1000	35.72	6.5
Relative permittivity, ε	3.48	3.53	-15.24

We kept the hot-end connection lead with variable heating capacity at the earth potential. The output is taken from the cold-end connection lead, maintained at room temperature. Adiabatic boundary conditions were applied on other surfaces for simulation. A schematic representation of the boundary conditions and an example of temperature distribution at a ΔT= 65 K are shown in Fig. 4.17a & b, respectively. A combined plot of experimental and simulated open-circuit voltage and output power as a function of ΔT is plotted in Fig. 4.18a & b. The simulated output current-voltage and current-power plots, are shown in Fig. 4.18c. The results were in good agreement except for the minor variations in higher ΔT. Therefore, the same model could be used for device performance simulations in different scenarios.

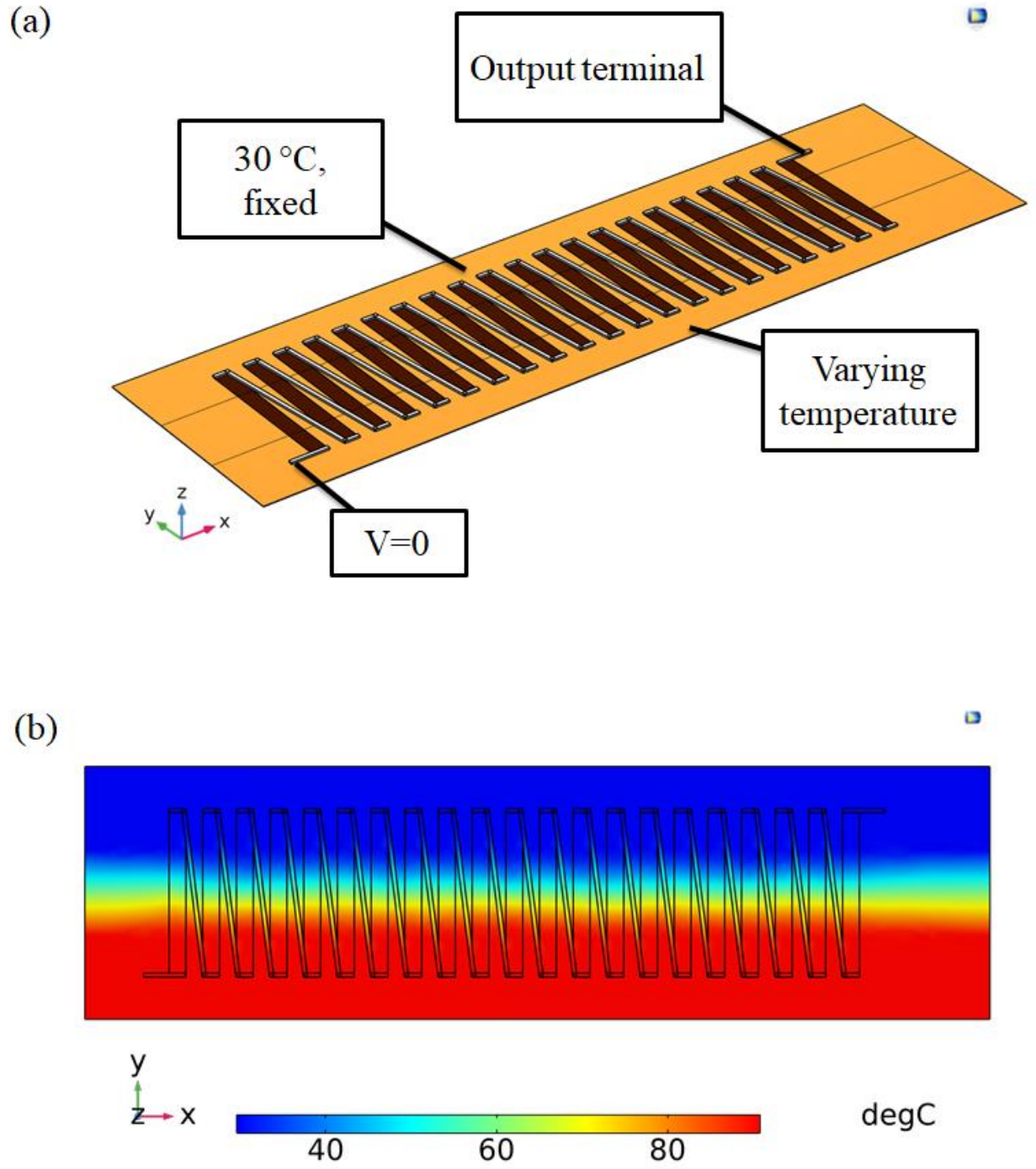

Fig. 4.17. (a) Boundary conditions applied to TEG and (b) Temperature distribution at ΔT = 65 K.

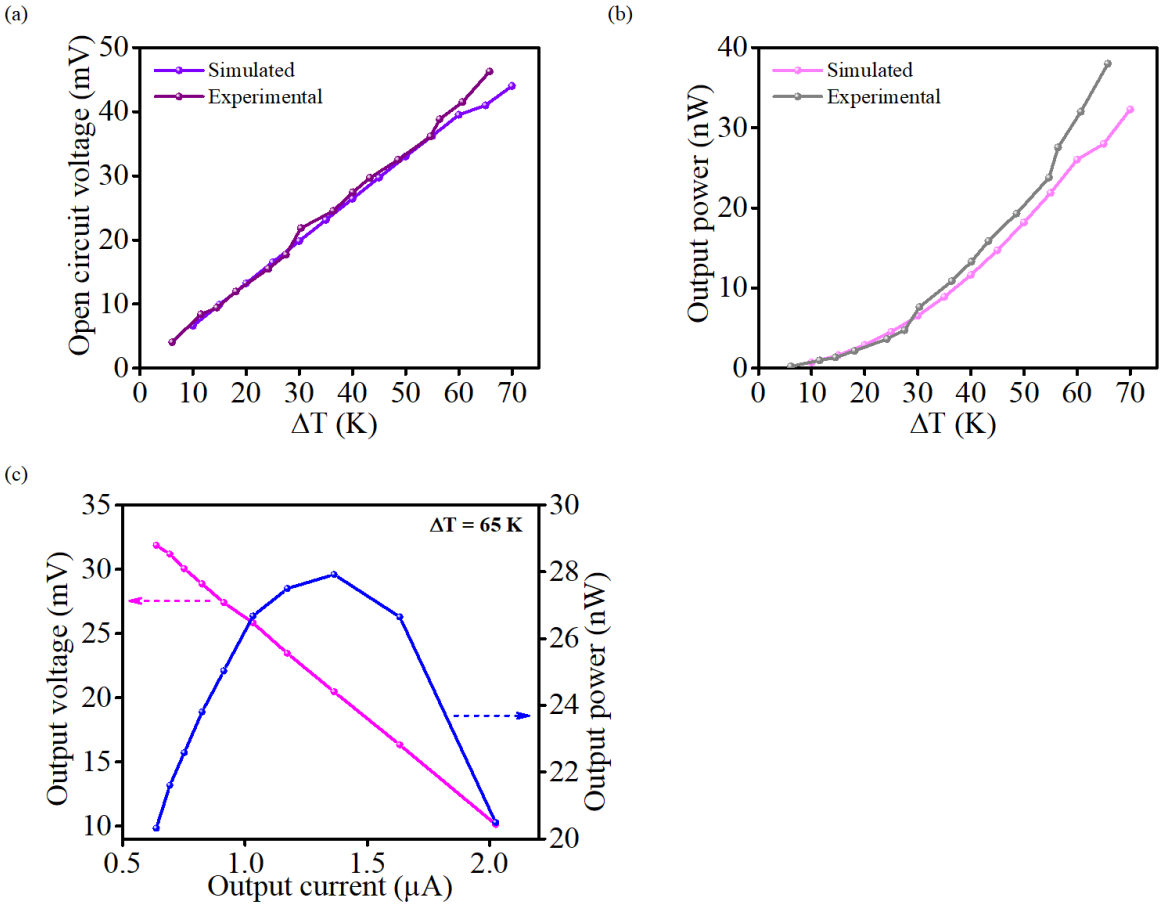

Fig. 4.18. The combined plot of the simulated and experimental (a) open-circuit voltage; (b) output power of flexible TEG versus ΔT and (c) Simulated output current-voltage and current-power plots at ΔT = 65 K.

The average resistance of each leg for the as-fabricated TEG and silver interconnects are ~350 Ω and 5 Ω, respectively. Thus, the total resistance for the 21-leg TEG should ideally be ~7.45 kΩ. Therefore, more than half of the device resistance (~15 kΩ) originated from the contact resistance at the junctions between TE legs and silver interconnects that significantly enhanced the Joule loss. Although the device power output obtained in our experiment matches with the literature reported values [19], the output power could be further enhanced by taking measures for resistance control. Fig. 4.19a shows that by reducing the device resistance by 5 and 7.5 kΩ, the

peak power output could be improved by 47% and 92% at the corresponding matching load resistance values. The resistance optimization is possible by using different interconnects or overlapping n-type TE materials with higher conductivity and by changing TE leg dimensions. The predicted output power variation with TE leg dimensions is plotted in Fig. 4.19b, which shows ~3.4× improvement by lowering the TE leg length to 10 mm. Such simulation models could be upgraded by incorporating a proper heat sink option on the cold side to optimize the device architecture for specific applications.

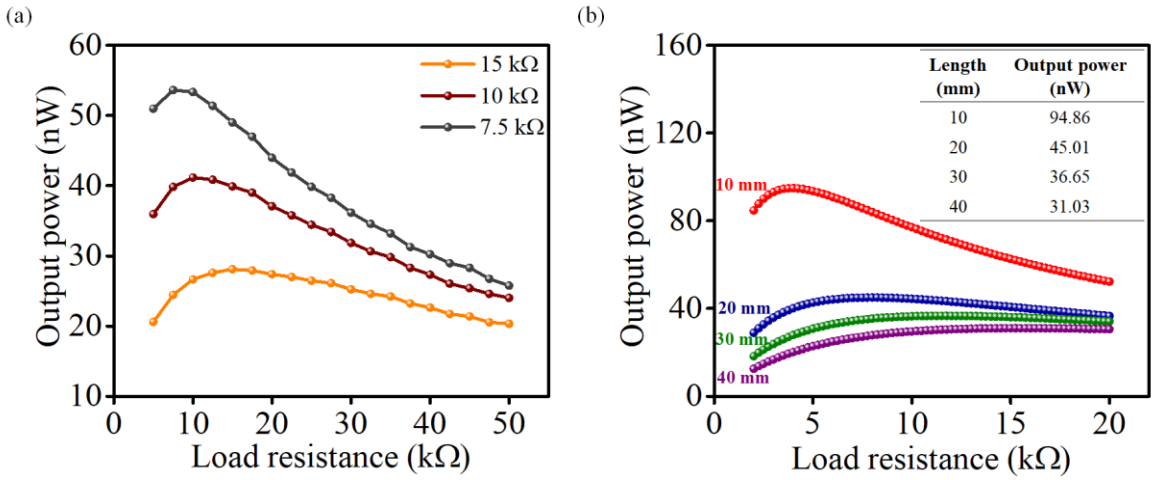

Fig. 4.19. Output power by varying load resistance for (a) different internal resistance and (b) different TE leg length.

4.3. Conclusions

The unique carrier transport mechanism of PBDTT-FTTE:SWCNT composites offered good potential for TE applications. The SWCNTs enhanced the mechanical strength and developed strong π-π interfacial interactions with PBDTT-FTTE, revealed through UV-vis-NIR, Raman, SEM, and TEM studies. A percolation-like behavior is observed for σ with SWCNT addition into the polymer host (peak value ~ 795 S/cm at 85 wt%), while post-$FeCl_3$ treatment, two different conductivity maxima appear at 55% and 85 wt% SWCNT. The position of the Fermi level and VBM remain unchanged, leading to the invariance in α in the composite. However, morphological understandings indicate a functionally 2D transport channel enhanced σ. The peak PF value (98 $\mu W/m.K^2$ at approximately 387 K) is obtained with 85 wt% SWCNT content. A 1D-VRH model effectively explained the charge transport mechanism in the composite films before and after doping. The simulation model is validated by obtaining a perfect fit for the σ variation trend, and the same model was used to predict κ. The maximum ZT (0.044 at 303 K) was obtained for the doped composite with 55 wt% of SWCNT. Power generation by a 21-legged flexible TEG is presented, and the ways to improve the maximum extractable power are discussed by mimicking the device in the COMSOL Multiphysics simulation platform.

References

[1] Z. Fan, Y. Zhang, L. Pan, J. Ouyang, Q. Zhang, Recent developments in flexible thermoelectrics: From materials to devices, Renew. Sustain. Energy Rev. 137 (2021) 110448. https://doi.org/10.1016/j.rser.2020.110448.

[2] M. Goel, M. Thelakkat, Polymer Thermoelectrics: Opportunities and Challenges, Macromolecules. 53 (2020) 3632–3642. https://doi.org/10.1021/acs.macromol.9b02453.

[3] C. Nath, A. Kumar, Y.-K. Kuo, G.S. Okram, High thermoelectric figure of merit in nanocrystalline polyaniline at low temperatures, Appl. Phys. Lett. 105 (2014) 133108. https://doi.org/10.1063/1.4897146.

[4] G.-H. Kim, L. Shao, K. Zhang, K.P. Pipe, Engineered doping of organic semiconductors for enhanced thermoelectric efficiency, Nat. Mater. 12 (2013) 719–723. https://doi.org/10.1038/nmat3635.

[5] O. Bubnova, Z.U. Khan, A. Malti, S. Braun, M. Fahlman, M. Berggren, X. Crispin, Optimization of the thermoelectric figure of merit in the conducting polymer poly(3,4-ethylenedioxythiophene), Nat. Mater. 10 (2011) 429–433. https://doi.org/10.1038/nmat3012.

[6] L. Liang, G. Chen, C.-Y. Guo, Polypyrrole nanostructures and their thermoelectric performance, Mater. Chem. Front. 1 (2017) 380–386. https://doi.org/10.1039/C6QM00061D.

[7] E. Lim, K.A. Peterson, G.M. Su, M.L. Chabinyc, Thermoelectric Properties of Poly(3-hexylthiophene) (P3HT) Doped with 2,3,5,6-Tetrafluoro-7,7,8,8-tetracyanoquinodimethane (F 4 TCNQ) by Vapor-Phase Infiltration, Chem. Mater. 30 (2018) 998–1010. https://doi.org/10.1021/acs.chemmater.7b04849.

[8] S. Qu, Q. Yao, L. Wang, Z. Chen, K. Xu, H. Zeng, W. Shi, T. Zhang, C. Uher, L. Chen, Highly anisotropic P3HT films with enhanced thermoelectric performance via organic small molecule epitaxy, NPG Asia Mater. 8 (2016) e292–e292. https://doi.org/10.1038/am.2016.97.

[9] H. Shang, H. Gu, F. Ding, Z. Ren, Recent advances in flexible thermoelectrics, Appl. Phys. Lett. 118 (2021) 170503. https://doi.org/10.1063/5.0049451.

[10] M.A. Zoui, S. Bentouba, J.G. Stocholm, M. Bourouis, A Review on Thermoelectric Generators: Progress and Applications, Energies. 13 (2020) 3606. https://doi.org/10.3390/en13143606.

[11] N. Nandihalli, C.-J. Liu, T. Mori, Polymer based thermoelectric nanocomposite materials and devices: Fabrication and characteristics, Nano Energy. 78 (2020) 105186. https://doi.org/10.1016/j.nanoen.2020.105186.

[12] X. Zhou, C. Pan, C. Gao, A. Shinohara, X. Yin, L. Wang, Y. Li, Q. Jiang, C. Yang, L. Wang, Thermoelectrics of two-dimensional conjugated benzodithiophene-based polymers: density-of-states enhancement and semi-metallic behavior, J. Mater. Chem. A. 7 (2019) 10422–10430. https://doi.org/10.1039/C9TA01437C.

[13] L. Wang, C. Pan, Z. Chen, X. Zhou, C. Gao, L. Wang, A study of the thermoelectric properties of benzo[1,2- b :4,5- b ′]dithiophene–based donor–acceptor conjugated polymers, Polym. Chem. 9 (2018) 4440–4447. https://doi.org/10.1039/C8PY00812D.

[14] Y.-Y. Hsieh, Y. Zhang, L. Zhang, Y. Fang, S.N. Kanakaraaj, J.-H. Bahk, V. Shanov, High thermoelectric power-factor composites based on flexible three-dimensional graphene and polyaniline, Nanoscale. 11 (2019) 6552–6560. https://doi.org/10.1039/C8NR10537E.

[15] C. Cho, J. Son, Organic Thermoelectric Multilayers with High Stretchiness,

Nanomaterials. 10 (2019) 41. https://doi.org/10.3390/nano10010041.

[16] R. Wu, H. Yuan, C. Liu, J.-L. Lan, X. Yang, Y.-H. Lin, Flexible PANI/SWCNT thermoelectric films with ultrahigh electrical conductivity, RSC Adv. 8 (2018) 26011–26019. https://doi.org/10.1039/C8RA04863K.

[17] T. Farrell, K. Wang, C.-W. Lin, R.B. Kaner, Organic dispersion of polyaniline and single-walled carbon nanotubes and polyblends with poly(methyl methacrylate), Polymer (Guildf). 129 (2017) 1–4. https://doi.org/10.1016/j.polymer.2017.09.032.

[18] N. Baghdadi, M.S. Zoromba, M.H. Abdel-Aziz, A.F. Al-Hossainy, M. Bassyouni, N. Salah, One-Dimensional Nanocomposites Based on Polypyrrole-Carbon Nanotubes and Their Thermoelectric Performance, Polymers (Basel). 13 (2021) 278. https://doi.org/10.3390/polym13020278.

[19] C.T. Hong, Y.H. Kang, J. Ryu, S.Y. Cho, K.-S. Jang, Spray-printed CNT/P3HT organic thermoelectric films and power generators, J. Mater. Chem. A. 3 (2015) 21428–21433. https://doi.org/10.1039/C5TA06096F.

[20] W. Fan, C.-Y. Guo, G. Chen, Flexible films of poly(3,4-ethylenedioxythiophene)/carbon nanotube thermoelectric composites prepared by dynamic 3-phase interfacial electropolymerization and subsequent physical mixing, J. Mater. Chem. A. 6 (2018) 12275–12280. https://doi.org/10.1039/C8TA04838J.

[21] X. Wang, H. Wang, B. Liu, Carbon Nanotube-Based Organic Thermoelectric Materials for Energy Harvesting, Polymers (Basel). 10 (2018) 1196. https://doi.org/10.3390/polym10111196.

[22] F. Liu, X. Zhou, C. Pan, L. Wang, A facile method to intimately contacted nanocomposites as thermoelectric materials: Noncovalent heterojunctions, J. Power

Sources. 412 (2019) 153–159. https://doi.org/10.1016/j.jpowsour.2018.11.028.

[23] Y.-J. Lee, K.-S. Jeng, J.-T. Chen, K.W. Sun, Exceptionally low thermal conductivity of poly(3-hexylthiophene) single nanowires, RSC Adv. 5 (2015) 90847–90851. https://doi.org/10.1039/C5RA09977C.

[24] J. Liu, X. Wang, D. Li, N.E. Coates, R.A. Segalman, D.G. Cahill, Thermal Conductivity and Elastic Constants of PEDOT:PSS with High Electrical Conductivity, Macromolecules. 48 (2015) 585–591. https://doi.org/10.1021/ma502099t.

[25] S. Liu, H. Li, C. He, Simultaneous enhancement of electrical conductivity and seebeck coefficient in organic thermoelectric SWNT/PEDOT:PSS nanocomposites, Carbon N. Y. 149 (2019) 25–32. https://doi.org/10.1016/j.carbon.2019.04.007.

[26] R.J. Patel, T.B. Tighe, I.N. Ivanov, M.A. Hickner, Electro-optical properties of electropolymerized poly(3-hexylthiophene)/carbon nanotube composite thin films, J. Polym. Sci. Part B Polym. Phys. 49 (2011) 1269–1275. https://doi.org/10.1002/polb.22307.

[27] P. Rathore, C.M.S. Negi, A. Yadav, A.S. Verma, S.K. Gupta, Influence of MWCNT doping on performance of polymer bulk heterojunction based devices, Optik (Stuttg). 160 (2018) 131–137. https://doi.org/10.1016/j.ijleo.2018.01.092.

[28] V. Ignatious, N. Raveendran, A. Prabhakaran, Y. Tanjore Puli, V. Chakkooth, B. Deb, MWCNT/Thienothiophene based All-Organic thermoelectric composites: Enhanced performance by realigning of the Fermi level through doping, Chem. Eng. J. 409 (2021) 128294. https://doi.org/10.1016/j.cej.2020.128294.

[29] L. Wang, C. Pan, Z. Chen, W. Zhou, C. Gao, L. Wang, Enhanced Thermoelectric Performance of Conjugated Polymer/Single-Walled Carbon Nanotube Composites with

Strong Stacking, ACS Appl. Energy Mater. 1 (2018) 5075–5082. https://doi.org/10.1021/acsaem.8b01126.

[30] C. Bounioux, P. Díaz-Chao, M. Campoy-Quiles, M.S. Martín-González, A.R. Goñi, R. Yerushalmi-Rozen, C. Müller, Thermoelectric composites of poly(3-hexylthiophene) and carbon nanotubes with a large power factor, Energy Environ. Sci. 6 (2013) 918–925. https://doi.org/10.1039/c2ee23406h.

[31] C.T. Hong, W. Lee, Y.H. Kang, Y. Yoo, J. Ryu, S.Y. Cho, K.-S. Jang, Effective doping by spin-coating and enhanced thermoelectric power factors in SWCNT/P3HT hybrid films, J. Mater. Chem. A. 3 (2015) 12314–12319. https://doi.org/10.1039/C5TA02443A.

[32] L. Hao, J. Kang, J. Shi, J. Xu, J. Cao, L. Wang, Y. Liu, C. Pan, Enhanced thermoelectric performance of poly(3-substituted thiophene)/single-walled carbon nanotube composites via polar side chain modification, Compos. Sci. Technol. 199 (2020) 108359. https://doi.org/10.1016/j.compscitech.2020.108359.

[33] V. Ignatious, N. Raveendran, S. Poovattil, N. Jacob, V. Chakkooth, B. Deb, Studies on the Doping Mechanism of Conjugated Thienothiophene Polymer/MWCNT Hybrids for Thermoelectric Application, Macromol. Mater. Eng. (2022) 2100916. https://doi.org/10.1002/mame.202100916.

[34] C. Vijayakumar, B. Balan, M.-J. Kim, M. Takeuchi, Noncovalent Functionalization of SWNTs with Azobenzene-Containing Polymers: Solubility, Stability, and Enhancement of Photoresponsive Properties, J. Phys. Chem. C. 115 (2011) 4533–4539. https://doi.org/10.1021/jp111248r.

[35] R.N. Gontijo, G.A.M. Sáfar, A. Righi, R.M. Jain, M.S. Strano, C. Fantini, Quantifying (n,m) species in single-wall carbon nanotubes dispersions by combining Raman and

optical absorption spectroscopies, Carbon N. Y. 115 (2017) 681–687. https://doi.org/10.1016/j.carbon.2017.01.041.

[36] Y. Piao, J.R. Simpson, J.K. Streit, G. Ao, M. Zheng, J.A. Fagan, A.R. Hight Walker, Intensity Ratio of Resonant Raman Modes for (n , m) Enriched Semiconducting Carbon Nanotubes, ACS Nano. 10 (2016) 5252–5259. https://doi.org/10.1021/acsnano.6b01031.

[37] Puech, Kandara, Paredes, Moulin, Weiss-Hortala, Kundu, Ratel-Ramond, Plewa, Pellenq, Monthioux, Analyzing the Raman Spectra of Graphenic Carbon Materials from Kerogens to Nanotubes: What Type of Information Can Be Extracted from Defect Bands?, C — J. Carbon Res. 5 (2019) 69. https://doi.org/10.3390/c5040069.

[38] M.S. Dresselhaus, A. Jorio, A.G. Souza Filho, R. Saito, Defect characterization in graphene and carbon nanotubes using Raman spectroscopy, Philos. Trans. R. Soc. A Math. Phys. Eng. Sci. 368 (2010) 5355–5377. https://doi.org/10.1098/rsta.2010.0213.

[39] T. Liu, A. Shinohara, G. Tan, C. Pan, L. Wang, The Cross-Linking Effect on the Thermoelectric Properties of Conjugated Polymer/Carbon Nanotube Composite Films, Macromol. Mater. Eng. 304 (2019) 1800730. https://doi.org/10.1002/mame.201800730.

[40] A. Kumar, J. Dalal, S. Dahiya, R. Punia, K.D. Sharma, A. Ohlan, A.S. Maan, In situ decoration of silver nanoparticles on single-walled carbon nanotubes by microwave irradiation for enhanced and durable anti-bacterial finishing on cotton fabric, Ceram. Int. 45 (2019) 1011–1019. https://doi.org/10.1016/j.ceramint.2018.09.280.

[41] O. Amargós-Reyes, J.-L. Maldonado, D. Romero-Borja, D. Barreiro-Argüelles, I. Caballero-Quintana, O. Barbosa-García, J.A. Gaspar, Organic photovoltaic cell analysis through quantum efficiency and scanning tunneling microscopy of the donor/blend as an active film, J. Mater. Sci. 54 (2019) 2427–2445. https://doi.org/10.1007/s10853-018-

2956-2.

[42] X. Zhou, C. Pan, A. Liang, L. Wang, T. Wan, G. Yang, C. Gao, W.-Y. Wong, Enhanced figure of merit of poly(9,9-di- n -octylfluorene-alt-benzothiadiazole) and SWCNT thermoelectric composites by doping with FeCl 3, J. Appl. Polym. Sci. 136 (2019) 47011. https://doi.org/10.1002/app.47011.

[43] S. Wang, Y. Zhou, Y. Liu, L. Wang, C. Gao, Enhanced thermoelectric properties of polyaniline/polypyrrole/carbon nanotube ternary composites by treatment with a secondary dopant using ferric chloride, J. Mater. Chem. C. 8 (2020) 528–535. https://doi.org/10.1039/C9TC06300E.

[44] Z.J. Han, K. Ostrikov, Controlled electronic transport in single-walled carbon nanotube networks: Selecting electron hopping and chemical doping mechanisms, Appl. Phys. Lett. 96 (2010) 233115. https://doi.org/10.1063/1.3449118.

[45] H. Peng, Aligned Carbon Nanotube/Polymer Composite Films with Robust Flexibility, High Transparency, and Excellent Conductivity, J. Am. Chem. Soc. 130 (2008) 42–43. https://doi.org/10.1021/ja078267m.

[46] V. Timoshevskii, Y. Ke, H. Guo, D. Gall, The influence of surface roughness on electrical conductance of thin Cu films: An ab initio study, J. Appl. Phys. 103 (2008) 113705. https://doi.org/10.1063/1.2937188.

[47] J. Tang, J. Ji, R. Chen, Y. Yan, Y. Zhao, Z. Liang, Achieving Efficient p-Type Organic Thermoelectrics by Modulation of Acceptor Unit in Photovoltaic π -Conjugated Copolymers, Adv. Sci. 9 (2022) 2103646. https://doi.org/10.1002/advs.202103646.

[48] N. Jayanth, P. Senthil, C. Prakash, Effect of chemical treatment on tensile strength and surface roughness of 3D-printed ABS using the FDM process, Virtual Phys. Prototyp. 13

(2018) 155–163. https://doi.org/10.1080/17452759.2018.1449565.

[49] M.A. Ali, H.H. Kim, C.Y. Lee, H.S. Soh, J.G. Lee, Effects of the FeCl3 concentration on the polymerization of conductive poly(3,4-ethylenedioxythiophene) thin films on (3-aminopropyl) trimethoxysilane monolayer-coated SiO2 surfaces, Met. Mater. Int. 15 (2009) 977–981. https://doi.org/10.1007/s12540-009-0977-8.

[50] J. M. Ziman, Electrons and phonons: the theory of transport phenomena in solids, 2001. https://global.oup.com/academic/product/electrons-and-phonons-9780198507796?cc=us&lang=en&.

[51] Y.-J. Hwang, B.A.E. Courtright, A.S. Ferreira, S.H. Tolbert, S.A. Jenekhe, 7.7% Efficient All-Polymer Solar Cells, Adv. Mater. 27 (2015) 4578–4584. https://doi.org/10.1002/adma.201501604.

[52] Y.H. Kang, U.-H. Lee, I.H. Jung, S.C. Yoon, S.Y. Cho, Enhanced Thermoelectric Performance of Conjugated Polymer/CNT Nanocomposites by Modulating the Potential Barrier Difference between Conjugated Polymer and CNT, ACS Appl. Electron. Mater. 1 (2019) 1282–1289. https://doi.org/10.1021/acsaelm.9b00224.

[53] J.P. Sun, Z.X. Zhang, S.M. Hou, G.M. Zhang, Z.N. Gu, X.Y. Zhao, W.M. Liu, Z.Q. Xue, Work function of single-walled carbon nanotubes determined by field emission microscopy, Appl. Phys. A Mater. Sci. Process. 75 (2002) 479–483. https://doi.org/10.1007/s003390201403.

[54] S. Suzuki, Y. Watanabe, Y. Homma, S. Fukuba, S. Heun, A. Locatelli, Work functions of individual single-walled carbon nanotubes, Appl. Phys. Lett. 85 (2004) 127–129. https://doi.org/10.1063/1.1768304.

[55] K. Yokoyama, Y. Sato, M. Yamamoto, T. Nishida, K. Motomiya, K. Tohji, Y. Sato, Work

function, carrier type, and conductivity of nitrogen-doped single-walled carbon nanotube catalysts prepared by annealing via defluorination and efficient oxygen reduction reaction, Carbon N. Y. 142 (2019) 518–527. https://doi.org/10.1016/j.carbon.2018.10.052.

[56] N. Nandihalli, C.-J. Liu, T. Mori, Polymer based thermoelectric nanocomposite materials and devices: Fabrication and characteristics, Nano Energy. 78 (2020) 105186. https://doi.org/10.1016/j.nanoen.2020.105186.

[57] Y.J. Kim, C.R. Park, Analysis of Problematic Complexing Behavior of Ferric Chloride with N , N -Dimethylformamide Using Combined Techniques of FT-IR, XPS, and TGA/DTG, Inorg. Chem. 41 (2002) 6211–6216. https://doi.org/10.1021/ic011306p.

[58] S. Nappini, A. Matruglio, D. Naumenko, S. Dal Zilio, F. Bondino, M. Lazzarino, E. Magnano, Graphene nanobubbles on TiO 2 for in-operando electron spectroscopy of liquid-phase chemistry, Nanoscale. 9 (2017) 4456–4466. https://doi.org/10.1039/C6NR09061C.

[59] I. Pełech, U. Narkiewicz, D. Moszyński, R. Pełech, Simultaneous purification and functionalization of carbon nanotubes using chlorination, J. Mater. Res. 27 (2012) 2368–2374. https://doi.org/10.1557/jmr.2012.243.

[60] M. V. Russo, G. Polzonetti, A. Furlani, XPS and IR investigations of FeCl3-doped polyphenylacetylene: the solvent effect, Synth. Met. 39 (1991) 291–301. https://doi.org/10.1016/0379-6779(91)91755-Y.

[61] B.W. Veal, A.P. Paulikas, Final-state screening and chemical shifts in photoelectron spectroscopy, Phys. Rev. B. 31 (1985) 5399–5416. https://doi.org/10.1103/PhysRevB.31.5399.

[62] D. Son, S. Cho, J. Nam, H. Lee, M. Kim, X-ray-Based Spectroscopic Techniques for

Characterization of Polymer Nanocomposite Materials at a Molecular Level, Polymers (Basel). 12 (2020) 1053. https://doi.org/10.3390/polym12051053.

[63] DIGIMAT for Nano-composites, Doc. Version 2.0.1. (2010). https://www.e-xstream.com/.

[64] L. Liu, Z. Huang, A Note on mori-tanaka's method, Acta Mech. Solida Sin. 27 (2014) 234–244. https://doi.org/10.1016/S0894-9166(14)60033-1.

[65] A.N. Norris, An Examination of the Mori-Tanaka Effective Medium Approximation for Multiphase Composites, J. Appl. Mech. 56 (1989) 83–88. https://doi.org/10.1115/1.3176070.

[66] S. Tamayo-Vegas, A. Muhsan, M. Tarfaoui, K. Lafdi, L. Chang, Effect of CNT additives on the electrical properties of derived nanocomposites (experimentally and numerical investigation), Mater. Today Proc. 52 (2022) 199–205. https://doi.org/10.1016/j.matpr.2021.09.361.

[67] S. Hiura, N. Okada, J. Wakui, H. Narita, S. Kanehashi, T. Shimomura, Thermoelectric Properties of Poly(3-Hexylthiophene) Nanofiber Mat with a Large Void Fraction, Materials (Basel). 10 (2017) 468. https://doi.org/10.3390/ma10050468.

[68] N.R. Pradhan, H. Duan, J. Liang, G.S. Iannacchione, The specific heat and effective thermal conductivity of composites containing single-wall and multi-wall carbon nanotubes, Nanotechnology. 20 (2009) 245705. https://doi.org/10.1088/0957-4484/20/24/245705.

[69] X. Zhou, A. Liang, C. Pan, L. Wang, Effects of oxidative doping on the thermoelectric performance of polyfluorene derivatives/carbon nanotube composite films, Org. Electron. 52 (2018) 281–287. https://doi.org/10.1016/j.orgel.2017.10.029.

[70] M. Al Musleh, E.V. Topriska, D. Jenkins, E. Owens, Thermoelectric generator characterization at extra-low-temperature difference for building applications in extreme hot climates: Experimental and numerical study, Energy Build. 225 (2020) 110285. https://doi.org/10.1016/j.enbuild.2020.110285.

[71] X. Gou, H. Xiao, S. Yang, Modeling, experimental study and optimization on low-temperature waste heat thermoelectric generator system, Appl. Energy. 87 (2010) 3131–3136. https://doi.org/10.1016/j.apenergy.2010.02.013.

[72] I.M. Abdel-Motaleb, S.M. Qadri, Multi-Physics Numerical Simulation of Thermoelectric Devices, J. Electron. Cool. Therm. Control. 07 (2017) 123–135. https://doi.org/10.4236/jectc.2017.74010.

CHAPTER 5

Summary and Outlook

Organic-based hybrid thermoelectric (TE) materials offer excellent R&D opportunities for various scientific disciplines such as physicists, chemists, and engineers. There are several open-ended questions regarding the physics of carrier transport in organic-based hybrid TE systems, even at the root of this field. Notably, it remains the case in many of the most well-studied systems that the understanding of specific carriers responsible for the measured property values or the density of states at the interfaces is unknown. However, the field is transitioning from proof-of-principle to realistic TE generator design and scaling, creating space for new commercial applications such as the Internet of Things (IoT) and wearable electronics. Throughout this thesis, we have focused on elucidating the fundamental phenomena in the effect of doping in conjugated thienothiophene polymer/ carbon nanotube (CNT) based material systems.

This thesis started with a nanocomposite of conjugated thienothiophene polymers, PBDTT-FTTE, and multi-walled carbon nanotube (MWCNT), followed by extrinsic doping with an oxidizing agent, and then made systematic enhancements in TE properties. Chapter 2 shows that the electrical conductivity is boosted by 6.7x with concurrent 2.5x enhancement in the Seebeck coefficient by doping. Thus the electronic properties of this easily processable nanocomposite can be tuned to attain a large power factor of 48.21 $\mu W/m.K^2$ while retaining excellent ambient stability, which was not reported previously. In chapter 3, two different conjugated thienothiophene polymers, PBDTTT-C and PBDTTT-C-T, were selected to fabricate organic hybrids with MWCNT, followed by exploring the effect of doping on both. The PBDTTT-C/MWCNT hybrid increases the electrical conductivity slightly, although the post-doping Seebeck

coefficient remained unaffected. In contrast, PBDTTT-C-T/MWCNT hybrid exhibited simultaneous enhancements in electrical conductivity and Seebeck coefficient, owing to the changes in electronic structure and density of valence state. These experiments show that the TE efficiency of PBDTTT-C-T/MWCNT hybrids could be maximized by following a specific doping protocol.

Furthermore, the observations and insight gained from the MWCNT composite study were extended to the single-walled carbon nanotube (SWCNT) based composites. In chapter 4, a composite was fabricated with PBDTT-FTTE and SWCNT, which were subsequently doped with oxidizing agents. The preliminary results show a transport decoupling of electrical conductivity and Seebeck coefficient, in contrast to the MWCNT composite discussed in chapter 2. This work includes the computational observation of thermal conductivity of the PBDTT-FTTE/SWCNT system and predicts a ZT value of 0.044 at 303 K. Based on these results, the doping rationale of conjugated thienothiophene polymer-based TE/CNT hybrids were discussed in detail.

While these hybrid composites are promising, there is also a need to demonstrate realistic TE device performance with these systems. The fabrication part is partially discussed in chapters 2 and 4, where two hybrids composite-based TE devices were fabricated to leverage their low thermal conductivity and solution processability. In chapter 2, the device performance of a 7 leg TE device exhibits a power delivery of 7 nW when tested with applied temperature difference across the hot and cold junction of 65 K.

Chapter 4 elucidates a flexible printed TE prototype with 21 TE legs, which returned 32.9 nW power delivery with an applied temperature difference of 65 K. This chapter also includes the theoretical simulation of output performance of 21 legs flexible TE prototype, which predicts the ways to improve the maximum extractable power are discussed by mimicking the device in the

COMSOL Multiphysics simulation platform.

Overall, our findings help in shaping the hybrid design strategies by leveraging doping effects at the organic-inorganic interface. Coupling this doping-level insight with new hybrid design strategies brings the field closer to realizing practical, flexible TE modules and their integration into applications such as wearable technologies and the IoT's. The device demonstrations open the door for future point-of-care power generation strategies.

ANNEXURE I

Experimental Techniques

The present thesis consists of various types of advanced experiments. All three working chapter contains composite preparation followed by characterization using different measurement techniques, as summarized below. Books and journal papers used for this write-up are referenced at the end. Some statements were used without modifications from various online sources to describe the working principles.

A.1. Wide Angle X-ray Scattering (WAXS)

Wide-angle X-ray scattering (WAXS) is an X-ray-diffraction technique often used to determine the crystalline structure of polymers. This technique refers explicitly to the analysis of diffraction peaks scattered to wide angles, which implies that sub-nanometer-sized structures cause them. The diffraction patterns generated are used to determine the film′s chemical composition or phase composition, crystallite size and presence of film stress [1].

The schematic diagram of a typical measurement is shown in Fig. A.1a. In this method, a highly collimated beam of monochromatic x-rays is transmitted through a sample with a thickness on the order of 1 mm. The scattered x-rays are collected on a 2-dimensional (2D) area detector azimuthally in 360 degrees at a continuous range of scattering angles which deviate from the direct, transmitted beam [2]. The scattering angle (2θ) is expressed as,

$$D = {}^{2\pi}/_{q}$$

$q = 4\pi \sin\theta/\lambda$, λ = wavelength of the x-rays.

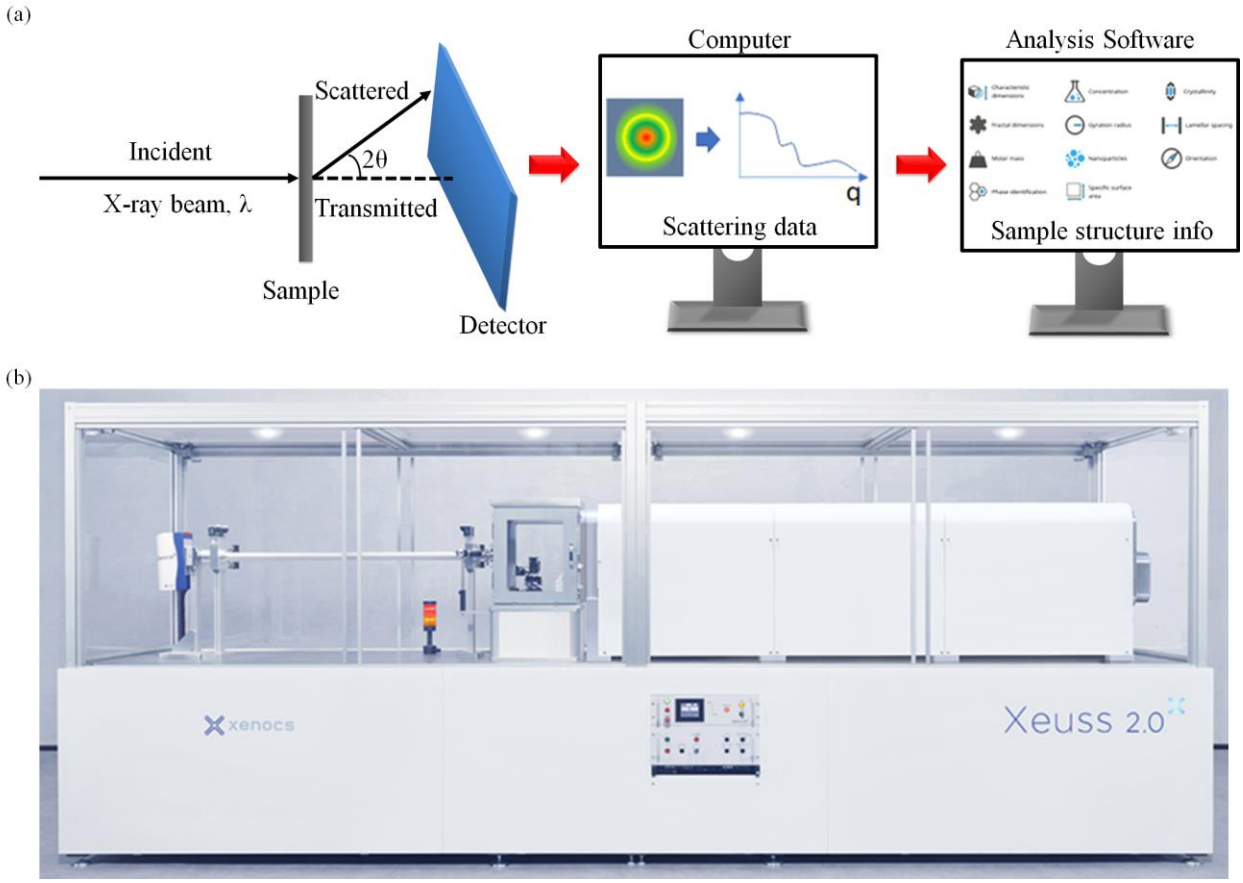

Fig. A.1. (a) The schematic diagram of WAXS measurement, (b) Photographic image of XEUSS 2.0 SAXS/WAXS system. Adapted from Ref. [2].

In the present thesis, the WAXS measurements were performed in transmission mode at ambient temperature using a XEUSS 2.0 SAXS/WAXS system (Fig. A.1b). The generator was operated at 50 kV and 0.60 mA, and the Cu- K_α radiation (λ = 1.54 Å) was sourced using a Genixmicro source from Xenocs. The X-ray beam was collimated with a FOX2D mirror and two pairs of scatterless slits from Xenocs. A Mar 345 image plate system (Mar-Research, Hamburg, Germany) detected the 2D patterns, and the Fit2D software was used for data processing. The sample-detector distance was set at 217.5 mm in the direction of the beam for data collection. Silver behenate was used as the standard sample for calibration of the scattering vectors of WAXS. As-casted film samples from polymer composite solution were used to obtain the data.

A.2. Scanning Electron Microscopy (SEM)

Scanning electron microscopy (SEM) is a technique for obtaining a sample′s image by scanning an electron beam across the surface of specially prepared specimens. When the electron beams interact with the specimen, it emits x-rays with a unique energy that can be detected to determine the composition of the material under examination. SEM is a tool used for materials characterization that provides information about the surface or near-surface structure, composition, surface topography, crystallography and defects [3].

The schematic diagram of the SEM is shown in Fig. A.2a. An electron gun is used to produce the electron beam and is focused onto the specimen surface by condenser lenses. Typically, an electron beam can focus on a small area about 10-20 nm in diameter. The image resolution is determined by this spot size, which is finally obtained by scanning. A set of scanning coils, made of wires carrying controlling current, are placed below the condenser lens to deflect the electron beams. The deflected beams are allowed to be rastered over the surface of the specimen, dwelling on each point for a period determined by the scan speed, usually in the microsecond range. Several signals like back-scattered electrons, secondary electrons, cathodoluminescence, and low-energy characteristic X-rays, are produced when the focused electron beam impinges on a specimen surface, which can be used to form an SEM image [4].

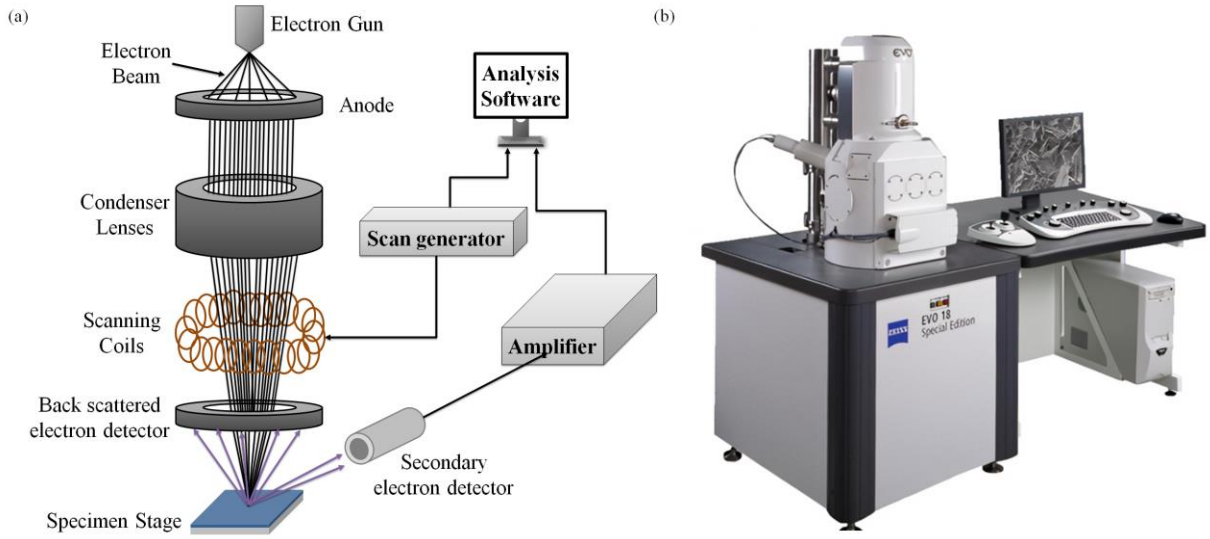

Fig. A.2. (a) The schematic diagram of SEM. Adapted from Ref. [3]. (b) Photographic image of ZEISS EVO18 Special Edition SEM. Adapted from Ref. [5].

The detector captures the secondary and back-scattered electrons and converts them into light flash that, in turn, produces electrical pulses. These pulses are then amplified by a signal amplifier and used to modulate the brightness of spots in a 2D picture that can be processed digitally. The brightness of a spot in an SEM image is a measure of the intensity of secondary electrons, which critically depends on the local surface topography.

It should be noted that it is necessary to make the sample conductive since, in the case of insulating samples, surface charges build up and deflect the course of secondary electrons. Therefore, a thin metal layer is usually deposited for nonconducting samples to make them conductive and prevent surface charging [4].

The SEM image was taken in chapters 2 & 3 using JOEL JSM-5600LV SEM equipped with a tungsten electron source. The electron beams are accelerated at a voltage of 15 kV, and the emitted secondary electrons were collected using an SE detector. In chapter 4, ZEISS EVO18 Special Edition SEM was used. The samples were imaged in a high vacuum at 15 keV beam energy

from a tungsten electron source, and the topographical information was collected using the five-segment diode SE detector. The collected signals were processed in ZEISS SmartSEM software. The samples were drop-cast onto a 10×10 mm glass substrate to form a film. In the present work, a thin layer of gold (~ 10 nm) was sputtered over the film samples to make them conductive and prevent surface charging.

A.3. Transmission Electron Microscopy (TEM)

Transmission electron microscopy (TEM) is a tool to analyze the structures of very thin specimens through which electrons are transmitted as probes. The most common use of TEM is to measure the distribution of particle size as well as the morphology of the specimen.

A TEM is constructed similar in principle to an optical microscope, where an electron beam, like the light in an optical microscope, travels through the sample and is affected by the structures in the specimen. However, the sample in the case of TEM is in a very high vacuum. The transmitted electron beam is projected onto a phosphor screen for imaging or digitally processed in a computer. An electron gun produces a stream of monochromatic electrons, which is focussed into a small beam using electromagnetic condenser lenses. The condenser lenses in TEM consist of current-carrying coils surrounded by iron. The electron beam is then focused on the specimen under examination. The transmitted beam is intercepted by objective lenses and finally captured on a fluorescent screen or detected by a CCD camera [4].

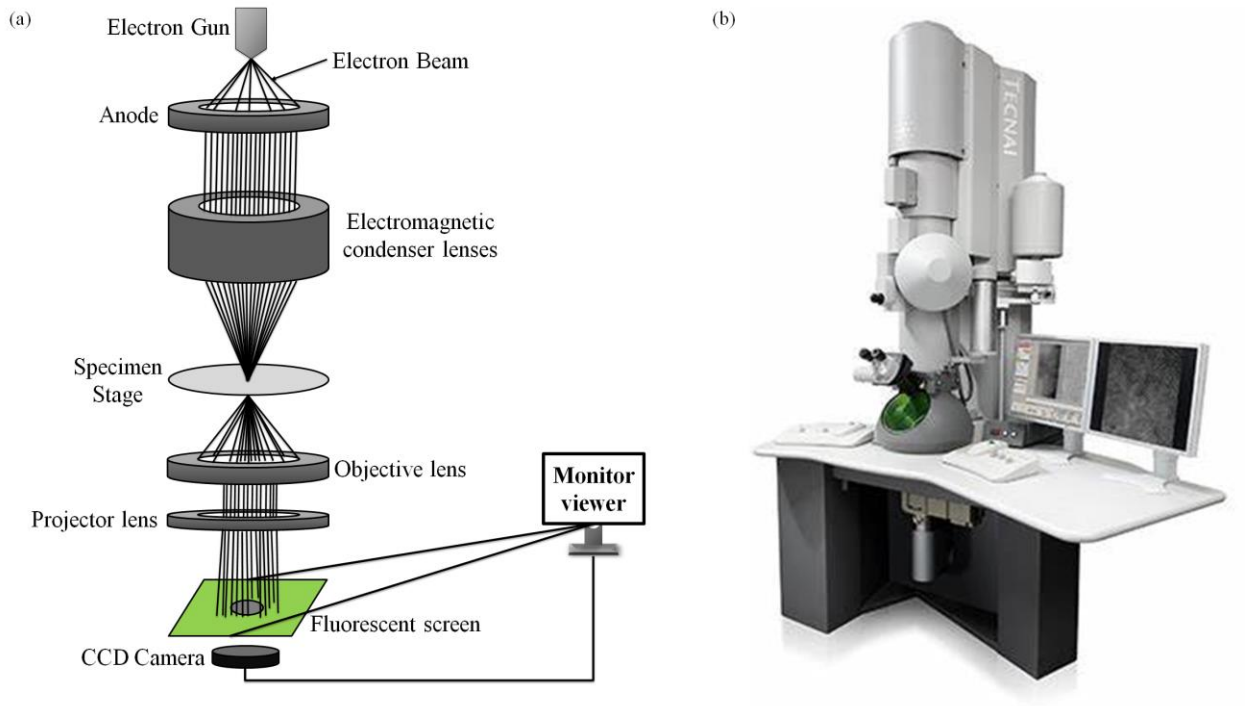

Fig. A.3. (a) The schematic diagram of TEM. Adapted from Ref. [6]. (b) Photographic image of FEI-Tecnai G2-30 TEM. Adapted from Ref. [7].

The specimens for TEM should be thin so that it allows the high-energy electrons to pass through. As the electrons pass through the sample, scattering occurs at the atoms because of Coulomb interactions. The degree of scattering (which can be elastic or inelastic) depends on the constituent atoms of the specimen. The heavy atoms (the ones with high atomic numbers) scatter the highest. The ray intensity transmitted through such areas is lower than that through the areas with light atoms. The number of electrons transmitted will determine the intensity distribution of the electrons reaching the fluorescent screen. Thus the area with heavy atoms will result in a relatively dark image [6]. Fig. A.3a shows the schematic of the working of a TEM.

The TEM image in chapter 4 was taken using FEI-Tecnai G2-30 TEM (Fig. A.3b), operated at an accelerating voltage of 300 kV with LaB6 cathode. The image was recorded using Multiscan 794 CCD camera (GATAN Inc.) and analyzed in GATAN Digital Micrograph 3 software suite.

For a typical TEM sample preparation, Ted Pella made 400 mesh carbon-coated Cu grids were used. 20 μL of nanocomposite solution was pipetted into a microsyringe and deposited on the grid. The mixture was allowed to air-dry for two days.

A.4 Absorption Spectroscopy

Absorption spectroscopy is a spectroscopic technique used to measure the absorption of radiation as it interacts with the sample. When electromagnetic radiation interacts with matter, it gets absorbed by matter and increases the energy content of molecules or atoms. The electromagnetic radiation could be a function of either frequency or wavelength. Ultraviolet-Visible (UV-Vis) spectroscopy utilizes the radiation in the UV range and adjacent visible range of the electromagnetic radiation spectrum [8]. The absorption wavelength mainly ranges from 100 - 700 nm. The Ultraviolet-Visible-Near Infrared (UV-Vis-NIR) operates between the wavelength 175 nm to 3300 nm.

In principle, when the sample absorbs the light, it undergoes excitation and de-excitation, producing a distinct spectrum. When the electrons undergo excitation, it jumps from a ground state (lower energy state) to an excited state (higher energy state). The difference in these energies is equal to the amount of radiation absorbed by the sample. These excited electrons are the bonding electrons of the molecules so that the absorption peaks correspond to different types of bonds present in the sample. Thus, absorption spectroscopy is used to identify the functional groups present in a molecule. The bands that appear in the spectrum are broad due to the overlap of vibrational and electronic transitions [8].

If a known wavelength and intensity of light (I_0) is directed at the sample and after passing through it, the final intensity be I, then the amount of light absorbed by the sample at that particular

wavelength can be calculated as,

$$A = \log \frac{I_0}{I}$$

Using the Beer-Lambert law, this absorption can be directly proportional to the sample path length and concentration of the sample, i.e.,

$$A = \log \frac{I_0}{I} = \varepsilon L c$$

In this equation, A is absorbance, ε is the molar extinction coefficient, c is the concentration of the sample, and L is the path length.

A spectrophotometer comprises four main parts: a source, a monochromator, a beam splitter, a sample area, and a detector. It also has optical elements such as lenses or mirrors to transmit light throughout the equipment. The basic schematic diagram is shown in Fig. A.4a. The light from the source splits into different wavelengths as it passes through the monochromator and gets absorbed by the sample. The sample takes a specific amount of energy to promote the electrons to a higher energy state that we can detect as absorption [9].

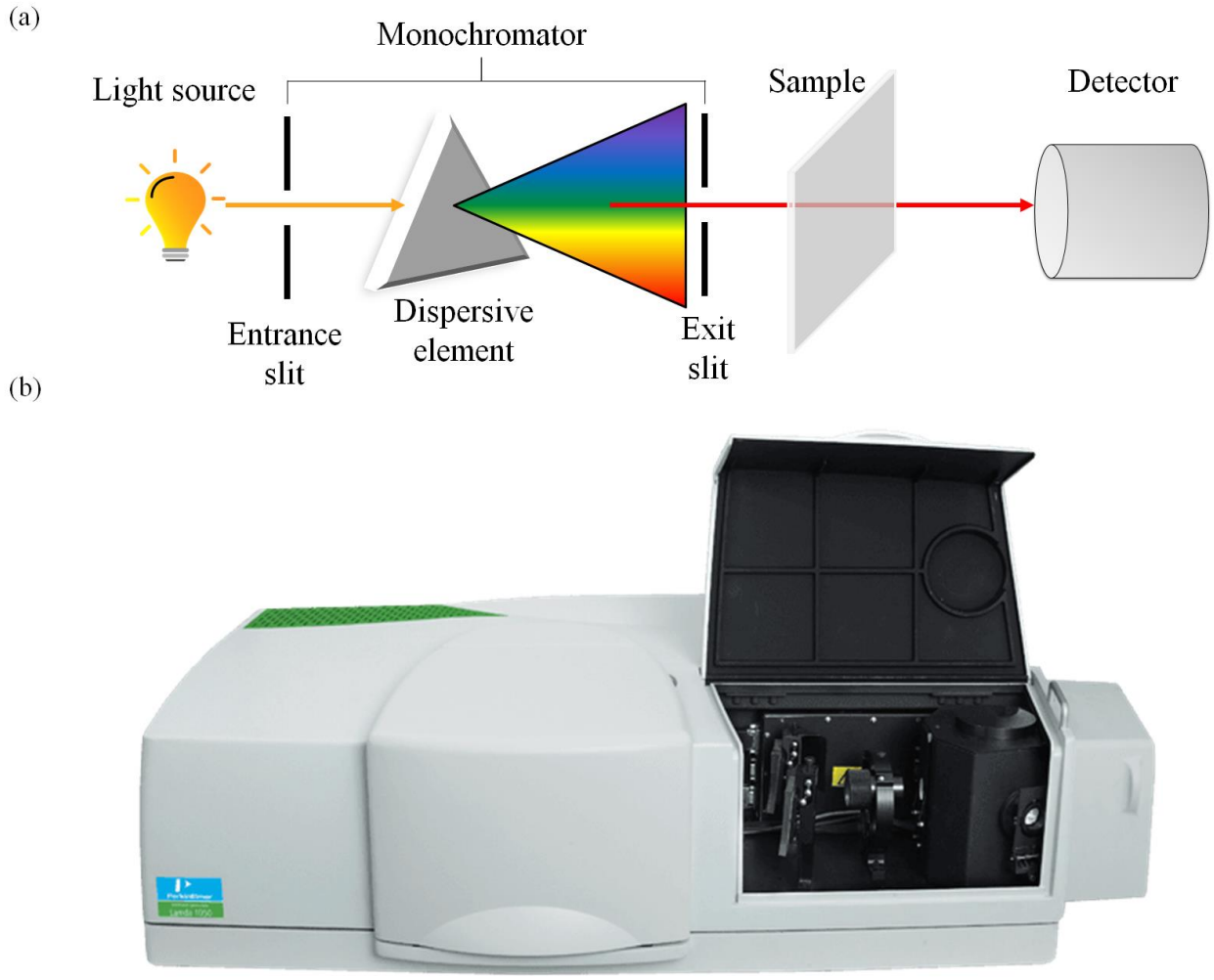

Fig. A.4. (a) The schematic diagram of the spectrophotometer. Adapted from Ref. [9]. (b) Photographic image of Lambda 950 UV/vis/NIR spectrophotometer. Adapted from Ref. [10].

Chapter 3 recorded the UV-vis absorption spectra of the hybrid films with an Ocean Optics (USB 4000 XR) UV-vis modular spectrophotometer. The absorption spectra were recorded in 200-800 nm ranges and processed using SpectraSuite software. In chapter 4, Perkin Elmer Lambda 950 UV/vis/NIR spectrophotometer (Fig. A.4b) was used to record the UV-vis-NIR absorption spectra. The spectrum was recorded from 250 to 1500 nm and UV WinLab is the instrument control and data manipulation software.The composite solutions were spin-coated on a quartz substrate (25×25 mm) at 8000 rpm for 120 min to form a thin film.

A.5 Raman Spectroscopy

Raman spectroscopy is a scattering technique based on Raman Effect, an inelastic scattering phenomenon. When monochromatic radiation strikes the matter, a small fraction of scattered radiation will have a different wavelength than the incident. Such a phenomenon happens due to the interaction of incident radiation with vibrating molecules. Hence, Raman spectroscopy probes the molecular vibrations. A polarizability change during molecular vibration is essential to obtain a Raman spectrum of the sample. The Raman spectrum is similar to a chemical fingerprint that identifies a molecule or material. It provides insights into a sample's chemical composition and properties, contaminations and defects, crystallinity and polymorphism and thermal and mechanical exposure [11].

Raman spectrometer consists of laser light, which has to be irradiated in the sample. The scattered light is allowed to pass through a filter to eliminate any light from the excitation laser. It is then directed onto a grating, which distributes the inelastic parts like a prism according to wavelength. Finally, these rays are directed to a CCD sensor that outputs a spectrum depending on the intensity. Fig. A.5a shows the schematic diagram of the Raman spectrometer.

Raman measurements in chapter 4 were carried out in a WI-Tec alpha 300R Confocal Raman microscope (Fig. A.5b) with a laser beam (633 nm excitation wavelength with 7 mW power) directed to the sample through a 20x objective with 600 g/mm grating and a Peltier cooled charge-coupled detector. Before every measurement, a calibration with a silicon standard (Raman peak centred at 520 cm^{-1}) was performed. WI-Tec Project plus v2.1 software package was used for data evaluation. The samples were drop-cast onto a 10×10 mm glass substrate to form a film. The as-casted film samples were used for Raman measurement.

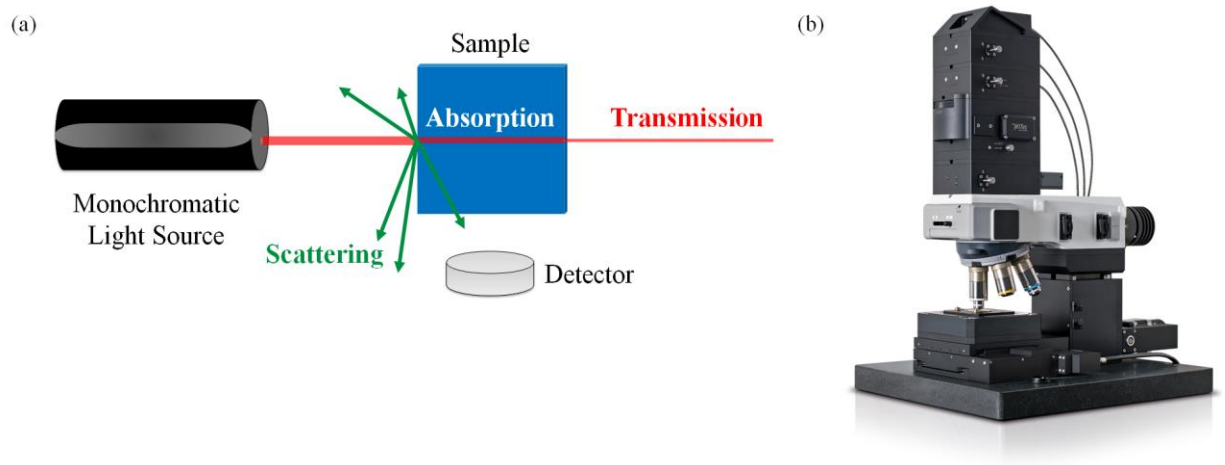

Fig. A.5. (a) The schematic diagram of the Raman spectrometer. Adapted from Ref. [11]. (b) Photographic image of WI-Tec alpha 300R Confocal Raman microscope. Adapted from Ref. [12].

A.6 Thermogravimetric Analysis (TGA)

Thermogravimetric Analysis (TGA) measures the mass of a substance as a function of temperature or time in a controlled atmosphere. When a substance is subjected to programmed heating or cooling, it usually undergoes changes, which may be physical, chemical, mechanical or magnetic. The analysis of these changes as a function of temperature permits the study of composition, structure, chemical and physical behavior and detect phase changes due to decomposition, oxidation, or dehydration [13].

The key component of TGA is the microbalance, which precisely measures the sample weight. The sample platform controls the loading and unloading of the sample to and from the balance. The furnace provides the controlled temperature, and the mass flow controllers control the purge gas to the balance and furnace. All the system electronics and mechanics are housed in the cabinet [14]. The schematic of the TGA is shown in Fig. A.6a.

In the present work, TA instruments Q-50 TGA is used to study the stability of the composite. Initially, the composite solutions were made into a film and scratched to form powder samples. Samples are analyzed in the temperature range from 30 °C to 800 °C at a heating rate of 10 °C/min in a nitrogen environment. Fig. A.6b shows the photographic image of Q-50 TGA.

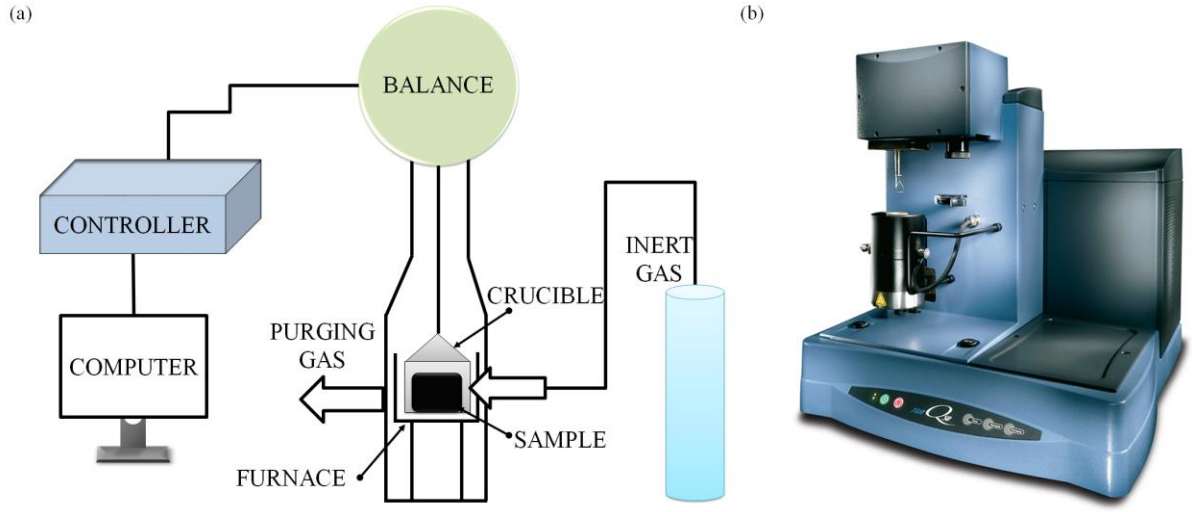

Fig. A.6. (a) The schematic diagram of TGA. Adapted from Ref. [14]. (b) Photographic image of Q-50 TGA. Adapted from Ref. [15].

A.7 X-ray Photoelectron Spectroscopy (XPS)

X-ray Photoelectron Spectroscopy (XPS) is a surface analytical technique that measures the chemical state, empirical formula and electronic state of elements within a material based upon the photoelectric effect [16]. When a solid surface is irradiated with a beam of X-rays, XPS spectra are obtained by measuring the kinetic energy of photoelectrons that escape from a depth of around 1 to 10 nm on the surface. Every element has its characteristic XPS core-level peak at characteristic binding energy values that enable identifying and quantifying each element from the surface (except hydrogen and helium). Similarly, the chemical shifts and presence of other unique features, like satellite peaks, in the XPS spectra are helpful for chemical state analysis.

In XPS, an atom in a solid absorbs the photon, leading to ionization and the emission of an inner core shell electron. Consider an X-ray photon of energy *hv* strikes on an atom. Following the absorption of the photon and the emission of the photoelectron, the binding energy (E_b) of the emitted electrons can be determined by,

$$E_b = hv - E_{kin} - W_f$$

E_{kin} = kinetic energy of the emitted electron as measured by the instrument, and W_f = work function of the material. The basic principle of XPS can be schematically shown in Fig. A.7a.

XPS is typically accomplished by exciting the surface of a sample with mono-energetic X-rays (especially Al-K_α), which emits photoelectrons from the sample surface. An electron energy analyzer measures the energy of the emitted photoelectrons (Fig. A.7b). XPS requires ultra-high vacuum conditions to remove adsorbed gases and eliminate contaminants' adsorption on the sample. An ultra-high vacuum also increases the mean free path for electrons, ions and photons. The elemental identity, chemical state, and quantity of an element can be determined from the detected binding energy and intensity of a photoelectron peak [17].

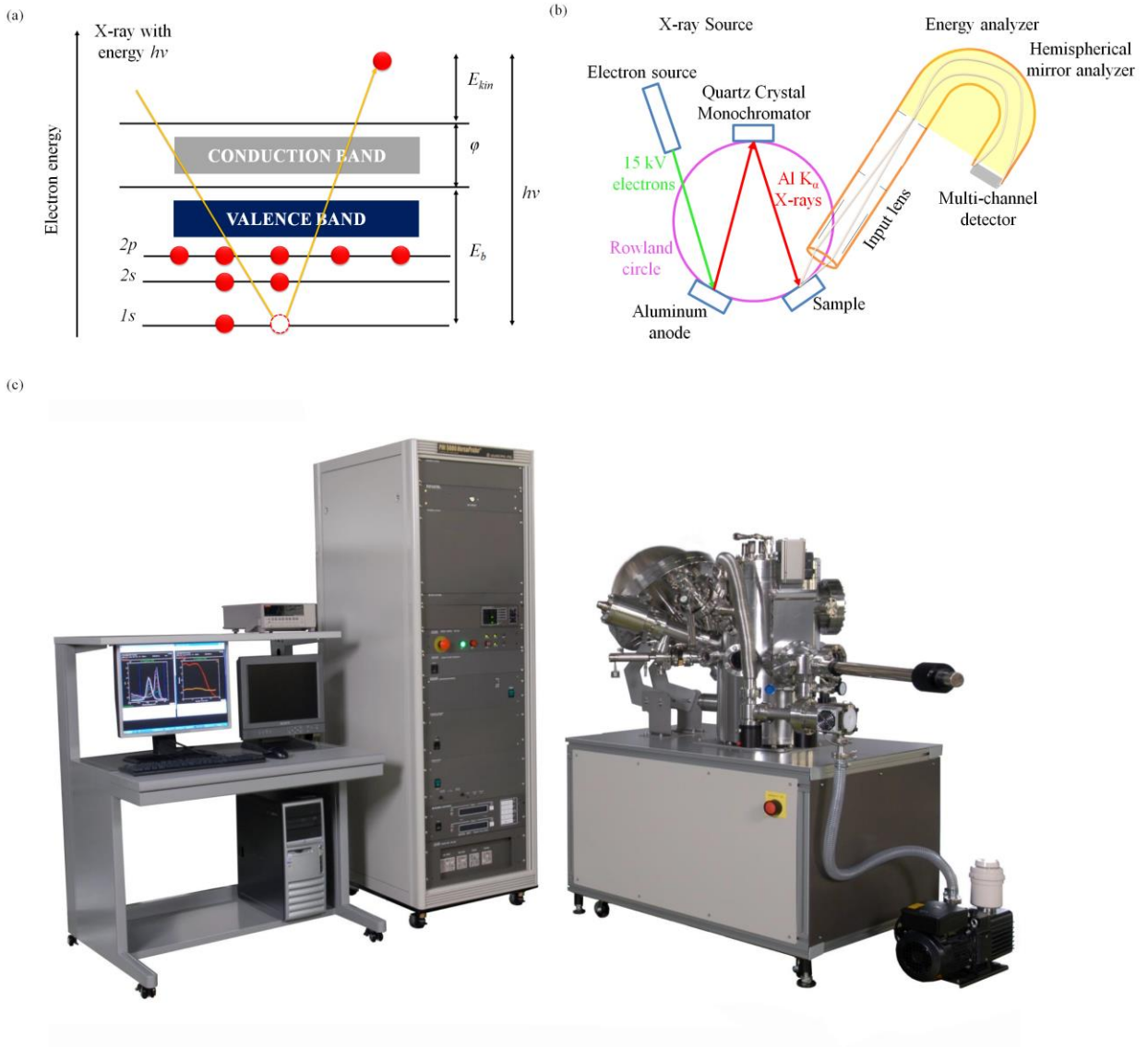

Fig. A.7. (a) The schematic diagram of XPS principle. Adapted from Ref. [16]. (b) The working of XPS. Adapted from Ref. [17]. (c) Photographic image of PHI 5000 Versa Probe II XPS system. Adapted from Ref. [18].

The surface chemistry was analyzed using PHI 5000 Versa Probe II, ULVAC-PHI Inc., USA (Fig.A.7c) equipped with a micro-focused (200 μm, 15 kV) monochromatic Al-K_α X-ray source (hv = 1486.6 eV). Both survey and narrow scan (high-resolution) spectra were recorded. Survey scans were recorded with an X-ray source having a power of 50 W and pass energy of

187.85 eV. High-resolution spectra of the major elements were recorded at 46.95 eV pass energy, and the peaks were fitted and analyzed using MultiPak software. The valance band maxima (VBM) spectra were recorded by sweeping the energy from -5 eV to 30 eV. The C1s line at 284.8 eV was used as an internal energy reference. The samples were drop-cast onto a 10×10 mm gold coated glass substrate to form a film.

A.8 Ultra-violet Photoelectron Spectroscopy (UPS)

Ultraviolet Photoelectron Spectroscopy (UPS) operates on the same principle as XPS, but UV radiation is the ionization energy used to induce a photoelectric effect. Typically, a gas discharge lamp filled with helium produces UV photons with energies of 21.2 eV (He-I) and 40.8 eV (He-II) [19]. Since low-energy photons are used in UPS, the spectral acquisition is limited to the valence-band region. UPS can accurately measure the Fermi edge, the electronic work function of the material and the density of states in the valence band.

Fig. A.8a shows a typical UPS spectrum. The spectrum consists of three important regions: Fermi level (or Fermi edge), valance band region and secondary cutoff region (or secondary edge). The Fermi level of the calibrated spectrum is at 0 eV binding energy. The Fermi edge manifests as a step since it separates occupied and empty states. To the left of the Fermi edge, at low binding energies of 0-10 eV, lies the valence band structures of the sample. Finally, the spectrum ends in a high binding energy cutoff region. At this region, the electrons will have zero kinetic energy after leaving the sample surface, i.e. they barely had enough energy to overcome the material's work function. The sloping up tail of electrons before the secondary edge is due to the inelastic scattering of electrons, which are initially emitted from the valence bands states but lose energy on their way to the sample surface through scattering processes. Thus the work function (φ) of the material can

be determined by [17],

$$\phi = h\upsilon - (E_{cutoff} - E_F)$$

$h\upsilon$ = energy of the UV photons (21.21 eV for He-I radiation), E_{cutoff} = binding energy of the electrons at the secondary cutoff, E_F = binding energy of the electrons at the Fermi edge (0 eV).

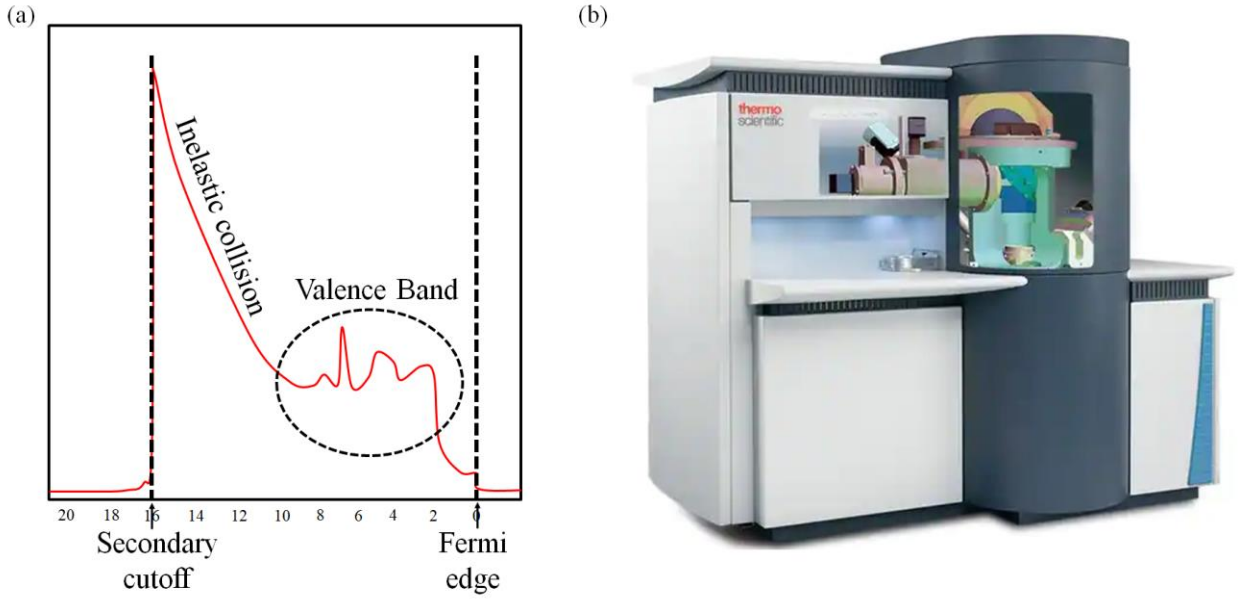

Fig. A.8. (a) A sample UPS spectrum, (b) Photographic image of K-ALPHA+ spectrometer XPS/UPS system. Adapted from Ref. [19].

The UPS spectra were obtained with a He lamp providing resonance line, He-I (hν = 21.2 eV) by Thermo Fisher Scientific Instruments make K-ALPHA + spectrometer (Fig. A.8b), armed with a high-intensity UV source with a photon flux of 1.5 x 10^{-12} photons/sec. The samples were drop-cast onto a 10×10 mm ITO substrate to form a film.

A.9. Atomic Force Microscopy (AFM)

Atomic Force Microscopy (AFM) is a powerful analytical tool for characterizing surfaces in the micro-to nanometer range. AFM technology uses a few nanometers' sharp tips to scan the

sample surface and provide high-resolution information without sample damage. The AFM consists of a flexible cantilever to measure the force between the tip and the sample. The tip is connected at the free end of a cantilever end and detects low forces of a few piconewtons. The variation in the sample surface height influences the force acting on the tip and therefore changes the bending of the cantilever. Therefore, an image of the observed surface can be created based on the tip deflection information [20].

The AFM works under the principle of the local attractive or repulsive force between the sample and the tip that can be converted into the cantilever deflection. The cantilever is fixed to a rigid substrate, and depending on the tip's interaction with the sample, whether attractive or repulsive, the cantilever will deflect towards or away from the surface. The cantilever deflection is then detected using a detection system consisting of a laser beam which is reflected from the back of the cantilever onto a photodetector. At the position of the reflected spot, any slight change in the cantilever bending angle is converted to a measurably large deflection. The reflected laser beam angle changes as the cantilever deflect; therefore, the spot falls on a different area of the photodetector. The signals from each area of the detector are compared to calculate the deflection signal [20]. The schematic diagram of the AFM working is shown in Fig. A.9a.

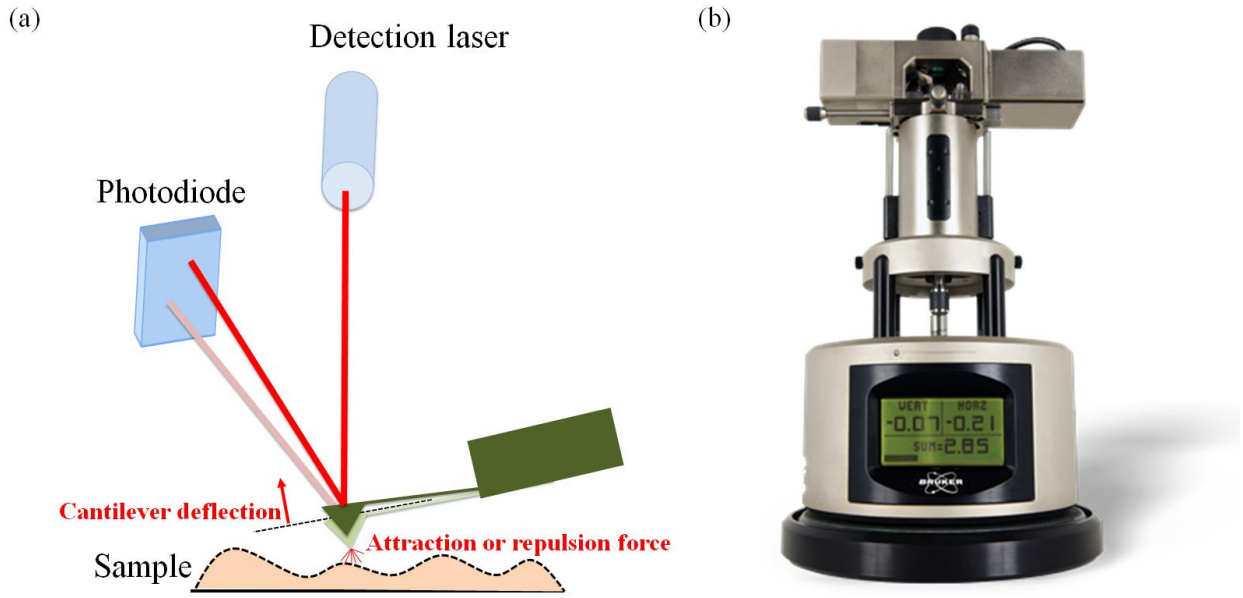

Fig. A.9. (a) The schematic working principle of AFM. Adapted from Ref. [20]. (b) Photographic image of Bruker Multimode-8HR AFM system. Adapted from Ref. [21].

AFM images were recorded in tapping mode on the Bruker Multimode-8HR AFM system (Fig. A.9b) using NSG10/Pt (NT-MDT) tip and processed in the NanoScope analysis 1.5 software package. The samples were drop-cast onto an 8×8 mm glass substrate to form a film.

A.10. Kelvin Probe Force Microscopy (KPFM)

Kelvin Probe Force Microscopy (KPFM) was introduced as a tool to map the sample's work function or surface potential with high spatial resolution. The instrumentation of KPFM is similar to the AFM system in contact mode. It measures the local contact potential difference between a conducting AFM tip and the sample. The AFM tip touches the sample surface in contact mode operation, and the repulsive force between the tip and sample deflects the cantilever. The deflection of the cantilever is scanned and used as a feedback signal [22].

The contact potential difference (V_{CPD}) between the tip and sample is given by the

formula,

$$V_{CPD} = \frac{\Phi_T - \Phi_S}{-e}$$

Φ_T = work function of the tip, Φ_S = work function of the sample, and e = electronic charge.

When the AFM tip and sample are brought together, the differences in their Fermi energy levels cause an electrical force. Fig. A.10 shows the different conditions of the energy level diagram of the tip and sample surface. The condition when the tip and sample surface are separated by a distance *d* and electrically not connected is depicted in Fig. A.10a. In this situation, the Fermi energy levels of tip and sample differ, but vacuum levels are aligned together. If the tip and sample surface is close enough for electron tunneling, Fermi levels should line up at a steady state to achieve equilibrium. Once an electrical contact is made between the tip and sample, the system will attain an equilibrium state, and thereby, the Fermi levels will align through electron flow, as shown in Fig. A.10b. However, the vacuum energy levels are no longer the same, and an apparent potential (V_{CPD}) has been formed between the tip and sample. Due to this V_{CPD}, an electrical force acts on the contact area, and this force can be nullified as shown in Fig. A.10c. If an external bias (V_{DC}) of the same magnitude and opposite direction as V_{CPD} is applied, the surface charge in the contact area can be eliminated. The amount of V_{DC} that nullifies the effect of V_{CPD} is equal to the work function difference between the tip and sample. Hence, if the tip work function is known, the work function of the sample can be calculated [22].

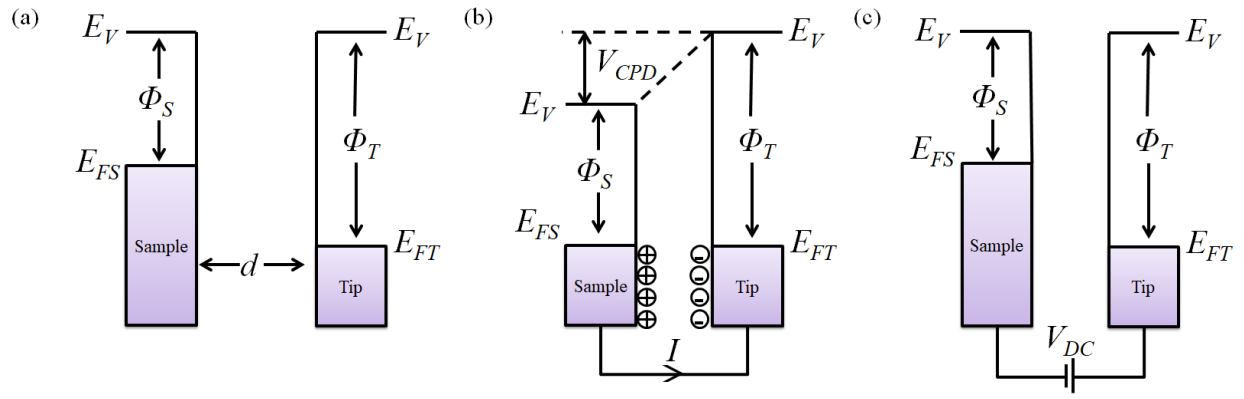

Fig. A.10. Electronic energy levels of the sample and AFM tip for three cases: (a) no electrical contact, (b) in electrical contact, and (c) applied external bias. E_V is the vacuum energy level. E_{FS} and E_{FT} are Fermi energy levels of the sample and tip, respectively. Adapted from Ref. [22].

KPFM data were recorded under ambient conditions on the Bruker Multimode-8HR AFM system in contact mode using CSG10_Ed/Pt (NT-MDT) tip and processed in the NanoScope analysis 1.5 software package. The samples were drop-cast onto an 8×8 mm glass substrate to form a film.

A.11. Hall Effect Measurement

Hall effect measurements are valuable tools for material characterization in many electronics industries. The Hall effect is a process in which a current-carrying material, when placed in a perpendicular magnetic field, develops a voltage that can be measured at the right angle to the current path. A Hall effect measurement system can be used to determine material parameters such as Hall coefficient (R_H), carrier mobility (μ), carrier concentration (n), resistivity (ρ), magnetoresistance (R), and the conductivity type (N or P) of the material.

The underlying principle of the Hall effect is the Lorentz force, i.e., the force exerted by a magnetic field on a moving electric charge. The Hall effect is illustrated in Fig.A.11a. A current

starts flowing when a conductive plate is connected to a circuit with a battery. Thus, the charge carriers will move linearly from the plate's one end to the other, producing magnetic fields. This magnetic field gets distorted and distresses the straight flow of the charge carriers when a magnet is placed near the plate. Due to the distortion in the charge carriers' magnetic field, the negatively charged electrons will deflect to one end of the plate and positively charged holes to the other. Thereby generating a potential difference between both sides of the plate known as the Hall voltage (V_H), given by the formula [23],

$$V_H = \frac{IB}{nqd}$$

I = current flowing through the plate, B = magnetic field strength, n = number of charge carriers per unit volume, q = charge and d = thickness of the plate.

The Hall coefficient R_H is expressed as,

$$R_H = \frac{E}{jB}$$

E = induced electric field, j = current density of the carrier and B = magnetic field strength. The Hall coefficient is positive for *P*-type material and negative for *N*-type material.

The Hall mobility can be calculated using the formula,

$$\mu_H = \frac{V_H d}{BI\rho}$$

V_H = Hall voltage, d = thickness of the plate, B = magnetic field strength, I = current flowing through the plate and ρ = resistivity.

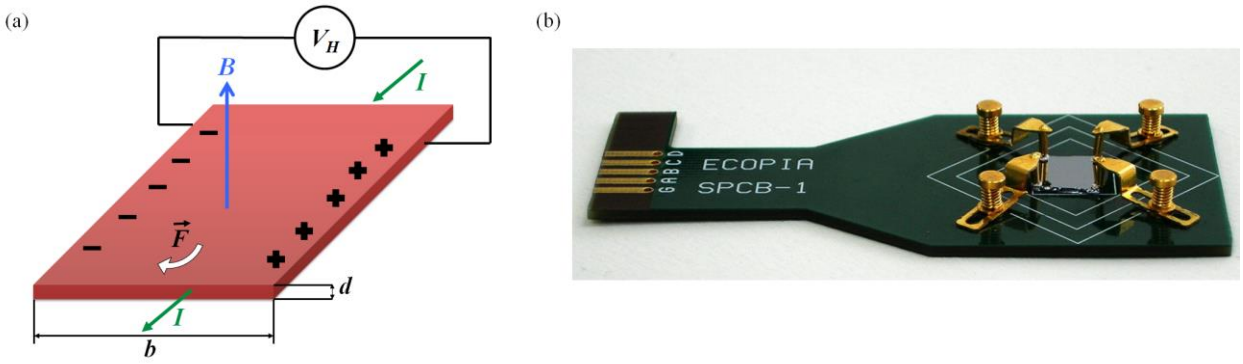

Fig. A.11. (a) The schematic diagram of Hall effect measurement. Adapted from Ref. [23]. (b) Photographic image of the sample holder in ECOPIA HMS 3000 Hall system. Adapted from Ref. [24].

In the present study, Hall effect measurement was employed to measure the carrier concentration and mobility. Hall effect measurement at room temperature was done with ECOPIA HMS 3000 system (0.54 T field and 15 mA current) using Van der Pauw's geometry. The photographic image of the sample holder is shown in Fig. A.11b. The samples were drop-cast onto a 10×10 mm glass substrate to form a film and thickness was measured using a profilometer.

A.12. Thermoelectric Measurement

Thermoelectric (TE) measurement of material includes electrical conductivity and Seebeck coefficient measurement. The DC four-terminal measurement technique is used to determine the electrical conductivity of the sample. Under thermal equilibrium conditions (ΔT = 0K), two electrodes pass a constant direct current (I) through the sample. It can be assumed that nearly an ideal 1-D current will flow through the sample. The resulting voltage drop (V) is measured using two thermocouple wires, L distance apart, over a portion of the sample, as shown in Fig. A.12a. Further knowing the area of cross-section (A), the electrical conductivity (σ) can be calculated as

[25],

$$\sigma = \frac{I}{V}\frac{L}{A}$$

In order to determine the Seebeck coefficient, the sample is positioned vertically between two electrodes (Fig. A.12b). The entire setup is located in a furnace, which heats the sample to a specific temperature for measurement. Additionally, the lower electrode block contains a secondary heater to establish a temperature gradient. The temperature at the hot (T_H) and cold (T_C) end is measured using two laterally contacting thermocouples. The thermovoltage (V_o) is measured using one of the two thermocouple leads. The Seebeck coefficient (α) can be calculated according to the formula [25],

$$\alpha = \frac{-V_O}{T_H - T_C}$$

TE assessment in the present thesis was carried out using the Linseis LSR-3 system (Fig. A.12c). The samples were drop-cast on a glass substrate of 16×4 mm to form a film. The thickness of the film was measured using a profilometer. The data was collected using Linseis LSR software and evaluated using Linseis Data Evaluation software.

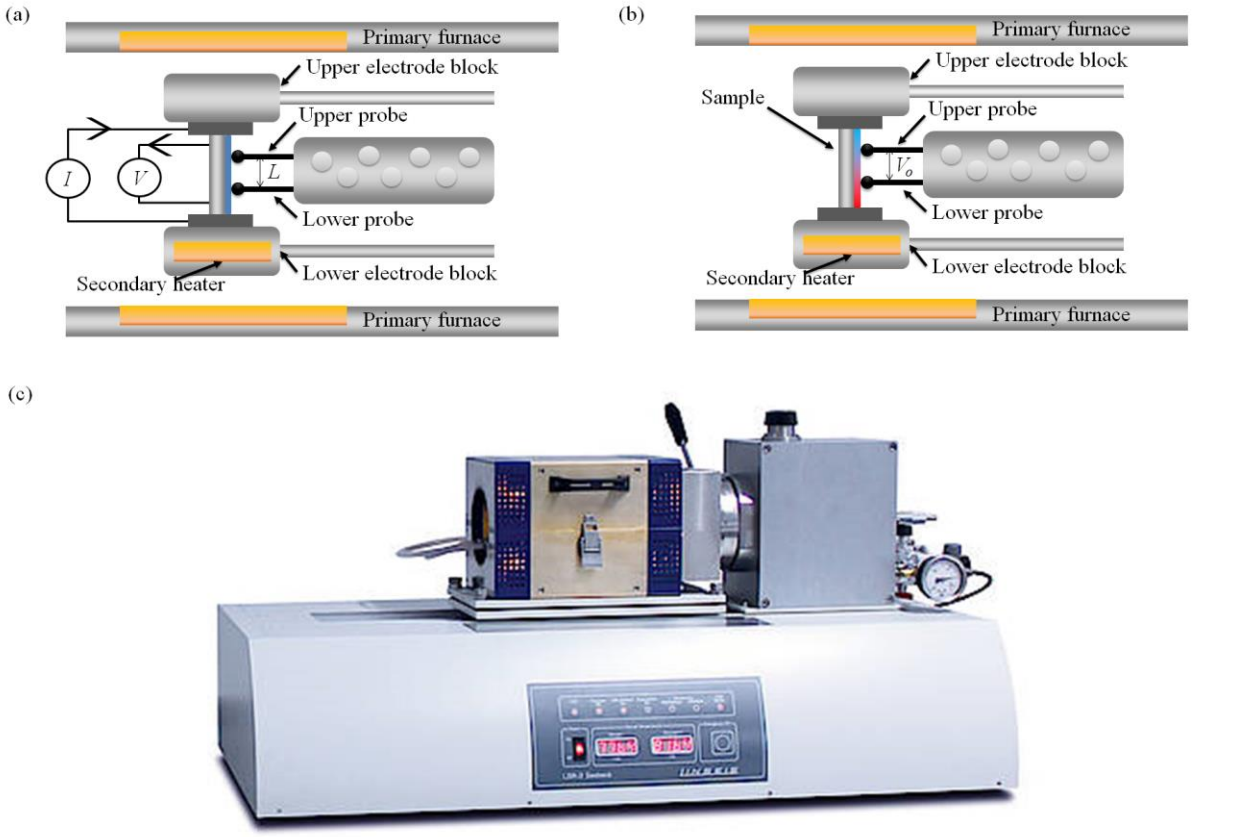

Fig. A.12. (a) The schematic diagram of resistivity measurement, (b) The schematic diagram of Seebeck measurement, (c) Photographic image of Linseis LSR-3 system. Adapted from Ref. [26].

A.13. Profilometer

A profilometer is an instrument used to measure a sample's thickness and surface profile, like roughness. The sample surfaces can be composed of peaks and valleys with varying heights, depths, and spacing. A physically moving probe along the surface can acquire these surface profiles, and such contact profilometers are called stylus profilometers. A stylus profilometer comprises a microscopic tip in contact with the surface, which can be moved along the X-axis. Due to the surface relief, the tip moves in the vertical direction, which is captured and amplified. The stylus tip consists of a microscopic sphere, often made of diamond or a hard stone like

sapphire. This sphere has a radius of a few microns and is attached to conical support, constituting a conispherical tip. The stylus rotates around a pivot, and the other end of the stylus is connected to a transducer device. The transducer converts the vertical movement of the tip into an electrical signal [27]. The schematic diagram is shown in Fig. A.13a.

The present work utilizes a Bruker Dektak XT stylus profilometer (Fig. A.13b) for the thickness measurement. The stylus tip radius is 2 µm, and Bruker Vision64 software is used as the visual user interface. Thickness has been taken for Hall measurement and TE measurement. The same samples of each measurement are used for thickness measurement.

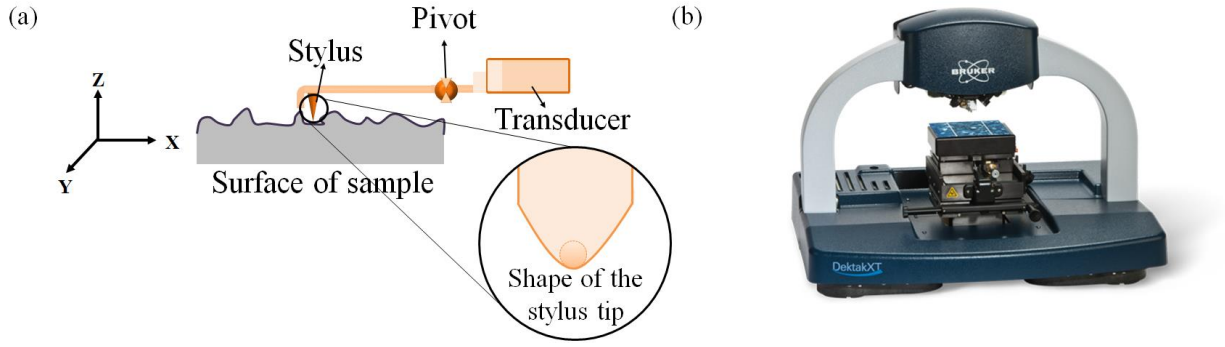

Fig. A.13. (a) The schematic diagram of a stylus profilometer. Adapted from Ref. [27]. (b) Photographic image of Bruker Dektak XT stylus profilometer. Adapted from Ref. [28].

References

[1] D. Lamba, Wide-Angle X-Ray Scattering (WAXS), in: Encycl. Membr., Springer Berlin Heidelberg, Berlin, Heidelberg, 2016: pp. 2040–2042. https://doi.org/10.1007/978-3-662-44324-8_1101.

[2] XENOCS, (n.d.). https://www.xenocs.com/knowledge-base/saxs/#whatissaxs.

[3] W. Zhou, Z.L. Wang, eds., Scanning Microscopy for Nanotechnology, Springer New York, New York, NY, 2007. https://doi.org/10.1007/978-0-387-39620-0.

[4] Paras N Prasad, Nanophotonics, Wiley, 2004.

[5] ZEISS, (n.d.). https://www.zeiss.com/microscopy/us/products/scanning-electron-microscopes/evo-18.html.

[6] L. Reimer, Transmission Electron Microscopy, Springer Berlin Heidelberg, Berlin, Heidelberg, 1984. https://doi.org/10.1007/978-3-662-13553-2.

[7] ThermoFisher Scientific, (n.d.). https://www.thermofisher.com/in/en/home/electron-microscopy.html.

[8] D.N. Sathyanarayana, Electronic Absorption Spectroscopy and Related Techniques, Universities Press, 2001.

[9] H.-H. Perkampus, UV-VIS Spectroscopy and Its Applications, Springer Berlin Heidelberg, Berlin, Heidelberg, 1992. https://doi.org/10.1007/978-3-642-77477-5.

[10] PerkinElmer, (n.d.). https://www.perkinelmer.com/product/lambda-950-uv-vis-nir-spectrophotometer-l950.

[11] E. Smith, G. Dent, Modern Raman Spectroscopy, 2nd ed., Wiley, 2019.

[12] WiTec, (n.d.). https://raman.oxinst.com/.

[13] P. Gabbott, ed., Principles and Applications of Thermal Analysis, Wiley, 2008.

[14] P.J. Haines, Thermal Methods of Analysis, Springer Netherlands, Dordrecht, 1995. https://doi.org/10.1007/978-94-011-1324-3.

[15] TA Instruments, (n.d.). https://www.tainstruments.com/products/thermal-analysis/thermogravimetric-analysis/.

[16] P. van der Heide, X-ray Photoelectron Spectroscopy An Introduction to Principles and Practices, Wiley, 2011.

[17] J.F. Watts, J. Wolstenholme, An Introduction to Surface Analysis by XPS and AES, Wiley, 2019. https://doi.org/10.1002/9781119417651.

[18] PHI, (n.d.). https://www.phi.com/surface-analysis-equipment/versaprobe.html.

[19] ThermoFisher Scientific, (n.d.). https://www.thermofisher.com/in/en/home/materials-science/learning-center/surface-analysis/uv-photoelectron-spectroscopy.html.

[20] Wesley C. Sanders, Atomic Force Microscopy Fundamental Concepts and Laboratory Investigations, CRC Press, 2019.

[21] Bruker, (n.d.). https://www.bruker.com/de/products-and-solutions/microscopes/materials-afm/multimode-8-hr-afm.html.

[22] W. Melitz, J. Shen, A.C. Kummel, S. Lee, Kelvin probe force microscopy and its application, Surf. Sci. Rep. 66 (2011) 1–27. https://doi.org/10.1016/j.surfrep.2010.10.001.

[23] C. Chien, ed., The Hall Effect and Its Applications, Springer US, 2013.

[24] ECOPIA, (n.d.). http://four-point-probes.com/ecopia-hms-3000-hall-measurement-system/.

[25] D.M. Rowe, ed., CRC Handbook of Thermoelectrics, CRC Press, 2018.

[26] LINSEIS, (n.d.). https://www.linseis.com/en/products/thermoelektrik/lsr-3/.

[27] M. Ohring, Characterization of Thin Films and Surfaces, in: Mater. Sci. Thin Film.,

Elsevier, 2002: pp. 559–640. https://doi.org/10.1016/B978-012524975-1/50013-6.

[28] Bruker, (n.d.). https://www.bruker.com/en/products-and-solutions/test-and-measurement/stylus-profilometers/dektakxt.html.

ABSTRACT

Name of the Student: **Vijitha I.** Registration No.: **10PP14A39010**

Faculty of Study: **Physical Sciences** Year of Submission: **2021**

AcSIR academic centre/CSIR Lab: **CSIR-National Institute for Interdisciplinary Science and Technology (CSIR-NIIST)**

Name of the Supervisor(s): **Dr. Biswapriya Deb**

Title of the thesis: **Organic-based hybrid materials for Thermoelectric Applications**

Using thermoelectric (TE) devices, the ability to convert heat into electricity using thermoelectric (TE) devices is expected to play a vital role in waste heat recovery, thereby promoting superior energy utilization. The present thesis consists of three working chapters. The introduction chapter (***Chapter 1***) outlines the working fundamentals and motivations for organic-based TE research. It also highlights the current benchmark in the material properties, transport theories, and state-of-the-art device fabrication strategies. In ***Chapter 2***, the preparation and characterization of a conjugated thienothiophene polymer/MWCNT hybrid TE system are discussed. The chapter provides insights into the usage of dopants to simultaneously enhance the Seebeck coefficient (α) and electrical conductivity (σ). Such composites are shown to be mechanically robust with good chemical stability for practical TE module fabrications. ***Chapter 3*** presents additional insights and the critical role of the p-doping mechanism in MWCNT based organic hybrids. A comparative study of the doping effect on the TE properties of the two conjugated thienothiophene polymer/MWCNT hybrid reveals that the carrier concentration and mobility of the composite could be tuned independently, which can mitigate the trade-off between the α and σ. An understanding of doping-induced TE properties of conjugated thienothiophene polymer/SWCNT composite system is discussed in ***Chapter 4***. This chapter also demonstrates the usage of various simulation platforms to predict materials and device properties, followed by their experimental validations. The overall summary and conclusion of the thesis are outlined in ***Chapter 5,*** with critical discussions on the future scope/roadmap. The materials developed in this thesis achieve some of the highest performance in organic hybrid TE to date. This work represents a step towards establishing cheaper and lighter TE materials and flexible TE modules to power new-generation electronic, IoT, and wearable devices.

Details of the publications emanating out of the thesis work

1. **Vijitha Ignatious**, Neethi Raveendran, Arjun Prabhakaran, Yuvaraj Tanjore Puli, Vijayakumar Chakkooth, Biswapriya Deb, MWCNT/Thienothiophene based All-Organic thermoelectric composites: Enhanced performance by realigning of the Fermi level through doping, *Chemical Engineering Journal, 409, 128294, 2021*

2. **Vijitha Ignatious**, Neethi Raveendran, Sruthy Poovattil, Navin Jacob, Vijayakumar Chakkooth, Biswapriya Deb, Studies on the doping mechanism of conjugated thienothiophene polymer/MWCNT hybrids for thermoelectric application, *Macromolecular Materials and Engineering, 307, 2100916, 2022*

3. **Ignatious Vijitha**, Navin Jacob, Neethi Raveendran, Chakkooth Vijayakumar, Biswapriya Deb, Studies on the thermoelectric performance of PBDTT-FTTE/SWCNT composites assisted by simulation and modelling *(Submitted –Materials Today Energy)*

Details of the publications not related to the thesis work

1. PTG Gayathri, S Sajitha, **I Vijitha**, SS Shaiju, R Remya, Biswapriya Deb, Tuning of physical and electrochemical properties of nanocrystalline tungsten oxide through ultraviolet photoactivation, *Electrochemica Acta, 272, 135-143, 2018*

2. Neethi Raveendran, Tanwistha Ghosh, **Vijitha Ignatious**, Vibhu Darshan, Navin Jacob, Biswapriya Deb, Chakkooth Vijayakumar, Effect of molecular structure on doping efficiency, Fermi level alignment and thermoelectric properties of self-assembled thiophene derivatives, *to be communicated - Materials Today Energy*

List of Conferences presentations

1. Participated in International Conference on Chemistry and Applications of Soft Materials (CASM 2022), held at CSIR-NIIST, Thiruvananthapuram, July 25-27, 2022.

2. Oral presentation on "Design and performance analysis of flexible organic thermoelectric generator", in 34th Kerala Science Congress, a virtual event held by Kerala State Science Technology and Environment, Thiruvananthapuram, February 10-12, 2022.

3. Oral presentation on " Effect of doping in the thermoelectric performance of conjugated thienothiophene polymer/MWCNT hybrids", in Recent Advances in the Physics of Materials (RAPM-2021), held at CSIR-NIIST, Thiruvananthapuram, December 9-10, 2021.

4. Oral presentation on "Tuning of physical and thermoelectric properties of SWCNT/Thienothiophene organic hybrid composite through doping", in 5th National Symposium on Shaping the Energy Future: Challenges & Opportunities (SEFCO-2021), a virtual event held by CSIR - Indian Institute of Petroleum, Dehardun, August 27, 2021. (**Best oral presentation award**)

5. Flash talk and poster presentation on "Thermoelectric Power Factor Enhancement in a Composite based on Thienothiophene Polymer and Single Walled-Carbon Nanotube", in 14th International Conference on Ecomaterials (ICEM 2020), held at CSIR-NIIST, Thiruvananthapuram, February 5-7, 2020. (**Best flash talk award**)

6. Poster presentation on "Side Chain Dependence on Thermoelectric Properties of Thienothiophene based Conjugated Polymers", in 32nd Kerala Science Congress, held at Yuvakshetra Institute of Management Studies, Palakkad, January 25-27, 2020.

7. Oral presentation on "Side Chain Dependence on Thermoelectric Properties of Thienothiophene based Conjugated Polymer nanocomposite with MWCNT", in Third International Conference on Advanced Functional Materials (ICAFM 2019), held at CSIR-NIIST, Thiruvananthapuram, December 9-10, 2019.

8. Poster presentation on "Development of thienothiophene based polymer thermoelectric nanocomposite filled with MWCNTs through the enhancement of power factor by doping", in Fifteenth JNC Research Conference on Chemistry of Materials, held at Vivanta Taj, Kovalam, Thiruvananthapuram, September 30- October 2, 2019.

9. Poster presentation on "Polymer Nanocomposite Materials for Thermoelectric Applications", in Second International Conference on Recent Trends in Materials Science and Technology (ICMST 2018), held at VSSC, Thiruvananthapuram, October 10-13, 2018.

10. Poster presentation on "Polymer Nanocomposite Materials for Thermoelectric Applications", in 29th MRSI National Symposium on Advances in Functional and Exotic

Materials, held at Bharathidasan University, Tiruchirappalli, Tamil Nadu, February 14-16, 2018.

11. Poster presentation on "Organic Based Hybrid Materials for Thermoelectric Applications", in 8th East Asia Symposium on Functional Dyes and Advanced Materials (EAS-8), held at CSIR-NIIST, Thiruvananthapuram, September 20-22, 2017.

12. Poster presentation on "Organic Based Hybrid Materials for Thermoelectric Applications", in Indo-Japan Joint Symposium on Polymeric Materials, held at Hotel Residency, Thiruvananthapuram, January 31- February 1, 2017.

13. Participated in 18th National Symposium in Chemistry, Chemical Research Society of India CRSI-2016, held at Punjab University, Chandigarh, February 5-7, 2016.

Chemical Engineering Journal 409 (2021) 128294

Contents lists available at ScienceDirect

Chemical Engineering Journal

journal homepage: www.elsevier.com/locate/cej

MWCNT/Thienothiophene based All-Organic thermoelectric composites: Enhanced performance by realigning of the Fermi level through doping

Vijitha Ignatious [a,b], Neethi Raveendran [a,b], Arjun Prabhakaran [a], Yuvaraj Tanjore Puli [c], Vijayakumar Chakkooth [a,b,*], Biswapriya Deb [a,b,*]

[a] Photosciences and Photonics, Chemical Science and Technology Division, CSIR-National Institute for Interdisciplinary Science and Technology (CSIR-NIIST), Thiruvananthapuram 695019, India
[b] Academy of Scientific and Innovative Research (AcSIR), Ghaziabad 201002, India
[c] GAIL India Limited, R&D Department, GAIL Training Institute, Plot No. 24, Sector 16A, Noida 201301, India

ARTICLE INFO

Keywords:
Multi-walled carbon nanotube
Conjugated polymer
Thermoelectric composite
Theinothiophene doping
Seebeck coefficient
Thermoelectric generator

ABSTRACT

Thermoelectric (TE) polymer nanocomposites are an emerging class of functional materials that have immense potential for commercial usage. In this work, a lightweight all-organic nanocomposite of benzodithiophene-thienothiophene (BDT-TTE) based conjugated polymer poly[4,8-bis(5-(2-ethylyhexyl)thiophene-2-yl)benzo [1,2-b;4,5-b']dithiophene-2,6-diyl-alt-(4-(2-ethylhexyl)3-fluorothieno[3,4-b']thiophene-)-2-carboxylate-2–6-diyl)] (PBDTT-FTTE) and multi-walled carbon nanotube (MWCNT) was prepared for TE applications. The peak electrical conductivity in the composite was obtained with 45 wt% MWCNT content and the resulting composite exhibited a temperature tolerance up to 350 °C. The as-prepared nanocomposite was further p-doped with an oxidizing agent for tuning its Fermi level positioning leading to the further enhancement in TE output. The electrical conductivity was further boosted by 6.7x post-doping with concurrent 2.5x enhancement in the Seebeck coefficient. Thus, the power factor increased from 1.28 μW/m.K^2 to 48.21 μW/m.K^2, leading to the highest value for the thienothiophene based conjugated polymer/MWCNT nanocomposite. The device performance was demonstrated with a prototype exhibiting the power delivery of ~ 7 nW/cm^2 when tested with applied temperature difference across the hot and cold junction of 65 K.

1. Introduction

The scavenging of waste heat using thermoelectric generators (TEG) has become highly relevant in the present scenario of a drastic increase in the world's energy demand [1]. TEGs are solid-state devices, therefore have no moving parts and are silent, reliable, lightweight, and durable. The automobile industry has already started to use thermoelectric (TE) technology to convert waste heat from the hot gas exhaust using inorganic based TEGs. In the automobile industry, the usage of TEGs improves the engine efficiency by converting the waste heat into usable power to run auxiliaries such as electronics & navigation, seat warmer, electronic braking, indoor lightings etc. [2]. Major multinational automobile brands like BMW [3] Ford [4] Renault [5] and Honda [6] already have a strong foothold in this field and many of their upscale models now have functional TEGs. However, significant cost reduction and other engineering challenges have to addressed to implement this technology in the mass market segment [7].

The efficiency of TEG is generally characterized by dimensionless figure-of-merit (ZT), defined as

$$ZT = \frac{\sigma\alpha^2}{\kappa}T \quad (1)$$

where σ, α, T, and κ are the electrical conductivity, Seebeck coefficient, temperature, and thermal conductivity, respectively [8]. In equation (1), the quantity σα^2 is called the power factor (PF). A high-performance TE material requires a high α, a high σ, and a low κ. Recent progress in the preparation and engineering of inorganic TE materials has led to the remarkable improvements in device performances [9,10]. The enhancements primarily accessed by the proper utilization of nanostructuring techniques such as creating phonon-blocking/electron-transmitting thin-film superlattices [11–14] quantum-dot superlattices [15–18] and nanoscale inclusions in bulk materials [19,20]. However, these materials involved high temperatures, high-cost, and time-

* Corresponding authors at: Academy of Scientific and Innovative Research (AcSIR), Ghaziabad 201002, India.
E-mail addresses: cvijayakumar@niist.res.in (V. Chakkooth), biswapriya.deb@niist.res.in (B. Deb).

https://doi.org/10.1016/j.cej.2020.128294
Received 15 July 2020; Received in revised form 23 November 2020; Accepted 21 December 2020
Available online 25 December 2020

consuming fabrication processes. Moreover, most of the high-performance inorganic TE materials have their operation temperature above 200 °C, which is not suitable for capturing waste heat generated at a temperature below 200 °C. In this context, there is an enormous need for cheaper and lighter TE materials, preferably flexible, and working at the low-temperature range.

Research on organic TE materials has emerged and made tremendous progress in the past few years [21–25]. Organic materials, which are made up of abundant and less/non-toxic elements, can be processed from solution, enable the construction of the sustainable, large area and flexible TE devices, for converting low-end thermal energy into electricity. In the last decade, significant improvements in the performance of organic TE materials was observed due to the development of new molecular design strategies and the fabrication of nanocomposites consisting of conducting/semiconducting polymers with various nanomaterials [26]. A clear disadvantage of TE modules consisting of composites using heavy inorganic fillers is their module weight, which reduces their overall energy efficiency and limits their large-area applications. Such modules are mainly suitable for off-site operations, where associated technology for concentrating thermal energy/heat circulation may be required. In comparison, substantial weight reduction of TEGs would enable us to fabricate flexible, portable, easily mountable systems with low processing, implementation and maintenance costs. New application areas such as point of care sensors and IoT based devices would immensely benefit from such power sources.

In contrast, developing an all organic-based composite such as polymer fused/reinforced with carbon nanotubes (CNT) could be a promising approach to deliver a functional ultra-lightweight TE module. The general approach would be incorporating CNT in the polymer matrix to improve σ and mechanical strength without affecting κ [27]. Kim *et al.* reported the enhancement of TE performance of PEDOT:PSS by incorporating CNT with the polymer matrix. The σ of the composite was enhanced up to ~ 400 S/cm, which is more than 100 times higher than those of the typical polymer composite, due to the formation of polymer matrix–CNT electronic junctions [28]. Another study on similar composites showed little variance in α with increased loading of single-walled CNT (0–85 wt%), but σ increases leading to a maximum power factor of 140 μW/m.K^2 [29]. This PF was in the range observed for Bi_2Te_3, one of the most explored inorganic TE materials [30]. Nevertheless, making a stable PEDOT composite is quite challenging due to the hydrophobicity of the CNT surface. The current state-of-the-art PEDOT:PSS has many disadvantages that include hygroscopicity, acidity, anisotropic charge injection and batch-to-batch variation in physical and electrical properties. Since the PSS chains contain sulfonic acid groups with labile protons, it makes the polymer acidic in nature [31]. Moreover, in the presence of water vapours, the PSS shell, which surrounds the conducting PEDOT-rich cores, takes up water vapours and subsequently swells making PEDOT:PSS hygroscopic [32]. Many studied have earlier been performed to suppress the acidic nature of PEDOT:PSS [33] and to reduce the hygroscopicity [34,35]. Recently, Cameron et al. reviewed about the damaging effects of PEDOT:PSS acidic nature on semiconductor device performances [31].

In pursuit of developing a stable, ultra-lightweight and high-performing all-organic based TE composite, we have selected a semiconducting polymer consisting of benzo-[1,2-b:4,5-b']dithiophene (BDT) and theinothiophene (TTE) units. Conjugated polymers based on BDT have attracted significant attention in the fields of Organic Solar Cells (OSCs) and Organic Field-Effect Transistors (OFETs), owing to their planar conjugated structures, excellent electron-donating ability and high oxidative stability [36–39]. To date, this class of polymers exhibited the highest hole mobility (0.25 cm^2 V^{-1} s^{-1}) and solar cell efficiency (17.3%) among semiconducting organic polymers [40,41]. However, the TE properties of such systems have been scarcely explored. Similarly, the TE properties of TTE based conjugated polymers are also not being studied even though they show good charge carrier mobility and good capability to interact with π-structures such as CNTs yielding hybrid structures with unique properties [42]. These polymers are more adaptive to CNTs than PEDOT and incorporation of CNTs with such polymers can enhance the σ without much effect on κ, thereby enhancing the TE performance. Among the different types of CNTs, the single-walled carbon nanotubes (SWCNT) have higher Seebeck coefficient. However, multi-walled carbon nanotube (MWCNT) has several advantages such as ease of mass production, low product cost per unit, and enhanced chemical stability than SWCNT. These aspects enhance the realization of polymer/ MWCNT composite materials for real-world application such as waste heat harvesting from effluent pipes in industries. In this work, we prepared a nanocomposite of BDT-TTE based conjugated polymer PBDTT-FTTE and MWCNT and studied the TE properties. The as-prepared nanocomposite was further p-doped with an oxidizing agent to improve the TE performance by realigning the Fermi level. The process is generic and could be utilized to raise the TE properties of TTE based conjugated polymer materials to a competitive level. Moreover, we demonstrate that planar TEGs could be readily prepared by the facile solution processing of PBDTT-FTTE/MWCNT composites, which is a prerequisite for the realization of flexible, large-area applications.

2. Experiment section

2.1. Chemicals

PBDTT-FTTE ($(C_{49}H_{57}FO_2S_6)_n$) was purchased from Solarmer Energy INC. MWCNT (containing greater than 90% carbon basis, diameter ~ 110–170 nm and length ~ 5–9 μm) and anhydrous *ortho*-dichlorobenzene (*o*-DCB) were obtained from Sigma-Aldrich. Anhydrous ferric chloride ($FeCl_3$) was purchased from SD Fine Chemicals and nitromethane (CH_3NO_2) was procured from Spectrochem. All chemicals were used as received without any further purification.

2.2. Preparation of nanocomposite

The nanocomposites were prepared by dispersing PBDTT-FTTE and MWCNT in *o*-DCB at a concentration of 0.05 mg/L using a bath sonicator (Elmasonic P30H Ultrasonic bath; 80 kHz and 192 W) for 60 min. The PBDTT-FTTE/MWCNT composition was varied by adding different weight percentages of MWCNT. The homogeneity of dispersions was confirmed by visual inspection. The dispersion was drop-cast on a pre-cleaned (with soap solution, water, and isopropanol in that order by ultrasound sonication for 15 min in each) and pre-heated (at 120 °C for 15 min) glass substrate and annealed at 120 °C for 30 min.

2.3. Doping of nanocomposite film

Samples were doped by immersing in 0.05 M $FeCl_3$ solution in nitromethane for 30 min, then washed with ethanol to remove excess dopant followed by annealing at 100 °C for 15 min.

2.4. Characterization and measurements

The UV–Vis absorption spectra were recorded using UV–Vis spectrometer (Ocean Optics OCEAN-HDX-UV–VIS). The nanocomposites' morphology was characterized by scanning electron microscopy (SEM; JEOL 5600 LV). Wide-angle X-ray scattering measurements (WAXS) were performed on a Xenocs XEUSS Simultaneous WAXS system with Ni-filtered Cu K_α radiation ($\lambda = 1.5405$ Å) in the transmission mode. The thermal stability was measured by thermogravimetric analysis (TGA; Q50 TGA from TA Instruments) at a heating rate of 10 °C/min from 30 °C to 800 °C. The TE studies were done on the Linseis LSR-3 system. The film thickness was measured using a Veeco Dektak 6 M stylus profilometer. The surface chemistry was analyzed using X-ray photoelectron spectroscopy (XPS, PHI 5000 Versa Probe II, ULVAC-PHI Inc., USA) equipped with micro-focused (200 μm, 15 kV) monochromatic Al-Kα X-

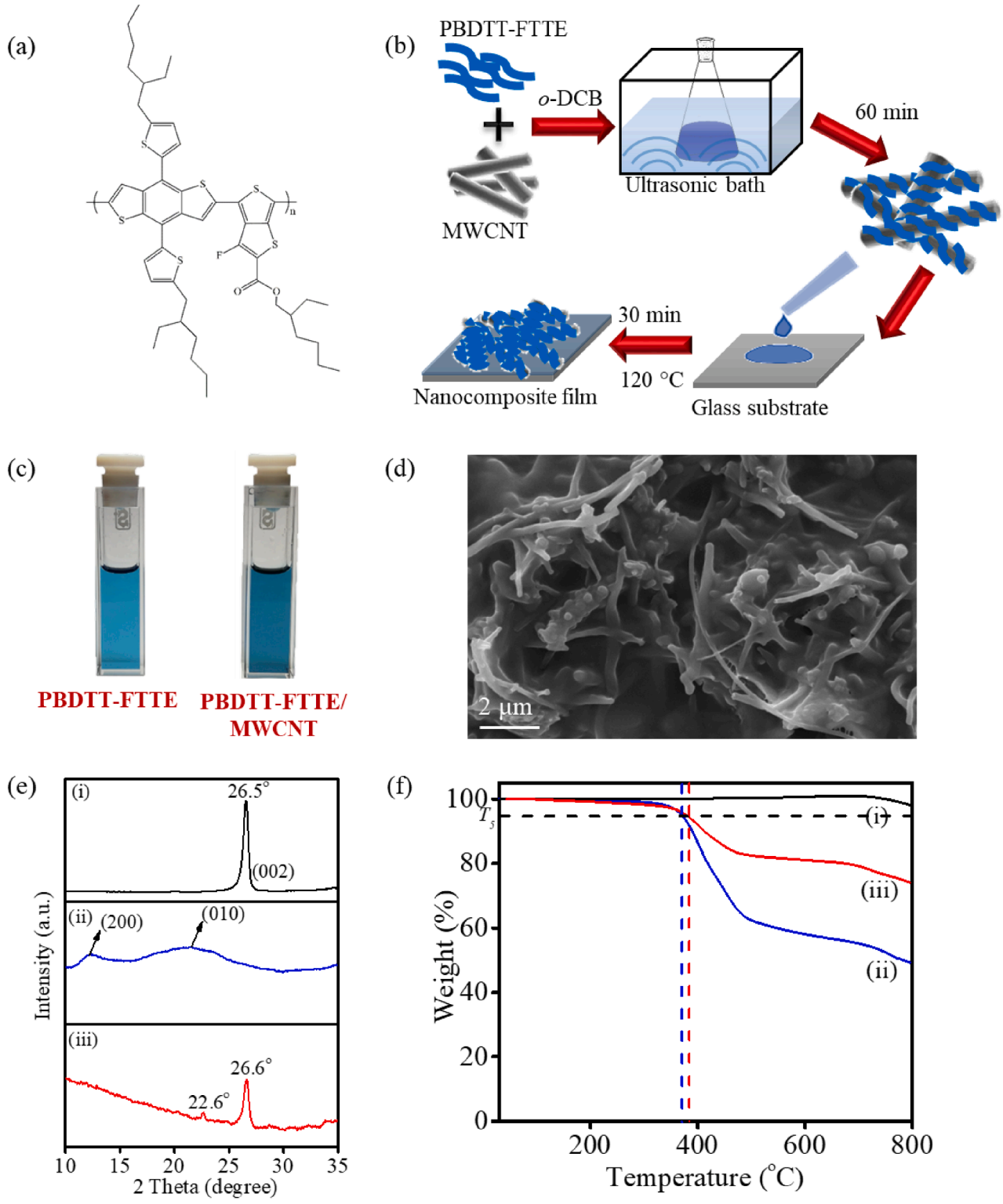

Fig. 1. (a) Molecular structure of PBDTT-FTTE. (b) Schematic representation of sample preparation. (c) Photographs of polymer and composite in *o*-DCB. (d) SEM image of the nanocomposite film. (e) WAXS patterns and (f) TGA plot of (i) as purchased MWCNT (ii) PBDTT-FTTE (iii) Nanocomposite with MWCNT ~ 45 wt%.

ray source ($h\nu$ = 1486.6 eV). Both survey and narrow scan (high-resolution) spectra were recorded. Survey scans were recorded with an X-ray source having a power of 50 W and pass energy of 187.85 eV. High-resolution spectra of the major elements were recorded at 46.95 eV pass energy and the peaks were fitted and analyzed using MultiPak software. The C 1 s line at 284.8 eV was used as an internal energy reference. Kelvin probe (KP) data were recorded under ambient conditions on the Bruker Multimode AFM-3COCF system in contact mode using CSG10_Ed/Pt (NT-MDT) tip. Mobility and carrier concentration of film were studied at room temperature in van der Pauw's geometry by employing ECOPIA HMS 3000 Hall measurement system under a magnetic field of 0.556 T and a current of 15 mA.

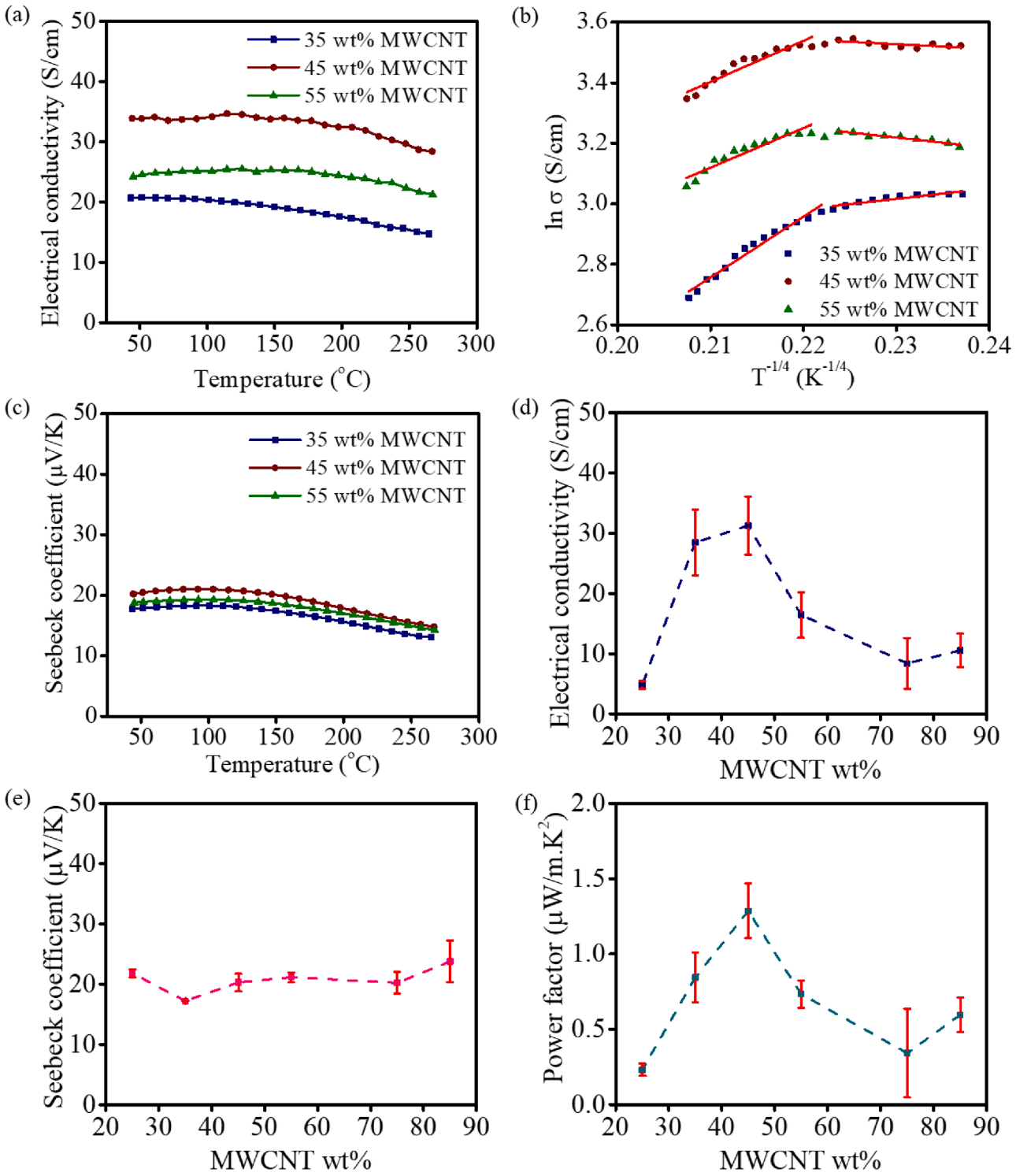

Fig. 2. Temperature-dependent changes of (a) electrical conductivity (b) Seebeck coefficient of nanocomposite with varying amounts of MWCNT. (c) The fitted curve of ln σ vs $T^{-1/4}$, according to Mott's VRH model. (d)-(e) TE properties of nanocomposite by varying MWCNT wt%.

2.5. Fabrication of TEG and testing

The TEG consist of 7 TE legs, drop cast on a glass substrate using a solution of PBDTT-FTTE/ 45 wt% MWCNT nanocomposite. The drop cast TE arrays were annealed on a hotplate at 120 °C for 30 min. For connection of the TE legs, metal electrodes were drop-casted using conductive silver paste (TED PELLA, Pelco ® Conductive Silver paint). The fabricated TEG was then annealed at 100 °C on a hot plate for 30 min to improve the electrical conductivity of the Ag electrodes and reduce the contact resistance between the Ag electrodes and TE elements. Each leg had dimensions of 4 mm × 2.5 cm and the overall size of the fabricated TEG was 4.5 cm × 2.5 cm.

The fabricated TEG evaluation was carried out in a home-built setup. The setup consisted of a silicon rubber heater (TEMPSENS Instruments Pvt. Ltd.) and a Peltier device (Laird Thermal Systems, Inc.) to maintain controlled stages that could independently function as the hot part and cold part, respectively. The exact temperature of each surface was measured using a K-type thermocouple. The temperature gradient

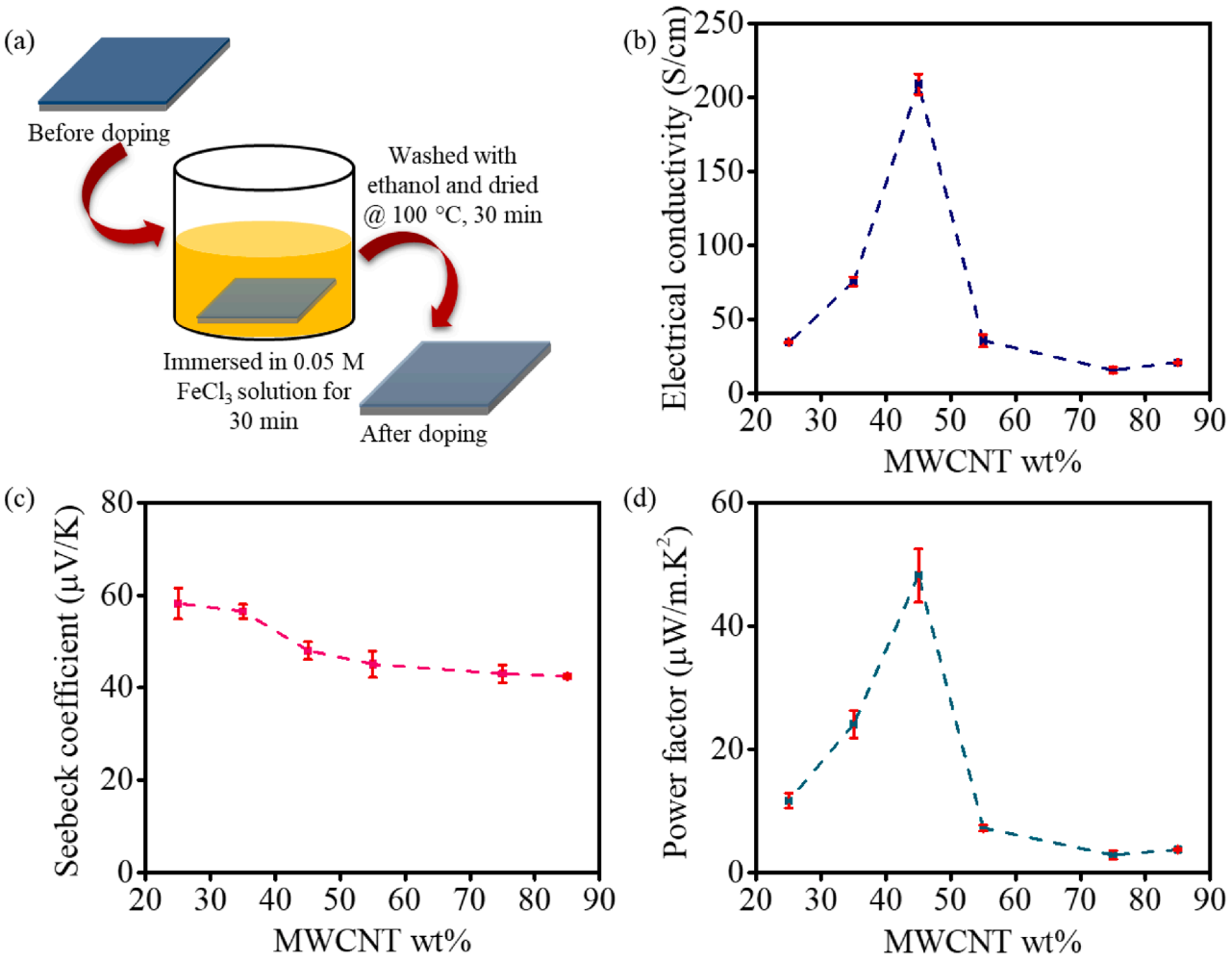

Fig. 3. (a) Schematic representation of the doping method. (b)-(d) TE properties of nanocomposite after doping by varying MWCNT wt%.

between the two electrodes was varied from 3 to 65 K. For the measurement, a Keithley 2450 source meter, a Keithley 2182A nano voltmeter and an Aplab PPD3003-S power supply were used.

3. Results and discussion

3.1. Nanocomposite characterization and analysis

The molecular structure of PBDTT-FTTE and the sample preparation method are depicted in Fig. 1a and Fig. 1b, respectively. Fig. 1c shows photographs of PBDTT-FTTE and PBDTT-FTTE/MWCNT nanocomposite in *o*-DCB at a concentration of 6.5 μg/mL. As evident from the photograph, the MWCNTs and PBDTT-FTTE formed a stable and homogeneous dispersion in *o*-DCB. It was stable for three weeks; no subsequent settling of material has been observed during this period. To test the dispersion homogeneity, a thin film was made on a quartz substrate (2.5 × 2.5 cm^2) and absorption spectra were taken from three different regions of the film as shown in Fig. S1a (#ESI). As shown in Fig. S1b (#ESI), the absorption spectra of PBDTT-FTTE reveal a characteristic sharp peak of the π-π* transition at 235.5 nm. The PBDTT-FTTE/MWCNT nanocomposite exhibited both strong quenching of the absorbance intensity and a redshift of the absorbance peak to a broad peak centred at 245.0 nm. The redshift in absorbance indicated the formation of ground state physical interactions of π-stacking between aromatic moieties and MWCNT [43,44]. This redshift is due to the wrapping of the conjugated polymer chains on the MWCNT surface, which increases the polymer conjugation length [44,45]. A similar absorbance intensity was observed for this peak at three different regions reveals the homogenous dispersion of MWCNT in the polymer matrix. The Fig. 1d shows a typical SEM topography of the nanocomposite coatings on glass substrates that shows the MWCNTs were covered with PBDTT-FTTE to form a hybrid structure. In such conditions, one can expect that the electron-rich fused thiophene units to promote π-stacking interactions with MWCNT leading to the hybrid structure [46,47].

The WAXS pattern of MWCNT presented in Fig. 1e reveals a diffraction peak at 26.5° corresponds to the diffraction plane (0 0 2) and confirms the highly graphitic structure of the CNTs [48]. PBDTT-FTTE showed a pronounced (2 0 0) diffraction peak at 12°, arising from alkyl chain packing with a *d*-spacing of ~ 7.36 Å. A broad peak at 21.3° with the *d*-spacing of ~ 4.16 Å, corresponds to (0 1 0) plane arising from π-π stacking of thiophene rings [49]. This peak gets shifted to 22.6° with the addition of MWCNT. A decrease in intensity of the characteristic peak of MWCNT was also observed. This implies that the walls of CNTs are distorted when the polymer overlaid on its walls. The thermal stability of nanocomposite was analyzed using TGA, which was done at a heating rate of 10 °C/min in a nitrogen atmosphere. The temperature at which the material loses its 5% of the weight is called T_5 value [50]. From the TGA plot (Fig. 1f), the T_5 value of nanocomposite was found to be about 380 °C, while that of pure polymer is about 370 °C. This observation suggests that the thermal stability of the polymer gets better after adding MWCNT.

3.2. Thermoelectric studies of undoped film

The TE behaviour of nanocomposite having MWCNT weight percentage (wt%) varying from 25 to 85 has been studied using LSR. We measured an error range of $0.025 \leq \rho \geq 0.038$ μΩm and $0.5 \leq \alpha \geq 2$ μV/K for resistivity and Seebeck coefficient respectively, which is explained in Fig. S2 (#ESI). The samples were drop-casted on a glass substrate of a dimension of 14 × 4 mm to form a thick film of micrometre thickness. The variation of film thickness with MWCNT wt% is shown in Fig. S3 (#ESI). To understand the TE behaviour of the nanocomposite film, initially, the σ and α of selected nanocomposites were measured by varying temperature from 30 °C to 260 °C. The σ of the composite films decreased with increasing temperature (Fig. 2a). The temperature dependence of σ mostly follows Mott variable range hopping (VRH) model [51]

$$\sigma = \sigma_0 \exp\left[-\left(\frac{T}{T_0}\right)^{\frac{1}{d+1}}\right] \quad (2)$$

where σ_0 is a characteristic coefficient which depends on the density of states of the material, the length of the average transition, and the frequency of the molecular vibration; T_0 is the Mott's characteristic temperature; T is the measured temperature and d is the dimensionality. The Mott's VRH model describes the charge transport in a disordered system in which the charge carriers hop from one localized site to another inside the network near Fermi level [52]. The plot of ln σ as a function of $T^{-1/4}$ is shown in Fig. 2b, which shows two different slopes for each sample within the investigated temperature range 303 K $\leq T \leq$ 533 K. Hence the charge transport in the films follows a three-dimension (3D) VRH model, where $d = 3$ in equation (2) (detailed calculations can be found in Fig. S4 and Table S1, #ESI) [53]. This result indicates that in the nanocomposites, the MWCNTs are densely coated with the polymer through strong π-π interfacial interactions, and the carriers in one localized MWCNT hopped to another and contributed to the conductance. The change in temperature shows only a negligible variation in α; the corresponding value of these composite films was stable from 14 to 20 μV/K (Fig. 2c). Hence, we did the subsequent measurements at ambient temperatures. Fig. 2d-f show the TE properties of the composite films by varying MWCNT wt%. We did not observe noticeable σ enhancements with a lower amount of CNT incorporation; rather a percolation threshold is apparent beyond 25 wt% that reaches a maximum value (σ = 31.26 S/cm) at 45% of MWCNT. The improvements could be ascribed to the increase in the electrical pathways composed of inter-CNT bundle connections. A further rise of MWCNT wt% has resulted in a decrease in σ attributed to the breaking down of polymer stacking in the film as the percentage of MWCNT increases. As the wt% of MWCNT becomes more than 45%, the MWCNT forms aggregates and gets isolated in the polymer matrix, as shown in Fig. S5 (#ESI). This results in a decrease in electrical conductivity as it loses the continuous pathway. The α shows an average value of 20.7 μV/K, regardless of MWCNT addition, equivalent to the α of MWCNT (Table S2, #ESI) [54]. Thus, the PF followed a similar trend to that of σ.

3.3. Doping of thermoelectric films

The electrical conduction of the as-prepared TE nanocomposite mainly occurs through MWCNT without any contribution from the overlaid polymer. Thus the conductivity of the polymer should be raised to metallic level for any further improvements in the composite properties. In a set of experiments, we explored the effect of p-doping in the nanocomposite and its impact on the overall TE response. In Fig. 3a, we presented a schematic representation of the adopted doping method. From a survey of the literature, $FeCl_3$ was used as an oxidizing agent for p-doping for PEDOT based systems [55,56]. However, their ability to dope the present thienothiophene systems was rarely exploited. For such experiments, both dopant concentration and doping time strongly affect

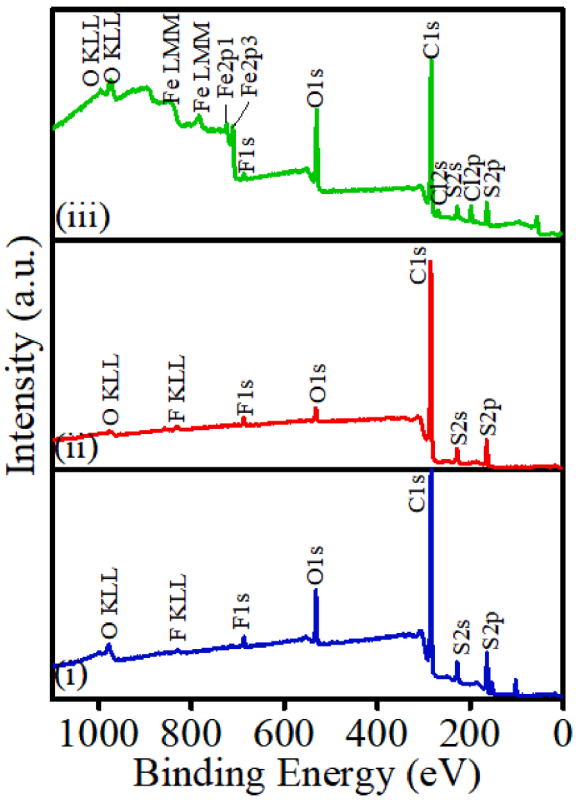

Fig. 4. XPS survey spectra of (i) pristine polymer (ii) nanocomposite with MWCNT ~ 45 wt% before doping and (iii) after doping.

the resulting TE properties of the composite (Fig. S6, #ESI). The thickness of the film shows a little change after doping and also within the error limit of that of before doping films (Fig. S7, #ESI). The nanocomposite after doping with $FeCl_3$ also exhibit the same temperature tolerance as shown in Fig. S8 (#ESI). Fig. 3b and c show that after doping, there is a significant rise in both σ and α compared to that of undoped nanocomposite films. The highest PF was obtained with MWCNT ~ 45 wt%, where the σ is increased by 6.70 times (~208.9 S/cm) than the undoped nanocomposite film. The Seebeck coefficient, in contrast, exhibited a different trend from the undoped samples, and we observed a shallow drop in values with an increasing percentage of MWCNT. As the weight percentage of MWCNT becomes more than 45%, the MWCNT forms aggregates and gets isolated in the polymer matrix. Hence, the charge carriers have to move through the polymer for electrical conduction to occur. After doping, the polymer matrix is p-doped and which increases the charge carriers. The amount of polymer is lesser in 55 wt% composite than in 45 wt%, which in turn limit the doping level and results in a decrease in active dopant species present in the polymer matrix. The increase in electrical conductivity and mechanism of charge transport depends on the extent of doping level and formation and distribution of conducting domains within the polymer matrix. However, the value of α was doubled from that of undoped film. Thus the resulting power factor exhibited a whopping 37x enhancement (1.28 μW/m.K^2 in undoped nanocomposite films to 48.21 μW/m.K^2 in doped samples) for PBDTT-FTTE/ 45 wt% MWCNT composites (Fig. 3d). Besides, we compared the TE properties of PBDTT-FTTE/MWCNT, other conjugated polymers/MWCNT composites and thienothiophene polymers as shown in Table S3 (#ESI), we found that PBDTT-FTTE/MWCNT composites show enhanced TE performance compared to other MWCNT composite systems.

The concept of doping of organic polymers generally accomplished by the charge-transfer process between the polymer and dopant (oxidizing or reducing agent). The p-doping of conducting polymers

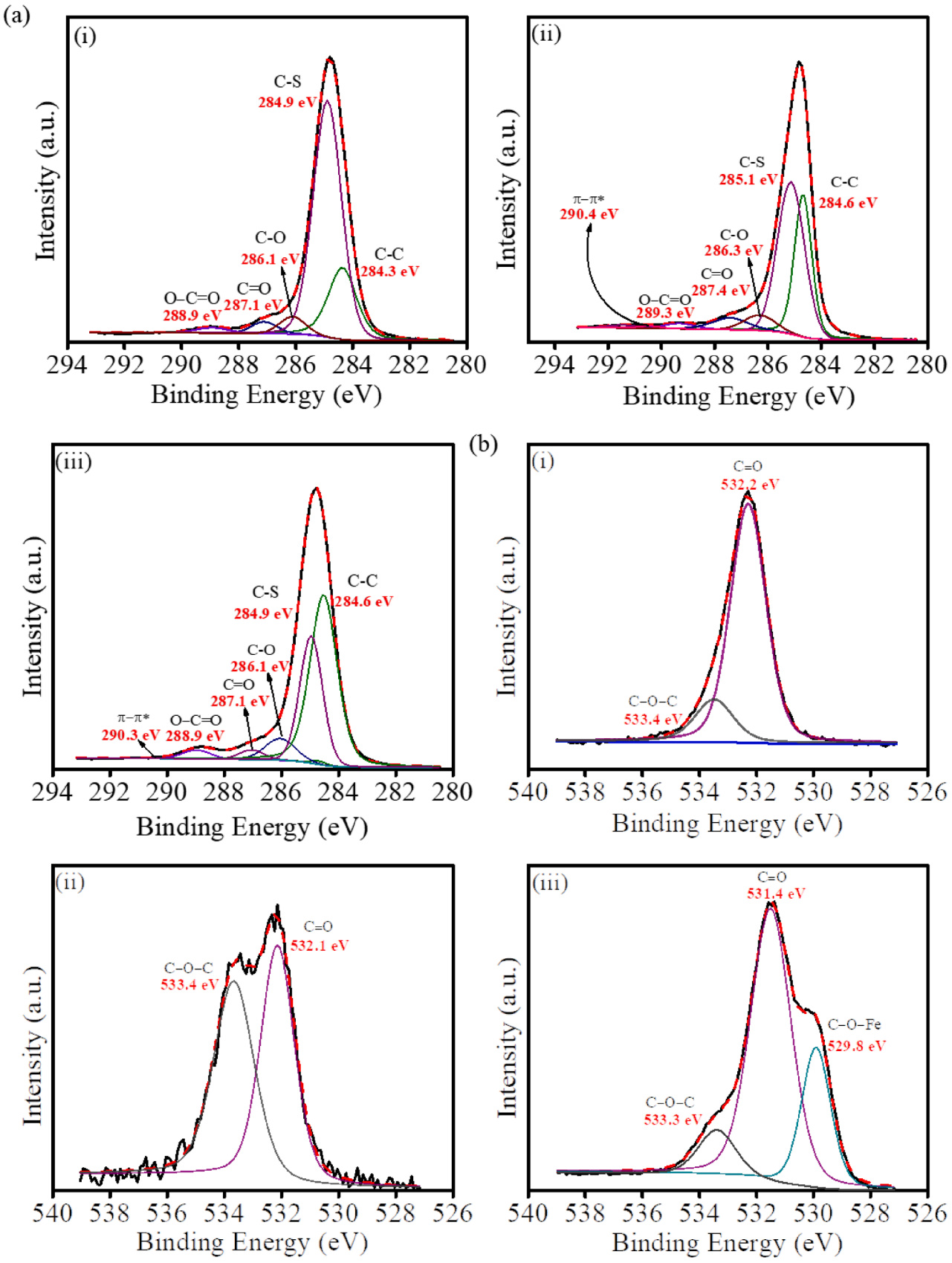

Fig. 5. (a) C1s XPS spectra and (b) O1s XPS spectra of (i) pristine polymer (ii) nanocomposite with MWCNT ~ 45 wt% before doping and (iii) after doping.

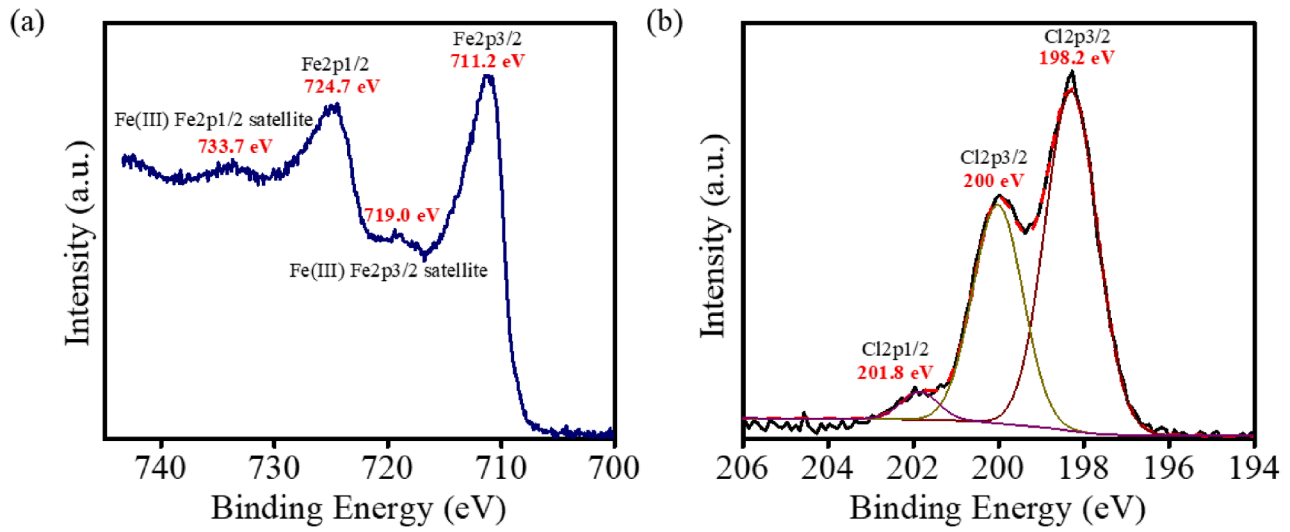

Fig. 6. (a) Fe2p XPS spectra and (b) Cl2p XPS spectra of nanocomposite with MWCNT ~ 45 wt% after doping.

refers to the partial oxidation of the polymer, where a counter-ion is provided to maintain the electrical neutrality [57]. The doping of PBDTT-FTTE has been achieved by using $FeCl_3$ (oxidant) involving the electron transfer between the two, resulting in the formation of PBDTT-FTTE:$FeCl_3$ charge-transfer complex. The concurrent improvements in σ and α in the PBDTT-FTTE:$FeCl_3$ complex could have resulted from the so-called "hole-doping" effect, where the Fermi level of the system is pinned below the valance band due to presence of Fe^{3+} [58]. To confirm the presence of the charge transfer complex, we conducted XPS measurement and valance band maxima (VBM) analysis. Fig. 4 shows a typical wide scan survey spectrum of pristine polymer, nanocomposite before and after doping. The photoelectrons peaks of the survey spectra reflect the major essentials, e.g., S, F, O and C. The $Fe2p_1$, $Fe2p_3$ and Cl2p peaks confirm the presence of intercalated dopant species.

Fig. 5a and Fig. 5b show the high resolution of C1s and O1s XPS results and the deconvoluted peaks (bonding components) for pristine polymer, nanocomposite before and after doping, respectively. The S2p and F1s XPS spectra are shown in Fig. S9 (#ESI) that showed a negligible change. The C1s XPS spectrum (Fig. 5a-i) represents the three oxygen functional groups of PBDTT-FTTE at 286.1, 287.1 and 288.9 eV, which are assigned to the C-O, C = O and O-C = O bonds, respectively [59,60]. The addition of MWCNT marginally shifts these functional group peaks to higher binding energies (Fig. 5a-ii). The peak at 290.4 eV is related to the π-π* bonds arises from the sp^2 carbon atom of MWCNT. However, after doping, the functional group peaks returned to that of the pristine polymer that confirmed the presence of strained bonds due to MWCNT-polymer interaction and their subsequent relaxation after doping (Fig. 5a-iii). The O1s XPS spectrum of PBDTT-FTTE (Fig. 5b-i) and nanocomposite (Fig. 5b-ii) exhibits the oxygen peak arising from C = O (~532.1 eV) and C-O-C (~533.4 eV). The intensity of C-O-C peak increases by adding MWCNT, as such groups were generated unintentionally when the MWCNTs were exposed to the environment containing natural oxidizing agents such as ozone and hydroxyl radicals [61]. The peak at 529.8 eV in Fig. 5b-iii corresponds to C-O-Fe due to the presence of charge transfer complex after doping.

The high-resolution Fe2p spectra were measured to evaluate the electronic nature of iron after doping. The Fe2p core level spectra are shown in Fig. 6a. The $Fe2p_{3/2}$ and $Fe2p_{1/2}$ peaks binding energies are located at 711.2 eV and 724.7 eV respectively corresponded to Fe^{3+} (oxide). The observed energy value for $Fe2p_{3/2}$ core level matches to the value found for Fe^{3+} in $(Et_4N)FeCl_4$ salt. Shake up satellite value at 719.0 eV, which is ~ 7.8 eV from the main $Fe2p_{3/2}$ peak supports that Fe is presented in Fe^{3+} ionic state. The Fe2p energy value suggests the presence of Fe^{3+} in the form of $FeCl_4^-$. In Fig. 6b, the Cl2p core level

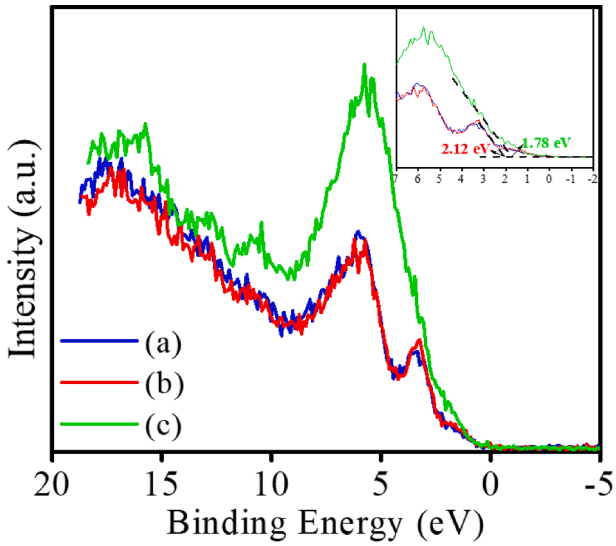

Fig. 7. XPS VB spectra of (a) PBDTT-FTTE (b) nanocomposite with MWCNT ~ 45 wt% before doping and (c) after doping.

signal gives two $Cl2p_{3/2}$ unresolved doublets with their maxima respectively at ~ 198.2 eV and ~ 200.0 eV on the binding energy scale. The peak at low energy that shows the similar energy value observed for $Cl2p_{3/2}$ in $(Et_4N)FeCl_4$ salt can be assigned as being due to $FeCl_4^-$ species [62–67].

The XPS valence band (VB) spectra for pristine polymer, nanocomposite before doping and after doping on a gold substrate are shown in Fig. 7. The valence band maxima (VBM) position is determined by linear extrapolation of the low binding energy edge of the valence band spectrum shown in the inset. The spectra exhibit a steep rise in the density of states (DOS) after doping that is primarily responsible for the massive increase in σ. The position of VBM is also shifted (from ~ 2.12 eV to ~ 1.78 eV) towards the reference Fermi level after doping that could cause overlap with its internal Fermi level. The work function (WF) of the nanocomposite is investigated by adjusting the obtained contact potential difference (CPD) from the tip WF using a Kelvin probe (KP) setup (Fig. S10, #ESI). With respect to the vacuum level, the work functions of the nanocomposite are estimated at 4.845 eV before doping and 4.969 eV after doping. Thus, the increase in WF after doping also suggests the shifting of Fermi level towards the valence band.

Table 1
Mobility and carrier concentration of PBDTT-FTTE nanocomposite with 45 wt% of MWCNT before and after doping.

Particulars	Before doping	After doping
Bulk concentration (/cm^3)	3.767E + 20	3.133E + 20
Sheet concentration (/cm^2)	3.940E + 17	3.277E + 17
Mobility (cm^2/Vs)	3.415E-1	5.614E-1

The dependence of carrier concentration and α could be explained by Mott's relation [68]

$$\alpha = \frac{8\pi^2 k_B^2 T}{3eh^2} m^* \left(\frac{\pi}{3n}\right)^{2/3} \quad (3)$$

where k_B, T, m*, and n are the Boltzmann constant, absolute temperature, carrier effective mass, and the reduction in carrier concentration, respectively. The Hall measurement studies suggest that the mobility of the charge carrier increases after doping, with a decrease in carrier concentration (Table 1). Along with the realignment of the Fermi level, the reduction in carrier concentration results in a significant increase in α.

Finally, a practical TE application using these all-organic composites does not solely depend on its PF values but require prevention from the thermal shorting. The actual thermal conductivity determination is beyond the scope of this work, as we need specialized systems to evaluate a polymer composite coating. Since the percolation threshold and peak PF values in the described system required ≤ 25 wt% of MWCNT usage, the existing theories are not applicable as these were developed lower wt% of the fillers [69–71]. An indirect assessment is possible by fabricating an actual device and evaluating its TE output [72–74]. We fabricated a TEG comprising seven legs arranged on a glass substrate using PBDTT-FTTE/ 45 wt% MWCNT solution, as shown in Fig. 8a. The fabrication of TEG and geometry adapted for measurement are shown in Fig. S11 (#ESI). Fig. 8b shows the measured voltage (V_{oc}), current (I_{sc}) and output power (P_o) of the device as a function of temperature difference (ΔT). The fabricated TEG shows a moderate output voltage of 9.12 mV and an output power of 6.92 nW at ΔT = 65 K with a load resistance of 1 kΩ. Furthermore, α determined by the V_{oc} and ΔT of the TEG is approximately 22 ± 2 μV/K, which corresponds to that of the PBDTT-FTTE/MWCNT thin film. The maximum power was observed at load resistance range ~ 15 Ω, as shown in Fig. 8c.

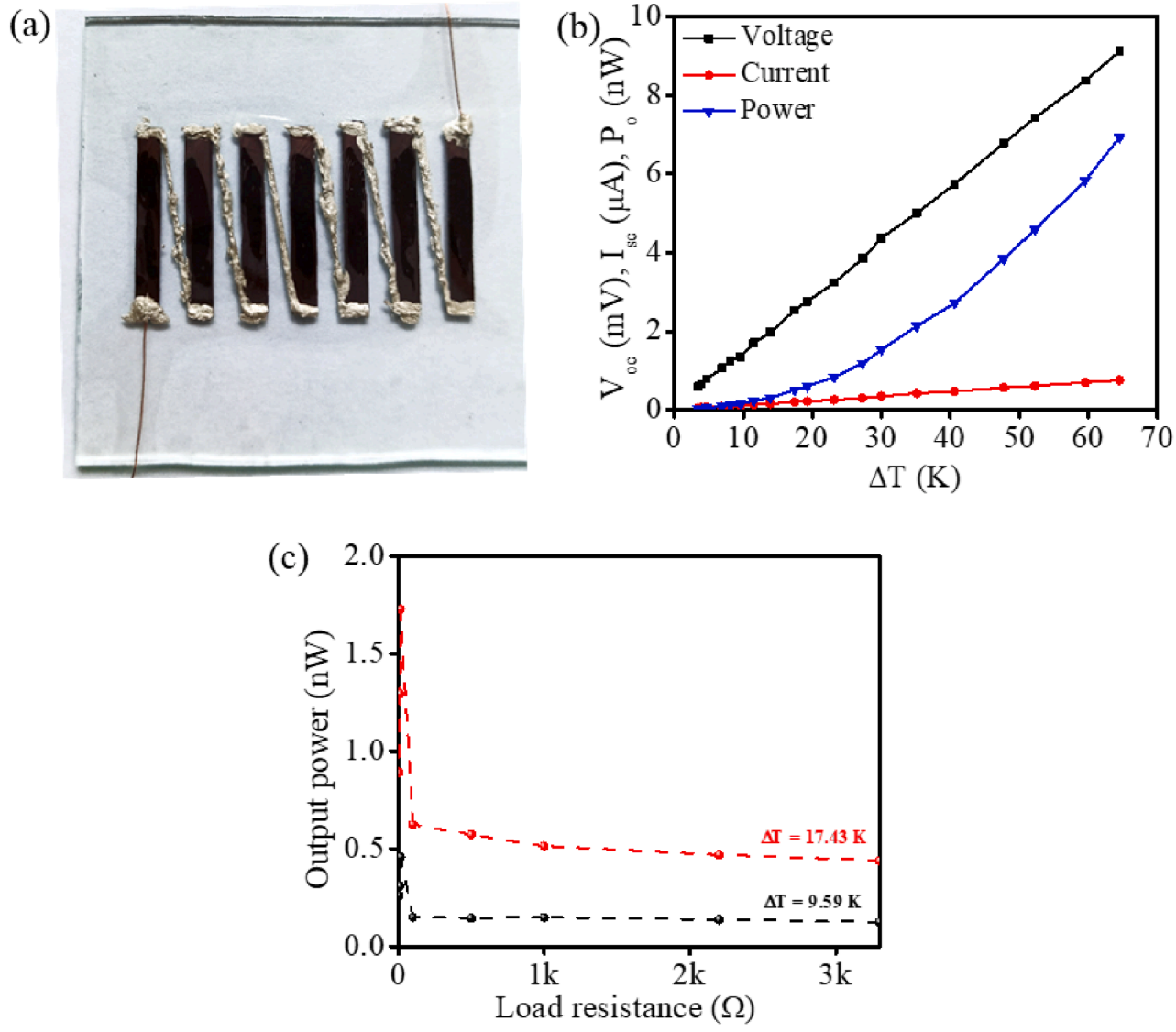

Fig. 8. (a) Image of planar TEG consisting of 7 legs. (b) The output voltage, short circuit current and output power of TEG versus ΔT. (c) The output power curves according to different load resistance at ΔT = 9.59 K and 17.43 K.

4. Conclusions

In summary, we prepared and characterized BDT-TTE based polymer nanocomposite films hybridizing with MWCNT that exhibited p-type TE response. Further enhancement of TE properties was achieved by doping with an oxidizing agent, $FeCl_3$, that increases both σ and α. The doping mechanism increases the DOS and results in the alignment of the Fermi level by introducing a charge-transfer complex. From this perspective, our work provides an insight into the relationship between doping mechanism and enhancement in thermoelectric properties. At room temperature, for doped PBDTT-FTTE/45 wt% MWCNT, the electrical conductivity is enhanced up to 6.7x compared to the as-prepared samples. At the same time, the Seebeck coefficient (thermos-voltage) exhibited ~ 2.5x improvement. Thus, the power factor raised from 1.28 μW/m.K^2 to 48.21 μW/m.K^2, leading to the highest value for the thienothiophene based conjugated polymer/MWCNT nanocomposite. TGA verifies the nanocomposite is stable up to ~ 350 °C, which boosts the application of nanocomposite as a low-temperature TE material. Devices based on these materials typically operate below 350 °C and could be used for on-the-spot sustainable power generation from thermal sources like hot water released by process plants, automotive exhausts, and even human/mammal body heat.

Declaration of Competing Interest

The authors declare that they have no known competing financial interests or personal relationships that could have appeared to influence the work reported in this paper.

Acknowledgement

This work is supported by the Council of Scientific and Industrial Research (CSIR), Govt. of India and Gas Authority of India Limited (GAIL) through the project SSP-135939. I.V. acknowledges her research fellowship from DST-INSPIRE. The authors extend their gratitude to Mr. Visakh M (CUSAT) for Hall measurement, Mr. Vibhu Darshan for the KP measurement, Dr. Saju Pillai and Mr. Peer Mohamed for XPS analysis.

References

[1] R. Freer, A.V. Powell, Realising the potential of thermoelectric technology: a Roadmap, J. Mater. Chem. C. 8 (2) (2020) 441–463, https://doi.org/10.1039/C9TC05710B.
[2] N. Jaziri, A. Boughamoura, J. Müller, B. Mezghani, F. Tounsi, M. Ismail, A comprehensive review of thermoelectric generators: Technologies and common applications, Energy Rep. 6 (2020) 264–287, https://doi.org/10.1016/j.egyr.2019.12.011.
[3] D.T. Crane, J.W. LaGrandeur, Progress report on BSST-Led US Department of Energy Automotive Waste Heat Recovery Program, J. Electron. Mater. 39 (9) (2010) 2142–2148, https://doi.org/10.1007/s11664-009-0991-0.
[4] Q.E. Hussain, D.R. Brigham, C.W. Maranville, Thermoelectric exhaust heat recovery for hybrid vehicles, SAE Int. J. Engines 2 (1) (2009) 1132–1142, https://doi.org/10.4271/2009-01-1327.
[5] N. Espinosa, M. Lazard, L. Aixala, H. Scherrer, Modeling a thermoelectric generator applied to diesel automotive heat recovery, J. Electron. Mater. 39 (9) (2010) 1446–1455, https://doi.org/10.1007/s11664-010-1305-2.
[6] M. Mori, T. Yamagami, M. Sorazawa, T. Miyabe, S. Takahashi, T. Haraguchi, Simulation of fuel economy effectiveness of exhaust heat recovery system using thermoelectric generator in a series hybrid, SAE Int. J. Mater. Manuf. 4 (1) (2011) 1268–1276, https://doi.org/10.4271/2011-01-1335.
[7] B. Orr, A. Akbarzadeh, M. Mochizuki, R. Singh, A review of car waste heat recovery systems utilising thermoelectric generators and heat pipes, Appl. Therm. Eng. 101 (2016) 490–495, https://doi.org/10.1016/j.applthermaleng.2015.10.081.
[8] Y. Lan, A.J. Minnich, G. Chen, Z. Ren, Enhancement of thermoelectric figure-of-merit by a bulk nanostructuring approach, Adv. Funct. Mater. 20 (3) (2010) 357–376, https://doi.org/10.1002/adfm.v20:310.1002/adfm.200901512.
[9] P. Ren, Y. Liu, J. He, T.u. Lv, J. Gao, G. Xu, Recent advances in inorganic material thermoelectrics, Inorg. Chem. Front. 5 (10) (2018) 2380–2398, https://doi.org/10.1039/C8QI00366A.
[10] D. Li, Y. Gong, Y. Chen, J. Lin, Q. Khan, Y. Zhang, Y. Li, H. Zhang, H. Xie, Recent progress of two-dimensional thermoelectric materials, Nano-Micro Lett. 12 (2020) 36, https://doi.org/10.1007/s40820-020-0374-x.
[11] I. Chowdhury, R. Prasher, K. Lofgreen, G. Chrysler, S. Narasimhan, R. Mahajan, D. Koester, R. Alley, R. Venkatasubramanian, On-chip cooling by superlattice-based thin-film thermoelectrics, Nat. Nanotechnol. 4 (4) (2009) 235–238, https://doi.org/10.1038/nnano.2008.417.
[12] R. Venkatasubramanian, Lattice thermal conductivity reduction and phonon localizationlike behavior in superlattice structures, Phys. Rev. B. 61 (4) (2000) 3091–3097, https://doi.org/10.1103/PhysRevB.61.3091.
[13] P. Hyldgaard, G.D. Mahan, Phonon superlattice transport, Phys. Rev. B. 56 (17) (1997) 10754–10757, https://doi.org/10.1103/PhysRevB.56.10754.
[14] H. Böttner, G. Chen, R. Venkatasubramanian, Aspects of thin-film superlattice thermoelectric materials, devices, and applications, MRS Bull. 31 (3) (2006) 211–217, https://doi.org/10.1557/mrs2006.47.
[15] J.P. Heremans, C.M. Thrush, D.T. Morelli, Thermopower enhancement in lead telluride nanostructures, Phys. Rev. B. 70 (2004), 115334, https://doi.org/10.1103/PhysRevB.70.115334.
[16] R.Y. Wang, J.P. Feser, J.-S. Lee, D.V. Talapin, R. Segalman, A. Majumdar, Enhanced thermopower in PbSe nanocrystal quantum dot superlattices, Nano Lett. 8 (8) (2008) 2283–2288, https://doi.org/10.1021/nl8009704.
[17] P. Trocha, J. Barnaś, Large enhancement of thermoelectric effects in a double quantum dot system due to interference and Coulomb correlation phenomena, Phys. Rev. B. 85 (2012), 085408, https://doi.org/10.1103/PhysRevB.85.085408.
[18] Z. Quan, Z. Luo, W.S. Loc, J. Zhang, Y. Wang, K. Yang, N. Porter, J. Lin, H. Wang, J. Fang, Synthesis of PbSeTe single ternary alloy and core/shell heterostructured nanocubes, J. Am. Chem. Soc. 133 (44) (2011) 17590–17593, https://doi.org/10.1021/ja207763p.
[19] J.P.A. Makongo, D.K. Misra, X. Zhou, A. Pant, M.R. Shabetai, X. Su, C. Uher, K. L. Stokes, P.F.P. Poudeu, Simultaneous large enhancements in thermopower and electrical conductivity of bulk nanostructured half-heusler alloys, J. Am. Chem. Soc. 133 (46) (2011) 18843–18852, https://doi.org/10.1021/ja206491j.
[20] J.W. Simonson, D. Wu, W.J. Xie, T.M. Tritt, S.J. Poon, Introduction of resonant states and enhancement of thermoelectric properties in half-Heusler alloys, Phys. Rev. B. 83 (2011), 235211, https://doi.org/10.1103/PhysRevB.83.235211.
[21] G. Zuo, H. Abdalla, M. Kemerink, Conjugated polymer blends for organic thermoelectrics, Adv. Electron. Mater. 5 (11) (2019) 1800821, https://doi.org/10.1002/aelm.201800821.
[22] H. Jin, J. Li, J. Iocozzia, X. Zeng, P.-C. Wei, C. Yang, N. Li, Z. Liu, J.H. He, T. Zhu, J. Wang, Z. Lin, S. Wang, Hybrid organic-inorganic thermoelectric materials and devices, Angew. Chemie Int. Ed. 58 (43) (2019) 15206–15226, https://doi.org/10.1002/anie.v58.4310.1002/anie.201901106.
[23] G. Chen, W. Xu, D. Zhu, Recent advances in organic polymer thermoelectric composites, J. Mater. Chem. C. 5 (18) (2017) 4350–4360, https://doi.org/10.1039/C6TC05488A.
[24] M. Culebras, K. Choi, C. Cho, Recent progress in flexible organic thermoelectrics, Micromachines 9 (2018) 638, https://doi.org/10.3390/mi9120638.
[25] L.M. Cowen, J. Atoyo, M.J. Carnie, D. Baran, B.C. Schroeder, Review—organic materials for thermoelectric energy generation, ECS J. Solid State Sci. Technol. 6 (3) (2017) N3080–N3088, https://doi.org/10.1149/2.0121703jss.
[26] C.-J. Yao, H.-L. Zhang, Q. Zhang, Recent progress in thermoelectric materials based on conjugated polymers, Polymers (Basel) 11 (2019) 107, https://doi.org/10.3390/polym11010107.
[27] T. Ramanathan, A.A. Abdala, S. Stankovich, D.A. Dikin, M. Herrera-Alonso, R. D. Piner, D.H. Adamson, H.C. Schniepp, X. Chen, R.S. Ruoff, S.T. Nguyen, I. A. Aksay, R.K. Prud'Homme, L.C. Brinson, Functionalized graphene sheets for polymer nanocomposites, Nat. Nanotechnol. 3 (6) (2008) 327–331, https://doi.org/10.1038/nnano.2008.96.
[28] D. Kim, Y. Kim, K. Choi, J.C. Grunlan, C. Yu, Improved thermoelectric behavior of nanotube-filled polymer composites with Poly(3,4-ethylenedioxythiophene) Poly (styrenesulfonate), ACS Nano. 4 (1) (2010) 513–523, https://doi.org/10.1021/nn9013577.
[29] G.P. Moriarty, S. De, P.J. King, U. Khan, M. Via, J.A. King, J.N. Coleman, J. C. Grunlan, Thermoelectric behavior of organic thin film nanocomposites, J. Polym. Sci. Part B Polym. Phys. 51 (2) (2013) 119–123, https://doi.org/10.1002/polb.23186.
[30] G.J. Snyder, E.S. Toberer, Complex thermoelectric materials, Nat. Mater. 7 (2) (2008) 105–114, https://doi.org/10.1038/nmat2090.
[31] J. Cameron, P.J. Skabara, The damaging effects of the acidity in PEDOT:PSS on semiconductor device performance and solutions based on non-acidic alternatives, Mater. Horizons. 7 (7) (2020) 1759–1772, https://doi.org/10.1039/C9MH01978B.
[32] B. Sarkar, M. Jaiswal, D.K. Satapathy, Swelling kinetics and electrical charge transport in PEDOT:PSS thin films exposed to water vapor, J. Phys. Condens. Matter. 30 (22) (2018) 225101, https://doi.org/10.1088/1361-648X/aabe51.
[33] B. Xu, S.-A. Gopalan, A.-I. Gopalan, N. Muthuchamy, K.-P. Lee, J.-S. Lee, Y. Jiang, S.-W. Lee, S.-W. Kim, J.-S. Kim, H.-M. Jeong, J.-B. Kwon, J.-H. Bae, S.-W. Kang, Functional solid additive modified PEDOT:PSS as an anode buffer layer for enhanced photovoltaic performance and stability in polymer solar cells, Sci. Rep. 7 (2017) 45079, https://doi.org/10.1038/srep45079.
[34] K. Norrman, M.V. Madsen, S.A. Gevorgyan, F.C. Krebs, Degradation patterns in water and oxygen of an inverted polymer solar cell, J. Am. Chem. Soc. 132 (47) (2010) 16883–16892, https://doi.org/10.1021/ja106299g.
[35] S. Shao, J. Liu, J. Bergqvist, S. Shi, C. Veit, U. Würfel, Z. Xie, F. Zhang, In situ formation of MoO 3 in PEDOT:PSS Matrix: A facile way to produce a smooth and less hygroscopic hole transport layer for highly stable polymer bulk heterojunction solar cells, Adv. Energy Mater. 3 (3) (2013) 349–355, https://doi.org/10.1002/aenm.v3.310.1002/aenm.201200609.
[36] Q. Peng, X. Liu, D. Su, G. Fu, J. Xu, L. Dai, Novel Benzo[1,2- b :4,5- b ′]dithiophene-benzothiadiazole derivatives with variable side chains for high-performance solar cells, Adv. Mater. 23 (2011) 4554–4558, https://doi.org/10.1002/adma.201101933.

[37] C. Wang, H. Dong, W. Hu, Y. Liu, D. Zhu, Semiconducting π-conjugated systems in field-effect transistors: A material odyssey of organic electronics, Chem. Rev. 112 (4) (2012) 2208–2267, https://doi.org/10.1021/cr100380z.

[38] J.-Y. Kim, S. Park, S. Lee, H. Ahn, S.-Y. Joe, B.J. Kim, H.J. Son, Low-temperature processable high-performance D-A-type random copolymers for nonfullerene polymer solar cells and application to flexible devices, Adv. Energy Mater. 8 (30) (2018) 1801601, https://doi.org/10.1002/aenm.v8.3010.1002/aenm.201801601.

[39] X. Guo, H.N. Tsao, P. Gao, D. Xia, C. An, M.K. Nazeeruddin, M. Baumgarten, M. Grätzel, K. Müllen, Dithieno[2,3-d;2′,3′-d′]benzo[1,2-b;4,5-b′]dithiophene based organic sensitizers for dye-sensitized solar cells, RSC Adv. 4 (96) (2014) 54130–54133, https://doi.org/10.1039/C4RA11873A.

[40] H. Pan, Y. Li, Y. Wu, P. Liu, B.S. Ong, S. Zhu, G.u. Xu, Low-temperature, solution-processed, high-mobility polymer semiconductors for thin-film transistors, J. Am. Chem. Soc. 129 (14) (2007) 4112–4113, https://doi.org/10.1021/ja067879o.

[41] L. Meng, Y. Zhang, X. Wan, C. Li, X. Zhang, Y. Wang, X. Ke, Z. Xiao, L. Ding, R. Xia, H.-L. Yip, Y. Cao, Y. Chen, Organic and solution-processed tandem solar cells with 17.3% efficiency, Science (80-.). 361 (2018) 1094–1098. https://doi.org/10.1126/science.aat2612.

[42] H. Luo, C. Yu, Z. Liu, G. Zhang, H. Geng, Y. Yi, K. Broch, Y. Hu, A. Sadhanala, L. Jiang, P. Qi, Z. Cai, H. Sirringhaus, D. Zhang, Remarkable enhancement of charge carrier mobility of conjugated polymer field-effect transistors upon incorporating an ionic additive, Sci. Adv. 2 (5) (2016) e1600076, https://doi.org/10.1126/sciadv.1600076.

[43] W. Feng, A. Fujii, M. Ozaki, K. Yoshino, Perylene derivative sensitized multi-walled carbon nanotube thin film, Carbon N. Y. 43 (12) (2005) 2501–2507, https://doi.org/10.1016/j.carbon.2005.05.014.

[44] E. Cohen, H. Dodiuk, A. Ophir, S. Kenig, C. Barry, J. Mead, Evidences for π-interactions between pyridine modified copolymer and carbon nanotubes and its role as a compatibilizer in poly(methyl methacrylate) composites, Compos. Sci. Technol. 79 (2013) 133–139, https://doi.org/10.1016/j.compscitech.2013.02.012.

[45] B.K. Kuila, S. Malik, S.K. Batabyal, A.K. Nandi, In-situ synthesis of soluble poly(3-hexylthiophene)/multiwalled carbon nanotube composite: morphology, structure, and conductivity, Macromolecules 40 (2007) 278–287, https://doi.org/10.1021/ma061548e.

[46] P. Imin, F. Cheng, A. Adronov, Supramolecular complexes of single walled carbon nanotubes with conjugated polymers, Polym. Chem. 2 (2) (2011) 411–416, https://doi.org/10.1039/C0PY00286K.

[47] A.W. Musumeci, G.G. Silva, J.-W. Liu, W.N. Martens, E.R. Waclawik, Structure and conductivity of multi-walled carbon nanotube/poly(3-hexylthiophene) composite films, Polymer (Guildf) 48 (6) (2007) 1667–1678, https://doi.org/10.1016/j.polymer.2007.01.027.

[48] R. Das, S. Hamid, M. Ali, S. Ramakrishna, W. Yongzhi, Carbon nanotubes characterization by X-ray powder diffraction – A review, Curr. Nanosci. 11 (2014) 23–35, https://doi.org/10.2174/15734137106661408182100 43.

[49] W. Li, B. Guo, C. Chang, X. Guo, M. Zhang, Y. Li, Efficient polymer solar cells based on a copolymer of meta-alkoxy-phenyl-substituted benzodithiophene and thieno[3,4-b]thiophene, J. Mater. Chem. A. 4 (26) (2016) 10135–10141, https://doi.org/10.1039/C6TA04030F.

[50] C. Vijayakumar, B. Balan, M.-J. Kim, M. Takeuchi, Noncovalent functionalization of SWNTs with azobenzene-containing polymers: Solubility, stability, and enhancement of photoresponsive properties, J. Phys. Chem. C. 115 (11) (2011) 4533–4539, https://doi.org/10.1021/jp111248r.

[51] K. Matsuda, W. Norimatsu, J. Bao, H. Kawarada, M. Kusunoki, In-plane electrical conduction mechanisms of highly dense carbon nanotube forests on silicon carbide, J. Appl. Phys. 123 (4) (2018) 045104, https://doi.org/10.1063/1.5004507.

[52] H. Peng, Aligned carbon nanotube/polymer composite films with robust flexibility, high transparency, and excellent conductivity, J. Am. Chem. Soc. 130 (1) (2008) 42–43, https://doi.org/10.1021/ja078267m10.1021/ja078267m.s002.

[53] M. Goswami, A. Mukherjee, A.K. Das, R. Ghosh, A.K. Meikap, Synthesis, characterization and electrical property of MWCNT-ZnS nanocomposite embedded in polyaniline, Adv. Nat. Sci. Nanosci. Nanotechnol. 8 (2017) 025018. https://doi.org/10.1088/2043-6254/aa71ec.

[54] C. Meng, C. Liu, S. Fan, A promising approach to enhanced thermoelectric properties using carbon nanotube networks, Adv. Mater. 22 (4) (2010) 535–539, https://doi.org/10.1002/adma.v22:410.1002/adma.200902221.

[55] D. Kelkar, A. Chourasia, Structural, thermal and electrical properties of doped Poly (3,4 ethylenedioxythiophene), Chem. Chem. Technol. 10 (4) (2016) 395–400.

[56] S. He, M. Mukaida, K. Kirihara, L. Lyu, Q. Wei, Reversible protonic doping in Poly (3,4-Ethylenedioxythiophene), Polymers (Basel) 10 (2018) 1065, https://doi.org/10.3390/polym10101065.

[57] A.G. MacDiarmid, R.J. Mammone, R.B. Kaner, S.J. Porter, R. Pethig, A.J. Heeger, D.R. Rosseinsky, The concept of 'doping' of conducting polymers: the role of reduction potentials [and Discussion], Philos. Trans. R. Soc. A Math. Phys. Eng. Sci. 314 (1985) 3–15, https://doi.org/10.1098/rsta.1985.0004.

[58] P. Mangelis, P. Vaqueiro, J.-C. Jumas, I. da Silva, R.I. Smith, A.V. Powell, The effect of electron and hole doping on the thermoelectric properties of shandite-type Co 3 Sn 2 S 2, J. Solid State Chem. 251 (2017) 204–210, https://doi.org/10.1016/j.jssc.2017.04.028.

[59] J. Beuvelot, C. Bergeret, R. Mallet, V. Fernandez, J. Cousseau, M.F. Baslé, D. Chappard, In vitro calcification of chemically functionalized carbon nanotubes, Acta Biomater. 6 (10) (2010) 4110–4117, https://doi.org/10.1016/j.actbio.2010.05.011.

[60] B. Singh, L. Murad, F. Laffir, C. Dickinson, E. Dempsey, Pt based nanocomposites (mono/bi/tri-metallic) decorated using different carbon supports for methanol electro-oxidation in acidic and basic media, Nanoscale 3 (8) (2011) 3334, https://doi.org/10.1039/c1nr10273g.

[61] T. Du, A.S. Adeleye, T. Zhang, N. Yang, R. Hao, Y. Li, W. Song, W. Chen, Effects of ozone and produced hydroxyl radicals on the transformation of graphene oxide in aqueous media, Environ. Sci. Nano. 6 (8) (2019) 2484–2494, https://doi.org/10.1039/C9EN00361D.

[62] A. Furlani, M.V. Russo, G. Polzonetti, K. Martin, H.H. Wang, J.R. Ferraro, Spectroscopic studies of FeCl 3 -doped polymers of polyphenylacetylene, Appl. Spectrosc. 44 (2) (1990) 331–334, https://doi.org/10.1366/0003702904085688.

[63] T. Yamashita, P. Hayes, Analysis of XPS spectra of Fe2+ and Fe3+ ions in oxide materials, Appl. Surf. Sci. 254 (8) (2008) 2441–2449, https://doi.org/10.1016/j.apsusc.2007.09.063.

[64] M.V. Russo, G. Polzonetti, A. Furlani, A. Bearzotti, I. Fratoddi, P. Altamura, X-ray photoelectron spectroscopy and scanning electron microscopy characterization of novel poly(monosubstituted) acetylenes containing doping species, J. Vac. Sci. Technol. A Vacuum, Surfaces, Film. 16 (1) (1998) 35–44, https://doi.org/10.1116/1.581006.

[65] A. Abidov, B. Allabergenov, J. Lee, H.-W. Jeon, S.-W. Jeong, S. Kim, X-ray photoelectron spectroscopy characterization of Fe doped TiO2 photocatalyst, Int. J. Mater. Mech. Manuf. 1 (2013) 294–296, https://doi.org/10.7763/IJMMM.2013.V1.63.

[66] B.W. Veal, A.P. Paulikas, Final-state screening and chemical shifts in photoelectron spectroscopy, Phys. Rev. B. 31 (8) (1985) 5399–5416, https://doi.org/10.1103/PhysRevB.31.5399.

[67] M.V. Russo, G. Polzonetti, A. Furlani, XPS and IR investigations of FeCl3-doped polyphenylacetylene: the solvent effect, Synth. Met. 39 (3) (1991) 291–301, https://doi.org/10.1016/0379-6779(91)91755-Y.

[68] Y.H. Kang, U.-H. Lee, I.H. Jung, S.C. Yoon, S.Y. Cho, Enhanced thermoelectric performance of conjugated polymer/CNT nanocomposites by modulating the potential barrier difference between conjugated polymer and CNT, ACS Appl. Electron. Mater. 1 (7) (2019) 1282–1289, https://doi.org/10.1021/acsaelm.9b00224.

[69] A.M. Almasri, Predicting the thermal conductivity of polypropylene-multiwall carbon nanotubes using the Krenchel model, Sci. Eng. Compos. Mater. 25 (2018) 383–388, https://doi.org/10.1515/secm-2016-0032.

[70] C.-W. Nan, Z. Shi, Y. Lin, A simple model for thermal conductivity of carbon nanotube-based composites, Chem. Phys. Lett. 375 (5-6) (2003) 666–669, https://doi.org/10.1016/S0009-2614(03)00956-4.

[71] C.-W. Nan, R. Birringer, D.R. Clarke, H. Gleiter, Effective thermal conductivity of particulate composites with interfacial thermal resistance, J. Appl. Phys. 81 (10) (1997) 6692–6699, https://doi.org/10.1063/1.365209.

[72] D. Yoo, J. Kim, J.H. Kim, Direct synthesis of highly conductive poly(3,4-ethylenedioxythiophene):poly(4-styrenesulfonate) (PEDOT:PSS)/graphene composites and their applications in energy harvesting systems, Nano Res. 7 (5) (2014) 717–730, https://doi.org/10.1007/s12274-014-0433-z.

[73] E. Jin Bae, Y. Hun Kang, K.-S. Jang, S. Yun Cho, Enhancement of thermoelectric properties of PEDOT:PSS and tellurium-PEDOT:PSS hybrid composites by simple chemical treatment, Sci. Rep. 6 (2016) 18805, https://doi.org/10.1038/srep18805.

[74] F. Jiao, C.-a. Di, Y. Sun, P. Sheng, W. Xu, D. Zhu, Inkjet-printed flexible organic thin-film thermoelectric devices based on p- and n-type poly(metal 1,1,2,2-ethenetetrathiolate)s/polymer composites through ball-milling, Philos. Trans. R. Soc. A Math. Phys. Eng. Sci. 372 (2013) (2014) 20130008, https://doi.org/10.1098/rsta.2013.0008.

MWCNT/Thienothiophene based All-Organic Thermoelectric Composites: Enhanced Performance by Realigning of the Fermi Level through Doping

Vijitha Ignatious[a,b], Neethi Raveendran[a,b], P. Arjun[a], T. P. Yuvaraj[c], C. Vijayakumar*[a,b] and Biswapriya Deb*[a,b]

[a] Photosciences and Photonics, Chemical Science and Technology Division, CSIR-National Institute for Interdisciplinary Science and Technology (CSIR-NIIST), Thiruvananthapuram-695019, India

[b] Academy of Scientific and Innovative Research (AcSIR), Ghaziabad-201002, India

[c] GAIL India Limited, R&D Department, GAIL Training Institute, Plot No. 24, Sector 16A, Noida-201301, India

Tel: +91-471-2515-478; E-mail: cvijayakumar@niist.res.in; biswapriya.deb@niist.res.in

---

Homogeneity of the MWCNT dispersion:-

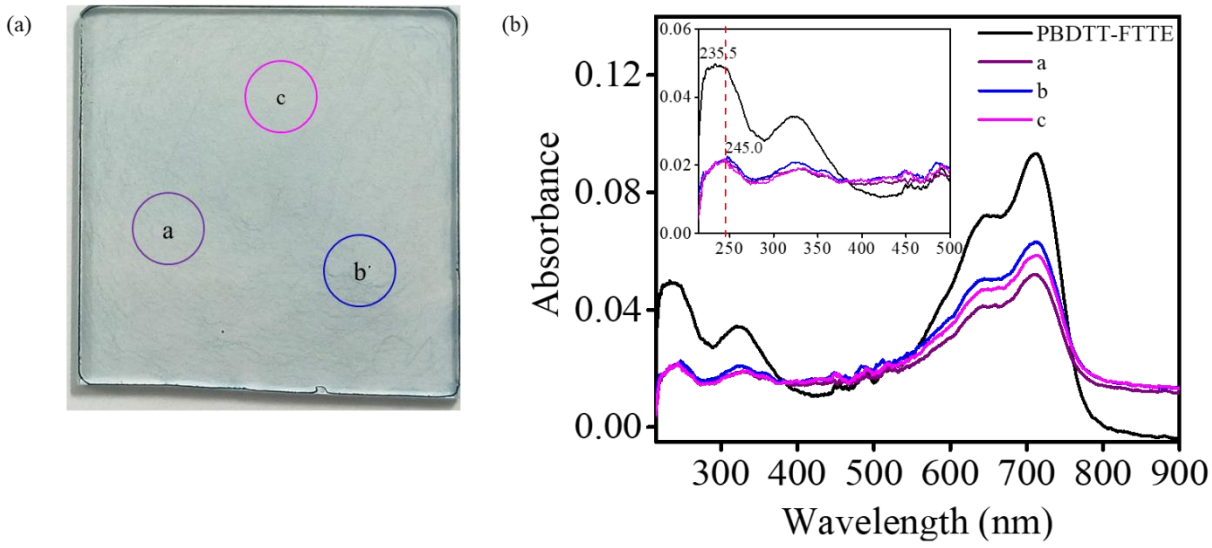

Fig. S1. (a) Image of PBDTT-FTTE/45 wt% MWCNT nanocomposite thin film (b) UV-Vis absorption spectra.

Thickness of the film sample before doping:-

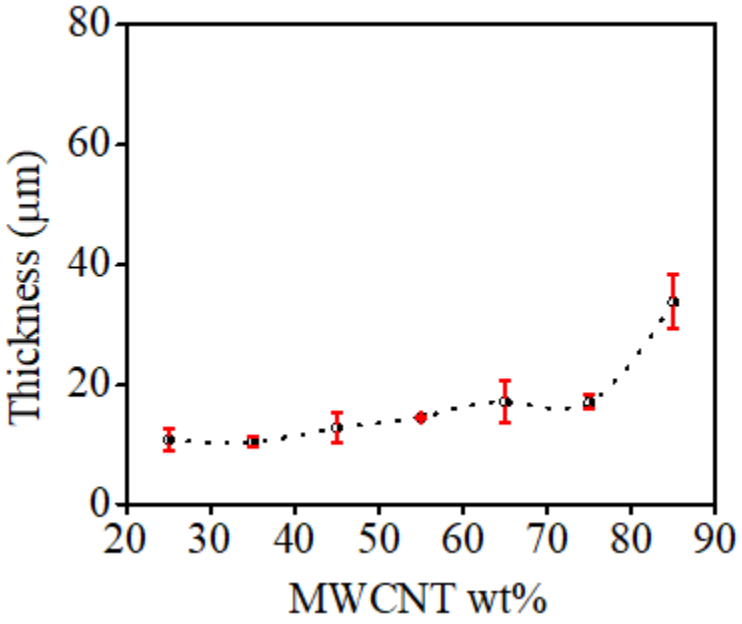

Fig. S2. Thickness variation of nanocomposite film with MWCNT wt%.

Test accuracy of LSR instrument:-

The TE performance of constantan is measured in a temperature range of 50 – 450 °C using LSR. The measured value and the reference datasheet of constantan are plotted in Fig. S3. An error range of $0.025 \leq \rho \geq 0.038$ μΩm and $0.5 \leq \alpha \geq 2$ μV/K is observed for resistivity and Seebeck coefficient respectively. A similar error range will be reflected in all the collected data in this instrument.

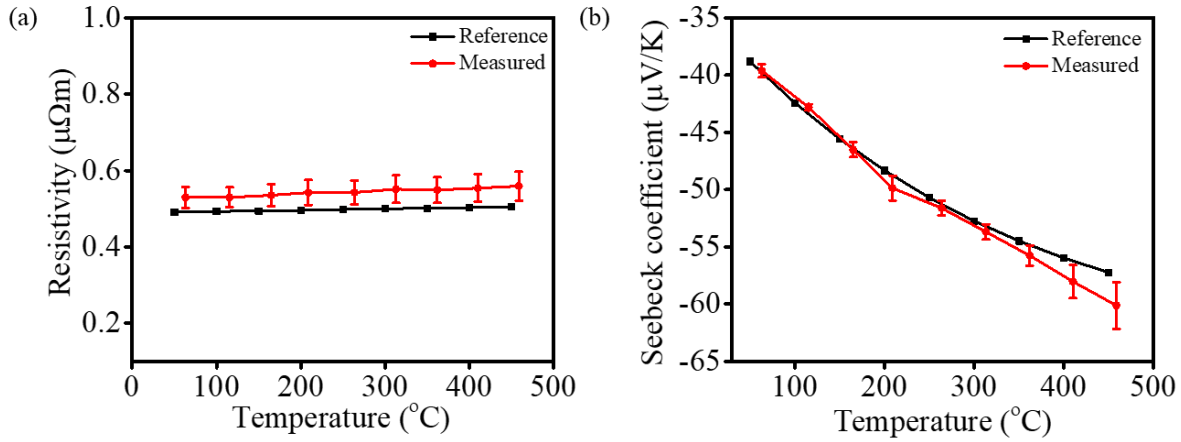

Fig. S2. (a) Resistivity and (b) Seebeck coefficient plot of constantan in the temperature range of 50-450 °C.

Mott's VRH model:-

The temperature-dependent electrical conductivity described by the Mott's VRH mechanism is,

$$\sigma = \sigma_0 \exp\left[-\left(\frac{T}{T_0}\right)^{\frac{1}{d+1}}\right]$$

where σ_0 is a constant; T_0 is the Mott's characteristic temperature which depends on the carrier hopping barriers; T is the measured temperature and d is the dimensionality. In the above equation, m = 1/(d+1), m is 1/2 for one-dimensional transport and 1/4 for three-dimensional transport.

The electrical conductivity data for PBDTT-FTTE/MWCNT at different weight percentage are plotted as functions of $T^{-1/2}$ and $T^{-1/4}$ in the temperature range 303-533 K in Fig. S3 and the linearity factor of $T^{-1/2}$ and $T^{-1/4}$ plots are given in Table S1. The linearity factor for $T^{-1/4}$ gives a

better fit for all the three samples than $T^{-1/2}$, which indicates that the charge transport in the films follows a three-dimensional VRH model, where $d = 3$.

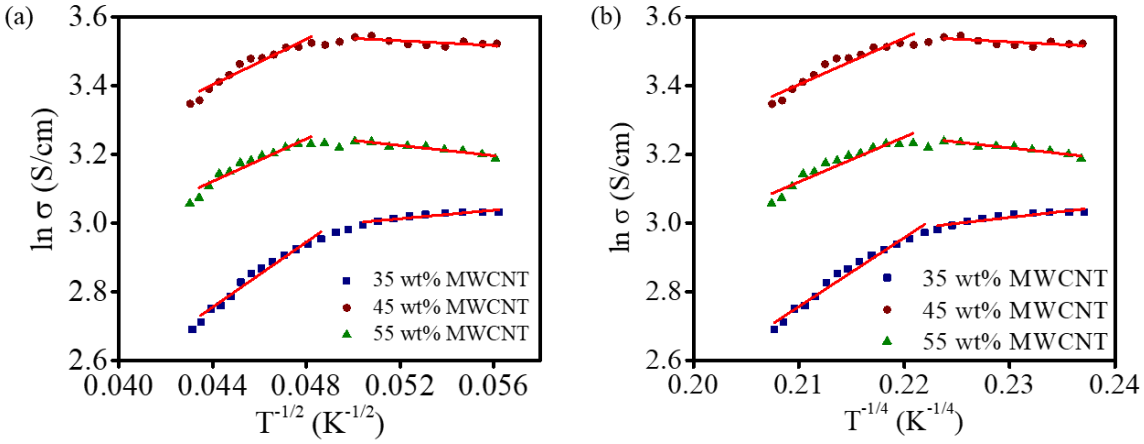

Fig. S4. The electrical conductivity of PBDTT-FTTE/MWCNT at different weight percentage plotted as functions of (a) $T^{-1/2}$ and (b) $T^{-1/4}$.

Table S1.

Linearity factor of $T^{-1/2}$ and $T^{-1/4}$ plots.

Sample	**Linearity factor**			
	$T^{-1/2}$		$T^{-1/4}$	
35 wt% MWCNT	0.81131	0.86812	0.90269	0.98012
45 wt% MWCNT	0.87353	0.91308	0.97021	0.92598
55 wt% MWCNT	0.89817	0.89955	0.90235	0.90931

SEM image of PBDTT-FTTE/75 wt% MWCNT:-

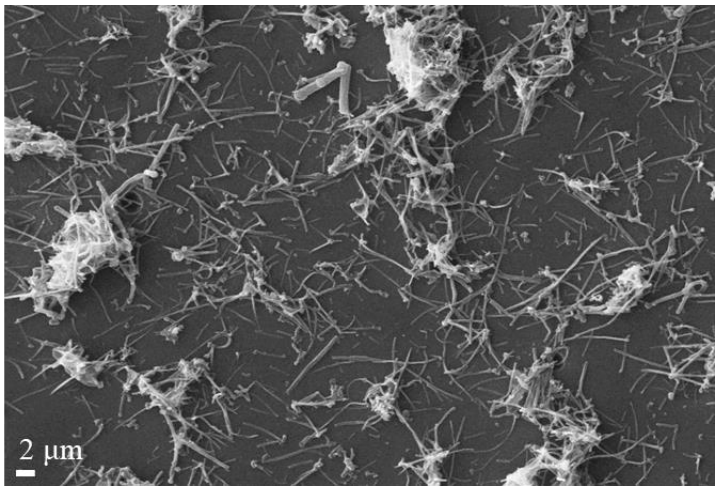

Fig. S5. SEM image of nanocomposite at 75 wt % of MWCNT.

TE performance of PBDTT-FTTE and MWCNT:-

The Seebeck coefficient was measured using a home-built setup. The setup consisted of a silicon rubber heater (TEMPSENS Instruments Pvt. Ltd.) and a Peltier device (Laird Thermal Systems, Inc.) to maintain controlled stages that could independently function as the hot part and cold part, respectively. The exact temperature of each surface was measured using a K-type thermocouple. The temperature gradient between the two electrodes was maintained at 50 K. The output voltage was measured using a Keithley DAQ6510. The electrical resistance was measured using a two-probe technique with Keithley 2450 source meter and the thickness of the film was measured using Dektak 6M stylus profilometer.

Table S2.

The TE performance of PBDTT-FTTE and MWCNT at room temperature.

Sample	Thickness (µm)	σ (S/cm)	α (µV/K)	PF (µW/m.K^2)
PBDTT-FTTE	12.5	2.3 x 10^{-6}	200	9.2 x 10^{-6}
MWCNT	12.9	2.6	25	0.16

TE properties by varying doping parameters:-

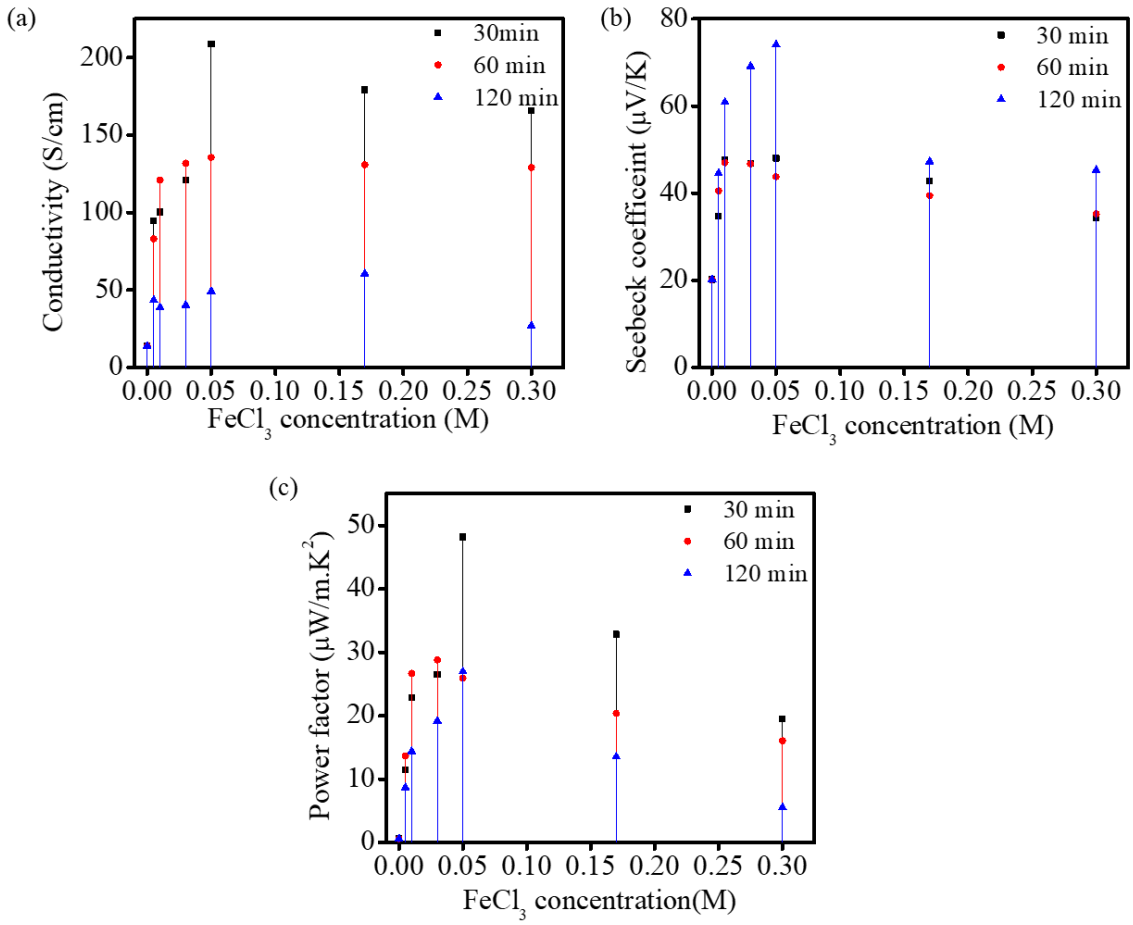

Fig. S6. TE properties by varying doping parameters.

Thickness of the film sample after doping:-

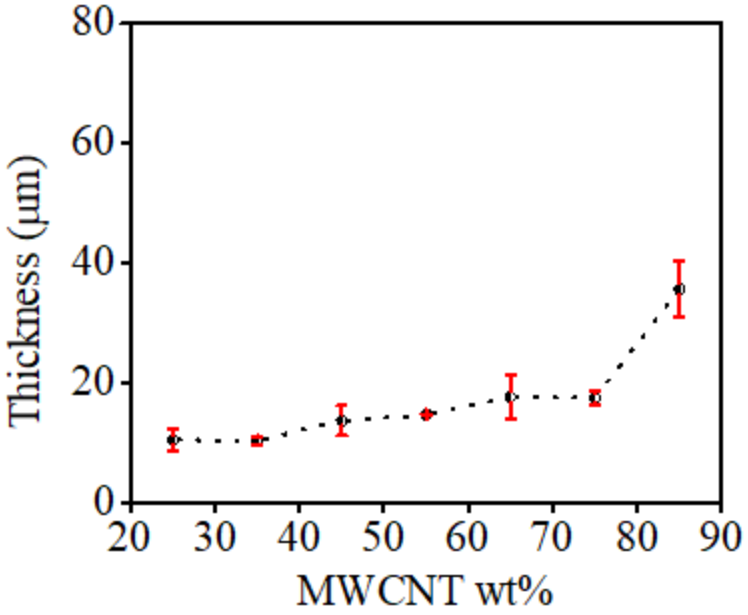

Fig. S7. Thickness variation of nanocomposite film with MWCNT wt%.

Temperature tolerance of nanocomposite before and after doping:-

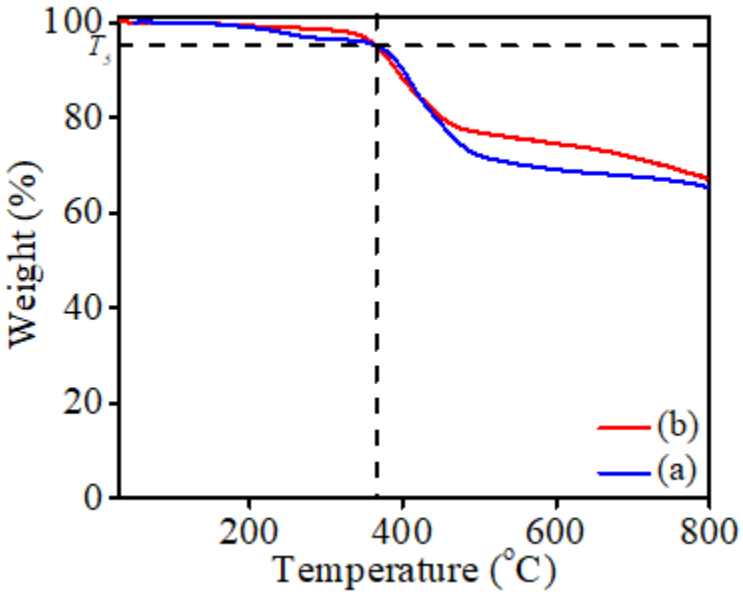

Fig. S8. TGA plot (a) before and (b) after doping.

Literature review:-

Table S3.

The TE performance for some conjugated polymer/MWCNT composites at room temperature.

Polymer	**Inorganic/ Dopant**	**Loading (wt %)**	**σ (S/cm)**	**α (μV/K)**	**PF (μW/m.K^2)**	**Ref.**
PANI/ HCl	MWCNT	1	14.1	79.8	8.98	[1]
PANI	MWCNT	84.2	50	28	5	[2]
PANI	MWCNT	40	17.1	10	0.17	[3]
PANI	MWCNT	30	159	25	0.1	[4]
PEDOT:PSS/Graphene	MWCNT	5	689	23.2	37.08	[5]
PPy	MWCNT	20	32	25	2.1	[6]
P3HT/ $FeCl_3$	MWCNT	10	71.3	29	6	[7]
PBDTTT-TEO	DDQ	25 mol%	2.84×10^{-3}	418	0.049	[8]
PBDTTT-TEO	F4TCNQ	25 mol%	2.13×10^{-3}	376	0.028	[8]
PBDT-EDOT	$FeCl_3$		0.81	67.60	0.37	[9]

PBDTTT-EDOT	$FeCl_3$		1.64	115.58	2.19	[9]
PBDTT-FTTE / $FeCl_3$	MWCNT	45	208.9	48.03	48.21	This work

High-resolution XPS spectra of S2p and F1s:-

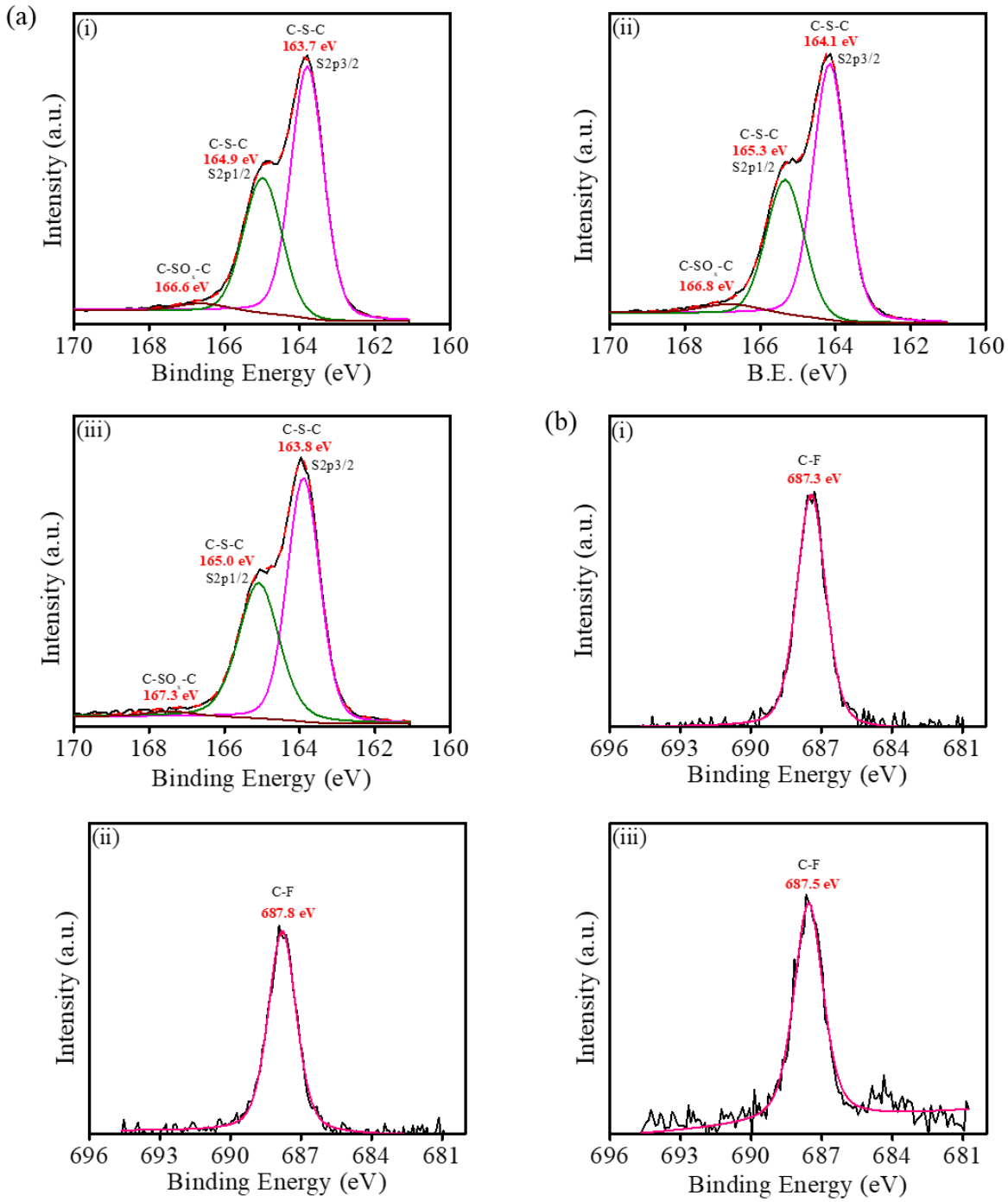

Fig. S9. (a) S2p XPS spectra and (b) F1s XPS spectra of (i) polymer PBDTT-FTTE (ii) nanocomposite with MWCNT~ 45 wt% before doping and (iii) after doping.

Estimation of work function using Kelvin-probe method:-

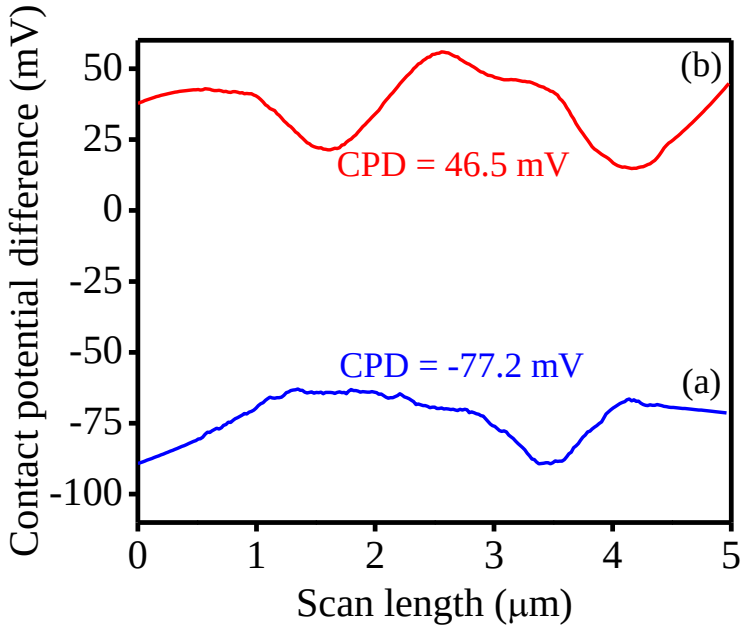

Fig. S10. Contact potential difference of nanocomposite with MWCNT~ 45 wt% (a) before doping and (b) after doping.

The work function of a sample is calculated using the equation,

$$\Phi_{sample} - \Phi_{tip} = V_{CPD} .e$$

$\Phi_{tip} = \Phi_{HOPG} - V_{CPD} .e =$ 4.6 eV – (-0.323 eV) = 4.923 eV

$\Phi_{before} = \Phi_{tip} + V_{CPD} .e =$ 4.923 eV + (-0.0772 eV) = 4.844 eV

$\Phi_{after} = \Phi_{tip} + V_{CPD} .e =$ 4.923 eV + 0.0465 eV = 4.969 eV

Steps involved in the fabrication of planar TEG:-

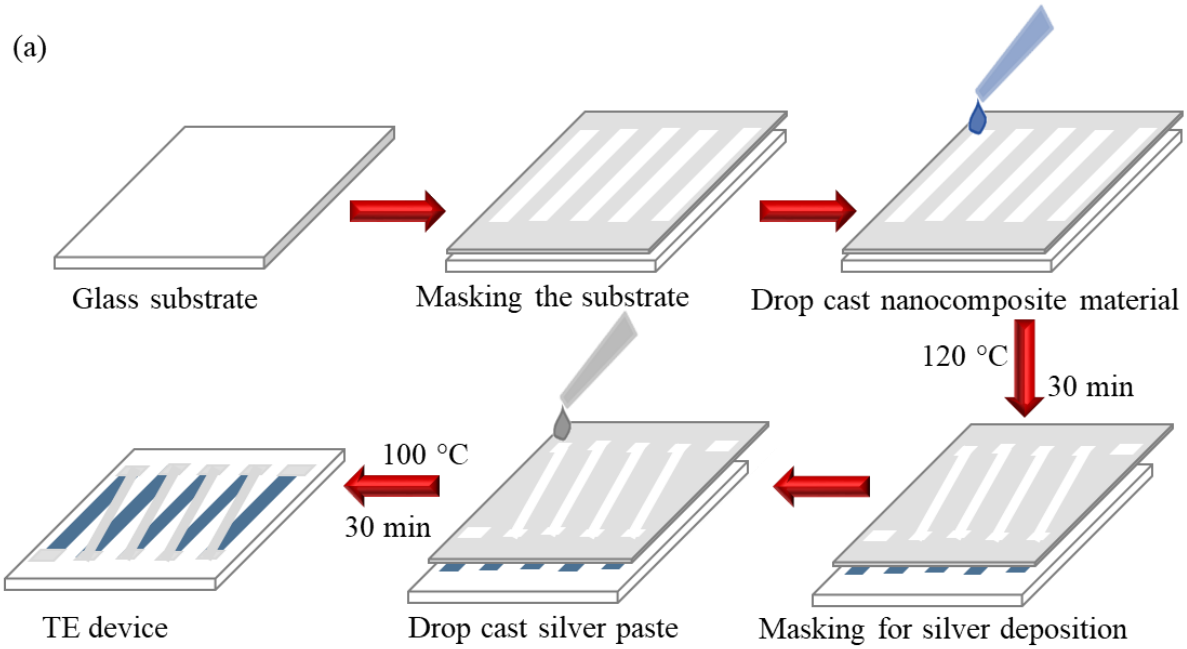

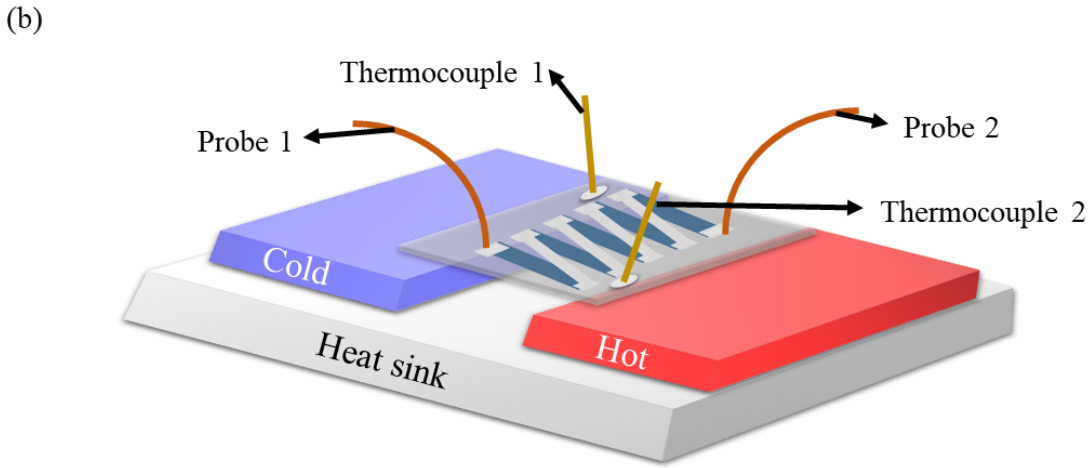

Fig. S11. (a) Fabrication of planar TEG consisting of 7 legs (b) Schematic diagram of geometry of TEG measurement.

References

[1] K. Zhang, M. Davis, J. Qiu, L. Hope-Weeks, S. Wang, Thermoelectric properties of porous multi-walled carbon nanotube/polyaniline core/shell nanocomposites, Nanotechnology. 23 (2012) 385701. https://doi.org/10.1088/0957-4484/23/38/385701.

[2] C. Meng, C. Liu, S. Fan, A Promising Approach to Enhanced Thermoelectric Properties Using Carbon Nanotube Networks, Adv. Mater. 22 (2010) 535–539. https://doi.org/10.1002/adma.200902221.

[3] Q. Wang, Q. Yao, J. Chang, L. Chen, Enhanced thermoelectric properties of CNT/PANI composite nanofibers by highly orienting the arrangement of polymer chains, J. Mater. Chem. 22 (2012) 17612. https://doi.org/10.1039/c2jm32750c.

[4] F. Paquin, J. Rivnay, A. Salleo, N. Stingelin, C. Silva-Acuña, Multi-phase microstructures drive exciton dissociation in neat semicrystalline polymeric semiconductors, J. Mater. Chem. C. 3 (2015) 10715–10722. https://doi.org/10.1039/C5TC02043C.

[5] D. Yoo, J. Kim, S.H. Lee, W. Cho, H.H. Choi, F.S. Kim, J.H. Kim, Effects of one- and two-dimensional carbon hybridization of PEDOT:PSS on the power factor of polymer thermoelectric energy conversion devices, J. Mater. Chem. A. 3 (2015) 6526–6533. https://doi.org/10.1039/C4TA06710J.

[6] J. Wang, K. Cai, S. Shen, J. Yin, Preparation and thermoelectric properties of multi-walled carbon nanotubes/polypyrrole composites, Synth. Met. 195 (2014) 132–136. https://doi.org/10.1016/j.synthmet.2014.06.003.

[7] C. Bounioux, P. Díaz-Chao, M. Campoy-Quiles, M.S. Martín-González, A.R. Goñi, R. Yerushalmi-Rozen, C. Müller, Thermoelectric composites of poly(3-hexylthiophene) and carbon nanotubes with a large power factor, Energy Environ. Sci. 6 (2013) 918. https://doi.org/10.1039/c2ee23406h.

[8] C. Pan, L. Wang, T. Liu, X. Zhou, T. Wan, S. Wang, Z. Chen, C. Gao, L. Wang, Polar Side Chain Effects on the Thermoelectric Properties of Benzo[1,2-b:4,5-b′]Dithiophene-Based Conjugated Polymers, Macromol. Rapid Commun. 40 (2019) 1900082. https://doi.org/10.1002/marc.201900082.

[9] X. Zhou, C. Pan, C. Gao, A. Shinohara, X. Yin, L. Wang, Y. Li, Q. Jiang, C. Yang, L. Wang, Thermoelectrics of two-dimensional conjugated benzodithiophene-based polymers: density-of-states enhancement and semi-metallic behavior, J. Mater. Chem. A. 7 (2019) 10422–10430. https://doi.org/10.1039/C9TA01437C.

RESEARCH ARTICLE

Macromolecular Materials and Engineering
www.mame-journal.de

Studies on the Doping Mechanism of Conjugated Thienothiophene Polymer/MWCNT Hybrids for Thermoelectric Application

Vijitha Ignatious, Neethi Raveendran, Sruthy Poovattil, Navin Jacob, Vijayakumar Chakkooth, and Biswapriya Deb**

Conducting polymer-based thermoelectric (TE) materials have great promise for fabricating lightweight modules that can directly convert waste heat into electricity. Doping is essential for these materials to tune the electrical conductivity and Seebeck coefficient, enhancing their overall TE response. However, the doping mechanism on polymer-based hybrid systems needs further clarification for materials design and selection. Herein, two different TE hybrids are fabricated using different side-chain groups containing benzodithiophene-thienothiophene (BDT-TTE) based conjugated polymers and multi-walled carbon nanotubes (MWCNT). The TE properties of the hybrids before and after p-doping are presented. Post-doping, a simultaneous increase in electrical conductivity and Seebeck coefficient is observed for the composites of alkylthiophene side-chain containing polymer, leading to ≈24× enhancements in the power factor (PF). The composite with alkoxy side-chain polymer showed a nominal increase in electrical conductivity after doping, and the Seebeck coefficient remained unaffected. Tracking of electronic structure and density of valence state (DOVS) revealed the presence of charge-transfer-complexes (CTC) with different coordination sites, along with repositioned Fermi level and valance band maximum (VBM) that contribute to the observed differences in the TE response. This work presents a general understanding of the doping mechanism and the underlying physics to design high-performance organic-based TE composites.

1. Introduction

The growing energy usage in the present world demands improving the efficiency of energy conversion and saving technologies. In recent years, thermoelectric (TE) devices have proved to be a promising sustainable energy source that directly converts waste heat into electricity. TE devices are robust, silent, and solid-state energy conversion systems that convert thermal energy to electrical energy and vice versa. They are widely used in many fields such as in aerospace,[1,2] automobile industry,[3,4] consumer electronic devices,[5,6] point-care devices,[7–9] micro-self powered wireless platforms,[10,11] and air conditioning appliances for particular targets.[12,13] Body heat can act as sustainable energy and can be exploited to power up emerging wearable medical devices allowing applications ranging from health monitoring and tracking systems to sports and fitness wearable devices.[7,8,14,15] TE devices have become an area of interest in energy harvesting for large and even small types of applications throughout the last years due to their attractive features, such as long life, easy maintenance, and energy efficiency. The energy conversion efficiency of a TE material is linked to its dimensionless figure of merit,

$$ZT = \frac{\alpha^2 \sigma}{\kappa} T \tag{1}$$

where σ, α, T, and κ are the electrical conductivity, Seebeck coefficient, absolute temperature, and thermal conductivity.[16] The term $\alpha^2\sigma$ in Equation (1) is called the power factor (PF). Conventionally, some low-bandgap/degenerate inorganic semiconductors or semimetals were used as TE materials. Well-known examples include bismuth chalcogenides for low to mid-temperature ranges and silicon for high-temperature applications. Lately, organic-based materials/composites/hybrids are being pursued because of their intrinsic advantages over traditional TE materials. Those include easy processing, lower weight, cost-effectiveness, high flexibility, inherently low thermal conductivity, etc.[17,18] These factors are substantial functionality multipliers for TE applications and must be prioritized along with the maximum-ZT hunt.

V. Ignatious, N. Raveendran, S. Poovattil, N. Jacob, V. Chakkooth, B. Deb
Photosciences and Photonics
Chemical Science and Technology Division
CSIR-National Institute for Interdisciplinary Science and Technology (CSIR-NIIST)
Thiruvananthapuram 695019, India
E-mail: cvijayakumar@niist.res.in; biswapriya.deb@niist.res.in
V. Ignatious, N. Raveendran, S. Poovattil, N. Jacob, V. Chakkooth, B. Deb
Academy of Scientific and Innovative Research (AcSIR)
Ghaziabad 201002, India

The ORCID identification number(s) for the author(s) of this article can be found under https://doi.org/10.1002/mame.202100916

DOI: 10.1002/mame.202100916

Prior studies on organic TE materials were primarily focused on conducting polymers such as polythiophene, polyaniline, polyfluorene, polypyrrole, and their derivatives by preparing organic/inorganic hybrids/composites.[19,20] Recently, significant progress has been made in studying the relationship between polymer structure and TE properties.[21,22] Wang et al. designed and synthesized donor-acceptor (D–A) type conjugated polymers and effectively enhanced their TE properties through side-chain engineering.[23] They reported that the polymer backbone structure prominently influences the TE properties, and the inclusion of thiophene and carbazole units can effectively improve the conversion efficiency of the polymers. Zhou et al. tailored the density of states (DOS) of two-dimensional conjugated polymers with different side-chain groups, leading to a dramatic PF improvement.[24] At 350 K, the PF of the doped film with alkylthienothiophene side-chain reached 101.3 $\mu Wm^{-1}K^{-2}$, which is more than two orders higher than that of the undoped film (0.9 $\mu Wm^{-1}K^{-2}$). Carbon nanotube (CNT) based organic TE materials were also of great importance for fabricating stable and lightweight modules.[14,25] However, detailed insight on the role of the doping mechanism of CNT-based hybrids is still lacking.

In recent years, benzo[1,2-b:4,5-b′]dithiophene (BDT) based conjugated polymers were found to be an excellent candidate for optoelectronic devices such as solar cells, field effect transistors (FET), and fluorescence sensors.[26,27] The BDT units are common organic semiconducting units with a planar backbone and high oxidative stability, effectively improving the charge carrier mobility.[28] Furthermore, the central benzene core of BDT can be anchored to different substituents for tuning the energy levels, solubility, absorption spectra, and thermal stability.[29] These polymers are more adaptive to π-structures such as CNTs resulting in hybrid structures with unique properties.[30] Since the BDT-based conjugated polymers have rarely been explored in TE, a detailed study linking their structure with TE performance is essential for improving *ZT*. Furthermore, very few studies have analyzed the effect of doping on the structure–property relation of TE materials

In the present study, we used two conjugated benzodithiophene-thienothiophene (BDT-TTE) polymers, poly[(4,8-bis-(2-ethylhexyloxy)-benzo(1,2-b:4,5-b′)dithiophene)-2,6-diyl-alt-(4-(2-ethylhexanoyl)-thieno[3,4-b]thiophene-)-2-6-diyl)] (PBDTTT-C) and poly[[4,8-bis[5-(2-ethylhexyl)-2-thienyl]benzo[1,2-*b*:4,5-*b*′]dithiophene-2,6-diyl][2-(2-ethyl-1-oxohexyl)thieno[3,4-*b*]thiophenediyl]] (PBDTTT-C-T). These two polymers have identical conjugated backbones but different side-chain; alkoxy and alkylthiophene groups are attached to the BDT units in PBDTTT-C and PBDTTT-C-T, respectively. Several scientific papers documented the excellent ambient stability and charge-transport for organic photovoltaics [31,32], and their structure-property correlation for solar cells.[33] Such properties could be favorable for TE applications with a judicious tuning of σ, α, and κ. Herein, we formed hybrids of these polymers with multi-walled carbon nanotube (MWCNT) and systematically investigated their TE properties and the effect of p-doping (with $FeCl_3$). A concurrent increase of σ and α is achieved for the hybrid consisting of alkylthiophene side-chain polymer after doping, while α remained unchanged for the hybrids fabricated using the polymer with alkoxy side-chain group although it showed a slight increase in σ. This work presents a universal understanding of the doping mechanism and the underlying physics to design high-performance organic-based TE hybrids.

2. Results and Discussion

2.1. Organic Hybrids Characterization and Analysis

The molecular structures of two BDT-based polymers, PBDTTT-C and PBDTTT-C-T, are shown in **Figure 1**a. Both polymers have identical conjugated backbones but different side-chain groups. The alkoxy and alkylthiophene groups are at the 4 and 8 positions of the BDT units in PBDTTT-C and PBDTTT-C-T, respectively. The PBDTTT-C/MWCNT (OH1) and PBDTTT-C-T/MWCNT (OH2) hybrids preparation processes are schematically shown in Figure S1 (Supporting Information). As shown in Figure 1b, both hybrids displayed an embedded network of MWCNT in polymer matrices. Such MWCNT-reinforced networks are expected to establish π-stacking interactions of the electron-rich fused thiophene units while enhancing mechanical strength.[34,35] The topographic morphology of the hybrids was unaffected by doping, and the corresponding scanning electron microscope (SEM) images are given in Figure S2 (Supporting Information). The UV-visible spectra of the pure polymer and their hybrid films are shown in Figure 1c. The intramolecular donor–acceptor copolymers commonly show a relatively strong absorption peak in 550 to 700 nm and a weak absorption peak in the shorter 300 to 500 nm range.[36,37] The long-wavelength absorption peak is due to intramolecular charge transfer between the acceptor and the donor, while the short-wavelength peak originates from the π--π* transition.[38] Here, the short-wavelength absorption peaks of PBDTTT-C and PBDTTT-C-T appeared at 343 and 350 nm and were redshifted to ≈344 nm (OH1) and ≈356 nm (OH2) upon hybrid formation. The shift is due to the elongation of the effective conjugation length upon incorporating CNT, which would enhance intermolecular orbital overlap.[39] The absorption peak maxima of PBDTTT-C and PBDTTT-C-T were observed at 579 and 636 nm, which broadened after the hybrid formation with a small energy blueshift (OH1≈576 and OH2 ≈634 nm). The shift indicates a change in intrachain and interchain hybrid connections due to the interaction between CNT and polymer.[40] Post-doping (Figure 1d), the absorption maxima of OH1 and OH2 films were redshifted to 613 and 643 nm, indicating the enhancement of intermolecular π--π interaction between the CNT and polymer.[24] The doped OH2 films showed a more prominent absorption shoulder toward the longer wavelength due to more robust intermolecular π--π stacking.

The crystal structure analysis exhibited a redshift in lamellar peak (100) of both the polymer after hybrid formation (**Figure 2**a), indicating an excellent local ordering.[41] The wide-angle X-ray scattering (WAXS) spectrum of pristine polymers shows a peak at 22.03° (for PBDTTT-C) and 21.19° (for PBDTTT-C-T), representing d_{010} spacing for the π–π stacking of thiophene rings.[42] Also, MWCNT shows a diffraction peak at 26.3°, corresponding to the characteristic graphitic peak (002) having a d-spacing of 3.4 Å. Upon hybrid formation, the (010) peak of polymer shifted toward a lower 2θ, and (002) peak of MWCNT shifted toward the higher value. A decrease in intensity is noted due to the overlaying of polymer on the surface of MWCNT. This observation confirmed a successful hybrid formation of the components. Post-doping

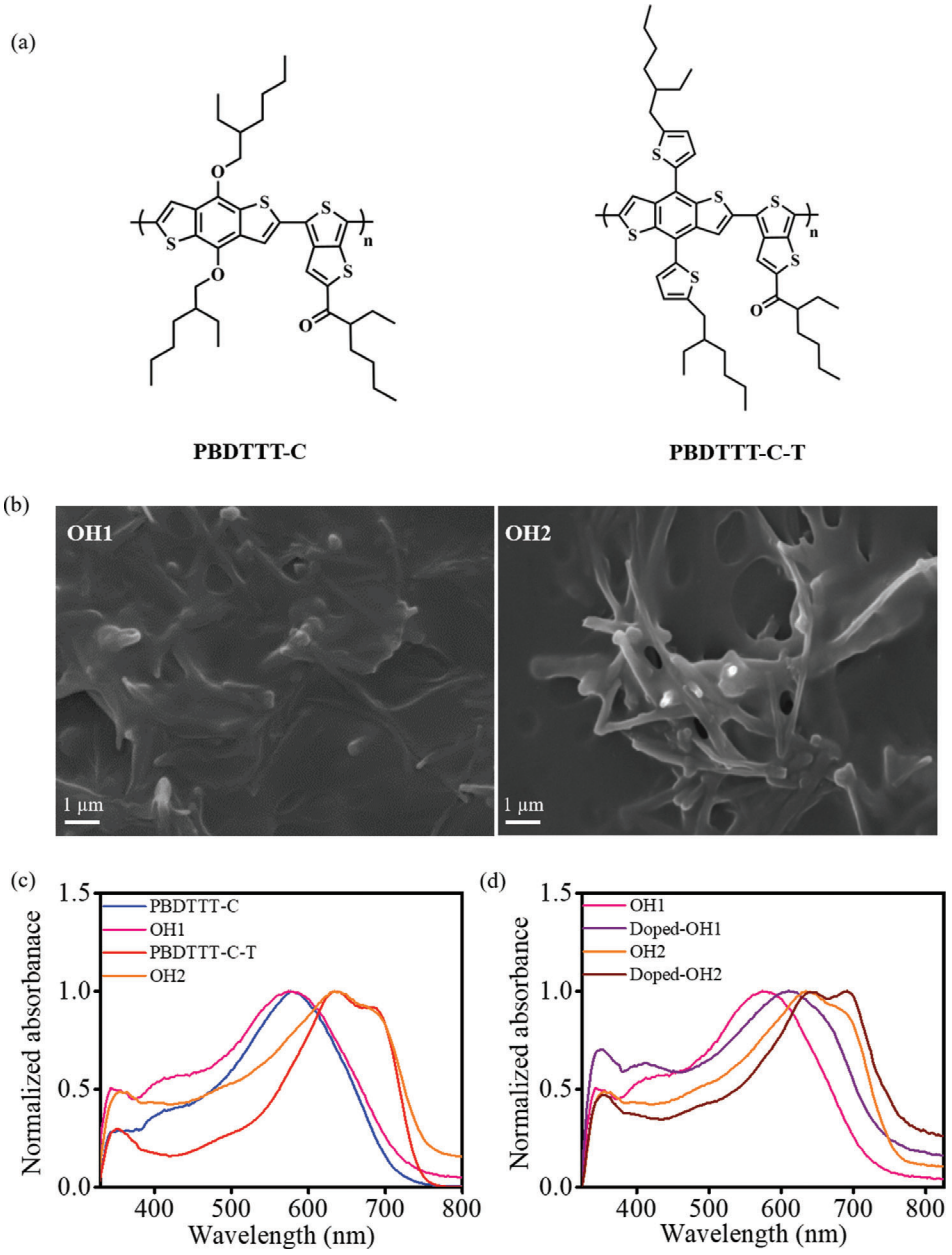

Figure 1. a) Molecular structures of PBDTTT-C and PBDTTT-C-T. b) Scanning electron microscope (SEM) images of OH1 and OH2 hybrids. c,d) Absorption spectra of the pristine polymers, hybrid films, and doped hybrid films.

(Figure 2b), a shift toward lower 2θ in the (100) peak of both hybrids was observed (OH1: 4.77°→ 4.67°; OH2: 4.20° → 4.04°) due to the elongation of lamellar stacking. A reduction of the peak intensity was observed for both the hybrid films, suggesting a decrease in the local order after doping.[43] The (010) peak intensity faded, and the peak at $2\theta = 26.37°$ shifted to 26.55° after doping due to the stronger interchain coupling between components. For the pristine polymers, hybrids, and doped hybrids, the variation of d-spacing for (100) and (002) peaks are plotted in Figure 2c,d. The *d*-value assigned to the lamellar-stacking direction is bigger for the doped- OH2 hybrid than the OH1. In OH1 and OH2, the d-spacing corresponding to π-stacking direction reduces upon hybrid formation and doping, implying a stronger π–π intermolecular interaction. These observations suggest that the doped-OH2 hybrid has a larger conjugated plane and better interchain π–π overlap postdoping, leading to higher carrier mobility and better charge transport properties.

2.2. TE Performance of Organic Hybrids

The TE parameters of hybrid films with different MWCNT weight percentages (wt%) at room temperature (≈28–30°C) were studied. The samples were drop-cast on a 16 × 4 mm glass

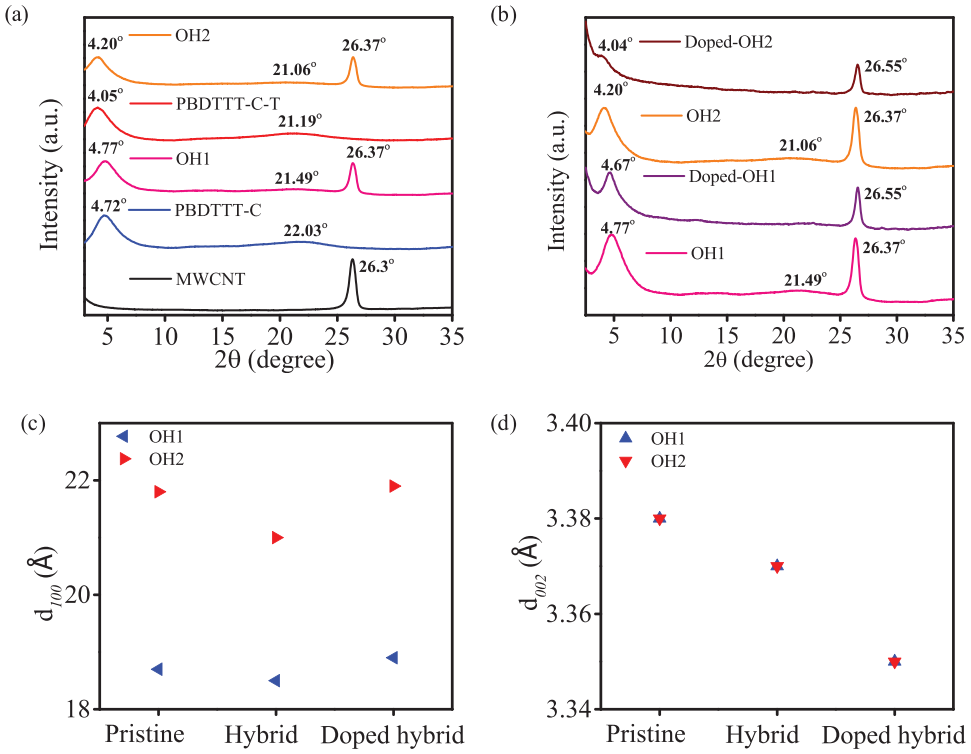

Figure 2. a,b) Wide-angle X-ray scattering (WAXS) plot; c,d) d-spacing of the pristine polymers, hybrid films, and doped hybrid.

substrate to form thick films. The average film thickness was obtained as ≈25 ± 5 μm. The significant thickness measurement error was due to the high roughness in surface topography. Figure S3 (Supporting Information) shows the variation of film thickness with MWCNT wt%. We noted minor thickness changes in the film thicknesses after doping, which lies in the relatively large thickness assessment error as stated before. With the addition of a lower amount of MWCNT, the undoped hybrids showed an imperceptible improvement in σ value. Beyond 15 wt%, a percolation threshold in σ value was observed that peaks at 45 wt% of MWCNT as plotted in **Figure 3**a. Such conductivity enhancement could be attributed to forming an inter-CNT bundle that creates new electrical pathways through the hybrid. Beyond this optimum level, a further increase in MWCNT wt% led to a decrease in σ, probably because of aggregates forming at higher MWCNT wt%, which eventually separates from the polymer support leading to a breakdown in the electrical network. However, α remained almost unaffected regardless of MWCNT addition with an average value ≈19.36 μVK^{-1} and 19.46 μVK^{-1} for OH1 and OH2, respectively (Figure 3b). α is essentially linked to the thermally activated charge carrier transport.[44,45] Beyond the percolation threshold, the energetic charge carriers primarily travel through the embedded CNT network. Therefore, the α value of these hybrids remains more or less constant and similar to that of MWCNT.[46] The TE properties of pristine MWCNT films were reported in our previous work.[34] Accordingly, the PF also peaks with the σ, as shown in Figure 3c.

There are prominent dissimilarities in the properties of OH1 and OH2 hybrids after $FeCl_3$ doping. The variation of σ, α, and PF with different wt% of MWCNT followed a similar trend for doped and undoped OH1 hybrids. The peak σ-value showed ≈1.3x enhancement, but α remained almost unaltered. Contrastingly, there was a substantial enhancement in both σ and α values of OH2 hybrids post-doping. The peak σ exhibited up to ≈5.45x increment (35.25 Scm^{-1} → 192.28 Scm^{-1}) after doping, and parallelly, α almost doubled from the undoped hybrids. Overall, a ≈24x enhancement in the PF (1.76 μWm^{-1}K^{-2} → 42.25 μWm^{-1}K^{-2}) could be obtained from a doped-OH2 hybrid. Typical reasons for such post-doping enhancements may include formations of charge-transfer-complexes (CTC) that augments polaron/bipolaron transports in the system, shortening the π-stacking distance, structural changes, etc.[47] The apparent shift in weak absorption band observed in the 400–500 nm range (Figure 1d) could be attributed to the existence of polaron/bipolarons.[48] Moreover, reducing interchain distance post-doping (Figure 2d) could overlap the π-electronic density of adjacent chains, creating a polaron/bipolaron network.[49] The formation of CTC and its interaction with the hybrids are detailed in the next section.

2.3. Role of Doping in Organic Hybrids

The X-ray photoelectron spectroscopy (XPS) survey spectrum of the pristine polymers, hybrids, and doped hybrids indicates the characteristic C1s, O1s, and S2p peaks, shown in Figure S4 (Supporting Information). **Table 1** presents the obtained chemical composition of the surface region in atomic percent (atomic %). Fe2p and Cl2p in doped-OH2 are higher than OH1, indicating that stronger doping of $FeCl_3$ is achieved with the OH2 hybrid.

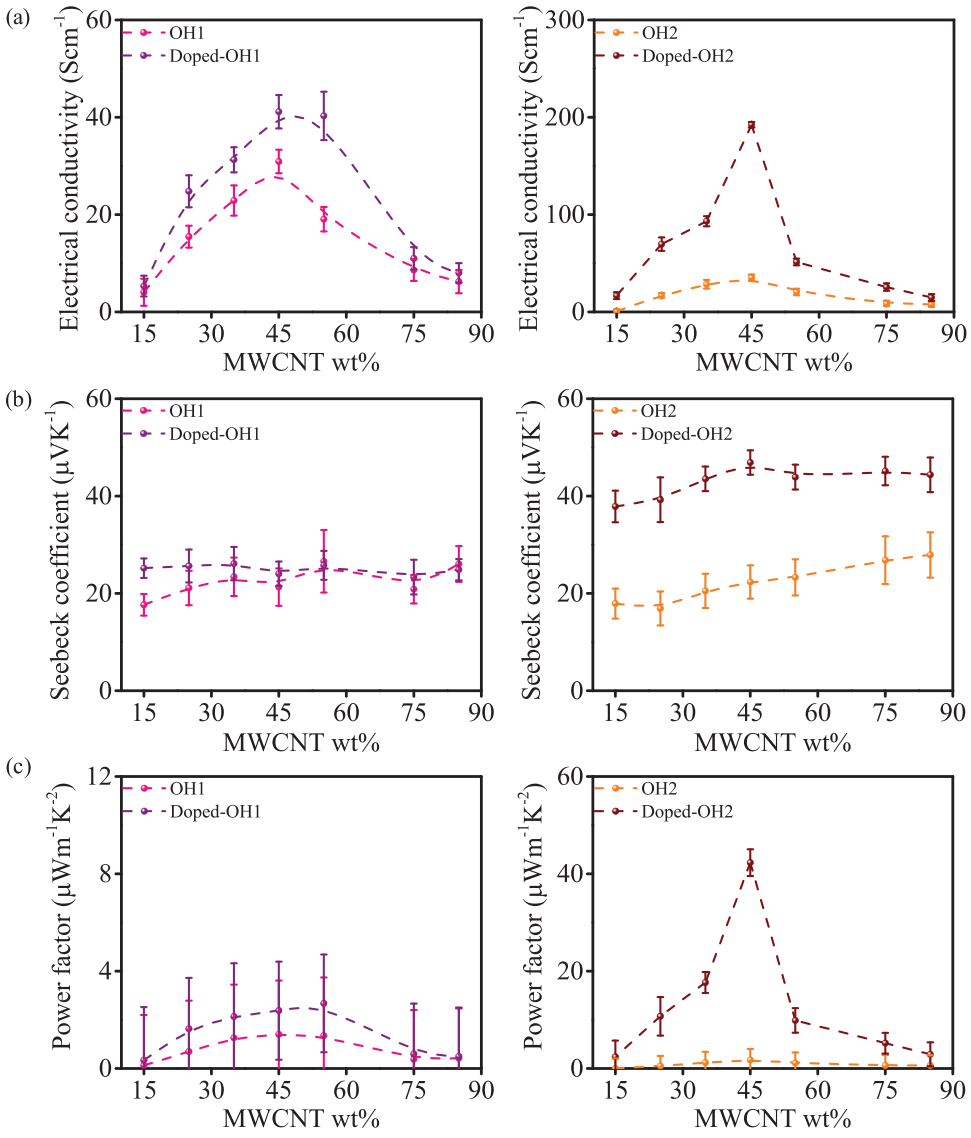

Figure 3. Variation of a) electrical conductivity; b) Seebeck coefficient; c) power factor (PF) with multi-walled carbon nanotube (MWCNT) wt% for undoped and $FeCl_3$ doped hybrids.

Table 1. Chemical composition in atomic %.

Sample	C1s	O1s	S2p	Fe2p	Cl2p
PBDTTT-C	83.53	10.06	6.41	0	0
OH1	90.68	4.66	4.66	0	0
Doped-OH1	89.45	5.52	4.11	0.5	0.41
PBDTTT-C-T	86.06	5.19	8.75	0	0
OH2	92.18	2.45	5.37	0	0
Doped-OH2	87.35	5.63	4.38	1.79	0.84

The C1s line at 284.8 eV was taken as the internal energy reference for shift compensation. The core-level O1s and S2p peaks (**Figure 4**) of both polymers were shifted to higher binding energies (BE) with the addition of MWCNT due to the polymer-MWCNT interactions. As shown in Figure 4a, the peaks in the OH1 hybrid shifted toward the higher BE after $FeCl_3$ doping. However, the peaks of doped-OH2 hybrids shift toward the lower BE side (Figure 4b). The BE shift could be attributed to the relative electronegativity of the dopant compared to the base elements.[50] Post $FeCl_3$ doping, the electron density around the OH1 hybrid decreases while that around OH2 increases. Such variations lead to the Fermi energy repositioning, i.e., the Fermi energy moving away or close to the valance band maxima (VBM).[24,51] The peak positions of high-resolution O1s and S2p spectra are listed in **Table 2**.

The CTC formation was investigated by the high-resolution Fe2p and Cl2p core level spectra of doped-OH1 and OH2 hybrids. **Figure 5**a shows that for the doped-OH1, the Fe2p region exhibits characteristic peaks of Fe2p3/2 and Fe2p1/2 with associated broad satellites at ≈711.34 and ≈725.46 eV. Graat et al. described

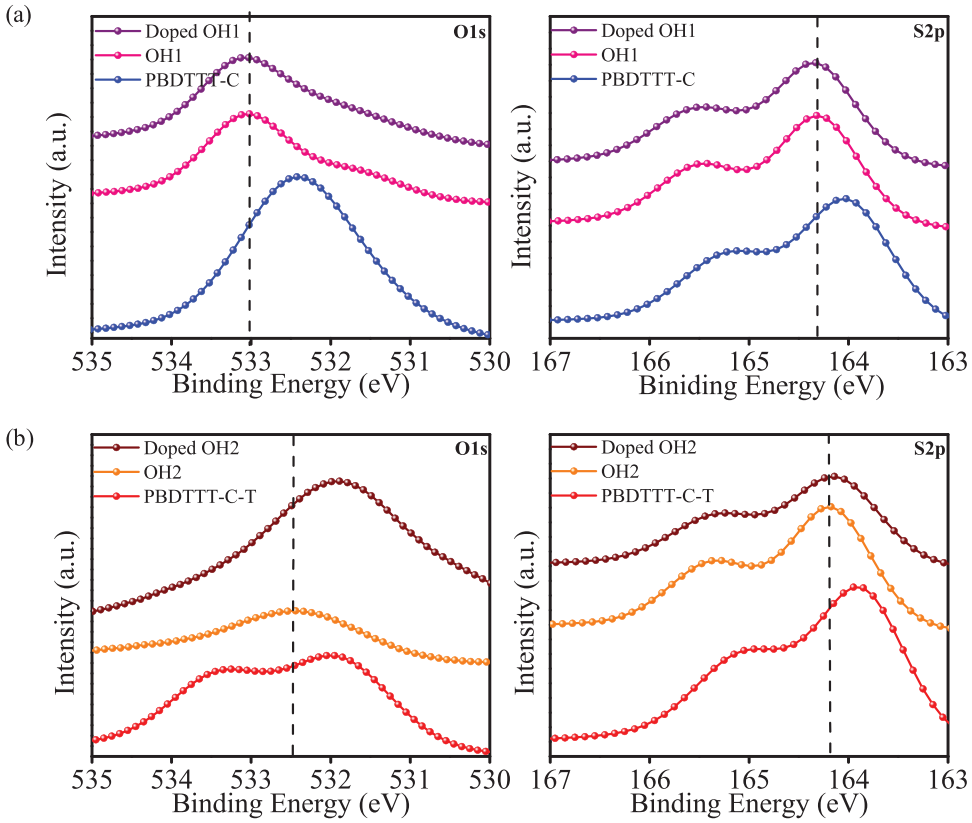

Figure 4. X-ray photoelectron spectroscopy (XPS) core-level spectra of a) OH1; b) OH2 hybrids before and after doping.

Table 2. X-ray photoelectron spectroscopy (XPS) peak positions of O1s and S2p core level spectra.

	PBDTTT-C	OH1	Doped-OH1	PBDTTT-C-T	OH2	Doped-OH2
O1s [eV]	532.41	533.02	533.13	532.03	532.48	531.88
S2p [eV]	164.02	164.31	164.36	163.91	164.21	164.14

that for iron oxide films, Fe^{3+} shows two distinguishing peaks at ≈711.2 and ≈724.3 eV attributed to Fe2p3/2 and Fe2p1/2, with corresponding satellites at ≈719.5 and ≈733.6 eV.[52] For the Fe^{2+} cation, the distinctive peaks are located at ≈709.8 and ≈722.8 eV, with satellites at ≈716.4 and ≈730.0 eV, respectively. Our experimental observations confirm the presence of Fe^{3+} cations, as evident from Figure 5a. A close examination of the Cl2p spectrum provided further information on the CTC. As seen in Figure 5b, the spectra consist of Cl2p3/2 spin-orbit doublets peaked at ≈198.79 and ≈200.61 eV and Cl2p1/2 peaked at ≈202.26 eV. The higher BE peak (200.61 eV) of Cl2p3/2 dominates with an area ratio of 2:3 that corresponds well to chlorine atoms covalently bonded to sp^2 carbon.[53–55]

For doped-OH2, as shown in Figure 5c, the Fe2p peaks are located at ≈711.32 eV (Fe2p3/2) and ≈725.36 eV (Fe2p1/2) with shakeup satellite peak offset by ≈7.9 eV from the main Fe2p3/2 peak. Ferraro and co-workers reported from the study of $FeCl_3$-doped polymers of polyphenylacetylene that post-doping, the Fe2p3/2 core level peak appears at ≈711.2–711.3 eV, consistent with the value for Fe^{3+} ions found in reference compound $(Et_4N)FeCl_4$ salt.[56] The Fe^{3+} shakeup satellite energies are usually found at ≈7 eV offset from the main 2p3/2 peak for $FeCl_3$.[57] The observed satellite energy value for doped-OH2 remains close to that, supporting the presence of Fe^{3+} state. The Cl2p core level emission spectrum doublet showed the highest intensity at ≈ 198.71 eV, followed by a weaker ≈200.30 eV peak. The more intense peak at the lower BE region of Cl2p3/2 doublet could be assigned to the presence of Cl^- ions, leading to the formation of the $FeCl_4^-$ complex.[34,58,59]

The XPS observation suggests that both hybrids possibly form Fe^{3+} species after doping, with OH1 forming a Cl–C bond and OH2 forming a Cl^- ion. It can be reasoned that the CTC created in two doped hybrids would attach at two different coordination sites. Further evidence of CTC formation could be obtained with a careful analysis of C1s and O1s spectra. **Figure 6**a shows the high-resolution spectrum for C1s of PBDTTT-C. Four definite peaks were observed due to the different bonding environments of carbon atoms. The incorporation of MWCNT led to the formation of π–π^* bonds due to the sp^2 carbon atoms of MWCNT.[60] A similar peak appears in the OH2 hybrid and the other characteristic peaks of PBDTTT-C-T, as shown in Figure 6b. However, in doped-OH1, an additional C-Cl bond was observed at ≈286.46 eV, confirming the presence of the CTC coordination site. The deconvoluted S2p XPS spectra of the pristine polymer, hybrids, and doped hybrids are shown in Figure S5 (Supporting Information).

Figure 7a shows the core level O1s spectra of the PBDTTT-C, OH1, and doped-OH1. Each spectrum consists of three peaks

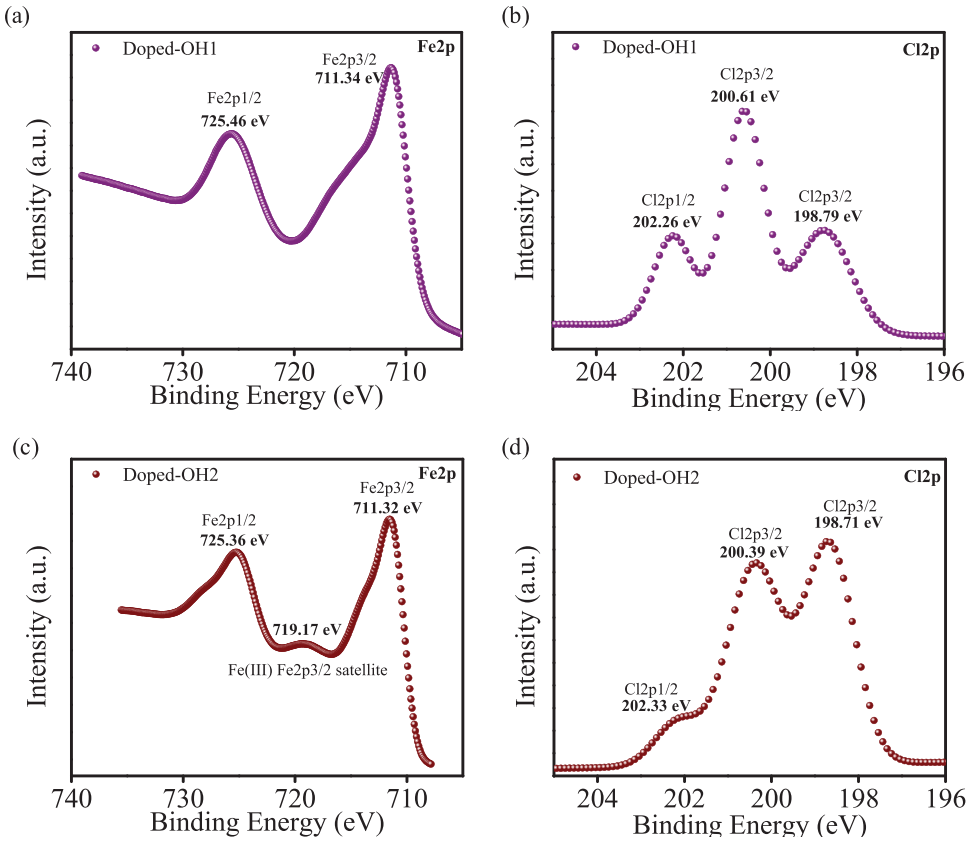

Figure 5. a) Fe2p and b) Cl2p core level spectra of doped-OH1; c) Fe2p and d) Cl2p core level spectra of doped-OH2.

corresponding to C=O, C−O−C, and O−H bonds, with BE shifts related to the hybrid formation and doping. The O1s spectra of the undoped and doped-OH2 show an additional peak at ≈530.31 eV that may be ascribed to the C−O−Fe bond formation (Figure 7b).[61] Therefore, it is reasonable to conclude that the CTC coordination sites in doped-OH2 differ from the doped-OH1.

The Fe2p and Cl2p spectra of the doped PBDTTT-C/PBDTTT-C-T are shown in Figure S6 (Supporting Information). Both the polymers exhibited the presence of Fe^{3+} and Cl^{-} ions upon doping with $FeCl_3$. The deconvoluted high-resolution O1s spectra (Figure S7, Supporting Information) revealed the occurrence of C−O−Fe bonds in the doped-polymers, confirming $FeCl_4^{-}$ complex formation. This observation differs from the earlier results as the $FeCl_4^{-}$ complex was not observed in OH1, suggesting that the presence of MWCNT hinders the formation of coordination sites in PBDTTT-C. It is reasonable to state that the wrapping of π-conjugated polymers over the surface of the MWCNT differs and results in the availability of different coordination sites for doping in hybrids. Both polymers have identical BDT backbone conjugated with TTE moiety but consist of different side-chain groups; PBDTTT-C has alkoxy, and PBDTTT-C-T has an alkylthiophene group.

It should be noted that the presence of =O in TTE moiety coordinates the formation of the C−O−Fe bond in doped polymers. During the hybrid formation, the presence of a more electron-rich alkylthiophene group in PBDTTT-C-T enhances the π–π interaction with the surface of MWCNT, providing the =O available for doping. On the other hand, the PBDTTT-C wraps around the surface of MWCNT to offer π–π interaction, resulting in a different coordination site for doping.

2.4. Fermi Level Repositioning

The ultraviolet photoelectron spectroscopy (UPS) characterization of the hybrids revealed their relative positioning of the VBM and the work function (φ). The full range UPS plots in BE scale of the hybrids are given in Figure S8a (Supporting Information). The φ is obtained from the secondary cut-off region, plotted in kinetic energy (KE) scale as shown in **Figure 8**a. The VBM is estimated through the linear extrapolation of the low BE edge, as shown in Figure 8b. The VBM position shifts to a higher BE for the doped-OH1, while in contrast, the doped-OH2 exhibited a lower BE. Also, φ of OH1 and OH2 is estimated to be 4.09 and 4.02 eV, respectively. After doping, φ shifted to 4.05 and 4.13 eV in OH1 and OH2. A schematic energy band diagram depicting these complementary behaviors of the two hybrids in consideration is shown in Figure 8c.

Following Mott's formula, the Seebeck coefficient can be considered as the contribution of a "mobility" term and a "density of states (DOS)" term, given by [24]

$$\alpha = \frac{\pi^2}{3}\,\frac{k_B^2 T}{e}\left(\frac{\partial \ln \mu}{\partial E} + \frac{\partial \ln N}{\partial E}\right)_{E_f} \tag{2}$$

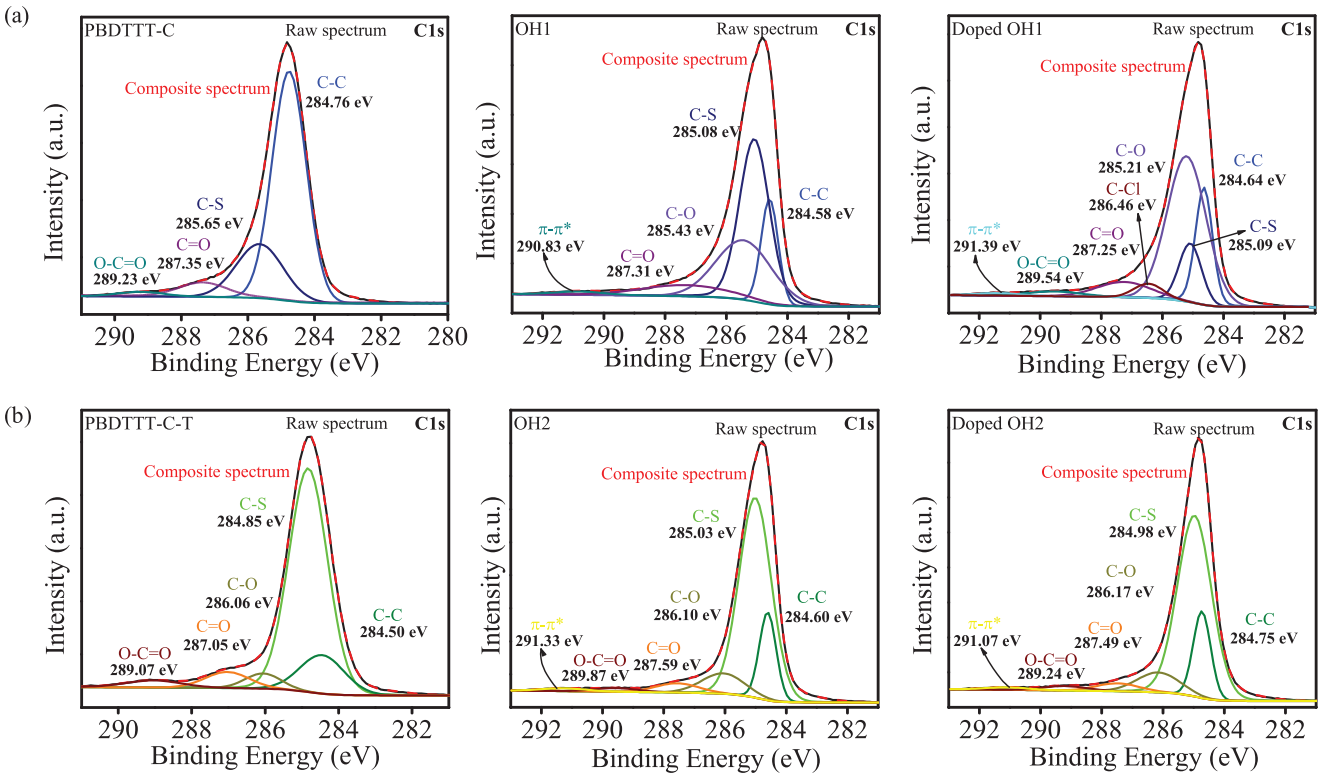

Figure 6. C1s core level spectra of a) PBDTTT-C, OH1, and doped-OH1; b) PBDTTT-C-T, OH2, and doped-OH2.

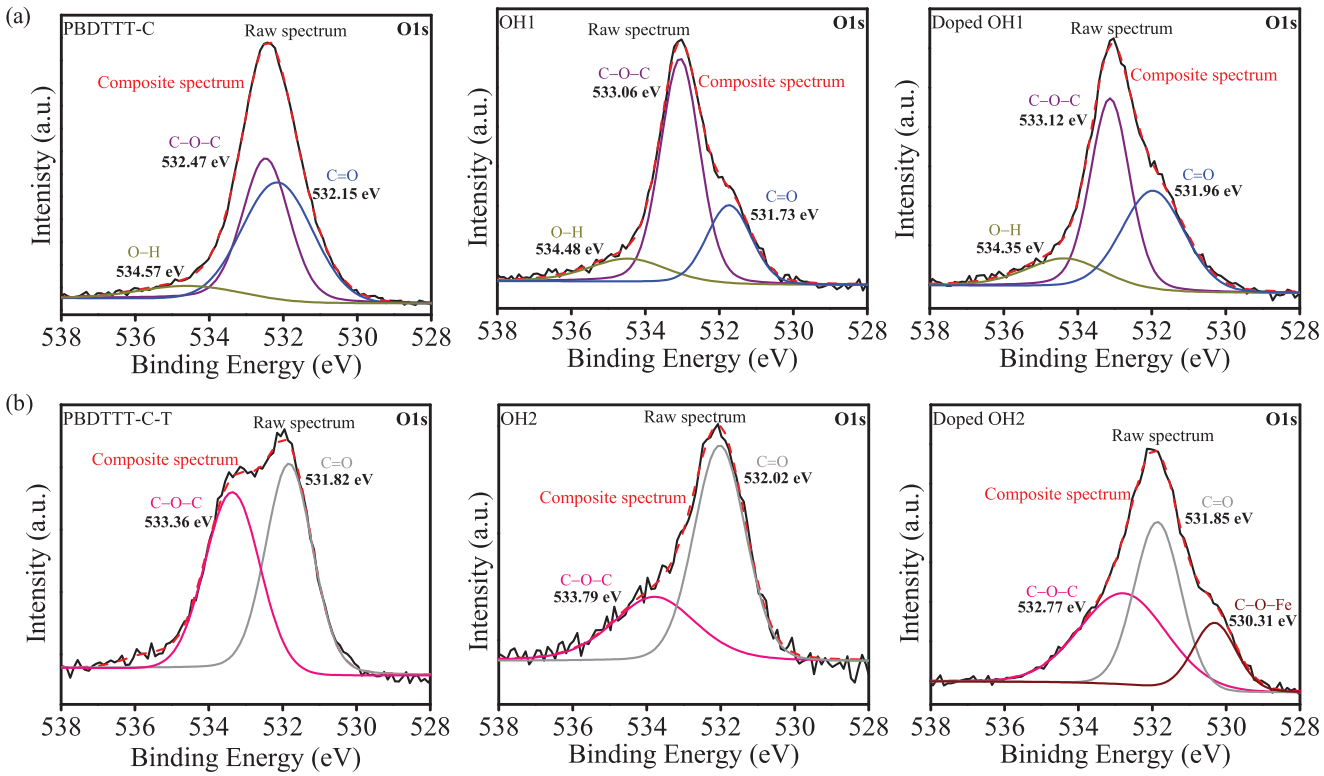

Figure 7. O1s core level spectra of a) PBDTTT-C, OH1, and doped-OH1; b) PBDTTT-C-T, OH2, and doped-OH2.

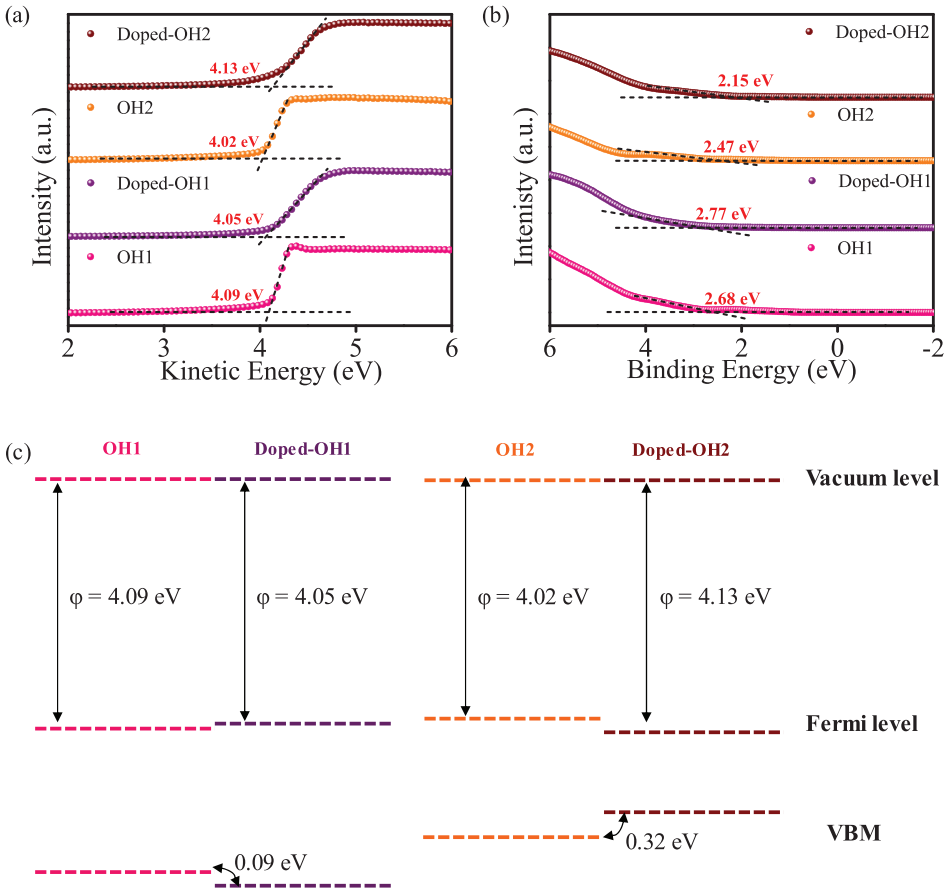

Figure 8. Ultraviolet photoelectron spectroscopy (UPS) spectra of the a) secondary cut-off region and b) low binding energies (BE) region; c) energy band diagram of OH1 and OH2 hybrids before and after doping.

where k_B, T, e, and μ are the Boltzmann constant, absolute temperature, electron charge, and carrier mobility, respectively. The latter term in Equation (2), $N(E_f)$, relates to DOS and its slope at the Fermi level. The density of valence electronic states (DOVS) of doped OH1 and OH2 were investigated by UPS (Figure S8b, Supporting Information). For the doped-OH1, the apparent decoupling of σ and α (i.e., increasing σ without affecting α) is due to the slight upward shift of the Fermi level from VBM with the DOVS remaining close to the undoped hybrids. However, for doped-OH2, the Fermi level moved closer to the VBM, increasing σ considerably. At the same time, a steep rise in DOVS is responsible for the concurrent enhancement of α. For OH1 hybrids, the carrier concentration and mobility increase after doping, thereby increasing σ. For doped-OH2 hybrids, there is a decrease in the carrier concentration due to post-doping carrier trap-state formation, which contributes to enhancing the α through Mott's relation,[62]

$$\alpha = \frac{8\pi^2 k_B^2 T}{3eh^2} m^* \left(\frac{\pi}{3n}\right)^{2/3} \quad (3)$$

m^* and n are the Boltzmann constant and carrier concentration. The increased mobility effectively compensates for the reduction in carrier concentration due to the post-doping dielectric environment change in the composite (**Table 3**). The repositioning of the Fermi level and the enhanced mobility results in the independent rise of σ and α for doped-OH2.

Table 3. Mobility and carrier concentration values of OH1 and OH2 (before and after doping) with 45 wt% of multi-walled carbon nanotube (MWCNT) obtained from Hall measurements.

Particulars	OH1	Doped-OH1	OH2	Doped-OH2
Bulk concentration [cm^{-3}]	1.57 E+20	2.56 E+20	3.66 E+20	3.01 E+20
Mobility (cm^2 Vs^{-1})	3.14 E-1	4.80 E-1	2.50 E-1	4.85 E-1

3. Conclusion

In summary, two p-type organic hybrids, OH1 and OH2, were prepared using BDT-TTE based polymers PBDTTT-C and PBDTTT-C-T with MWCNT fillers. Both hybrids show a percolation threshold in σ value beyond 15 wt% of MWCNT incorporation, with the peak value at 45 wt%. After doping, a sharp increase in σ and α is observed for OH2 while OH1 exhibited an unaltered α with a minor rise in σ. Such post-doping enhancements are due to the formation of CTC that augments polaron/bipolaron transports in the system, shortening the π-stacking distance and inducing structural changes. The doping

increased DOVS of the OH2 hybrid that led to the Fermi level shift toward the VBM. However, doping of OH1 exhibited the Fermi level shifting away from the VBM with an almost unchanged DOVS pattern. A detailed spectroscopic investigation revealed that the π–π interaction with the surface of MWCNT is strengthened by the more electron-rich alkylthiophene group in PBDTTT-C-T and =O is available for doping. In contrast, PBDTTT-C wraps around the surface of MWCNT to offer π–π interaction, resulting in a different coordination site for doping. These results highlight some salient features of the $FeCl_3$ doping mechanism for polymer/MWCNT hybrids that could be used for designing high-performing materials in the future.

4. Experimental Section

Organic Hybrids Preparation: The polymers PBDTTT-C (Solarmer Energy Inc. – $(C_{40}H_{52}O_3S_4)_n$) and PBDTTT-C-T (Solarmer Energy Inc. – $(C_{48}H_{56}OS_6)_n$) along with MWCNT(Sigma-Aldrich – containing >90% carbon basis, diameter = 110–170 nm and length = 5–9 μm) were dispersed in 1,2-dichlorobenzene (Sigma-Aldrich) to produce 0.05 mg μL^{-1} of solutions of each. A bath sonicator (Elmasonic P30H Ultrasonic bath; 80 kHz and 192 W) was used for 1 h for the sample preparation. The hybrid composition was tuned by different wt% of MWCNT addition. The subsequent mixture showed good stability over 3 weeks, with no settling of materials was observed. The dispersion was drop-cast on a precleaned (with soap solution, water, and isopropanol in that order by ultrasound sonication for 15 min in each) and pre-heated (at 120°C for 15 min) glass substrate and annealed at 120°C for 30 min. For doping, the hybrid films were immersed into 0.05 M $FeCl_3$ (SD Fine Chemicals) solution in nitromethane (Spectrochem) for 30 min and washed with ethanol to remove the excess dopants, similar to the process adopted in our previous work.[34]

Characterization of Organic Hybrids: The surface topography of the hybrids was recorded with a JEOL 5600 LV SEM. The UV-visible spectra of the hybrid films were recorded with an Ocean Optics (USB 4000 XR) UV-vis modular spectrophotometer. The crystal structure analysis was performed using a Xenocs XEUSS WAXS measurement system with Ni-filtered Cu K_α radiation (λ = 1.5405 Å) in the transmission mode.

Thermoelectric Characterization: Linseis LSR-3 thermopower measuring system was used to assess the TE properties that can simultaneously measure α and the σ of solid materials. All samples were positioned vertically between two electrodes, and a temperature gradient was produced by the lower electrode block consisting of a heating coil. The complete arrangement was placed in a chamber furnace for isolation and overall thermal control. Two thermocouples laterally contacting the sample's surface were used to detect the temperature difference between the hot and cold regions. For σ of the sample, the specific electrical resistance was measured using the DC four-terminal measurement technique. A constant direct current (≈1 mA) was passed through the two electrodes into the sample under thermal equilibrium conditions. The resulting voltage drop over a portion of the length of the sample was again measured using one of the two thermocouples. The specific resistance and the electrical conductivity were calculated based on the measured data and the thermocouple distance. The film thickness was measured using a Veeco Dektak 6M stylus profilometer.

Characterization of Doped Organic Hybrids: The XPS studies were carried out in a ULVAC-PHI 5000 Versa Probe II equipped with a monochromatic Al-K_α X-ray source ($h\nu$ = 1486.6 eV, 15 kV). The C1s line corresponding to the C–C bond (284.8 eV) was used for internal energy referencing and calibration. Survey and high-resolution scans were recorded with a 50 W X-ray source with pass energies of 187.85 and 46.95 eV, respectively. MultiPak software was used for peak fitting and area analysis. Thermo Fisher Scientific Instruments (K-ALPHA + spectrometer, equipped with a high-intensity UV source) was used to record He-I (21.2 eV) UPS spectra with a photon flux of 1.5×10^{-12} photons s^{-1}. Mobility and concentration of charge carrier were obtained from the Hall measurement studies at room temperature. The data is collected from an ECOPIA HMS 3000 system (with 0.54 T magnetic field and 19 mA current) using Van der Pauw's geometry.

Supporting Information

Supporting Information is available from the Wiley Online Library or from the author.

Acknowledgements

The authors acknowledge the financial support of the Council of Scientific and Industrial Research (CSIR), Govt. of India, and the Gas Authority of India Limited (GAIL) (Project number: SSP-135939 and SSP-160139). I.V. acknowledges her research fellowship from DST-INSPIRE. The authors thank Dr. Saju Pillai and Mr. Peer Mohamed for XPS results, Dr. S. N. Potty (C-MET) for Hall measurement, and Mr. Shriniwas S Deo (CSIR-NCL) for UPS measurement.

Conflict of Interest

The authors declare no conflict of interest.

Data Availability Statement

The data that support the findings of this study are available from the corresponding author upon reasonable request.

Keywords

carbon nanotubes, conjugated polymers, doping, Fermi levels, thermoelectricity

Received: December 2, 2021
Published online:

[1] Z. Yuan, X. Tang, Z. Xu, J. Li, W. Chen, K. Liu, Y. Liu, Z. Zhang, *Appl. Energy* **2018**, *225*, 746.
[2] K. Liu, Y. Liu, Z. Xu, Z. Zhang, Z. Yuan, X. Guo, Z. Jin, X. Tang, *Appl. Therm. Eng.* **2017**, *125*, 425.
[3] S. A. Mostafavi, M. Mahmoudi, *Appl. Therm. Eng.* **2018**, *132*, 624.
[4] J. Yang, F. R. Stabler, *J. Electron. Mater.* **2009**, *38*, 1245.
[5] S. Qing, A. Rezania, L. A. Rosendahl, A. A. Enkeshafi, X. Gou, *Energy Convers. Manage* **2018**, *156*, 655.
[6] Y.-W. Chen, C.-C. Wu, C.-C. Hsu, C.-L. Dai, *Appl. Sci.* **2018**, *8*, 1047.
[7] M. Thielen, L. Sigrist, M. Magno, C. Hierold, L. Benini, *Energy Convers. Manage* **2017**, *131*, 44.
[8] A. Amar, A. Kouki, H. Cao, *Sensors* **2015**, *15*, 28889.
[9] A. Proto, L. Peter, M. Cerny, M. Penhaker, D. Bibbo, S. Conforto, M. Schmid, in *2018 IEEE 20th Int. Conf. on e-Health Networking, Applications and Services (Healthcom)*, IEEE, Piscataway, NJ **2018**, pp. 1–5.
[10] M. Guan, K. Wang, D. Xu, W.-H. Liao, *Energy Convers. Manage* **2017**, *138*, 30.
[11] B. Iezzi, K. Ankireddy, J. Twiddy, M. D. Losego, J. S. Jur, *Appl. Energy* **2017**, *208*, 758.

[12] X. Li, C. Xie, S. Quan, L. Huang, W. Fang, *Appl. Energy* **2018**, *231*, 887.
[13] X. Li, Z. Zhong, J. Luo, Z. Wang, W. Yuan, G. Zhang, C. Yang, C. Yang, *Int. J. Photoenergy* **2019**, *2019*, 3725364 .
[14] C. Bounioux, P. Díaz-Chao, M. Campoy-Quiles, M. S. Martín-González, A. R. Goñi, R. Yerushalmi-Rozen, C. Müller, *Energy Environ. Sci.* **2013**, *6*, 918.
[15] M. Wahbah, M. Alhawari, B. Mohammad, H. Saleh, M. Ismail, *IEEE J. Emerging Sel. Top. Circuits Syst.* **2014**, *4*, 354.
[16] B. T. McGrail, A. Sehirlioglu, E. Pentzer, *Angew. Chem., Int. Ed.* **2015**, *54*, 1710.
[17] M. Lindorf, K. A. Mazzio, J. Pflaum, K. Nielsch, W. Brütting, M. Albrecht, *J. Mater. Chem. A* **2020**, *8*, 7495.
[18] H. Jin, J. Li, J. Iocozzia, X. Zeng, P.-C. Wei, C. Yang, N. Li, Z. Liu, J. H. He, T. Zhu, J. Wang, Z. Lin, S. Wang, *Angew. Chem., Int. Ed.* **2019**, *58*, 15206.
[19] R. Tian, C. Wan, Y. Wang, Q. Wei, T. Ishida, A. Yamamoto, A. Tsuruta, W. Shin, S. Li, K. Koumoto, *J. Mater. Chem. A* **2017**, *5*, 564.
[20] H. J. Lee, G. Anoop, H. J. Lee, C. Kim, J. W. Park, J. Choi, H. Kim, Y. J. Kim, E. Lee, S. G. Lee, Y. M. Kim, J. H. Lee, J. Y. Jo, *Energy Environ. Sci.* **2016**, *9*, 2806.
[21] C. Pan, L. Wang, T. Liu, X. Zhou, T. Wan, S. Wang, Z. Chen, C. Gao, L. Wang, *Macromol. Rapid Commun.* **2019**, *40*, e1900082.
[22] L. Wang, C. Pan, Z. Chen, W. Zhou, C. Gao, L. Wang, *ACS Appl. Energy Mater.* **2018**, *1*, 5075.
[23] L. Wang, C. Pan, A. Liang, X. Zhou, W. Zhou, T. Wan, L. Wang, *Polym. Chem.* **2017**, *8*, 4644.
[24] X. Zhou, C. Pan, C. Gao, A. Shinohara, X. Yin, L. Wang, Y. Li, Q. Jiang, C. Yang, L. Wang, *J. Mater. Chem. A* **2019**, *7*, 10422.
[25] M. Tonga, L. Wei, P. S. Taylor, E. Wilusz, L. Korugic-Karasz, F. E. Karasz, P. M. Lahti, *ACS Appl. Mater. Interfaces* **2017**, *9*, 8975.
[26] J. Kim, S. Park, S. Lee, H. Ahn, S. Joe, B. J. Kim, H. J. Son, *Adv. Energy Mater.* **2018**, *8*, 1801601.
[27] L. Meng, Y. Zhang, X. Wan, C. Li, X. Zhang, Y. Wang, X. Ke, Z. Xiao, L. Ding, R. Xia, H.-L. Yip, Y. Cao, Y. Chen, *Science* **2018**, *361*, 1094.
[28] H. Luo, C. Yu, Z. Liu, G. Zhang, H. Geng, Y. Yi, K. Broch, Y. Hu, A. Sadhanala, L. Jiang, P. Qi, Z. Cai, H. Sirringhaus, D. Zhang, *Sci. Adv.* **2016**, *2*, e1600076.
[29] L. Huo, X. Guo, S. Zhang, Y. Li, J. Hou, *Macromolecules* **2011**, *44*, 4035.
[30] H. Luo, C. Yu, Z. Liu, G. Zhang, H. Geng, Y. Yi, K. Broch, Y. Hu, A. Sadhanala, L. Jiang, P. Qi, Z. Cai, H. Sirringhaus, D. Zhang, *Sci. Adv.* **2016**, *2*, e1600076.
[31] P. Adhikary, S. Venkatesan, N. Adhikari, P. P. Maharjan, O. Adebanjo, J. Chen, Q. Qiao, *Nanoscale* **2013**, *5*, 10007.
[32] A. Zusan, B. Gieseking, M. Zerson, V. Dyakonov, R. Magerle, C. Deibel, *Sci. Rep.* **2015**, *5*, 8286.
[33] Y. J. Kim, W. Jang, D. H. Wang, C. E. Park, *J. Phys. Chem. C* **2015**, *119*, 26311.
[34] V. Ignatious, N. Raveendran, A. Prabhakaran, Y. Tanjore Puli, V. Chakkooth, B. Deb, *Chem. Eng. J.* **2021**, *409*, 128294.
[35] A. W. Musumeci, G. G. Silva, J.-W. Liu, W. N. Martens, E. R. Waclawik, *Polymer* **2007**, *48*, 1667.
[36] A. Ajayaghosh, *Chem. Soc. Rev.* **2003**, *32*, 181.
[37] J.-L. Brédas, D. Beljonne, V. Coropceanu, J. Cornil, *Chem. Rev.* **2004**, *104*, 4971.
[38] Z. Ma, W. Sun, S. Himmelberger, K. Vandewal, Z. Tang, J. Bergqvist, A. Salleo, J. W. Andreasen, O. Inganäs, M. R. Andersson, C. Müller, F. Zhang, E. Wang, *Energy Environ. Sci.* **2014**, *7*, 361.
[39] Y.-S. Choi, W.-H. Lee, J.-R. Kim, S.-K. Lee, W.-S. Shin, S.-J. Moon, J.-W. Park, I.-N. Kang, *Bull. Korean Chem. Soc.* **2011**, *32*, 417.
[40] P. Rathore, C. M. S. Negi, A. Yadav, A. S. Verma, S. K. Gupta, *Optik* **2018**, *160*, 131.
[41] S. Sahare, N. Veldurthi, S. Datar, T. Bhave, *RSC Adv.* **2015**, *5*, 102795.
[42] W. Li, B. Guo, C. Chang, X. Guo, M. Zhang, Y. Li, *J. Mater. Chem. A* **2016**, *4*, 10135.
[43] L. Hrostea, L. Leontie, M. Dobromir, C. Doroftei, M. Girtan, *Coatings* **2020**, *10*, 1074.
[44] Y. S. Kim, D. Kim, K. J. Martin, C. Yu, J. C. Grunlan, *Macromol. Mater. Eng.* **2010**, *295*, 431.
[45] Y. Choi, Y. Kim, S.-G. Park, Y.-G. Kim, B. J. Sung, S.-Y. Jang, W. Kim, *Org. Electron.* **2011**, *12*, 2120.
[46] C. Meng, C. Liu, S. Fan, *Adv. Mater.* **2010**, *22*, 535.
[47] E. Bilotti, O. Fenwick, B. C. Schroeder, M. Baxendale, P. Taroni-Junior, T. Degousée, Z. Liu, *Comprehensive Composite Materials II*, Elsevier, Oxford **2018**, pp. 408–430.
[48] T. R. Naveen Kumar, P. Karthik, B. Neppolian, *Nanoscale* **2020**, *12*, 14213.
[49] O. Bubnova, Z. U. Khan, H. Wang, S. Braun, D. R. Evans, M. Fabretto, P. Hojati-Talemi, D. Dagnelund, J.-B. Arlin, Y. H. Geerts, S. Desbief, D. W. Breiby, J. W. Andreasen, R. Lazzaroni, W. M. Chen, I. Zozoulenko, M. Fahlman, P. J. Murphy, M. Berggren, X. Crispin, *Nat. Mater.* **2014**, *13*, 190.
[50] P. S. Bagus, F. Illas, G. Pacchioni, F. Parmigiani, *J. Electron Spectrosc. Relat. Phenom.* **1999**, *100*, 215.
[51] Y. Zou, D. Huang, Q. Meng, C. an Di, D. Zhu, *Org. Electron.* **2018**, *56*, 125.
[52] P. C. J. Graat, M. A. J. Somers, *Appl. Surf. Sci.* **1996**, *100–101*, 36.
[53] S. Yuan, J. Gu, Y. Zheng, W. Jiang, B. Liang, S. O. Pehkonen, *J. Mater. Chem. A* **2015**, *3*, 4620.
[54] E. Papirer, R. Lacroix, J.-B. Donnet, *Carbon* **1996**, *34*, 1521.
[55] A. F. Pérez-Cadenas, F. J. Maldonado-Hódar, C. Moreno-Castilla, *Carbon* **2003**, *41*, 473.
[56] A. Furlani, M. V. Russo, G. Polzonetti, K. Martin, H. H. Wang, J. R. Ferraro, *Appl. Spectrosc.* **1990**, *44*, 331.
[57] B. W. Veal, A. P. Paulikas, *Phys. Rev. B* **1985**, *31*, 5399.
[58] H. Piao, K. Adib, M. A. Barteau, *Surf. Sci.* **2004**, *557*, 13.
[59] I. Pełech, U. Narkiewicz, D. Moszyński, R. Pełech, *J. Mater. Res.* **2012**, *27*, 2368.
[60] D. Puentes-Camacho, E. F. Velázquez, D. E. Rodríguez-Félix, M. Castillo-Ortega, R. R. Sotelo-Mundo, T. del Castillo-Castro, *Adv. Nat. Sci. Nanosci. Nanotechnol.* **2017**, *8*, 045011.
[61] Y. Pang, K. Luo, L. Tang, X. Li, Y. Song, C. Li, L. Wang, *Environ. Sci. Pollut. Res.* **2018**, *25*, 30575.
[62] Y. H. Kang, U.-H. Lee, I. H. Jung, S. C. Yoon, S. Y. Cho, *ACS Appl. Electron. Mater.* **2019**, *1*, 1282.

((Supporting Information can be included here using this template))

Supporting Information

Studies on the doping mechanism of conjugated thienothiophene polymer/MWCNT hybrids for thermoelectric application

Ignatious Vijitha, Neethi Raveendran, Sruthy Poovattil, Navin Jacob, Chakkooth Vijayakumar[*]*, and Biswapriya Deb*[*]

I. Vijitha, N. Raveendran, S. Poovattil, N. Jacob, Dr. C. Vijayakumar, Dr. B. Deb
Photosciences and Photonics, Chemical Science and Technology Division, CSIR-National Institute for Interdisciplinary Science and Technology (CSIR-NIIST), Thiruvananthapuram-695019, India
Academy of Scientific and Innovative Research (AcSIR), Ghaziabad-201002, India
E-mail: cvijayakumar@niist.res.in; biswapriya.deb@niist.res.in

Sample preparation and doping:

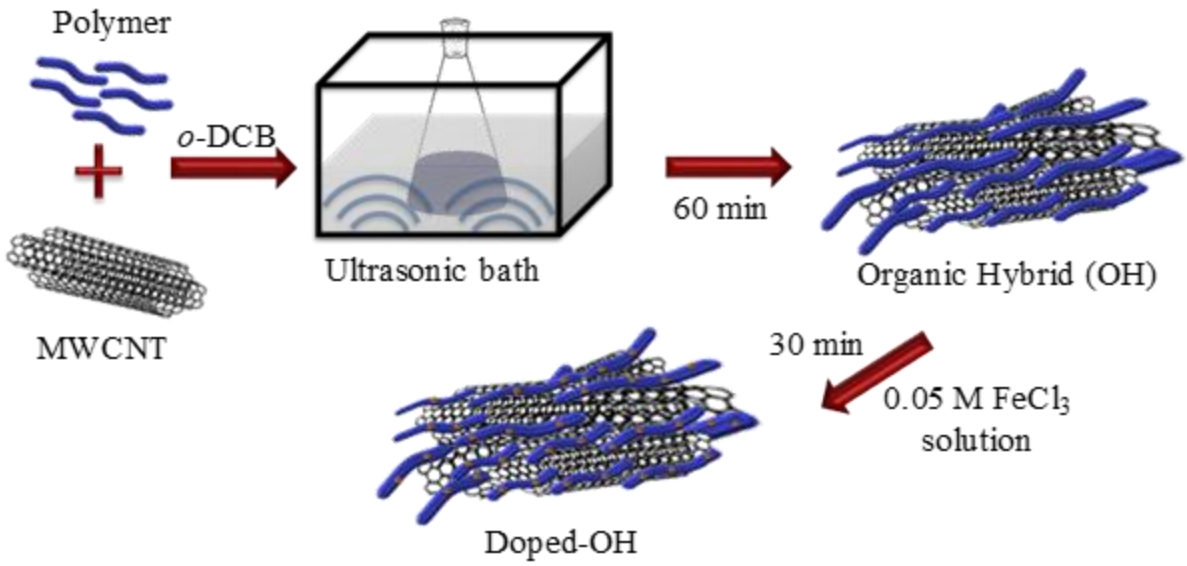

Figure S1. Schematic representation of sample preparation.

SEM image of organic hybrids after doping:

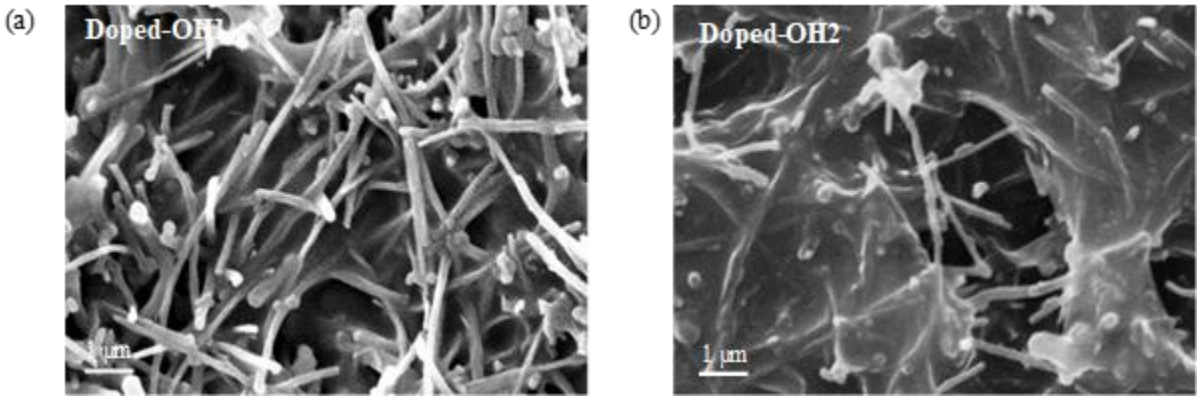

Figure S2. SEM images of typical a) Doped-OH1; b) Doped-OH2 films.

The thickness of the samples before and after doping:

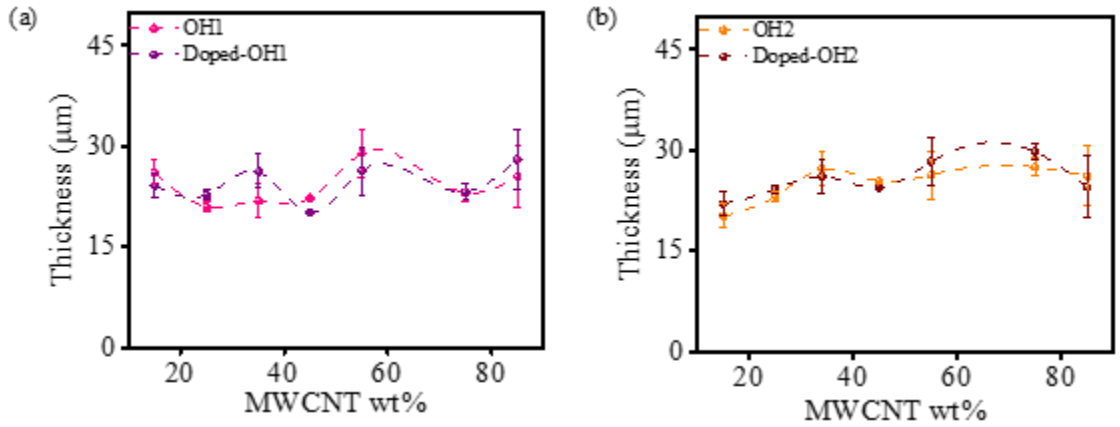

Figure S3. The thickness of a) OH1; b) OH2 hybrid films by varying MWCNT wt% in undoped and doped conditions.

XPS survey spectrum:

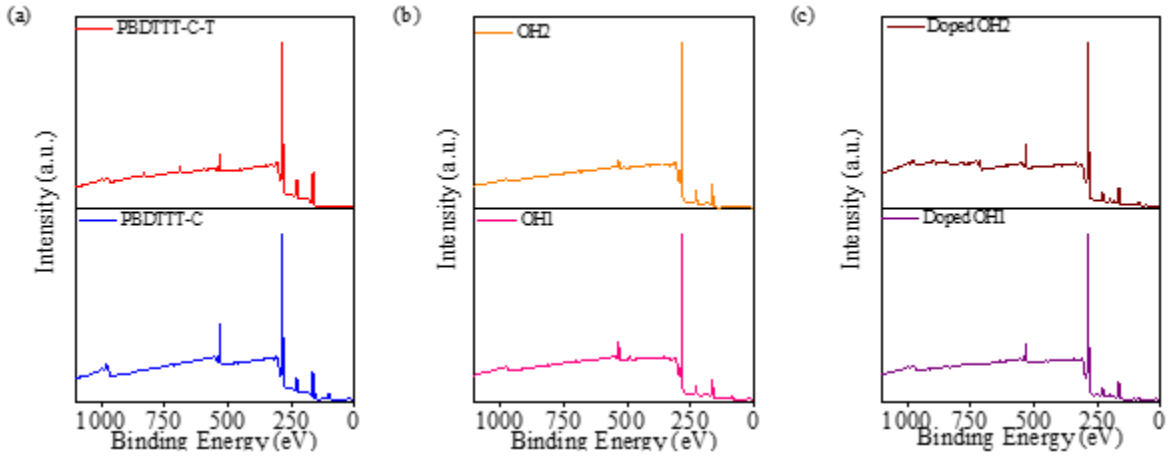

Figure S4. XPS survey spectra of a) pristine polymer; b) organic hybrids; c) doped hybrids.

High-resolution S2p spectra of organic hybrids:

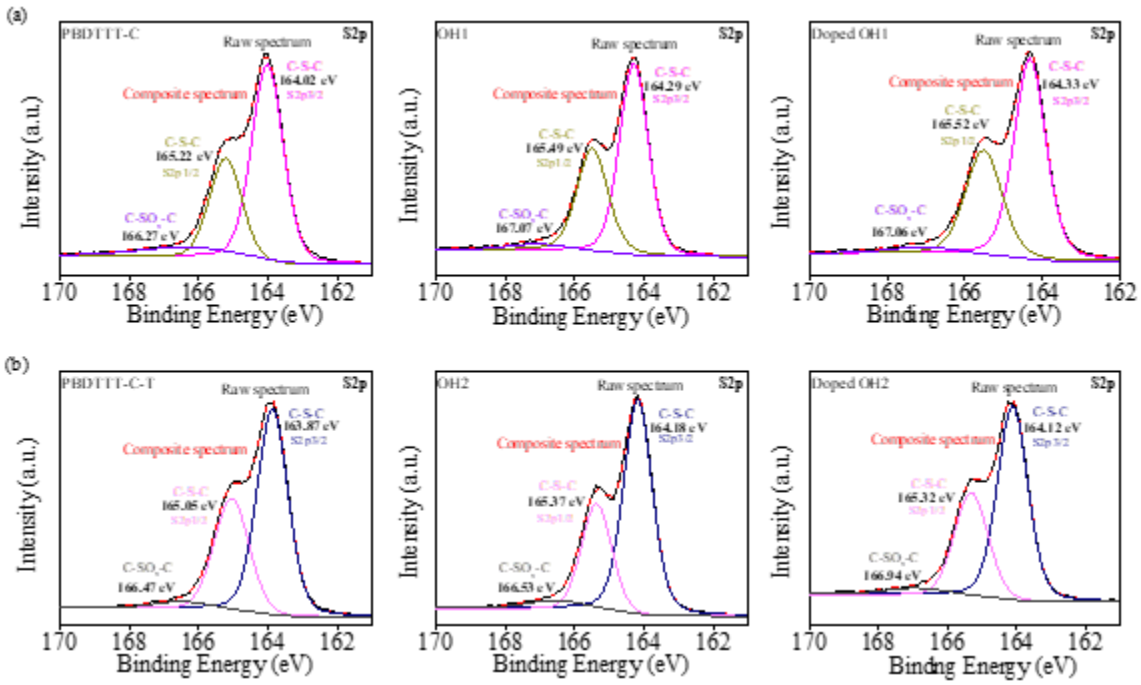

Figure S5. Core level S2p XPS spectra of a) OH1 and b) OH2.

High-resolution Fe2p and Cl2p spectra of doped polymers:

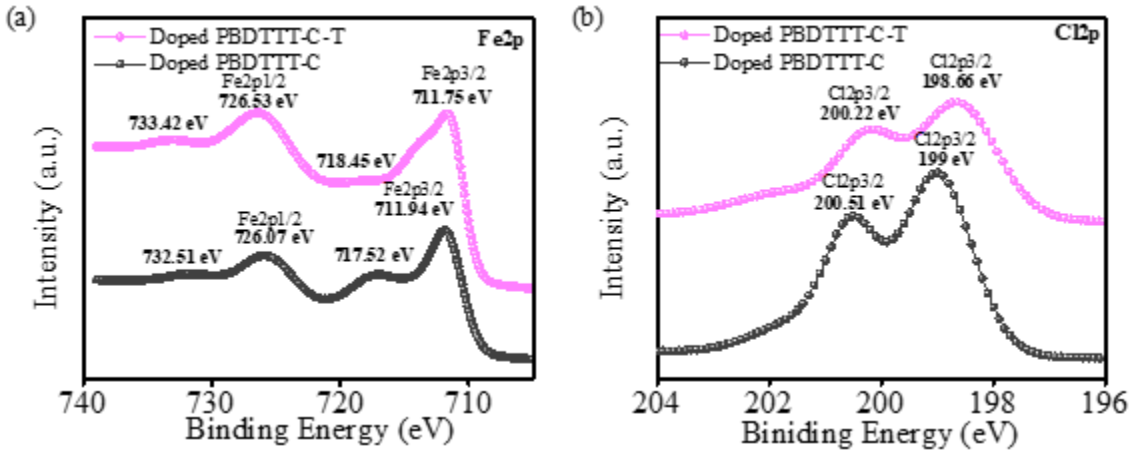

Figure S6. Core level a) Fe2p and b) Cl2p XPS spectra.

High-resolution C1s, O1s and S2p spectra of doped polymers:

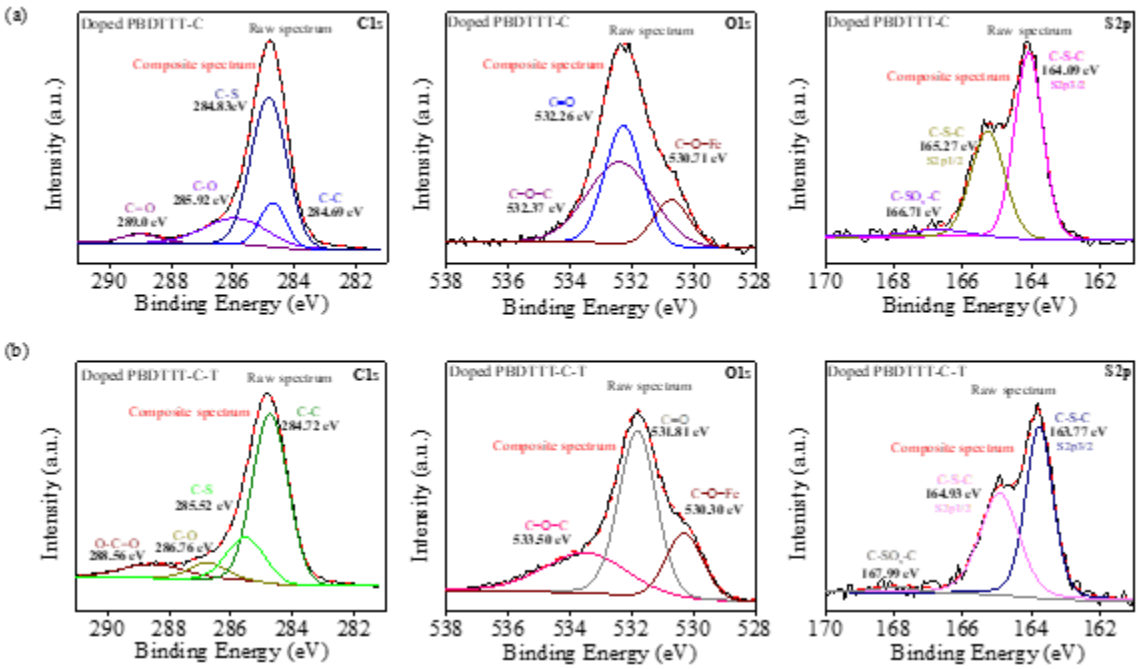

Figure S7. Core level C1s, O1s and S2p XPS spectra of a) doped PBDTTT-C and b) doped PBDTTT-C-T.

UPS valence band spectra of the organic hybrids:

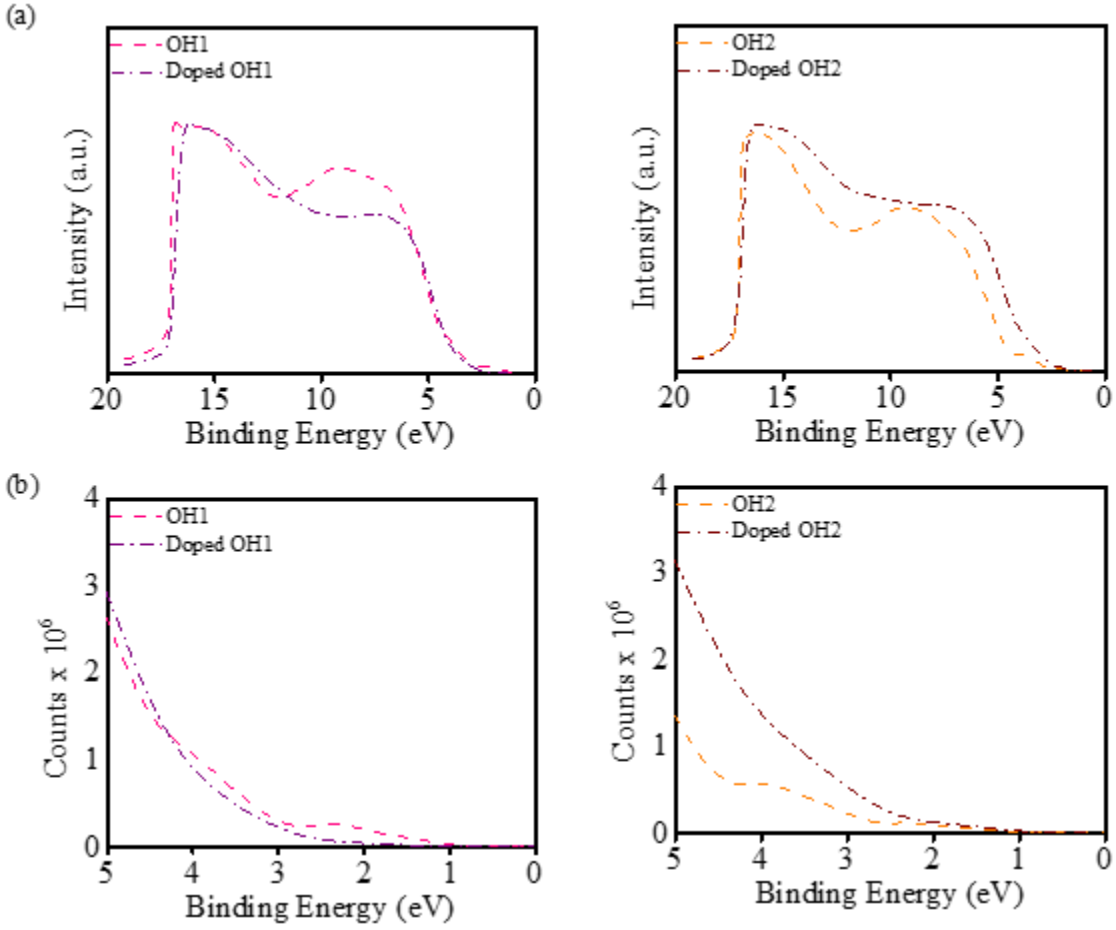

Figure S8. a) UPS valence band spectra (He I radiation) of OH1 and OH2 in pristine and doped conditions. b) A magnified view of the low BE region showing the DOVS.